AN ABSTRACT OF THE DISSERTATION OF

Joel Edward Geier for the degree of Doctor of Philosophy in Geology presented on December 10, 2004.

Title: Groundwater Flow and Radionuclide Transport in Fault Zones in Granitic Rock

Abstract approved:

Redacted for privacy

Roy D. Haggerty

Fault zones are potential paths for release of radioactive nuclides from radioactive-waste repositories in granitic rock. This research considers detailed maps of en échelon fault zones at two sites in southern Sweden, as a basis for analyses of how their internal geometry can influence groundwater flow and transport of radioactive nuclides.

Fracture intensity within these zones is anisotropic and correlated over scales of several meters along strike, corresponding to the length and spacing of the en échelon steps. Flow modeling indicates these properties lead to correlation of zone transmissivity over similar scales.

Intensity of fractures in the damage zone adjoining en échelon segments decreases exponentially with distance. These fractures are linked to en échelon segments as a hierarchical pattern of branches. Échelon steps also show a hierarchical internal structure. These traits suggest a fractal increase in the amount of pore volume that solute can access by diffusive mass transfer, with increasing distance from en échelon segments. Consequences may include tailing of solute breakthrough curves, similar to that observed in underground tracer experiments at one of the mapping sites.

The implications of échelon-zone architecture are evaluated by numerical simulation of flow and solute transport in 2-D network models, including deterministic models based directly on mapping data, and a statistical model. The simulations account for advection, diffusion-controlled mixing across streamlines within fractures and at intersections, and diffusion into both stagnant branch fractures and macroscopically unfractured matrix.

The simulations show that secondary fractures contribute to retardation of solute, although their net effect is sensitive to assumptions regarding heterogeneity of transmissivity

and transport aperture. Detailed results provide insight into the function of secondary fractures as an immobile domain affecting mass transfer on time scales relevant to field characterization and repository safety assessment.

In practical terms, secondary fractures in these en échelon zones are not indicated to limit release of radiation to the surface environment, to a degree that is significant for improving repository safety. Thus en échelon zones are to be regarded as detrimental geologic features, with potentially complex transport behavior which should be considered in the interpretation of in-situ experiments.

Groundwater Flow and Radionuclide Transport in Fault Zones in Granitic Rock

by

Joel Edward Geier

A DISSERTATION

submitted to

Oregon State University

in partial fulfillment of
the requirements for the
degree of

Doctor of Philosophy

Presented December 10, 2004
Commencement June 2005

Doctor of Philosophy of Joel Edward Geier presented on December 10, 2004.

APPROVED:

Redacted for privacy

Major Professor, representing Geology

Redacted for privacy

Chair of the Department of Geosciences

Redacted for privacy

Dean of the Graduate School

I understand that my dissertation will become part of the permanent collection of Oregon State University libraries. My signature below authorizes release of my dissertation to any reader upon request.

Redacted for privacy

Joel Edward Geier, Author

ACKNOWLEDGEMENTS

I am deeply grateful to all of the members of my committee for their enduring patience, helpfulness and flexibility in what turned out to be a very long process.

I thank my Major Advisor, Roy Haggerty, for his extreme helpfulness in offering encouragement, ideas and suggestions on interpretations, as well as a great example of commitment to scientific inquiry, and a good sense of humor to boot.

I also owe special thanks to John Logan, for helpfulness and sacrifice of his own time in sharing insights on fault-zone structure, for joining in the field work, and in general as a wise and patient voice of encouragement throughout the process.

I owe Bob Yeats thanks for his consistent encouragement, and for his guidance both in the realm of active faulting and in the realm of geological thinking, which was a new challenge for me, coming to this department as I did from an engineering background.

My thanks also go to Jack Istok, in particular for his emphasis on physical understanding of processes, and for his always calm and helpful attitude.

I thank Court Smith for his helpfulness in his role as Graduate School representative, in helping me to navigate through the process, as well as for the fresh perspective he has brought on the social dimensions of my research.

This research was funded by the Swedish Nuclear Power Inspectorate (SKI), in part through a fellowship grant to Oregon State University. My special thanks go to Björn Dverstorp (now with the Swedish Radiation Protection Institute) for his early encouragement in this research, as well as many good discussions on flow and transport in fracture network models and for his continuing encouragement to finish. I also thank Bo Strömberg and Eva Simic for their ongoing encouragement, and for being so understanding when I needed to balance work on other ongoing projects against this research.

Also at SKI, I wish to thank Fritz Kautsky in particular for his support of the mapping study at the Ekolsund/Grillby site. Öivind Toverud, Benny Andersson, and Kristina Lilja of SKI have also provided many helpful insights on the context of this work with respect to radioactive-waste repository safety.

I thank Sven Tirén of Geosigma AB for many hours sharing his enjoyable company and for sharing his vast knowledge of Swedish geology and cultural history, whether in the southern Swedish highlands or walking over the ice to check fracture patterns on the

archipelago off the northern Baltic coast of Uppland in early spring. His help and suggestions on the mapping at both Äspö and Ekolsund were indispensable to this research. Thanks also go to Krister Wedholm, and Thomas Sträng of Geosigma AB for their participation in the field mapping and analysis of data from Ekolsund, and for their tolerance of my cooking.

At Oregon State University, I wish to thank Sherman Bloomer, Anita Grunder, and Andrew Miegs in the Geosciences Department, and John Selker in the Bioresources Engineering Department, for helpful insights and encouragement at various stages of my tenure as a graduate student. I would also like to thank George Moore and John Dilles for helpful comments on my research proposal. Thanks also go to my fellow graduate students in the hydrology group, especially Sebastian Geiger, Sean Fleming and Mike Kelley. Special thanks go to Karen Logan and Joanne van Geest in Geosciences, and Marianne Mesford at OSU Foundation for their helpfulness in getting through these years.

My sincere thanks also go to Jonathan Caine, Tim Hicks, Jim Evans, Craig Forster, Attila Aydin, Leslie Smith and Tom Clemo for helpful responses to questions and useful suggestions on my research topic.

This research builds on the experience of nearly 25 years of alternating university studies and consulting work. It is scarcely possible to thank all of the people who have helped me over the years. However, I would like to recognize and thank a few individuals who were particularly helpful.

At the University of California, Berkeley, I owe Michael Hood thanks for getting me started in rock mechanics with my first technical job as a laboratory technician, and for his encouragement in pursuing a graduate degree – even if it took me a while. Neville G.W. Cook was a great inspiration as a teacher, scientist, and simply as a person I am grateful to have known. Among other things I particularly owe to him the encouragement to stick with a difficult course in finite-element theory which proved useful in the long run. Paul Witherspoon and T.S. Narasimhan provided my first introduction to fluid flow in rock, and Jane C.S. Long introduced me to the specialty of fracture flow, where rock mechanics meets fluid flow. I will always value the memory of my friend and co-worker, Duncan Ellinger. Among my fellow students in Berkeley, I particularly appreciated the friendship and stimulating discussions with Levent Tutluoglu, Ziqiong Zheng, Deb Hopkins, John Kemeny, Galen Hesler, Cliff Schenkel, and Naresh Dhar.

In my consulting work at Golder Associates, I owe much to the stimulating environment fostered by the many colleagues who participated in the fracture-flow group, including Bill Dershowitz, Glori Lee, Eric Labolle, Tom Doe, Andy Thomas, Ian Miller, Charlie Wilson, Scott Warner, Todd Schrauf, John Black, Mark Brightman, Lars Hässler, and Paul LaPointe.

I owe special thanks to Hakim Benabderrahmane and Yrjö Lintu for their friendship during my time in Uppsala. I also thank Masahiro Uchida of PNC for his insights and good company in our earliest attempt to understand the fracture zones around Äspö.

From my brief and tentative return to graduate school at Washington State University, I would like to thank Richard Thiessen, John Watkinson, David Gaylord, and Rachelle Allen-King for their particular helpfulness.

I have also benefitted greatly from interactions with my co-workers on projects over the years, who have shared their insights and provided encouragement. Yvonne Tsang and Chin-Fu Tsang have both been inspirational to work with, on the SITE-94 and INSITE projects for SKI, respectively. I have appreciated the opportunities to work with Cliff Voss, Pierre Glynn, Anders Wörman, Shulan Xu, Ghislain de Marsily, Ove Stephansson, Adrian Bath, Neil Chapman, Peter Robinson, and Philip Maul as colleagues in the SITE-94 and INSITE projects.

I would also like to thank my colleagues in the European Union RETROCK project, in particular Ivars Neretnieks, Aimo Hautojärvi, Antti Poteri, Vladimir Cvetkovic, and Johan Andersson.

For the present research, I would like to thank the staff of the Swedish Nuclear Fuel and Waste Management Co., especially Olle Olsson, Anders Winberg, and Mansueto Morosini, for their helpfulness during our mapping near Äspö, and for the loan of a ladder. Thanks also go to the Swedish Roadway Authority (Vägverket) and the Swedish police for permission to map along the E-18 motorway at the Ekolsund site.

I thank our good friends and former neighbors Suzanne Agduhr and Verner Eronen for joining me on initial scouting of the area, and Verner Eronen again for help in assembling the frame used to establish a rectilinear grid in the mapping. Lorna Logan deserves abundant thanks for her help and good cheer during the field mapping at the Äspö site.

I also thank Lena Glantz Eriksson and Göran Eriksson of Brunnsta Gård farm for their hospitality and enjoyable discussions of farming, rocks, and groundwater during visits to the Ekolsund site.

Finally, it is impossible to think of doing this work without the support of family and friends over the years, especially Becky for her long-running love and patience, and our children, Wil, Nik and Martha for their love. Thanks also to Karl and Kathy, Max and Gilda, Hans and Marilyn, and Lisa and Mike for their help in many ways over the years.

CONTRIBUTIONS OF AUTHORS

Chapters 4, 5 and 6 of this dissertation are written in the form of papers that are intended for publication subsequent to completion of this thesis. The individuals mentioned below have contributed substantially to the research on which these chapters are based, although the texts of these chapters do not yet incorporate their specific views:

Chapter 4 describes an analysis of spatial variability in en échelon fault zones at two sites in Sweden, Äspö and Ekolsund. John M. Logan and Sven A. Tirén participated in the planning and execution of the field mapping at the Äspö site. Sven Tirén also did so at the Ekolsund site, and coordinated additional investigations which contribute to the understanding of the geologic context. John Logan, Sven Tirén, and Roy Haggerty contributed ideas and comments on the analysis and toward the understanding of results.

Chapter 5 describes an analysis of hierarchical structure in en échelon fault zones based on data from the same sites. Roy Haggerty contributed ideas on the interpretation of the block-size distribution data and relationship to transport. John Logan contributed ideas on the structure and genesis of fault zones. Sven Tirén assisted in planning and execution of the field work, as for the previous chapter, and contributed suggestions on the interpretation.

Chapter 6 evaluates the role of secondary fractures for transport in en échelon fault zones. Roy Haggerty contributed numerous suggestions on the method of modeling and interpretation of results.

TABLE OF CONTENTS

Page

TABLE OF CONTENTS (Continued)

Page

TABLE OF CONTENTS (Continued)

LIST OF FIGURES

LIST OF FIGURES (Continued)

LIST OF FIGURES (Continued)

LIST OF FIGURES (Continued)

LIST OF TABLES

DEDICATION

To Becky, Wil, Nik and Martha

Groundwater Flow and Radionuclide Transport in Fault Zones in Granitic Rock

1. INTRODUCTION

Granitic rock[1] is a major constituent of continental crust. In geologic provinces such as the Canadian Shield in North America and the Fennoscandian Shield in Europe, large expanses of granitic rock lie close to the ground surface, and are a dominant factor in the regional hydrology.

In hydrogeologic studies, granitic rock is sometimes treated as impermeable or nearly impermeable, due to its typically low permeability relative to sedimentary rock and unconsolidated sediments. The hydraulic conductivity of an intact piece of granite without macroscopic fractures is extremely low (on the order of 10^{-13} m/s). Seepage of groundwater through such rock is so slow as to be negligible for many practical situations, if more permeable rocks such as sediments are present.

However, at shallow depths of less than a few km, granitic rock accommodates strain primarily by brittle processes including brittle fracture, shear displacements along fractures, and cataclasis. The fractures (joints or simple faults) may connect to form networks with discrete paths via which advective transport is rapid. The small amount of contact area with the rock, per unit volume of flowing water, limits the possibility for transport of dissolved species to be retarded by sorption to the rock surface, or diffusion into the rock.

---

[1] In this dissertation, the term "granitic rock" is used in the sense of the broader definition of granite as "any holocrystalline quartz-bearing plutonic rock" (Bates and Jackson, 1984), versus more specific petrologic definitions. The bedrock of the first site from which new data are presented here is mainly monzonite to quartz monzonite, with some diorite, granodiorite, and granite, based on petrologic analyses discussed in Section 2.2. The bedrock at the second site is mainly granodiorite to diorite based on field examination. In the field of radioactive-waste repository design and safety assessment, the term "crystalline rock" is often used as a nonspecific term for granitic (in this broad sense) and gneissic rocks, excluding crystalline salt which poses a distinct set of geoscientific problems, along with other types of crystalline rock which are not currently under consideration as host rock for repositories. The term "granitic" is adopted here as a more specific, although still general term for the geological setting that this work is concerned with. When more specific lithology is meant, terms such as "granite,""granodiorite" *etc.* are used.

Fracture zones, defined as zones within which the fracture intensity exceeds that of the surrounding rock by more than an order of magnitude (Gustafson, 1990), may include active and relict fault zones, and can be important conduits for groundwater flow and contaminant transport in granitic rock. Fracture zones often have complex internal structures in which fracture intensity and connectivity vary from place to place (Committee on Fracture Characterization and Fluid Flow *et al.*, 1996, p. 58). Field studies show that transmissivity and porosity can vary by orders of magnitude along an individual fracture zone (*e.g.*, Andersson *et al.*, 1989ab).

Flow properties may vary within a fracture zone due to large-scale structural trends, local variations in fracturing patterns and intensity, or even the details of pore-space variation within individual fractures (Mazurek *et al.*, 1996; Tsang and Tsang, 1987). Transport may be affected by additional types of heterogeneity, such as spatial variability in the abundance of minerals affecting sorption, or local variation of fragment size in fault breccia, leading to local variability in diffusive equilibration between the relatively mobile water that flows between breccia fragments and the relatively immobile water within breccia fragments (Mazurek *et al.*, 1996; Poteri *et al.*, 2002).

Fractured granitic rock is heterogeneous with respect to groundwater flow and solute transport, over a wide range of scales. Groundwater flow tends to be concentrated in zones of relatively high fracture intensity, manifested on length scales ranging from more than 10 km down to the outcrop scale (Tirén *et al.*, 1996). These zones of high fracture intensity are considered to be formed by brittle faulting, often along zones of ductile deformation which serve as precursors, and often showing evidence of multiple stages of reactivation in the brittle regime, including evidence of fracture mineral precipitation under different pressure, temperature, and chemical regimes (Tullborg *et al.*, 1996; Tirén *et al.*, 1996). These fractured zones combine in larger-scale networks in which the effective flow and transport properties vary both between and within the individual zones.

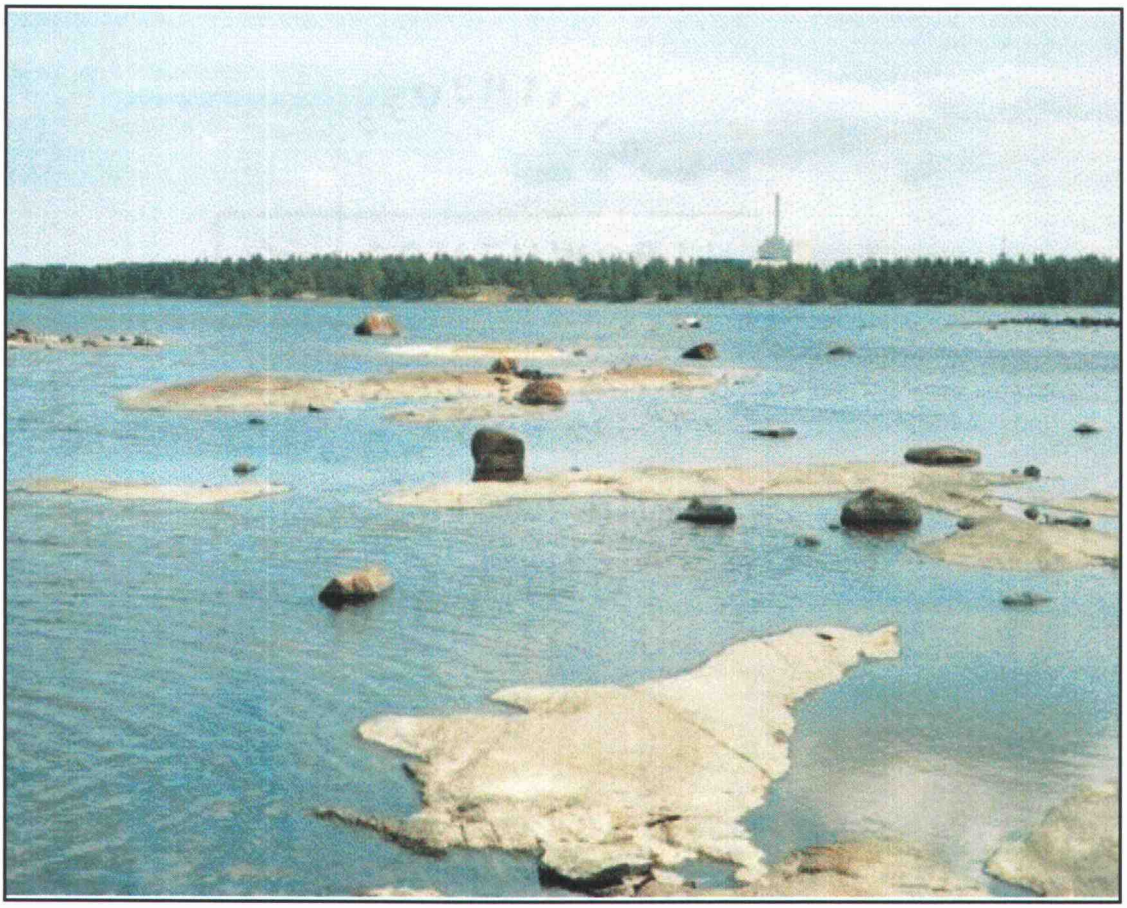

Figure 1-1. A typical view of sparsely fractured bedrock outcrops, on islets along the Baltic coast of SE Sweden near the Äspö study site. The Oskarshamn nuclear power plant on the Simpevarp peninsula is visible in the background.

1.1 Motivation: Why are we concerned with fracture zones in granitic rock?

The hydrologic characteristics of fault zones in granitic rock are of concern for several reasons. In shield settings, fracture zones often serve as aquifers for domestic and municipal water supplies. The characteristics of groundwater flow and contaminant transport in fault zones are essential for monitoring and remediation of contaminated fracture-zone aquifers.

Water flow and solute transport through fault zones are also of fundamental interest for geologic issues including fault mechanics, hydrothermal system evolution, and secondary mineralization.

A particular concern that motivates the present study is the potential for radionuclides (nuclides of radioactive elements) to contaminate the surface environment, if they are released from an underground repository for radioactive waste. Granitic rock is under consideration as an option for permanent disposal of high-level radioactive waste (*i.e.*, spent nuclear fuel) in at least nine countries, and is the primary option in Sweden, Canada, Finland, Japan and Argentina (McCombie, 1997).

High-level radioactive-waste disposal concepts for this geologic setting are based on a multiple-barrier principle, in which the waste is encased in a metal canister which is in turn encased in low-permeability buffer materials such as bentonite, when placed in a deposition hole deep in the bedrock. The metal canister is designed to withstand mechanical stresses and corrosion over periods of thousands of years or more, under hydrological and chemical conditions that are expected to be maintained by the surrounding bedrock and buffer material (McCombie, 1997).

If and when leaks eventually develop in the engineered barriers (canister and buffer), release of radionuclides into the surrounding groundwater is expected to be limited and delayed by fuel dissolution rates as well as a slow rate of transport through the leaking barriers. From that point, the typically very low permeability of intact granitic rock implies that transport of radionuclides via groundwater should be very slow. Hence granitic rock has been proposed to constitute a natural barrier that would impede the release of radiation to the surface environment,

In assessing the risk of radionuclide migration from a repository in granitic rock, a key question is how the multiple scales of heterogeneity interact to control groundwater flow and radionuclide transport. Models which have been developed for sediments or sedimentary

rock may be unreliable, as the basic assumption that an equivalent permeability tensor exists (the continuum assumption) might not be valid at any scale of practical relevance. A scientific consensus has developed over several decades of research, that the discrete nature of fractured crystalline rock such as granite needs to be represented (Committee on Fracture Characterization and Fluid Flow *et al.*, 1996). The work presented in this dissertation aims to further that understanding, by examining how the detailed geometry of fractures in a particular class of discrete structures, en échelon fault zones, can affect groundwater flow and radionuclide transport.

1.2 Objectives of this study

The general aim of this study is to investigate the role of fault-zone architecture for fluid flow and solute transport in granitic rock. This is done by means of a descriptive, statistical approach, in which fault-zone architecture is described in terms of statistics obtained from field mapping, and the statistics thus obtained are used to construct models with the same statistical properties.

An alternative approach is to model the development of fault zones by a mechanistic, genetic approach, using knowledge of the tectonic history and mechanical properties of the rock in combination with rock mechanics models to simulate the sequence of fracture system evolution. This approach has been applied to model fracture system development in relatively young rocks with simple deformational histories (*e.g.*, Hestir *et al.* 2001). However, for sites with a long and complex structural history, especially the Precambrian rocks of the Canadian Shield or Fennoscandian Shield, modeling of fault-zone structure from a mechanistic, genetic perspective is likely to be neither tractable nor fruitful. In many cases, the sense, amount, and sequence of offset along these structures are difficult to ascertain, even if field evidence (*e.g.* presence of breccias) indicates they were at some point fault zones.

In this study, the descriptive, statistical approach is the main line of investigation. However, results of mechanistic models and past experimental studies are used to guide the formulation of descriptive models. The specific goals are:

- Examine field evidence for variability and hierarchical aspects of fault-zone architecture on scales from 1 cm to 1 km,
- Formulate models to describe spatial variation and hierarchical aspects of fault-zone architecture.
- Evaluate the hydrologic and transport consequences of fracture-zone structural variability and hierarchical structure.
- Assess the implications for large-scale modeling of flow and solute transport in granitic rock.

These goals are addressed as a series of scientific papers, which form Chapters 4 through 7 of this dissertation. This work is supplementary to previous research on statistical description of joint sets in crystalline rock (*e.g.* Dershowitz, 1984), which describes the background fracture

systems within which fault zones (or fracture zones, in more generic terms) are distinguished by a much higher intensity of fracturing.

2 BACKGROUND

2.1 Site Descriptions

Detailed maps of fracture geometry were developed from two sites in Sweden. The first of these sites, on the island of Äspö in coastal Östergötland (Figures 2-1 and 2-2), is the site of the Äspö Hard Rock Laboratory, a 450 m deep underground laboratory (Bäckblom and Karlsson, 1990). Geologic, geophysical, and hydrologic data are available from more than 15 years of intensive investigations at this location, during investigations prior to and during the construction of the underground laboratory (Stanfors *et al.*, 1991; Geier *et al.*, 1996b), as well as more recent data from the laboratory construction. Two areas of the mainland adjacent to Äspö are presently under investigation as two of the three candidate sites in Sweden for proposed construction of a high-level radioactive-waste repository.

The second site, near the village of Ekolsund in southern Uppland (Figure 2-3) has been the focus of a study of lineament-interpretation methodology, sponsored by the Swedish Nuclear Power Inspectorate since 2001. Detailed mapping of fracture zone internal architecture, including results for the en échelon zone presented in this dissertation, was performed as one component of that study. The site is <u>not</u> a candidate repository site, in the Swedish radioactive-waste disposal program.

The difference in level of investigation for the two sites results in a disparity in the level of information available on the geologic history and structural development in the two areas. This justifies a relatively extensive account of the geologic history of the Äspö site, relative to the Ekolsund site. However, both sites are similarly positioned with respect to the main tectonic events that affected the brittle-deformation history of this region, and therefore comparable types of structures are to be expected at the two sites.

2.1.1 Äspö, eastern Småland

Äspö is a 1.5 km^2 island in the coastal archipelago along Sweden's southeastern Baltic coast (Figure 2-1). The dominant lithology on the island is a suite of Lower Proterozoic igneous rocks of variable composition (mainly quartz syenite and granite grading to granodiorite and quartz monzodiorite), near the boundary of the Svecofennian and Gothian provinces of the

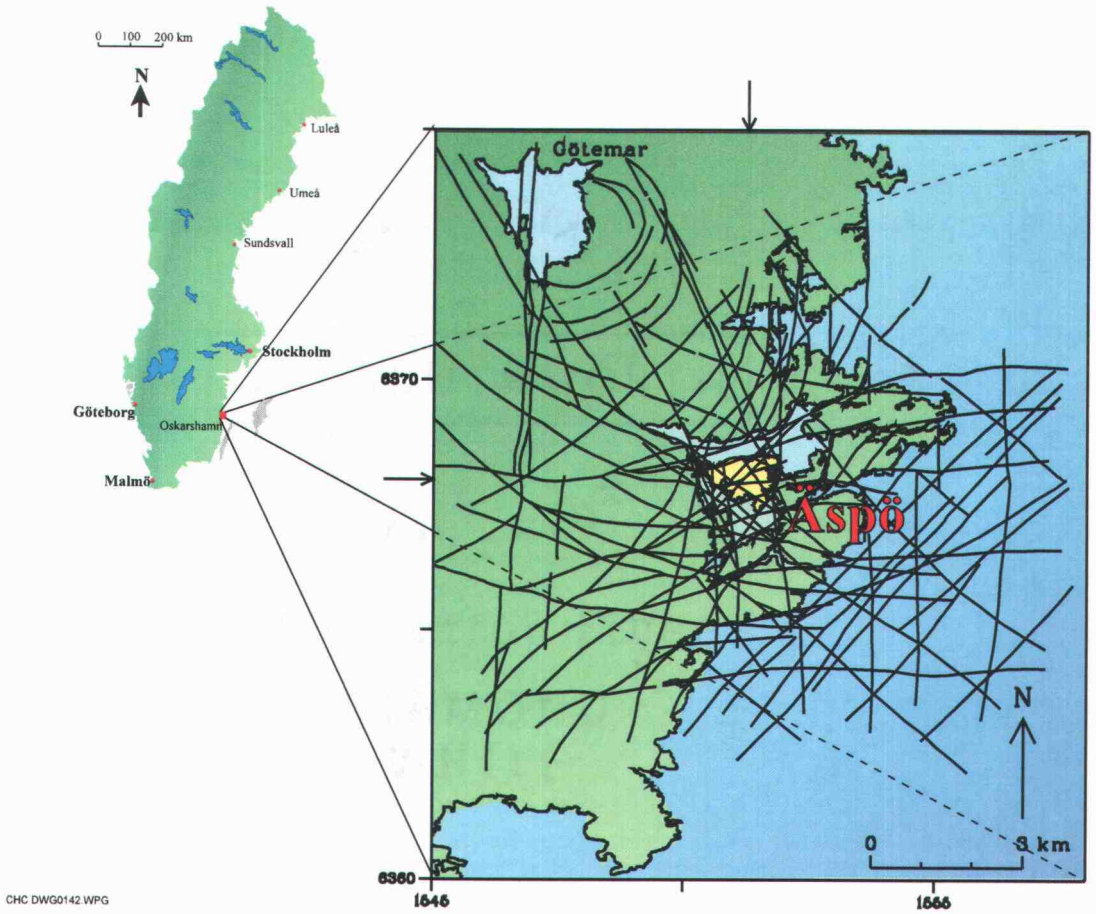

Figure 2-1. Location and regional structural setting of Äspö, Sweden. Äspö is the island in the center of the inset box. Lines show the pattern of regional lineaments interpreted as fracture zones, based on elevation, geophysical and remote-sensing data (Tirén *et al.*, 1996).

Baltic Shield (Anderson, 1978; Gorbatschev, 1980). As summarized below, these rocks have been subject to a long history of ductile and brittle deformation, leading to multiple sets of fault zones, including the en échelon fault zones considered in this study.

The glaciated upper surface of the bedrock is well exposed on outcrops, and has been mapped in terms of bedrock lithology and brittle deformation features. The subsurface has been studied to depths in excess of 1 km by geologic, geophysical, hydrologic, and geochemical methods, in more than 20 shallow (less than 200 m deep) percussion-drilled holes and 16 deep core-drilled holes (up to 1000 m deep) that were drilled from the surface, and from more than 4 km of mapped tunnels and shafts, extending to a depth of 450 m.

Mapping for the present study (Figure 2-2) was performed on a N striking en échelon fracture zone, exposed on the shoreline about 50 m south of the reference point P47 on Äspö Trench 3, as described by Kornfält and Wikman (1988).

Brief geologic history of Äspö vicinity focusing on major tectonic events

The oldest rocks exposed in the vicinity of Äspö are metamorphosed sedimentary and volcanic rocks in the Blankaholm area 20 km to the north. The metasedimentary rocks have been constrained to 1.87-1.86 Ga (Sultan *et al.*, 2004). Approximately 1.81 Ga to 1.76 Ga, these oldest rocks were intruded by an igneous suite belonging to a late stage of the Trans-Scandinavian Igneous Belt (Kornfält *et al.*, 1997). These igneous rocks range in composition from granite and quartz syenite to granodiorite and monzodiorite (Bergman *et al.*, 1998), and account for the dominant lithology of the bedrock at the present-day erosional level on Äspö (Kornfält and Wikman, 1987; Kornfält and Wikman, 1988). A modal analysis of these rocks from the nearby Simpevarp peninsula (Wahlgren *et al.*, 2003), shows compositions from monzodiorite to quartz monzodiorite, quartz monzonite, monzogranite and granite. Contacts between these rock types are locally gradational or migmatitic, and are not always discernible in the field (Tirén *et al.*, 1996), and by tradition these rocks are referred to collectively as "Småland granites" (*e.g.* Anderson, 1978). Minor sheet-like inclusions of other igneous rock (basaltic to andesitic and later aplite dikes) occurring in the area are interpreted as being approximately coeval with this igneous suite based on magma-mingling and back-veining relationships (Kornfält and Wikman, 1987; Talbot and Munier, 1989). These rocks are interpreted as having formed near a continental margin with the present-day ground surface at a depth of 10 to 15 km in the inferred mountains that had their roots in the Trans-Scandinavian Igneous Belt (Tullborg *et al.*, 1996). Paleomagnetic reconstructions place this area at the margin of the Proterozoic supercontinent (Piper, 1987).

Younger granite bodies were intruded on a smaller scale in the Götemar and Uthammar areas (3 km NW and 6 km SW of Äspö, respectively), as well as at the offshore Baltic island of Blå Jungfrun, 20 km SSE, around 1.4 Ga when the present-day ground surface is interpreted as having been at a depth of about 7 km (Tullborg *et al.*, 1996). Tirén *et al.* (1999) suggest that isostatic uplift accompanying the mid-Proterozoic erosional unroofing of the Trans-Scandinavian Igneous Belt mountains was accompanied by faulting with relative

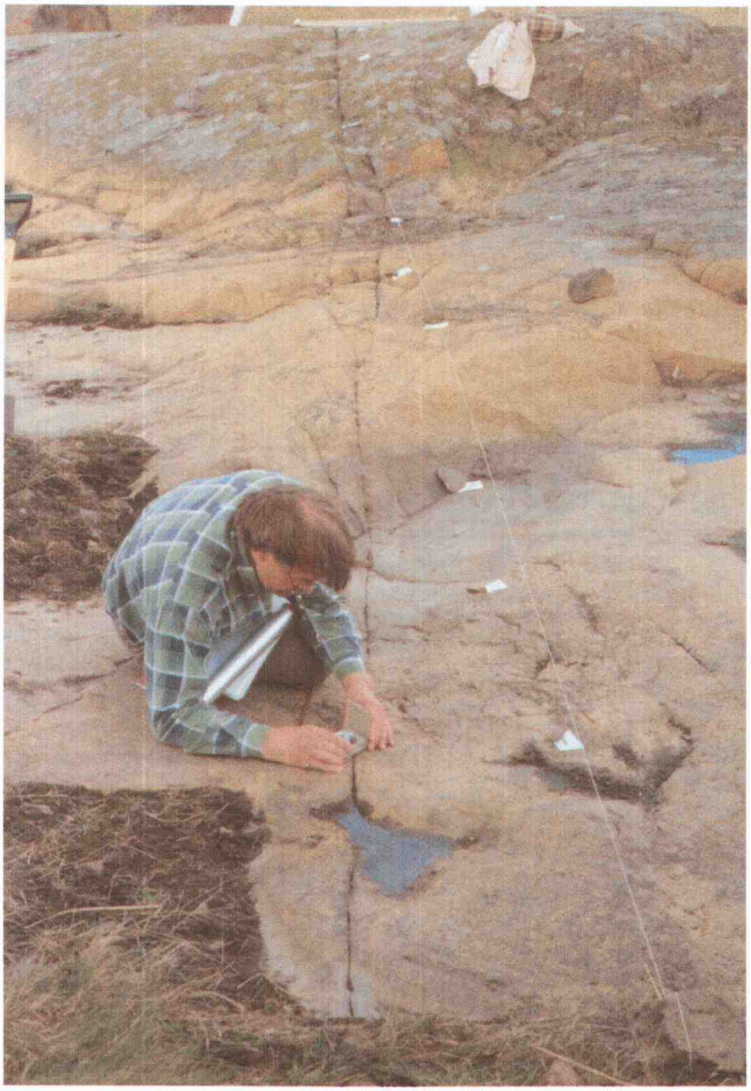

Figure 2-2. View of N striking en échelon fault on Äspö (view looking northward along strike).

vertical displacements on the order of a few kilometers. Ductile and ductile-brittle deformation during the 1.8 to 1.4 Ga period gave rise to three distinct foliations and two sets of mylonite zones in the Äspö/Simpevarp area.

The Sveconorwegian/Grenvillean orogeny affected southwestern Baltica 1.25 to 1.0 Ga BP. The tectonics and consequential state of stress and deformations in this period are complicated, with apparent early Grenvillean rifting between Laurentia and Baltica followed by rotation of Baltica and re-docking with Laurentia (Larsson and Tullborg, 1993) expressed as large-scale shear zones including the Protogine Zone and Mylonite Zone in south-central Sweden, to the west of Äspö. Thrust-faulting in association with the Protogine Zone may be locally expressed by SW dipping thrust faults just west of Äspö (Nordenskjöld, 1944; Tirén *et al.*, 1999).

The youngest igneous rocks in the Äspö area are sub-vertical, N-S striking dolerite dikes 1.0 to 0.9 Ga (Tirén *et al.*, 1999; Larsson and Tullborg, 1993). The age of these dikes coincides with rifting and opening of the Iapetus Ocean between Laurentia and Baltica along a line east of modern-day Greenland (Anderson, 1978; Larsson and Tullborg, 1993), which continued into the Lower Cambrian.

For the last part of Proterozoic (Precambrian) time the region was on a passive margin of the Baltica paleocontinent as the Iapetus Ocean continued to open. Erosion during this time led to formation of a sub-Cambrian peneplain with a relief of only a few tens of meters (Rudberg, 1954), close to the modern bedrock surface.

A switch from divergence to convergence between Laurentia and Baltica in the Late Cambrian (ca. 510 Ma BP) and continuing through the Ordovician (430 Ma BP) led to obduction of Iapetus oceanic crust and several island-arc or microcontinental terranes on the western margin of Baltica, culminating in the Caledonian orogeny and continental collision in the Silurian ca. 425 Ma BP, with extensive eastward thrusting (Stephens, 1988; Larsson and Tullborg, 1993). During much of this time the sub-Cambrian peneplain was below sea level, as marine sediments including Ordovician limestones accumulated in the foredeep over the western margin of Baltica. The compressional stress regime (E-W in the modern configuration) in this period may have led to reactivation of thrust faults and NE and NW striking, strike-slip fault zones in the Äspö area during this period.

The Silurian docking of Laurentia and Baltica was followed by a period of intracontinental extension in the resulting paleocontinent of Laurasia, which is manifested as

backsliding in the accretional wedge in the western Scandinavian Caledonides and westward-dipping normal faults in the southwestern part (Fossen and Rykkelid, 1992).

Uplift and an estimated 5 km of erosion of the Caledonides during the late Devonian and early Carboniferous (390 Ma to 306 Ma BP) led to further deposition of sediments in what is now the eastern part of Sweden, with accumulations of 2 to 3 km of sediments atop the sub-Cambrian peneplain indicated by fission-track dating of fracture minerals (Larsson and Tullborg, 1993). The extensional tectonics (E-W with respect to the modern location of Äspö) and subsequent isostatic compensation in response to the eastward transport of sediments from the Caledonides were accommodated by vertical displacements of tens of meters along vertical faults in the Äspö region (Tirén *et al.*, 1999).

During the middle to late Carboniferous (ca. 325 Ma BP), the convergence of Laurasia and Gondwana is represented by the Hercynian/Appalachian orogeny in a broad belt across what is now southern Europe and eastern North America. This orogeny would have led to compressional stresses directed roughly NNW with respect to the present location of Äspö. The late Carboniferous and early Permian were a time of active volcanism in southernmost Sweden, represented by dike injections within the NW-trending Tornquist Zone which bounds the modern Baltic Shield, and N-S rifting in the Oslo region (Larsson and Tullborg, 1993). Corresponding crustal movements in the Äspö region presumably led to further tilting and differential uplift of the sub-Cambrian peneplain (Tirén *et al.*, 1999).

The late Carboniferous and Permian rifting at the end of the Paleozoic was followed by the Mesozoic break-up of the Pangea supercontinent. In the Baltic region, the main consequences of this break-up were reactivation of the Tornquist Zone on the south boundary of the Baltic Shield, during the opening of the Tethys Sea as Gondwana and Laurasia separated , and the opening of the Norwegian-Greenland Sea Rift and subsequent sea-floor spreading, forming a passive margin (Kearey and Vine, 1990; Larsson and Tullborg, 1993). Effects of these events interior to the Baltic Shield appear to have been minor away from the Tornquist Zone, with erosion of Paleozoic sediments and deep weathering of basement by the late Cretaceous, about 80 Ma (Larsson and Tullborg, 1993; Tirén *et al.*, 1999).

Crustal uplift in the Småland highlands inland (west) of Äspö during the late Cretaceous and early Tertiary led to further denudation and some downcutting into the sub-Cambrian basement. These events are indicated by erosional scarps south of the Småland highlands, and vertical relative displacements along faults in neighboring portions of southern

Sweden (Lidmar-Bergström, 1991). However, over the main part of southeastern Sweden, the present ground surface coincides with the sub-Cambrian peneplain (Tirén *et al.*, 1999).

Repeated glaciations in Quaternary time, culminating with the Weichselian glaciation 20,000 to 18,000 years BP, produced lithospheric loading by ice thicknesses of up to 2.5 km. Striations showing the last direction of ice movement are visible on the exposure that was mapped in this research. The Weichselian ice cap melted approximately 12,000 years ago, leaving Äspö below sea level. Post-glacial isostatic rebound of the lithosphere is ongoing at a rate of approximately 1 cm/year (Larsson and Tullborg, 1993). Post-glacial neotectonic features associated with this uplift, with displacements of up to 25 m, have been documented in northern Sweden (Lagerbäck and Witschard, 1983). Nordenskjöld (1944) found evidence of lesser displacements along faults in the vicinity of Äspö.

The net result of this long and complex tectonic history has been the formation and repeated activation of multiple sets of fracture zones, including a steeply dipping NE-striking set that formed by reactivation of the early mylonites, as well as steeply-dipping NW-striking and NNW-striking fault zones, and gently dipping to sub-horizontal fracture zones of variable strike. The later deformations tend to be taken up along existing fault zones bounding rock blocks. Many of these fault zones have been reactivated in a different sense of shear in the later deformation episodes, in response to changes in the direction of maximum compressive stress (Tirén and Beckholmen, 1990; Tirén *et al.*, 1996).

The current direction of the regional maximum compressive stress in southern Sweden is interpreted from overcoring and hydraulic fracturing stress measurements to be NW and nearly horizontal. This direction of the maximum compressive stress is attributed to ridge-push forces from continued spreading on the Norwegian-Greenland Sea ridge. Hydraulic fracturing stresses measurements at the Finnsjön site in northern Uppland indicate that the vertical stress is the minimum principal stress down to depths of about 500 m (Bjarnasson and Stephansson, 1988; Stephansson *et al.*, 1991). Hence subhorizontal fractures may tend to be more conductive than subvertical fractures at shallow depth, but at greater depths subvertical fractures striking NW may be more conductive.

Hydromechanical modeling by Min (2004) indicates that maximum permeability in fractured granitic rock should be in a direction parallel to planes of incipient slip, which are conjugate to the maximum principal stress direction, at an angle of about 33° for fracture friction properties typical of Swedish granitic sites. Thus at depths of 500 m (a typical design

depth for high-level radioactive waste repositories) or deeper, the expected directions of maximum fracture permeability are expected to be about 33° to either side of the NW direction, *i.e.* W to WNW or N to NNW.

2.1.2 Ekolsund, southern Uppland

The Ekolsund site is in southern Uppland, on the west side of Ekolsundsvik, an inlet (*vik*) of Lake Mälaren, between Stockholm and Enköping (Figure 2-3). A unique set of four nearly parallel exposures up to 15 m high and 500 m long are provided by the roadcuts for the two roadways of the E-18 motorway adjacent to the bridges over Ekolsundsviken. The study site is named for the nearby village of Ekolsund.

The Ekolsund site was selected for a method study sponsored by the Swedish Nuclear Power Inspectorate, primarily to check lineaments identified from prior aerial photos, topographic and remote sensing data by direct mapping on the relatively recent (1987) road cuts for the motorway. The two road cuts are each 30 m to 40 m wide and 5 to 10 m deep, and are separated by a distance of 30 m to 80 m within the area studied.

The cuts thus provide four near-vertical exposures of the bedrock, with a separation of roughly 50 m between exposures. An example of one of these exposures is shown in Figure 2-4. Figure 2-5 shows a closer view of the same exposure, with field annotations from the mapping which is described in Chapter 3. Adjoining horizontal exposures where soil cover was removed (or was absent) along the tops of the road cut provide further insight into the 3-D character of the fracture zones.

This configuration provides an excellent opportunity, in the present study, to evaluate fracturing on scales of 30 to 150 m, which are difficult to investigate on outcrops or tunnels due to the typically more limited scale of exposure. The interpretations of lineaments at Ekolsund also provide a larger-scale context for interpretation of individual fracture zones.

The rock is sparsely to moderately fractured, similar to candidate sites under consideration for a high-level radioactive waste repository in Sweden.

In addition to the fresh exposures along the road cuts, the bedrock is exposed on scattered natural outcrops (pavements and minor scarps or benches of uncertain origin and age). The study site is interpreted from topographic and remote sensing data as being within a block of several square km which is uplifted relative to surrounding blocks, with an elevation of 35 to 50 m above sea level (Tirén *et al.*, 2005). Most of the area of this block is forested, with mossy ground cover and thin soil development as is typical of other uplifted blocks in the area. Adjacent down-thrown blocks are mostly covered with lacustrine sediments and arable soils, with sparse outcrops. The bottom of the adjacent Ekolsund *vik* (narrow inlet) is

20-30 m below the present sea level.

The rock is granodioritic to dioritic based on field exposures (personal communication, Sven A. Tirén, 2003). Over most of the study site (including the areas of the detailed mapping presented here), the rock is weakly foliated. More gneissic rocks and mylonites are found at the eastern edge of the study site, adjacent to Ekolsundsviken.

Geologic history of Ekolsund study area focusing on major tectonic events

The lithology and age of the bedrock at Ekolsund has not yet been analyzed (pending investigations at the University of Uppsala), but by regional association, these rocks are assumed to belong to the early Svecofennian granitoids of the Trans-Scandinavian Igneous Belt, emplaced 1.9 – 1.86 Ga (Larsson and Tullborg, 1993). Thus these rocks are likely to be slightly older than the granitoids in the Äspö region.

The Ekolsund area was similarly situated with respect to most of the major events described for Äspö. The early events include isostatic uplift accompanying the mid-Proterozoic erosional unroofing of the Trans-Scandinavian Igneous Belt, the Sveconorwegian orogeny 1.25 to 1.0 Ga, and emplacement of dolerite dikes during rifting and opening of the Iapetus Ocean, 1.0 to 0.9 Ga. The regional direction of these dikes (the Blekinge-Dalarna dike swarm) is NNW in the Ekolsund region, vs. N-S near Äspö (Gorbatschev *et al.*, 1987), but Ekolsund is at a similar distance from the eastern boundary of the dike swarm.

Ekolsund was closer to the late Cambrian to Silurian convergence between Baltica and Laurentia, and therefore may have experienced a different depth of foredeep sedimentation. Effects of Devonian to early Carboniferous extension and the subsequent Hercynian orogeny were likely similar between the two sites.

The modern bedrock surface at Ekolsund is interpreted as being close to the level of the sub-Cambrian peneplain. This surface may have been distorted by block movements and tilting similar to that seen elsewhere in southern Sweden. Based on an evaluation of digital topographic data, tilted blocks and relative vertical displacements; the block containing the Ekolsund site appears to be upthrown relative to surrounding blocks (personal communication, Sven A. Tirén, 2003). Erosional features suggestive of deep weathering consistent with warm, humid climate such as in the Mesozoic were noted during the field mapping.

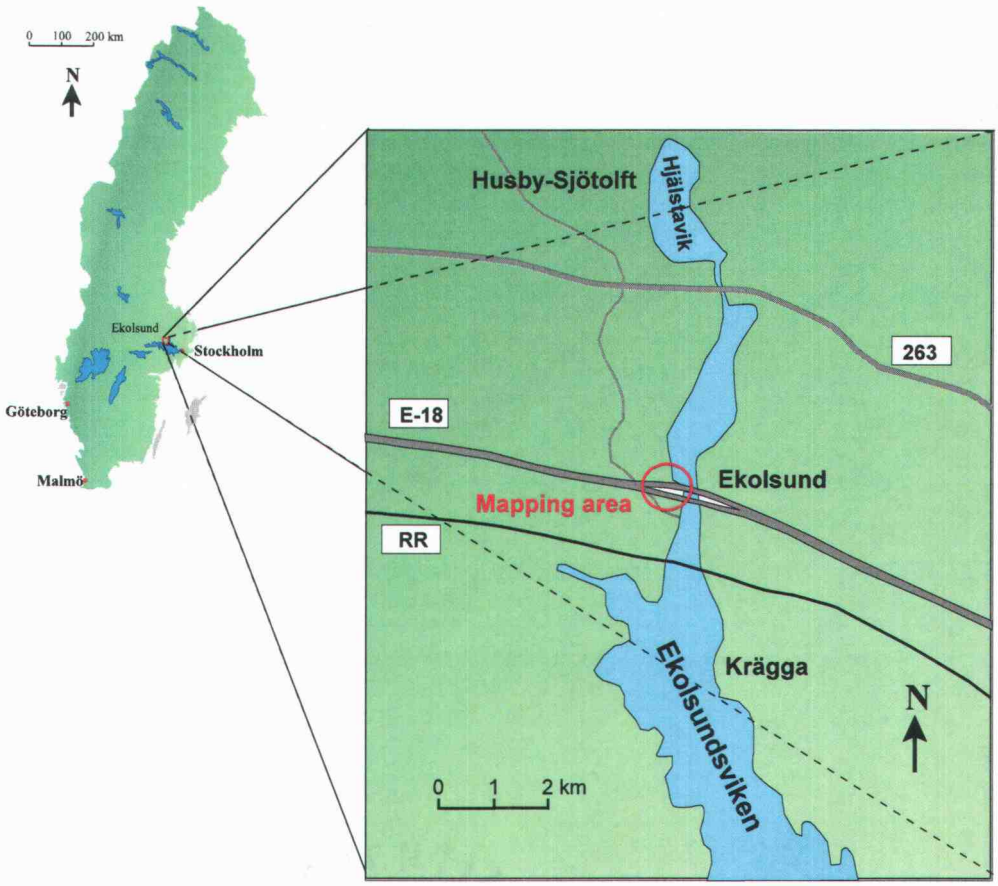

Figure 2-3. Location of the Ekolsund site, southern Uppland, Sweden.

Ice striae from Quaternary glaciation are evident on many of the exposed bedrock surfaces, showing ice movement in a SSE direction, which correlates to the direction of low ridges. One example was found of a pothole approximately 50 cm in diameter on an inclined, glacially polished bedrock surface, tentatively interpreted as having been eroded by a meltwater stream below the glacier. The Ekolsund block is 30 to 50 m higher in elevation than Äspö, so has been subject to subaerial processes for a longer period than the latter site. Based on typical uplift rates of 0.006 m/yr for this part of Sweden (Påsse, 2001), the period of subaerial exposure may have be 5000 years or more.

No stress measurements have been performed at Ekolsund, but the regional stress field described by Stephansson *et al.* (1991) is expected to apply here. Hence subhorizontal

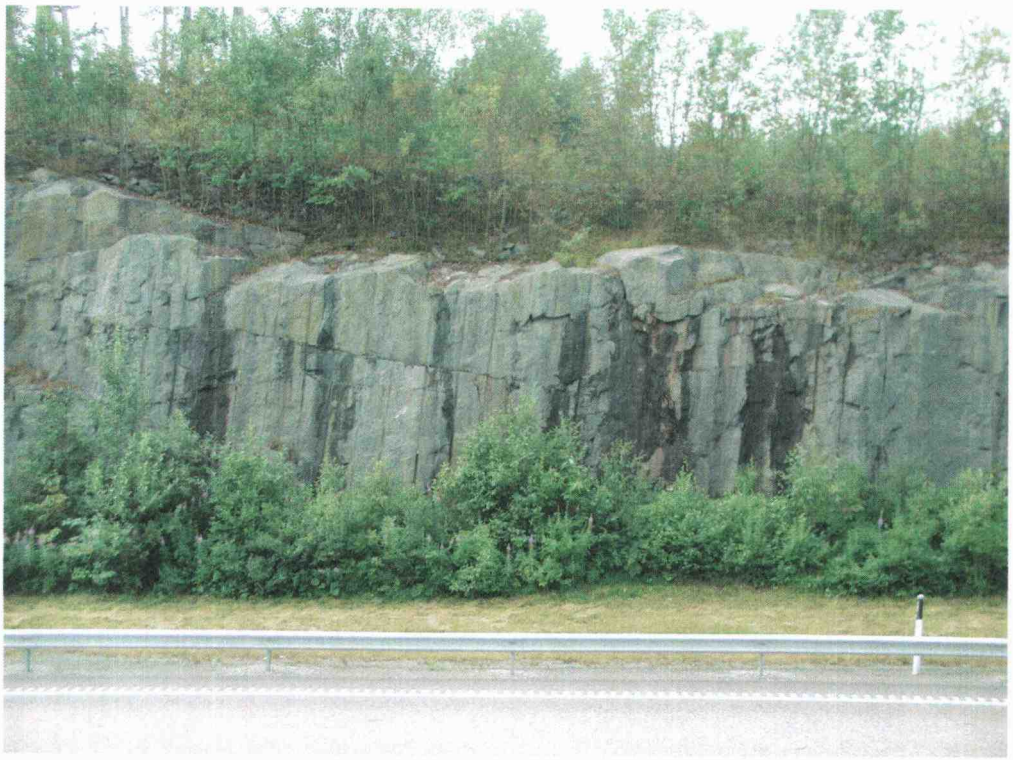

Figure 2-4. Photograph of a portion of the northern road cut, south side at Ekolsund showing exposure forming part of detailed mapping of Zone MY-1 (to right of center), in area which is wet due to groundwater seepage running down face of exposure (apparently mainly from one of the subhorizontal joints). The pattern of joints visible in this photo is typical of the area, outside of zones of more intense fracturing such as Zone MY-1.View is southward, prior to clearing brush for detailed mapping. Note guard rail in foreground for sense of scale. Photo by Sven A. Tirén.

fractures may tend to be more conductive than subvertical fractures at shallow depth, but at greater depths subvertical fractures striking at directions 33° to either side of NW , *i.e.,* W to WNW or N to NNW, may be more conductive.

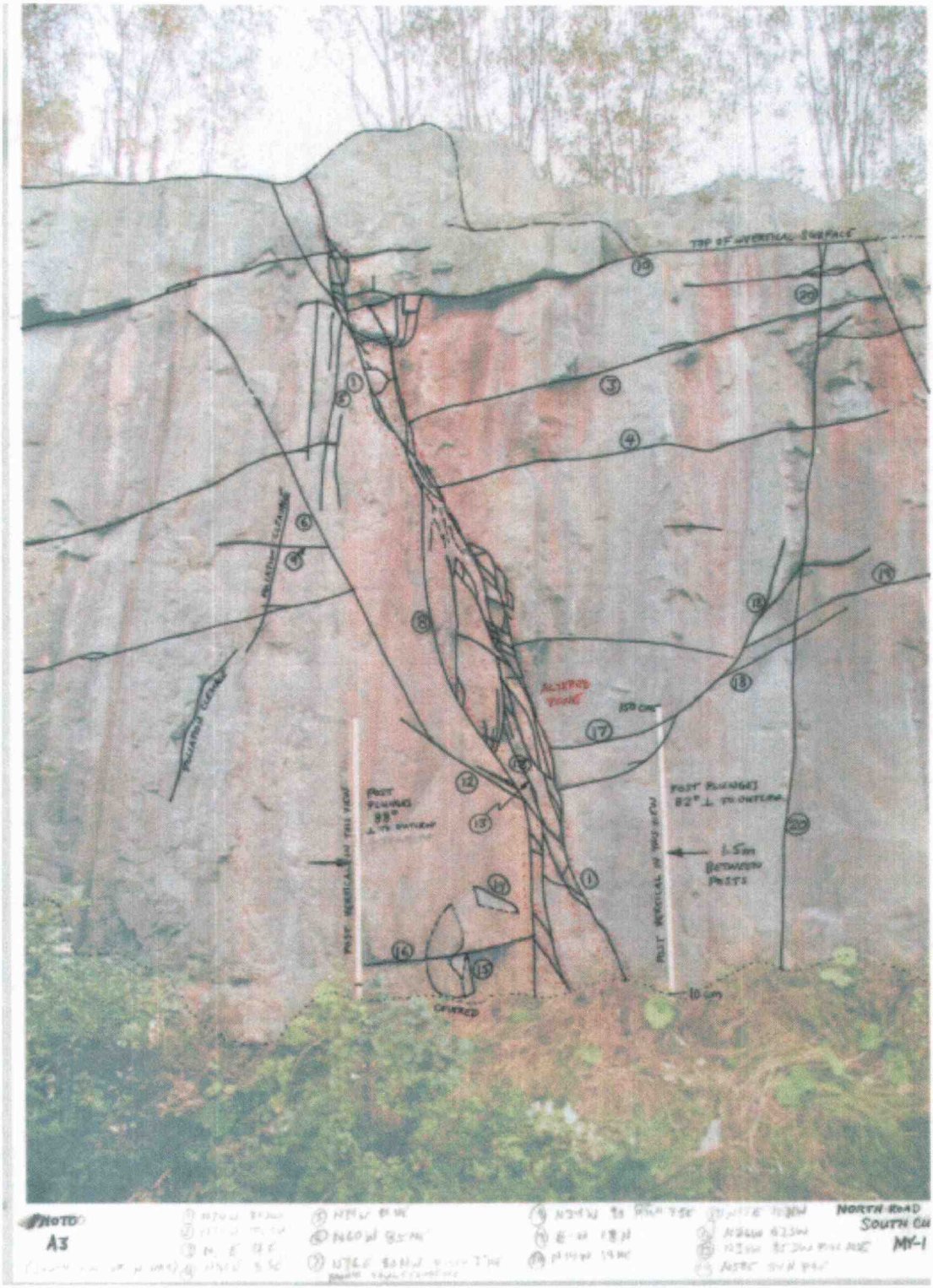

Figure 2-5. Scanned photograph with field annotations from detailed mapping of Ekolsund Zone MY-1, northern road cut, south side. Scale is indicated by the 1.5 m high stakes. Note that adjacent joints as well as fractures within the more intensely fractured area within the zone are mapped. Original photo by Sven A. Tirén.

2.2 Literature review

The following literature review summarizes past research on fault-zone architecture and fractured-rock hydrogeology, focusing on aspects relevant to flow and transport in fault zones in crystalline-rock settings similar to the granitic sites considered in this research. The approach taken in this study follows the general approach of Caine (1999), starting from the viewpoint that faults are made up of certain architectural elements, and endeavoring to understand fault zone hydrologic behavior in terms of those elements.

This literature survey begins with research on fault-zone architecture, starting with observations from field and laboratory studies which lead to basic conceptual models for fault-zone evolution and scaling relationships. Key architectural elements that emerge from this survey are en échelon fractures and échelon steps, splays and other secondary fractures, fault breccias, and fault gouge.

Next we review previous research on the relationships between fault-zone architecture and groundwater flow and solute transport. The key architectural elements of fault zones, fractures and fault breccias, appear to be particularly important elements of pathways for fluid flow and solute transport in granitic rock. The flow and transport properties of individual fractures (including hydromechanical effects) and their aggregate behavior in networks has been the focus of a large body of research over the past three decades. Key developments from that research are reviewed here, with a focus on findings of significance for fault zones in the geologic setting considered here.

A brief review is also given of matrix diffusion, the term used to describe diffusion into the protolith and/or breccia fragments adjoining fractures. Matrix diffusion is considered to be a principal mechanism by which transported radionuclides may be delayed in their passage through a fault zone. Finally we review past efforts to model fault zones in terms of their discrete architectural components.

2.2.1 Fault zone architecture

Structural types that have been identified by investigations at research sites in shield settings in Sweden and Canada include simple and compound fracture zones, diffuse fracture swarms, en échelon fractures, and reactivated mylonite zones characterized by anastomosing fractures (Tirén *et al.*, 1996; Martel, 1990; Andersson *et al.*, 1989b; Davison and Kozak, 1988; Brown *et al.*, 1995). This work is complemented by a large body of field research on fault-zone architecture in sedimentary rocks (*e.g.*, Aydin, 1978; Chester and Logan, 1986; Schulz and Evans, 1998 & 2000) and by laboratory studies of fault fabric development (Logan *et al.*, 1992).

Detailed studies of fault zones reveal a heterogeneous fabric with an intensely comminuted fault core, outside of which the fault zone extends as a fractured "halo" or "damage zone" (Smith *et al.*, 1989; Logan, 1992; Antonellini and Aydin, 1994). The core commonly consists of a macroscopically fractured breccia zone bounded by a pair of intensely comminuted gouge zones along which shear strain is localized (Logan, 1992).

The character of the fault core may vary depending on the lithology of the country rock, amount of displacement across the fault, and secondary mineralization. Fault cores may be present as single slip surfaces (Caine *et al.*, 1991, as cited by Caine *et al.*, 1996), unconsolidated clay-rich gouge zones (Anderson *et al.*, 1983, as cited by Caine *et al.*, 1996), brecciated and geochemically altered zones (Sibson, 1977, as cited by Caine *et al.*, 1996), or highly indurated cataclasite zones (Chester and Logan, 1986).

In sedimentary rocks, fault cores show a reduction in grain size, which is accompanied by reductions in porosity and permeability, particularly when accompanied by mineral precipitation (research as summarized by Caine *et al.*, 1996). Laboratory and field studies (Logan, 1992; Logan *et al.*, 1992) show that further grain size reduction occurs along a regular array of slip surfaces and fractures within the gouge or cataclasite.

In higher-strength granitic rocks such as granite subjected to brittle deformation in the shallow crust, the fault core commonly develops as a breccia zone which may be highly conductive to fluids. For example, at the Äspö research site in Sweden, borehole investigations show a strong correlation between high-flow zones and brecciated zones (Voss *et al.*, 1996). However, with sufficient displacement, shear localization may lead to bands of breccia fragment-size reduction and low-porosity bands similar to that seen in sedimentary

rocks.

The damage zone adjacent to the core may show a variety of fault-related subsidiary structures including smaller faults, veins, fractures, cleavage, and folds (Bruhn *et al.* 1994), all of which may contribute to heterogeneity in the permeability structure and elastic properties of the fault zone (Caine *et al.*, 1996). Modeling studies using a distributed damage evolution model predicts development of damage zones as process zones and branching faults along incipient faults (Lyakhovsky *et al.*, 1997). Given that similar processes can be expected to occur along branching faults, this points toward a possible hierarchical structure within damage zones, a possibility which is considered further in the present study.

Kim *et al.* (2004) have proposed a unified classification system for fault damage zones into three basic categories: tip damage zones (which form around a propagating fault tip), wall damage zones (which may form by the propagation of fault tips and the associated tip damage zones, or with increased slip along a fault), and linking damage zones which form between overlapping échelon fault segments, and which may be either extensional (if the sense of slip is the same as the sense of steps), or contractional (if the sense of slip is opposite to the sense of steps).

Conceptual models for fault-zone evolution

Conceptual models for fault-zone evolution in granitic rock begin with Griffith crack theory (Brace, 1960; Jaeger and Cook, 1979). By this it is assumed that granitic rock contains a large array of pre-existing, minute flaws such as grain boundaries, referred to as Griffith flaws or Griffith cracks. The largest of these flaws may propagate due to stress concentrations at their tips, if they are favorably aligned with respect to the stresses. When all principal components of stress are compressive (as typical of rock at depth), cracks in nominally isotropic rock tend to propagate in a plane perpendicular to the minimum principal stress.

As crack growth progresses, isolated clusters of fractures coalesce in a process of shear localization (*e.g.*, Menendez *et al.*, 1996). Peng and Johnson (1972) and Schulson *et al.* (1999) proposed mechanisms for shear initiation, whereby growth of closely spaced cracks leads to shear failure by buckling-mode failure and rotation of the intervening, slender columns of rock. Shear surfaces may also develop by linkage of cracks in en échelon arrays. Modeling studies (Du and Aydin, 1991; Renshaw and Pollard, 1994) as well as field observations (Olson and Pollard, 1991) suggest that en échelon arrays can develop due to the influence of stress concentrations around propagating cracks on the initiation and propagation of neighboring Griffith flaws. These studies and further research on shear fault localization are summarized in the second chapter of Committee on Fracture Characterization and Fluid Flow *et al.* (1996).

Based on field observations in the Sierra Nevada granite batholith, Martel *et al.* (1988), Martel and Pollard (1989) and Martel (1990) proposed a model for formation of fault zones by linkage between adjacent faults which begin as smaller, non-coplanar, simple strike-slip faults. Dilatant fracturing between zones of overlap between neighboring simple faults develops into fault zones that accommodate strain by distributed brittle deformation, becoming the focus of continued deformation while the rock outside the bounding faults stays relatively unfractured. Kim *et al.* (2004) pointed out the similarity of damage-zone structural features formed across a wide range of scales in strike-slip, normal, and thrust faulting environments, despite the different orientation of these features with respect to vertical.

Childs *et al.* (1996a,b) proposed a model for the evolution of segmented fault traces, wherein the fault is segmented into a set of en échelon fractures formed by bifurcations near the tip of the propagating fault, but these are progressively eliminated by a process of "offset

destruction" leading to a more planar fault with a well-developed core of fault rock (breccia and gouge) in the older portions of the fault closer to the fault center, where the fault has been subject to greater displacement over time. The offsets formed by the initial bifurcation of fracture tip lines are first linked by the growth of relay structures and then, with continued fault growth, rejoining of the en échelon fractures to enclose lenses of deformed rock.

The progressive bypassing and shearing of asperities along a fault result in the generation of additional slip surfaces and an approximately linear increase in fault zone thickness with displacement. At intermediate stages in this development, both fault rock (core) thickness and overall fault zone thickness are increased within and around offsets, but remain small on the intervening segments, leading to a heterogeneous distribution of fault rock. At progressively larger displacements, progressively larger offsets are destroyed and the material transport of fault rock by displacement leads to more uniform distributions of fault rock.

Secondary fractures and splays

Schulson *et al.* (1999) suggest that wing cracks (developing from the tip of sliding cracks and propagating parallel to the maximum principal stress) and splay cracks (developing from the sides of such cracks) are significant for the development of compressive shear faults.

Although linear elastic fracture mechanics predicts only a single opening-mode fracture at a fault tip, multiple splays or joint clusters are commonly observed (Cooke, 1997). Opening-mode splay fractures at fault tips can be produced by stress gradients due to slip gradients, possibly due to spatial variation in frictional properties (Martel, 1997; Cooke, 1997). Cruikshank *et al.* (1991a) advocated the use of kinks and splays (horsetails) at faulted joint tips as indicators of the sense of faulting and state of stress. However, Willemse and Pollard (1998) suggest that the kink angle can be ambiguous depending on effects of cohesive end zones, and suggest that kink angles need to be considered alongside evidence from solution surfaces.

Martel and Boger (1998) have presented results of 3-D elastic modeling which predicts the configuration of wing cracks around a growing fault. Among the implications of this work is a prediction that secondary fractures are likely to be longer near the ends of small strike-slip faults than at their tops and bottoms, so faults are more likely to link end-to-end

than top to bottom, where slip is small.

Field observations of hydrothermal mineralization and alteration along secondary fractures near the ends of faults indicate that these function as very effective fluid conduits, at least during the period when the faults are active (Sibson, 1981; Segall and Pollard, 1983; Martel, 1997). Even when these fractures appear to be 'sealed,' hydraulic tests and in some cases direct observations of fluid flow show these seals are incomplete; thus secondary fractures are critically important to the hydraulic conductivity of faults systems (Martel, 1997).

En échelon fractures

The non-colinearity of fault traces was recognized by Wallace (1973). Segall and Pollard (1980) investigated theoretical stress and displacement fields at duplexes formed by the overlap between fault segments in en échelon arrangements. Aydin and Nur (1985) observed that steps and bends are a fundamental feature of strike-slip faults.

Aydin and Schultz (1990) presented overlap and separation data for 120 examples of en échelon strike-slip faults, and noted an approximately linear correlation over scales of overlap ranging from 10 m to 10^5 m. Based on numerical modeling they suggested fault interaction enhances growth as the inner tips approach one another, but impedes growth after the tips pass.

Cruikshank *et al.* (1991b) described en échelon band faults that propagated toward each other in the Entrada sandstone at Arches National Park. The faults propagated toward each other regardless of the sense of shear or fault step direction.

Based on numerical fracture-mechanics modeling, Du and Aydin (1993) argued that en échelon fractures propagating as Mode I (tensile) fractures converge only if the sense of the step is the same as the sense of displacement along the fault band. Thus Mode I fractures should converge at extensional steps, but diverge at contractional steps. In contrast, Du and Aydin's model results show that en échelon segments propagating as Mode II (shear) cracks converge regardless of whether the sense of a step is the same or opposite to the sense of offset.

Laboratory testing of sandstone samples under triaxial compression stresses and pore pressure (Lin and Logan, 1991) showed that in a rock sample with heterogeneity,

development of secondary fractures in stepovers between en échelon fractures is largely dependent on the geometry of preexisting fractures. This work showed differences in secondary fracture geometries depending on whether the sense of stepping was syn- or antithetic to the sense of shear across the en échelon fractures.

Robeson and Evans (1997) observed that most faults in a system they studied terminated as splays. They also noted that the dip direction of connecting fractures in an en échelon system could be antithetic to the main fractures or unconstrained, depending on whether the step is extensional or contractional.

Myers and Aydin (1997) described faults that develop by slip along preexisting en échelon joint zones and proposed three different styles of development which depend upon the original joint zone step/shear sense. They used numerical modeling to explore the consequences of these different faulting styles for fluid flow.

Fault gouge properties and fabric

The properties of fault gouge have been studied primarily with regard to mechanical properties of faults. Field studies include investigations of cataclasite structure and spatial variability along the Punchbowl fault, interpreted as an exhumed strand of the San Andreas fault in California (Chester and Logan, 1986; Schulz and Evans, 1998; Chester and Chester, 1998). Switek (1994) examined the role of fault gouge for fault-sealing behavior at the Arroyo Grande site in southern California, where a road cut exposes tar-impregnated sands on one side of an anastomosing fault, and tar-free sands on the other side.

Experimental studies include studies of gouge permeability under compression, and the effects of dilation and fabric development during frictional sliding (Morrow *et al.*, 1981, 1984; Morrow and Byerlee, 1989; Switek,1994).

Particle-size distributions within fault gouge have often been characterized as power-law or fractal. Laboratory experiments by Marone and Scholz (1989) showed that synthetic fault gouges subjected to shear tend to stabilize with this type of distribution. A fractal characterization has been used as the basis for recent numerical modeling of shear localization and frictional flow in cataclasites using micromechanical particle-flow models (*e.g.*, Morgan and Boettcher, 1999; Morgan, 1999; Hazzard and Mair, 2003).

The fine grain sizes as well as the wide range of particle sizes implied by a fractal

distribution can lead to low permeability in fault gouge. Permeability of fault gouges from locations along the San Andreas fault in California ranged from around 10^{-21} m^2 to 10^{-18} m^2. Permeability of comminuted rock flours did not differ significantly from that of clay-rich samples, and grain size appeared to be the main determinant of permeability (Morrow *et al.*, 1981; Morrow *et al.*, 1984). In sedimentary rocks such permeability values are low enough relative to the protolith that gouge bands can act as flow barriers (Logan, 1992).

Fischer *et al.* (1998) presented a method for characterization of gas/water relative permeability and detailed pore structures in undisturbed fracture zone samples with cohesionless fault gouge layers under confining pressure, and presented results from mylonites in granodiorite at the Grimsel site in Switzerland. Permeability of the gouge was found to be in the range $4x10^{-14}$ m^2 to $1x10^{-13}$ m^2, as compared with $3x10^{-18}$ m^2 in the protolith. Resin-impregnated sections through the samples revealed a mesh of fractures filled by gouge. In thin section the gouge showed a porous-medium appearance with large rock fragments in a fine-grained matrix, and little apparent fabric development. The relative permeability measurements showed characteristics similar to a porous medium, which the authors attributed to the porous-medium character of the gouge and its elevated permeability relative to the protolith.

Scaling relationships for fault zones and fault zone networks

Numerous recent studies support a view of faults as showing similarities describable in terms of scaling laws that apply across broad scales. A few examples are mentioned here to illustrate the broad range of properties for which scaling of fault zone properties has been observed.

Hull (1988) proposed a correlation model between thickness and displacement for fault zones. Examining normal faults in chalk, Childs *et al.* (1996a) found that fault rock (gouge and breccia) thickness appears to scale linearly with fault displacement, in conformance with Hull's postulated correlation; however, total fault zone thickness was not found to scale linearly.

Lee and Bruhn (1996) found evidence for fractal (self-affine) scaling of fault-surface topography, based on profiles of fault surfaces in the Wasatch fault zone and Oquirrh Mountains, Utah, over scales from 1 mm to 5 km. Kim *et al.* (2004) presented examples

pointing out qualitative structural similarity in fault damage-zone geometry, from scales of centimeters to hundreds of kilometers. Scaling properties such as described in these examples can provide a rationale for extrapolating or interpolating from the scales on which fault zones can be observed, to scales that are more difficult to observe.

2.2.2 Relationships between fault-zone architecture and fluid flow

Recent studies of the relationships between fault-zone architecture and fluid flow include work by Caine (1999), Hicks *et al.* (2000), and Mazurek *et al.* (1996; 2003). These studies form the main scientific backdrop for the present study, in terms of presenting integrated views of fault-zone structural geology and hydrogeological behavior.

Caine *et al.* (1996; as published in Chapter 1 of Caine, 1999) presented a general survey of research on fault-related fluid flow. They described a conceptual model for fault zone architectural styles and associated permeability structures, and proposed a set of "fault zone architectural indices" as a way of classifying fault-zone architecture and relating the structure to the expected fluid-flow characteristics.

When considering fault zones in granitic rock, some architectural elements may be present which are not well described as line segments or plates, for example, volumes of fault breccia, fault gouge, microfracturing and/or alteration along the fractures. Flow and solute transport within architectural elements may be governed by specific physical relations, but the conditions of continuity and mass conservation between such volumes and the fractures must still hold.

Caine *et al.* (1996) proposed four end-member architectural styles of fault zones:

- *Localized conduit*: Localized slip along a single curviplanar surface or along discretely segmented planes. Both fault core and damage zone are absent to poorly developed.
- *Distributed conduit*: Distributed slip accommodated along distributed surfaces and fractures. Fault core is absent to poorly developed; damage zone is well developed.
- *Localized barrier*: Localized slip accommodated within cataclastic zones. Fault core is well developed; damage zone is absent to poorly developed.
- Combined conduit-barrier: Deformation accommodated within a localized cataclastic zone and distributed zone of subsidiary structures. Both fault core and damage zone are well developed.

These end-members are related to expected hydraulic properties of the fault zones.

Caine *et al.* (1996) also proposed a numerical index to quantify a given fault zone's position relative to the last three end members:

$$F_a = \text{(damage zone width)/(total fault zone width)}$$

The ideal case $F_a = 0$ corresponds to the localized barrier end-member, where the entire width of the fault zone is made up of fault core cataclasites. The ideal case $F_a = 1$ corresponds to the distributed-conduit end-member, where the fault zone width is entirely made up of damage zone. Intermediate values of F_a indicate a combination of strain localization (to produce a core) and distributed deformation (to produce a damage zone) which yields a combined conduit-barrier permeability structure.

Caine *et al.* (1996) further defined measures of the mean and variation of F_a as well as a symmetry index:

F_m = mean of F_a values measured at different points along a single fault zone.

$F_{sv} = \max(F_a) - \min(F_a)$

$$F_{sym} = \frac{\text{[(core width)/2 + (hanging wall damage zone width)]}}{\text{[(core width)/2 + (footwall damage zone width)]}}$$

They noted that clay content in the core, or secondary mineralization either in the core or in the damage zone will influence the actual hydraulic behavior, and give examples from Traill Ø, east Greenland, where silicification of the fault core breccias can be interpreted as having produced a shift from syndeformational behavior as flow conduits, to post-deformational behavior as combined conduit-barriers.

Hicks *et al.* (2000) presented a recent review of fault-zone studies of relevance for investigations and modeling of fault-zone heterogeneity. This review gave particular attention to radioactive-waste disposal and hot-dry rock energy generation studies. Based on their review, Hicks *et al.* (2000) explored several simple models of heterogeneous fault zones, including a model of en échelon zones modeled as simple planar fractures linked either by a randomly fractured zone in each fault jog, or by single fractures parallel to the direction of the fault jog. They presented illustrative calculation cases for fault models based on this conceptualization, as discussed later in this chapter.

On a large scale, Sibson (1996) describes how mesh structures comprising faults interlinked with extensional-shear and purely extensional vein fractures can be important conduits for large-volume flow of hydrothermal and hydrocarbon fluids. Sibson proposes these meshes may be self-generating by infiltration of fluids into a stressed, heterogeneous rock, and notes strong directional permeability may develop in the σ_2 direction (*i.e.* parallel to fault-fracture intersections and orthogonal to fault slip vectors).

Mazurek *et al.* (1996; 2003) proposed conceptual models for fault zones in granitic rock on the scale of decameters, based on mapping and detailed characterization of water-bearing fractures and faults observed in tunnels at the Äspö Hard Rock Laboratory in SE Sweden. The authors described five types of water-conducting features: (1) single fault with discrete master fault, splay cracks and discrete steps, (2) swarm of single faults (two or more master faults with splays, not well connected), (3) fault zone (two or more master faults with connecting splays), (4) fault zone with rounded geometry (two or more master faults with connecting splays and lens-shaped geometry), and (5) fault zone with long splays (two or more master faults with abundant, long splays forming a blocky zone). They suggested these different types should be viewed as representing the possible variability of faults along strike, rather than fundamentally different families of faults.

An extensive literature has developed on the effects of fluids on the mechanical behavior, motivated in part by an interest in understanding the mechanics of faults. A general review of laboratory and field evidence for flow in faults from this perspective is given by Logan (1992). A particularly active direction of research has concerned the role of fluids in "weak" faults, which have anomalously low ratios of shear stress to normal stress across the fault, for example the San Andreas Fault in southern California (Zoback *et al.*, 1987). Chester *et al.* (1992) presented field evidence for the role of fluid flow and fault-zone architecture on weakening mechanisms of the San Andreas Fault. Byerlee (1993) proposed a model for episodic flow and pressurization of water in active fault zones, due to shear deformation generating high pressures in water trapped in compartments formed by gouge bands and mineral precipitation; a similar model is also proposed by Sibson (1992). Most of this work supposes a role of the fractured fault damage zone adjacent to the fault core, as a contributing factor in replenishing water in the fault core following major rupture. However, the role of a fractured fault damage zone in one intensively studied locale (Parkfield, California) along the San Andreas Fault has recently been questioned by Park and Roberts (2003), who present

geophysical evidence suggesting these are conductive sedimentary rocks.

For the present study, the main value of these studies is that they have advanced understanding of conductivity around fault zones. Studies of active fault zones such as the San Andreas provide also insight, as modern analogs of stages of fault-zone development in ancient faults in what are now more tectonically stable settings, such as the Fennoscandian Shield in Europe or the Canadian Shield in North America.

The studies by Caine (1999) and Hicks *et al.* (2000) demonstrate how different forms of hydrologic heterogeneity can occur in fault zones with different structural characteristics. Permeability reduction in fault cores leads to a tendency for fault cores to act as barriers to fluid flow, while the fractured damage zone may enhance fluid flow (Caine *et al.*, 1996).

Fairley *et al.* (2003) studied the heterogeneity of groundwater flow along an en échelon fault system at Borax Lake in southeastern Oregon, in the Basin and Range province of western North America. Using temperature of hot springs along an en échelon fault system as a surrogate for hydraulic property variations, they fitted a kriging model to the temperature data to obtain estimates of correlation length for large-scale fault permeability.

Forster *et al.* (2003) described the hydrologic properties and structure of the Mozumi Fault, in central Japan. Field evidence indicates a hydrologic structure with high-permeability pods isolated by flow barriers, which the authors suggest may be of significance for the mechanical behavior of the fault.

2.2.3 Effects of fault zone architecture on solute transport

Field studies of a gently-dipping fracture zone named Zone 2 at the Finnsjön study site in northern Uppland, Sweden (Andersson *et al.*, 1989a; Andersson *et al.*, 1991; Gustafsson and Nordqvist, 1993) investigated the role of fracture-zone heterogeneity for fluid flow and transport. Andersson *et al.* (1989a) conducted cross-hole flow and tracer tests at the Finnsjön site. Tests included hydraulic interference tests with multiple observation intervals, and pulse injection tracer tests. The test results within Zone 2 indicate strong local heterogeneity. In some cases, better connections were seen between boreholes for sections in the same horizon of the zone, than sections that were in the same borehole but in different horizons (Andersson *et al.*, 1991). This suggests that Zone 2 consists of distinct, laterally extensive subzones, as suggested by the structural interpretation of Tirén (1989). The tests also indicated anisotropy within the plane of the zone. The conductivity in the strike direction appears to be higher than in the dip direction. Andersson *et al.* speculate that this may be due to a second, intersecting zone.

The tracer test results were analyzed in terms of an equivalent, single fracture (Andersson *et al.*, 1991), to estimate transport parameters. The estimated zone conductivities from tracer residence times were roughly 0.1 to 1 m/s, several orders of magnitude higher than the conductivities estimated from hydraulic tests. Comparison in terms of transmissivity showed much better agreement. This indicates that the hydraulically most active part of the zone is only a small fraction of the tested thickness. The tracer data showed multiple arrival peaks, indicating multiple distinct flow paths.

Andersson *et al.* proposed that a model of compound fault zones as suggested by Martel *et al.* (1988) could explain the observed heterogeneity. In such a structure, the hydrologic properties could be expected to be relatively uniform within a given segment, but may have contrasting values between segments, and between segments and step-over zones. Based on this supposition, hydrologic parameters would be expected to exhibit correlation over scales less than the typical fault segment length.

Mazurek *et al.* (1996; 2003) developed a model for fault zones on the scale of decimeters based on mapping and detailed characterization of water-bearing fractures and faults observed in tunnels at the Äspö Hard Rock Laboratory in SE Sweden, including thin-section analysis of resin-impregnated sections from fault strands. They developed a

conceptual model for transport consisting of open-aperture fractures adjoined by cataclasite, fault gouge, and mylonite. This conceptual model was used as a basis for modeling a dipole tracer test conducted in situ in the laboratory (Jakob *et al.*, 2003). The authors recognized the variable geometry of stepped fault zones at larger scales, but used a simplified planar-fault representation for predictive modeling and subsequent inverse modeling of the results.

The comb-crack model for compressive shear fault development proposed by Schulson *et al.* (1999) implies a process zone of finite extent in the vicinity of faults. This model implies a well-connected porosity of finite extent in the rock adjacent to a fault slip surface, and thus a finite zone of elevated matrix connectivity and matrix diffusivity. Furthermore it can be expected that these properties are heterogeneous, as elevated contact stresses at asperities could require greater shear stresses and therefore more extensive comb cracks prior to failure.

2.2.4 Saturated fluid flow and solute transport in single fractures

From the review of research on fault zone architecture in granitic rock, fractures are clearly important as conduits for fluid flow and solute transport. This section summarizes major points of relevance from the large and active literature on flow and transport properties of individual fractures.

The emphasis here is limited to flow and transport under saturated conditions (single-phase flow, with water as the single phase). This is a primary situation of concern for fault zones in fractured granitic bedrock in moist temperate climates, typical of most countries (*e.g.*, Sweden, Canada, Finland, and Japan) where granitic rock is being considered as the host rock for high-level radioactive waste. However it may be noted that unsaturated (two-phase air/water) conditions may be important for understanding near-surface hydrology and the potential for solute exchange with the surficial environment in these settings. Since fault zones are commonly expressed as topographic lineaments in these settings and may act as the loci for both recharge and discharge on a regional scale, investigation of unsaturated flow and transport in fault zones may be a fruitful topic for future research.

Flow in a single fracture

The classical model for fluid flow through a single fracture is the parallel-plate model, in which the fracture is idealized as two parallel, planar surfaces separated by a constant aperture b. Assuming that the fluid is Newtonian and of uniform density, that flow is laminar and quasi-steady or creeping (*i.e.*, that inertial forces due to fluid acceleration are negligible relative to viscous and pressure forces) and that there is no slippage at the fracture walls (*i.e.* the fluid velocity $v(z) = 0$ at $\zeta = \pm b/2$, where ζ is the local coordinate perpendicular to the plane of the fracture), the flow rate in a parallel-plate fracture is readily derived by a static force balance as (Snow, 1969):

$$\frac{Q}{w} = -\frac{\rho g b^3}{12\mu}\frac{\Delta h}{\Delta x} \qquad (2\text{-}1)$$

where $h = z + p/\rho g$ is the hydraulic head, ρ is the fluid density, g is gravitational acceleration μ is the fluid viscosity, and Δh is the change in h over a distance Δx. This formula is called

the "cubic law" due to the cubic dependence of flow on aperture. The formula may be written in differential form as:

$$q_x = -\frac{\rho g b^3}{12\mu}\frac{\partial h}{\partial x} \tag{2-2}$$

where q_x is the flowrate density [L^2/T] in the x direction.

Bear (1993) gives more general equations for 1-D flow through a fracture of variable aperture and possibly permeable walls (so that the fluid velocity at the fracture walls need not be zero), arriving at a form similar to the cubic law after subsequent simplifications. For an arbitrarily oriented head gradient within the plane of the fracture, we may more generally write the cubic law in vector form as:

$$\boldsymbol{q} = -\frac{\rho g b^3}{12\mu}\nabla_f h \tag{2-3}$$

where $\boldsymbol{q} = (q_x, q_y)$ and ∇_f is the two-dimensional gradient operator in the plane of the fracture, so that $\nabla_f h = (\partial h/\partial x, \partial h/\partial y)$, with the coordinate y being orthogonal to x in the nominal plane of the fracture.

For steady-state flow, conservation of mass leads to:

$$\nabla_f \cdot \left[\frac{\rho g b^3}{12\mu}\nabla_f h\right] = 0 \tag{2-4}$$

which is in the form of the Reynolds equation. Zimmerman and Bodvarsson (1996) showed that this equation can be generalized to the case where the aperture b varies as a function of position in the nominal fracture plane, provided that the mean aperture is sufficiently large relative to the standard deviation and correlation length of aperture. In other words, under these limiting assumptions the Reynolds equation based on local cubic-law behavior can describe flow in a variable-aperture fracture.

In the case where the fluid happens to be water, comparing the cubic law with the 2-D form of Darcy's law for a laterally isotropic aquifer:

$$\boldsymbol{q} = -T\nabla h \tag{2-5}$$

where T is the aquifer transmissivity [L/T], we see that the term $\rho g b^3/12\mu$ can be viewed as the transmissivity for a parallel-plate fracture.

The concept of a fracture transmissivity (here denoted T_f) is useful in considering flow through fracture networks, especially when considering natural fractures in which the aperture is variable, or if the fracture is partly or completely filled with permeable material such as fault gouge, breccia, weathering products, or precipitated minerals. In such cases the measured aperture of a fracture might not give a meaningful prediction of the net flow through the fracture for a given gradient. In practice, fracture aperture and its variability can be very difficult to measure accurately in situ, and large errors can result in predicted flowrates due to the cubic dependence of flow on aperture. For these reasons, some practitioners (*e.g.*, Osnes *et al.* 1988) advocate estimation of T_f from hydraulic tests in boreholes, rather than from measurements of aperture.

Experimental evidence and modeling results (*e.g.* Matthäi and Belayneh, 2004) show that coupled fracture-matrix flow can be significant in cases where the ratio of fracture permeability to matrix permeability is less than about 10^4 to 10^5. In granitic rocks at the Swedish sites considered in this study, the ratio of fracture permeability to matrix permeability (or equivalently, the corresponding ratio of hydraulic conductivities) is 10^5 or larger, so matrix flow can usually be neglected.

In considering flow and transport through non-ideal fractures with a given (measured) T_f, it is sometimes convenient to speak in terms of the equivalent hydraulic aperture. The hydraulic aperture b_h is defined with reference to a parallel-plate fracture having the same T_f as the non-ideal fracture:

$$b_h = \sqrt[3]{\frac{12\mu T_f}{\rho g}} \tag{2-6}$$

The aperture that can physically be measured, for example in a section perpendicular to the plane of the fracture, is termed the mechanical aperture. The notation b_m is used here when this type of aperture is explicitly meant. The notation b_t is used to represent effective apertures for transport, such as effective apertures estimated from tracer tests, as discussed later in this section.

Non-linear flow in single fractures

The assumption of linear laminar flow in fractures might not always apply, particularly under conditions such as at the start of a constant-pressure injection or withdrawal test, when steep hydraulic gradients close to the wellbore induce relatively high fluid velocities which may result in partly or fully turbulent flow.

Non-laminar flow of fluids in rock fractures was studied by Louis (1969), who investigated the influence of varying Reynolds number *Re* and fracture surface roughness on the relationship between flow and pressure gradient, and by Elsworth and Doe (1986) and Kohl *et al.* (1997) who considered the effects of turbulent flow for flow during well tests. While the phenomenon is of concern for well tests, the hydraulic gradients under which turbulent flow is found to develop in natural fractures are orders of magnitude higher than expected gradients around a post-closure repository.

Yeo and Ge (2001) pointed out that non-linear laminar flow can develop in variable-aperture fractures at lower *Re* than the onset of turbulence, due to inertial effects, and that this situation can occur in the elevated gradients used in some contaminated-groundwater cleanup situations. Using a lattice Boltzmann simulation model based on fracture aperture profiles, they identified the point at which flow diverge from Darcian (laminar and linear), and showed that this can lead to a non-linear dependence of dispersion on velocity which has been observed in some cases.

Inhomogeneity of flow in variable-aperture fractures

It is widely recognized that aperture and flow are non-uniformly distributed within individual fractures. The use of a uniform transmissivity (rather than uniform aperture) throughout the fracture plane (*e.g.*, Dershowitz *et al.*, 1991) may be sufficient for flow (and some transport)

predictions where only the average flow is important. However, theoretical calculations and experimental observations (Gelhar, 1987) indicate that the inhomogeneous distribution of flow within a single fracture may be significant for radionuclide transport.

Experimental evidence of inhomogeneous flow within a single fracture includes both laboratory studies and *in situ* experiments. Early laboratory studies using natural fractures (Sharp, 1970; Iwai, 1976) were concerned mainly with the effective transmissivity of fractures with variable aperture, and did not explicitly consider the distribution of flow within the fracture. Witherspoon *et al.* (1979; 1980) analyzed the experimental data of Iwai (1976) and confirmed that deviations from ideal parallel-plate geometry caused a reduction in fluid flux through natural fractures in rock. Schrauf and Evans (1986) used a roughness index to explain discrepancy between cubic law and experimental gas flow measurements in a natural fracture in granodiorite.

Later experiments focused on the distribution of flow and transport within the fractures. Neretnieks *et al.* (1982) performed tracer tests in a natural fracture from the Stripa mine. The area of fracture tested was roughly 0.06 m^2. The breakthrough curves for two non-sorbing tracers showed plateaus, which were interpreted as the superposed effect of two distinct transport paths with different flow velocities.

Hakami (1989) produced clear plastic replicas of five fractures, and mapped the flow velocity distribution by injecting colored dye to indicate the streamlines. The areas of the fractures tested ranged from 0.008 to 0.03 m^2. The channeling character differed among samples. The fraction of fracture area through which 75% of the flow passed ranged from roughly 30 to 70% of the total fracture surface area. Estimated velocities varied within a single sample by up to a factor of 20.

Piggott and Elsworth (1990) measured pore volume, pneumatic, hydraulic, and electrical conductivity, and tracer transport characteristics of a 0.06 m^2 natural fracture in granite, first in a mated configuration, and then after shifting one surface of the fracture slightly to produce a dilation of 1 mm. A grid of probes measured variations in the induced fields, and showed that these were more uniform for the fracture after "shearing." This suggests that a small shear displacement and dilation may produce a reduction in aperture variance. However, the variation within the fracture tested was very small, and effective apertures from all measurement techniques were within a factor of 4 of b_h.

Keller *et al.* (1999) used computer tomography X-ray scanning to measure the aperture in a 0.008 m^2 (5 cm x 16 cm) rectangular area of a natural fracture in a jacketed granite core sample, under atmospheric confining pressure. They also used the same technique to measure concentrations of a potassium iodide solution which was injected at one end, for runs with different hydraulic gradients to produce flow velocities in the range 1.53 x 10^{-5} m/s to 4.74 x 10^{-4} m/s.

Detwiler *et al.* (2000) performed flow visualization and solute transport experiments in textured-glass analog fractures with aperture statistics and correlation lengths similar to those obtained measurements on natural fractures. They used these models to characterize the flow velocity ranges within which single-fracture dispersion is dominated by molecular diffusion, macrodispersion due to velocity variations in the plane of the fracture, or Taylor dispersion due to the velocity profile across the aperture.

Applicability of laboratory results is limited by two considerations:

- The scale is small relative to fractures on the scale of 1-100 m^2 area or larger, which are of practical concern for modelling flow and transport around underground excavations.
- The aperture distribution may be different from *in situ*, due to possible disturbance of the fracture in the sample collection and preparation process leading to possible mismatch of the fracture surfaces, as well as stress relief (including hysteresis effects even if confining pressures are subsequently applied), and disruption of infilling in weakly sealed parts of the fractures.

Depending on the experimental technique, concerns about sample disturbance and mismatches can be minimized. However, the problems of scale and stress relief are difficult to avoid in the laboratory.

In situ experiments give data on a larger scale, with less disturbance of the fractures. Novakowski *et al.* (1985) analyzed injection-withdrawal flow and tracer tests in a single fracture in monzanitic gneiss at the Chalk River site in Canada. The interpreted b_h was 60 μm, compared with an estimated effective aperture for transport of 510 μm. This difference seems to indicate the presence of stagnant zones of water adjacent to the flow paths.

Raven *et al.* (1988) analyzed four injection-withdrawal tests and one radially converging test in a single fracture at the same site. A transient "solute storage" model was used to analyze the results. For the tests with a distance of 12.7 m from injection to

withdrawal point, good fits were obtained by assuming there was no stagnant water. For tests over a longer distance of 29.8 m and much longer residence times, good fits were obtained by assuming that 35 to 65% of the water volume was stagnant.

Shapiro (1988) conducted radially convergent tracer tests in an areally extensive, horizontal fracture in dolomite. The scale of the tests was about 20m. Transmissivity and storativity for the fracture tested by Shapiro (1988) were estimated as 1.9×10^{-2} m^2/s and 2.7×10^{-5} to 9.7×10^{-5}. The product $b_v\phi$ and longitudinal dispersivity α were estimated by fitting to the first and second moments of the mass arrival curves. Estimated values of $b_v\phi$ were 8.5 mm, 8.7 mm, and 10.1 mm in three tests. Effective longitudinal dispersivity estimates were 2.0 m, 2.7 m, and 11.0 m. Different values of longitudinal dispersivity were measured in different directions, although hydraulic tests showed no anisotropy in the horizontal plane. Simulations of the tracer test using these parameters and a finite-difference approximation gave mass arrival curves that had much a less steep initial rise in the mass arrival curves.

The possibilities of correlations *between* fracture planes, or distinct channels at the intersections between fractures, have been investigated in only a few instances (Abelin *et al.* 1985, 1990). Abelin *et al.* (1985) describe tracer migration experiments over distances of 5 to 10 m in a single fracture in the Stripa mine. Based on pressure pulse testing in one intersecting borehole, H2, they estimate $T_b = 2.8\text{-}6.5\times10^{-10}$ m^2/s and $S = 3.6\text{-}7.5\times10^{-8}$ m^2/s for the fracture. Testing in four other boreholes that intersected the fracture gave $T_b \leq 4\times10^{-11}$ m^2/s . Thus the range in T_b was at least an order of magnitude. Hydraulic diffusivities estimated from small-scale crosshole tests ranged from 1.3×10^{-4} to 6.1×10^{-2} m^2/s (Abelin *et al.* suggest that these may be underestimated due to possibly high wellbore storage effects). More than 90% of the water flowing into the drift from the fracture came in through 5 of 27 measurement sections. The four highest-flow sections were localized in one side of the drift cross-section. However, high head gradients in the rock around the drift, due to nearby mine openings, complicate interpretation of the observed irregularity in the inflow distribution.

Experiments by Abelin *et al.* (1990) to investigate channeling in a single fracture provided more detailed information regarding distribution of flow and b_m in a single fracture *in situ*. In these experiments, pairs of boreholes were drilled along the planes of single fractures. Detailed observations of b_m and fracture infilling thickness variation were made. Multiple crosshole flow and tracer tests were performed, using multi-port packers to isolate

multiple 5 cm sections of the fractures. The crosshole flow tests showed an uneven distribution of responses along the length of the monitoring holes. Tracer tests between holes yielded an even more uneven distribution of responses for transport. Some tracer disappeared into the fracture or possibly into other, intersecting fractures. Abelin *et al.* concluded that there were stagnant volumes which they interpreted as dead-end channels, in the fractures studied.

Other experiments in granitic rock at Cornwall, England (Heath, 1984; Bourke, 1987) showed highly variable cross-hole connections for boreholes intersecting single fractures at different points. In the single-fracture experiment described by Bourke (1987), the flow was interpreted as being restricted to a few channels occupying approximately 10% of the fracture area.

Taken together, the results of the *in situ* experiments indicate that:

- The transmissivity (or effective hydraulic aperture b_h) is not uniform within fracture planes, over a scale of millimeters to decimeters.
- The flow distribution in single fractures is not uniform.
- The main pathways for flow may occupy a small fraction (less than 20 percent) of the fracture plane.
- There are stagnant volumes of water associated with single fractures, even in fractures subjected to high gradients.
- Hydraulic connections between different parts of a fracture are irregular.

Beyond these basic observations, a variety of interpretations are possible for any given *in situ* experiment. Since the local aperture within the fractures is known at only a few points or along a few profiles, the observed flow and transport responses do not yield unique interpretations of how aperture varies in the remainder of the fracture.

An important point of uncertainty for in-situ single-fracture experiments is the possible of additional fractures that intersect the tested fracture. The possibility of flow along such fractures cannot be excluded. In the case of the Stripa channeling experiment (Abelin *et al.*, 1990) two transport paths identified by use of the multi-port packer system apparently crossed; this can only be explained if there are transport channels that make excursions outside of the tested fracture plane.

Estimation of mechanical aperture from surface profiles

Direct measurements of aperture in granitic rock provide a basis for models of aperture variation in single fractures. The earliest efforts to obtain such were generally based on fracture surface height profiles. Bandis *et al.* (1981) measured fracture surface profiles in various sedimentary rocks. Tsang and Witherspoon (1983) used a profile from Bandis *et al.* to generate synthetic b_m profiles, by shifting a mirror image of the profile laterally along the original profile. For a very small displacement, the distribution of b_m was roughly normal, but for increasing displacements it became multimodal.

Gentier (1986) constructed b_m profiles for a natural joint in granite, by combining surface profiles from opposite sides of the fracture. Brown and Scholz (1985) measured fracture roughness along multiple, perpendicular directions on single fracture surfaces in sedimentary and plutonic rock (columnar cooling joints in diabase). Measurement scales ranged from 1 μm to 1 m. Brown and Scholz characterized fractures in terms of power spectral densities, as a function of roughness wavelength, and related this to a fractal dimension for surface height variation, which appeared to vary with scale. For the larger-scale wavelengths, they estimated an apparent fractal dimension D_p = 1.18-1.26. Brown (1987) used these measurements to simulate b_m variation between uncorrelated fractal surfaces with a specified mean b_m.

Brown *et al.* (1986) investigated correlation between fracture surfaces by taking surface profiles from opposite faces of joints in granodiorite, and combining the profiles to estimated b_m after the method of Gentier (1986). The joints were well-mated (with correlation lengths for b_m from 0.5 to 5 mm) and were coated with chlorite and epidote.

Estimates of b_m derived from surface profiles are open to certain questions. Studies of fractures with shear displacements are lacking, although other research (discussed below) indicates that small shear displacements may increase fracture transmissivity by dilation. The composite-profile measurements have been limited to very well-mated joints. Furthermore, because uncertainties about the precise relative position of the opposing profiles are resolved by optimizing the match, the degree of mating may be overestimated (Brown, 1987). Simulation of shear displacement by shifting surfaces does not account for processes such as normal stress, shearing of asperities, or precipitation of mineral fillings. These shortcomings can be better addressed by direct measurements of b_m.

Direct measurements of fracture mechanical aperture

The simplest direct method for measuring b_m variation is to take a profile along a cross-section of a fracture. Gale (1987) injected epoxy resin into fractures in Stripa granite, under normal stress. After the resin hardened, the rock was sectioned and the resin thickness was measured. The distribution of b_m was approximately lognormal, or left-skewed, in contrast to the right-skewed distributions obtained by Gentier (1986), based on surface profiles. The mean b_m was 4 to 5 times b_h measured under normal load.

In situ profiles of b_m in Stripa granite were produced by Abelin *et al.* (1990), by photography in boreholes drilled along fracture planes. The cross-sectional areas of infilling and void space were measured on photographs for 5 cm sections of the fractures. The average b_m for each section was calculated as the void area divided by the length.

A few researchers have measured two-dimensional variations in b_m by producing casts of fractures. Pyrak-Nolte *et al.* (1985) produced Wood's metal casts of fractures in Stripa granite (52 mm diameter) under stress. Pyrak-Nolte *et al.* (1988) analyzed these to determine the pattern of contact areas and voids. The measurements were binary (contact or void) but by use of a fractal, stratified-continuum percolation model, a distribution of b_m was produced. Gentier *et al.* (1989) produced casts of fractures (12.5 cm diameter) under normal stress using a silicone polymer resin which absorbs light in (nonlinear) proportion to its thickness. Gray-scale images produced by illuminating the resin cast from below give a two-dimensional characterization of b_m.

Hakami (1989) produced maps of b_m by placing measured drops of fluid at evenly spaced points, between clear plastic replicas of fracture surfaces. The distribution of b_m in each of the fractures was approximately lognormal. The distributions became increasingly left-skewed with increasing normal load.

Most of these studies are based on measurements on scales that are small in relation to typical field scales, with the exception of the *in situ* profiles of Abelin *et al.* (1990). As a group, the direct measurements of b_m give results similar to data from surface profiles. However, the direct measurements show strong effects of normal stress on b_m. This implies surface profile data cannot be applied without making a theoretical compensation for rough fracture deformation.

Models for fracture aperture variation

Early models for variation of b_m within a single fracture were based on spatially uncorrelated, random distributions of b_m. Neuzil and Tracy (1981) proposed a lognormal distribution for b_m. Tsang (1984) modeled the data of Gentier (1986) as a normal distribution, truncated at zero. Tsang also suggested a right-skewed distributional form based on b_m distributions derived from load-displacement data for granites and basalts, according to the theory of Tsang and Witherspoon (1981). These models tend not to produce high-conductivity channels, due to the absence of spatial correlation.

Models that tend to produce channel-like structures include 2-D stochastic-continuum (geostatistical) models (Tsang and Tsang, 1987; Moreno *et al.*, 1988; Stratford *et al.*, 1990) and two types of fractal models: a stratified continuum percolation model (Pyrak-Nolte *et al.*, 1988), and composite topography models (Brown, 1987; Wang *et al.*, 1988).

All of these models provide methods for extrapolating from b_m profiles to b_m variation within the fracture plane. None of these models accounts for possible correlations between fracture planes, or distinct channels at the intersections between fractures. Tsang and Tsang (1987) discussed the possibilities of spatial correlation between planes but their mathematical formulation did not account for this.

Stratford *et al.* (1990) applied the model of Moreno *et al.* (1988) to fractures in a network, with no correlation of channels between intersecting fractures. They observed that, in this model, channeling is a local effect, and persistence of dominant pathways over several fracture planes depends mainly on the T_f of the interconnecting fractures.

Simulation of variable b_m fractures, based on the various models, have been presented by the respective authors. With suitable parameter values, all of the models reproduce the qualitative characteristics of single fractures, as deduced from the field experiments described above. Abelin *et al.* (1990) compared their experimental results directly to the model of Moreno *et al.* (1988), showing reasonably good quantitative agreement.

Brown (1987) superposed two uncorrelated surfaces with the same fractal dimension D_s. This can be calculated from the fractal dimension of a surface profile as (Brown, 1987):

$$D_s = D_p + 1 \qquad (2\text{-}7)$$

The surfaces were placed a fixed distance apart. For small values of this distance, the surfaces may overlap. In these cases, Brown ignored deformation mechanisms and assumed $b_m = 0$ in the regions of overlap. Hakami (1989) compared direct flow measurements with results from Brown's model, and reported good qualitative agreement in terms of tortuosity and velocity variation. The main shortcomings of the model are the assumption of uncorrelated surfaces, and the simplistic removal of overlapping regions.

An improved version of the model (Wang *et al.*, 1988) consists of two initially mated surfaces, both of fractal dimension D_s. One of the surfaces is shifted by a vector displacement of magnitude r_c within the plane of the fracture. The authors derived an expression for the isotropic variogram of b_m for a given relative shear displacement, and noted a correspondence between their model and a geostatistical model with isotropic covariance.

Wang and Narasimhan (1988) suggested a type-curve matching approach to estimate the parameters r_c and D_s from log-log variograms of b_m. This model accounts for possible correlation of the fracture surfaces. Since the parameters are obtained directly from b_m profiles, the simplifying assumptions about contact regions are less of a problem. An example of application of this method, using the in-situ data of Abelin *et al.* (1990), is given by Geier *et al.* (1992). Estimates of D_s were in the range 2.1 and 2.5, with a median value of 2.15.

Flow models for variable-aperture fractures

Zimmerman *et al.* (1991) and Zimmerman and Bovardsson (1996) used the Reynolds equation to examine effects of surface roughness on fluid flow through fractures, and derived limits on its applicability and the local cubic-law assumption as mentioned above. Ge (1997) derived an analytical model based on this conceptualization which takes into account the aperture variation and the tortuosity of the fracture

Several research groups (Brown *et al.*, 1995; Di Pietro, 1996; Gutfraind and Hansen, 1995) have examined the applicability of the Reynolds equation for modeling fluid flow between rough fracture surfaces by comparing lattice-gas automata simulation models with computational simulations based on this equation, but without comparison to experiments on actual fractures or physical models.

Waite *et al.* (1998) compared lattice-gas modeling with physical flow experiments for the cases of synthetic parallel-plate and sinusoidal fractures (machined in aluminum alloy blocks). They found close agreement between the lattice-gas model and physical experiments in terms of the permeability and effective aperture, for vertical separations of 0.25 mm to 0.71 mm. For the sinusoidal fracture (wavelength 5.08 mm, amplitude 1.02 mm) the observed permeability was less than predicted by the analytical model of Ge (1997) which takes into account the aperture variation and the tortuosity of the fracture. Waite *et al.* suggest the discrepancy was due to momentum dissipation in regions of flow instabilities (*Re* up to 58 in the experiments), but good agreement between the physical model and the lattice-gas model (where $Re < 5$ and no flow instabilities were observed). An alternative explanation might be viscous dissipation in the bends.

As described above, Detwiler *et al.* (2000) have used experiments in textured-glass analog fractures with aperture statistics and geostatistics similar to natural fractures, to characterize the flow velocity ranges within which single-fracture dispersion is dominated by molecular diffusion, macrodispersion, or Taylor dispersion. They compared the experimental results with theoretical calculations and with computations based on an advective-diffusive particle-tracking algorithm. They found good agreement between theoretical and computational model results, but divergence of both from the physical model, which they attributed to deviations of the physical flow field from the local cubic-law behavior assumed by the Reynolds equation.

The general picture that emerges from the theoretical and experimental work is that the local-cubic-law assumption (or local effective transmissivity assumption) as embodied in the Reynolds equation formulation for steady-state flow provides a suitable model for single-fracture flow and mechanistic modeling of dispersion, although the predictions of computational models may diverge from physical models for fractures with high variability and/or long correlation lengths of aperture, in relation to the mean aperture.

Hydromechanical effects in single fractures

The term "hydromechanical effects," for a single fracture, refers to the interrelationships of rock stress, fluid pressure, and flow within the fracture. Principal effects include:

- Reduced transmissivity due to closure under normal stress.
- Changes in transmissivity due to shear stress and displacements.
- Changes in fluid storage due to changes in pressure and state of stress.

These effects are discussed in the following subsections.

Normal stress and transmissivity

The effects of normal stress σ_n on cross-fracture transmissivity T_f have been studied over a range of measurement scales, from laboratory studies on a 0.15 m scale (Iwai, 1976) to *in situ* experiments on scales above 1 m (Carlsson and Olsson, 1986; Makurat *et al.*, 1990b). From these it is clear that increasing σ_n causes fracture closure and hence decreasing T_f. However, there are difficulties in interpreting both laboratory and field experiments, due to uncertainty as to the correct initial conditions for the tests.

In granitic rock, tests both on fractured core samples (Gale and Raven, 1980) and *in situ* (Carlsson and Olsson, 1986; Makurat *et al.* 1990b) show hysteresis when the normal load is increased and decreased in several cycles. The strongest hysteresis is seen for the initial loading cycle. The later cycles usually show less hysteresis. An interpretation of this behavior is that the initial condition of the joint is disturbed, producing a slight shift from mated conditions (Note that fractures in laboratory samples are undoubtedly disturbed, but Witherspoon *et al.*, 1979 point out that fractures *in situ* may also be disturbed by slight shear movements due to excavation of the site). The initial loading cycles are presumed to correct for this mismatch by non-elastic deformation around the contacting asperities. The later cycles are therefore considered to be more similar to undisturbed *in situ* conditions.

Experimental data from Carlsson and Olsson (1986) and a compilation by Dershowitz *et al.* (1991) show a roughly log-log relation between T_f and σ_n:

$$\frac{T_f}{T_{fo}} = \left(\frac{\sigma_n}{\sigma_{no}} \right)^{b_{Tn}} \tag{2-8}$$

where:

σ_{no}	= reference level for normal stress	$[M/LT^2]$
T_{fo}	= fracture transmissivity at $\sigma_n = \sigma_{no}$	$[L^2/T]$
b_{Tn}	= empirical constant	[-]

The range of b_{Tn} from experiments in Swedish granitic rock is approximately $-3 \leq b_{Tn} \leq -0.2$ (Carlsson and Olsson, 1986).

There is a tendency for the tangent value of b_{Tn} to decrease with increasing σ_n. Witherspoon *et al.* (1979) suggested that this happens because, for rough fractures, the contact area between opposing fracture surfaces increases with σ_n, increasing the fracture stiffness. The Barton-Bandis joint model (Bandis *et al.*, 1983 and subsequent papers) gives an empirical description of this behavior. The hydraulic aperture is related to mechanical aperture by:

$$b_m[\mu m] = \sqrt{b_h[\mu m] \cdot JRC_o^{2.5}} \tag{2-9}$$

where JRC_o is the joint roughness coefficient (dimensionless). A hyperbolic model for the change in ϵ_m is expressed in terms of joint normal stiffness κ_n as:

$$\kappa_n = \kappa_{no} \left(1 - \frac{\sigma_n}{\delta_m \kappa_{no} + \sigma_n} \right)^{-2} \tag{2-10}$$

where:

κ_{no}	= tangent value of κ_n at start of loading cycle	[M/TL^3]
δ_m	= maximum joint closure, *i.e.* maximum b_{mo} - b_m	[L]
b_{mo}	= initial mechanical aperture	[L]

Integrating $1/\kappa_n$ along the loading path gives b_m as a function of σ_n:

$$b_m - b_{mo} = \delta_m \left[\frac{\sigma_n}{\delta_m \kappa_{no} + \sigma_n} \right] \qquad (2\text{-}11)$$

Bandis *et al.* (1983) suggested empirical relations relating κ_{no} and δ_m to b_{mo}, JRC_o, and JCS_o (the joint compressive strength), with parameters depending on the stress history of the joint. κ_n for mismatched joints can differ from κ_n for interlocked joints by a ratio of 0.4 to 0.15 (Bandis *et al.*, 1983). This model is implemented in the Universal Distinct Element Code, UDEC (Itasca, 2002) and has been used by Min (2004) for modeling coupled mechanical and hydrologic response in network flow problems.

Apart from the Barton-Bandis model, there have been many attempts to develop theoretical models of joint normal stiffness, based on fundamental rock properties and statistical models of surface roughness (*e.g.*, Tsang and Witherspoon, 1983; Brown and Scholz, 1986). Difficulties arise from the need to consider deformation of the rock adjacent to the fracture and coupling among asperities, as well as deformation of the asperities (Hopkins *et al.*, 1990). Numerical modelling of this behavior for an isolated crack is possible (Zimmerman *et al.*, 1990) but the approach is computationally intensive for even a single fracture.

Effects of shear stress and shear displacement

The effect of shear stress on T_f has also been the subject of laboratory experiments, but the results are even more complex than for σ_n. Apparently the change in T_f is controlled by the shear displacement. In shear-loading tests on fractures in 200 mm granite cores, Makurat *et al.* (1990b) found that small displacements in an initially mated fracture produced increased T_f due to dilation of the fracture. However more extensive shear deformation sometimes reduced

T_f due to changes in mating of the fracture surfaces, failure of asperities, and/or gouge formation.

Thus, depending on a number of processes and the amount of displacement during shear deformation, T_f may increase or decrease. Results of the Stripa Site Characterization and Validation project (Olsson, 1992) indicate that, in the highly disturbed zone adjacent to a tunnel, shear deformation may have a greater effect than normal stress on fracture transmissivity.

Based on temperature anomaly data used to identify fractures with significant flow in boreholes, Barton *et al.* (1995) found that 70-80% of conductive fractures were configured such that the shear stress $\tau > 0.6\ (\sigma_n - p)$ where p is the pore pressure. Transmissivity of fractures under shear displacement is affected by fracture roughness or the formation of microfractures adjacent to the sliding surface, so one criterion for fluid flow along faults is that the rock is critically stressed, in a state of incipient shear failure. This empirical observation was utilized in fault zone hydromechanical models by Hicks *et al.* (2000), described later in this chapter, and also in network simulations by Min (2004).

Dispersion of solutes in a single fracture of variable aperture

Dispersion of solutes within a fracture occurs by a combination of molecular dispersion and fluid velocity variations within the fracture. The variation of fluid velocity across the fracture aperture gives rise to Taylor-Aris dispersion (Taylor, 1953; Aris, 1956) while variation of the fluid velocity from point to point along the fracture results in macrodispersion. Roux *et al.* (1998) used scaling arguments to suggest that the net longitudinal dispersion coefficients can be expressed as the sum of three components:

$$\frac{D_L}{D_m} = \tau + a_{macro} Pe + a_{Taylor} Pe^2 \qquad (2\text{-}12)$$

where a_{macro} and a_{Taylor} are dimensionless coefficients, Pe is the Peclet number Pe = $\langle v \rangle \langle b \rangle / D_m$, $\langle v \rangle$ is the mean solute velocity, $\langle b \rangle$ is the mean aperture, D_m the molecular diffusion coefficient, and τ is the tortuosity for diffusion within the fracture (typically $\tau <$ 1.0).

For a variable fracture in which the logarithm of aperture $\beta = \ln b$ is a stationary, Gaussian variable, a stochastic analysis by Gelhar (1987) assuming small variance σ_β^2 leads to expressions for the coefficients (Detwiler *et al.*, 2000):

$$\alpha_{Taylor} = \frac{1}{210} \tag{2-13}$$

$$\alpha_{macro} = \frac{\sigma_\beta^2 \lambda B}{\langle b \rangle} \tag{2-14}$$

where λ is the integral scale of β, and:

$$B = 3 + \frac{1}{\pi \sigma_\beta^2} \int_0^\infty \{\exp[C_\beta(u)] - 1\} du \tag{2-15}$$

where $C_\beta(u)$ is the covariance function of β and u is the dimensionless separation variable equal to the separation variable divided by λ.

Detwiler *et al.* (2000) compared theoretical values calculated from the above expressions with three-dimensional particle-tracking simulations of advection and diffusion in variable-aperture fractures, and found that the results of theory and simulations agreed well over a wide range of *Pe*, for simulated aperture fields with $\sigma_\beta^2 = 0.073$ and λ ranging from 0.035 to 1.8 cm. Divergence of simulations from theory was noted for high and low *Pe* for an aperture field with $\sigma_\beta^2 = 0.56$ and $\lambda = 0.035$.

Detwiler *et al.* (2000) also compared theoretical dispersion coefficients with values obtained from physical experiments using synthetic glass analogues of rough-walled fractures. They found that the theoretical and simulated values were comparable to values observed in the physical experiments, but that macrodispersion values were systematically underestimated by the theory. They suggested that the difference was in the quasi-two-dimensional representation of the flow field that was assumed by the theory.

In their transport experiments in a 0.008 m^2 rectangular section of a natural fracture in granite, with a fixed transport distance of 16 cm, Keller *et al.* (1999) observed a linear dependence of dispersion coefficient on flow velocity for flow velocities in the range 1.53 x 10^{-5} m/s to 4.74 x 10^{-4} m/s. The dispersivity for this section of fracture was evaluated as 0.043 ± 0.003 m. Keller *et al.* obtained a dispersivity estimate of 0.095 m by numerical modeling of the solute breakthrough, based on velocities calculated from a flow model of the fracture as a variable-transmissivity aquifer based on the measured apertures, and integrating over streamlines with an assumption of negligible longitudinal dispersion along streamlines. A stochastic theoretical estimate of the dispersivity based on the geostatistics of aperture gave an estimate of 0.078 m, closer to the experimentally observed value. The transmissivity of the fracture was approximately $2x10^{-4}$ m^2/s, which is high relative to typical in-situ transmissivities in granite, possibly due to the unconfined (atmospheric-pressure) conditions of this experiment.

Matrix diffusion

Diffusion of solute molecules into the protolith adjoining fractures and fault zones occurs in response to concentration gradients between water in the pore space of the protolith and the more mobile water in the fractures. In granitic rock, the pore space within which this process takes place is generally understood to comprise microscopic transgranular fractures and intergranular flaws.

By convention the protolith (and sometimes breccia fragments bounded by fractured surfaces) are referred to as the "matrix" in solute-transport literature, and the process is called matrix diffusion. The potential importance matrix diffusion for radionuclide transport around a repository was pointed out by Neretnieks (1980), and has come to be recognized as a process of fundamental importance for repository safety (Jakob, 2004).

Within an individual pore considered as a tortuous pipe of a given cross sectional area A_p, the governing principle is essentially Fick's first law of diffusion:

$$\frac{dm_p}{dt} = -A_p D_m \frac{\partial c_p}{\partial \ell} \tag{2-16}$$

where dm_p/dt is the rate at which solute mass passes through the cross section, D_m is the coefficient of molecular diffusion for the given chemical species, c_p is the concentration in the pore, and ℓ is the distance along the pore. The word "essentially" is used here because, in the very small pores of the matrix, effects such as electrostatic surface chemistry can affect the mobility of solute molecules, and D_m may be an effective coefficient for the specific pore geometry, rather than the coefficient for molecular diffusion in free water (Ohlsson and Neretnieks, 1995).

At a mesoscopic level, large enough to encompass many tiny pores, the average effective pore area per unit area A of a section through the matrix is $A_p/A = \theta/\tau$, where θ is the porosity and τ is the tortuosity defined as the actual length of the pore divided by the nominal length per unit distance z normal to the plane (using the usual geophysical definition of tortuosity; note that another commonly used definition of tortuosity is the inverse square of this quantity).

The mass flux through A (that is, the rate of mass passing through A per unit area) for a unidirectional gradient in the z direction perpendicular to A is then:

$$\frac{1}{A}\frac{dm_p}{dt} = -\frac{\theta}{\tau}D_m\frac{dz}{d\ell}\frac{\partial c_p}{\partial z} = -\frac{\theta D_m}{\tau^2}\frac{\partial c_p}{\partial z} \qquad (2\text{-}17)$$

The term $(\theta/\tau^2)D_m$ is called the pore diffusivity. Ohlsson and Neretnieks (1995) suggest that this may be further scaled by a constrictivity term δ_D to account for the effect of constrictions along a variable-cross section pore. With this modification, the effective pore diffusivity is: $D_p = (\delta_D\theta/\tau^2)D_m$, or $D_e = F_f D_m$ where $F_f = \delta_D\theta/\tau^2$ is the formation factor (Löfgren and Neretnieks, 2002).

The formation factor may be viewed as a property of the pore geometry independent of the chemistry of the diffusing solute species, although Ohlsson and Neretnieks (1995) note that ion size and surface electrochemistry can influence the apparent formation factor. Thus the mass flux j_p due to Fickian diffusion through pore space in the matrix can be described as:

$$j_p = -F_f D_m\frac{\partial c_p}{\partial z} = -D_p\frac{\partial c_p}{\partial z} \qquad (2\text{-}18)$$

where the first formulation in terms of formation factor may be useful for comparing to electrical conductivity/resistivity measurements (Löfgren and Neretnieks, 2002) while the second is more conventionally used in modeling of solute transport in fractured rock (*e.g.*, Jakob, 2004).

In the case where the network of pores provides diffusion pathways in all directions isotropically, for an arbitrarily directed gradient ∇c_p the mass flux vector is:

$$\boldsymbol{j}_p = -D_p\nabla c_p \qquad (2\text{-}19)$$

Conservation of mass leads to the diffusion equation:

$$\frac{\partial c_p}{\partial t} = D_p\nabla^2 c_p \qquad (2\text{-}20)$$

Boundary conditions in applying this equation depend on the shape of the matrix blocks into which the solute is considered to diffuse, and how the solute interacts with the fracture. In typical applications the matrix blocks are assumed to be of a simple geometry that permits ready solution of the equations by choosing appropriate systems of coordinate: spheres,

cylinders, finite slabs, or semi-infinite slabs, and solute within each matrix block is assumed to be at equilibrium with mobile water at every point on the exterior of the block.

Mathematically, the one-dimensional form of the matrix diffusion equation arising from Fick's law is also satisfied by distribution of displacements arising from the transition frequency function for a particle in a Wenner-Einstein random walk with expected value and variance of the displacement $x(t)$–$x(0)$ during a given time interval $(0, t)$ equal to (*e.g.*, Prabhu, 1965):

$$E[x(t) - x(0)] = 0$$

$$V[x(t) - x(0)] = 2D_p t \qquad (2\text{-}21)$$

Thus a mathematical equivalence can be shown between Fickian diffusion and a symmetric random walk with a standard deviation of displacement equal to $\sqrt{(2D_p t)}$ for a given time t. This equivalence provides an alternate description of diffusion phenomena in terms of the random motions of an assemblage of solute particles of a given mass, *e.g.* an assemblage of molecules.

The phenomenon of matrix diffusion in granitic rock has been confirmed by through-diffusion experiments in the laboratory as well as by in-situ experiments; a thorough review and compilation of experimental values for the rock properties controlling diffusion are given by Ohlsson and Neretnieks (1995).

Questions have been raised as to the homogeneity of the matrix pore space of granitic rock on a macroscopic scale (cm or larger), including the connectivity of the pore space at distances of more than a few cm from fractures. Xu *et al.* (2001) found evidence of heterogeneity of matrix properties within the rock adjacent to single fractures. A few in-situ diffusion experiments (Abelin *et al.*, 1990) and electrical conductivity measurements (Löfgren and Neretnieks, 2002) suggest that matrix diffusion may act over penetration distances of up to 0.4 m. Malowszewski and Zuber (1985) argued that the assumption of an infinite depth for matrix diffusion is applicable for many practical cases where the time scale for transport through the fracture is small in relation to the time scale for matrix diffusion into a matrix of finite depth.

Heterogeneity on mesoscopic scales may give rise to diffusion phenomena that is not well described by the diffusion equation based on Fick's law, as above. For example, if a collection of pores within are dead-end paths of different lengths, molecules diffusing into

pores will have different distributions of first return times (*i.e.* the time at which a molecule passing into a dead-end matrix pore will return to the mobile water in the fracture), depending on the lengths of the paths they happen to enter. Fractal pore geometry with power-law distribution of path lengths for diffusion in the matrix a heavy-tailed distribution of residence times during transport through the system, *i.e.* with more of the mass arriving at late times than would be expected based on Fick's law (Haggerty, 2001).

When diffusion takes place into fragments, such as in fault breccias, distribution of the fragment sizes can also lead to apparently non-Fickian behavior (Haggerty, 2001). Although the diffusion into each fragment may follow Fick's law, the power-law size distribution means that the diffusion depths, and hence the residence times of molecules entering the fragments, follow a power-law distribution analogous to the case where the pores themselves are fractal.

Examples of power-law behavior at late time in breakthrough curves have been observed in situ, in fractured dolomite (McKenna *et al.*, 2001; Haggerty *et al.*, 2001). Several studies in Fennoscandian granitic rocks have found diffusivities that decrease exponentially with the scale of length in the measurement (Valkiainen *et al.*, 1996; Hartikainen *et al.*, 1996; Johansson *et al.*, 1998).

2.2.5 Fluid flow in networks of fractures

Flow through fractured granitic rock is fundamentally similar to flow through more porous, granular materials such as sandstone or unlithified sediments, in that fluid movement through a discrete network of voids is governed by the laws for viscous fluid motion (the Navier-Stokes equations), and that this flow moves around portions of the rock that are essentially impermeable. In sandstone these impermeable portions are small enough that flow splits and recombines on a scale of a few millimeters or less, and the voids are typically well connected in all directions (depending of course on the degree of cementation). In sparsely fractured granitic rock, the impermeable parts of the rock may be on the scale of several meters or more, and the void network is restricted to nominally planar features that may be poorly connected or even non-connected in some directions.

This difference means that on practical field scales of a few meters to a kilometer, flow and transport in sparsely fractured granite can be affected by individual segments of the void network than is the case in porous media over similar scales. In terms of the concept of a representative elementary volume or REV (*e.g.*, de Marsily, 1986), the minimum scale of an REV in fractured rock (if one exists at all) is typically many times larger than in porous media. Thus, although the fundamental processes governing flow in these two types of media, there is a significant practical distinction in terms of the scale at which the "macroscopic" properties of the medium can be considered independent of irregularities among discrete voids.

To address this practical distinction, a conceptual view of sparsely fractured crystalline rock in terms of discrete fracture networks has developed over recent decades (Wilson, 1970; Endo *et al.*, 1984; Long *et al.*, 1985; Dershowitz *et al.*, 1991; Clemo, 1994). In this conceptual view, fluid flow and transport in fractured granitic rock are considered to take place in networks of discrete fractures, usually idealized as line segments in 2-D models, or as plates in 3-D models (Figure 2-6). The processes in each fracture are governed by the appropriate single-fracture physical relations (as discussed in the foregoing sections), while certain conditions of continuity and mass conservation are satisfied at the intersections between the line sections or plates representing fractures.

2-D steady-state flow model

The simplest example of the discrete-fracture network (DFN) approach is the case of a 2-D model composed of 1-D line segments representing the fractures. Steady-state groundwater flow in such a network is directly analogous to the idea of an electrical circuit or a plumbing network:

1) Each fracture is idealized as a linear conductor.
2) At any junction I between two fractures, there is a single value of hydraulic head h_i which is common to both fractures.
3) The flowrate $Q_{i,j}$ (for an arbitrary thickness w) through a fracture segment from junction I to junction j is given by Darcy's law as:

$$\frac{Q_{i,j}}{w} = -T_{i,j}\frac{dh}{dL} = T_{i,j}(h_i - h_j)/L_{i,j} \qquad (2\text{-}22)$$

where $T_{i,j}$ is the transmissivity of the segment and $L_{i,j}$ is the segment length.
4) The net flowrate into any junction is zero (except in the case of a source or sink located at the junction).
5) Specified-head or specified-flux boundary conditions are imposed by fixing h or Q, as appropriate, at fracture intersections with the boundary.

In the analogy to electric circuits composed of resistors soldered together at their junctions, we can think of h as voltage, Q as current through a resistor, and L/Tw as the resistance, in which case (3) corresponds to Ohm's law while (2) and (4) correspond to Kirchhoff's laws.

Applying the DFN version of Kirchhoff's laws to each junction leads ultimately to a set of linear equations that can be solved by matrix methods to obtain the heads at each junction, and from these the fluxes through each segment of the network.

2-D transient flow model

The 2-D DFN model is readily extended to the case of transient flow. However, in the transient case the flowrate can no longer be assumed to be constant along each fracture segment. This is because the amount of fluid stored at a given point along a fracture depends

upon the time-varying head. Incorporating conservation of mass within each segment leads means that any decrease in flowrate with distance along a segment must be balanced by an increase in fluid storage within the fracture:

$$-\frac{\partial}{\partial L}\left(\frac{Q}{w}\right) = S\frac{\partial h}{\partial t} + q \tag{2-23}$$

where q is a source/sink term equal to 0 everywhere within the fracture segment. Combined with Darcy's law this leads to the condition that:

$$\frac{\partial}{\partial L}\left(T\frac{\partial h}{\partial L}\right) - S\frac{\partial h}{\partial t} = q \tag{2-24}$$

If T is treated as constant within each segment, this gives the 1-D transient flow equation:

$$T\frac{\partial^2 h}{\partial L^2} - S\frac{\partial h}{\partial t} = q \tag{2-25}$$

At the ends of the segment the Kirchhoff condition [4] still holds, so the sum of all q's at the endpoints of fracture segments connecting into a junction must equal zero (unless there is a source or sink at the junction).

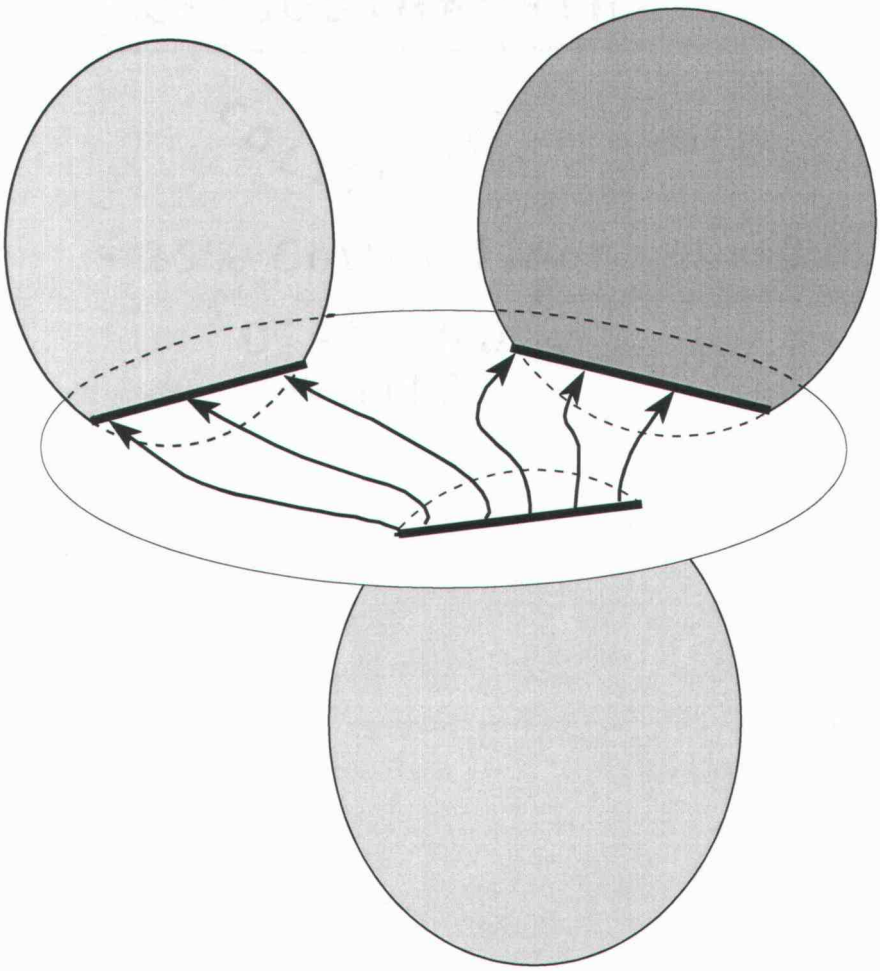

Figure 2-6. Conceptualization of flow in fracture networks idealized as 2-D plates in 3-D space.

3-D Steady-state and transient flow models

For the case of a 3-D model in which each fracture is idealized as a 2-D conductive "plate" (Figure 2-6), the approach is similar:

1) Each fracture is idealized as a conductive plate with either homogeneous or heterogeneous properties.

2) At any *point along the line segment of intersection* between two fractures, there is a single value of hydraulic head h_i which is common to both fractures.

3) The flowrate density vector $\boldsymbol{q}$ at any given point on a single fracture is related to the head gradient by Darcy's law:

$$\boldsymbol{q} = -T\nabla h \qquad (2\text{-}26)$$

where T is the (local) fracture transmissivity, and where the gradient of head is taken with respect to a 2-D coordinate system in the plane of the fracture. Taking account conservation of mass as in the 1-D case leads to:

$$T\nabla^2 h + S\frac{\partial h}{\partial t} = q \qquad (2\text{-}27)$$

where the source/sink flowrate density term $q = 0$ at points internal to the single fracture. In the steady-state case $\partial h/\partial t = 0$, so that this reduces to the Laplace equation:

$$T\nabla^2 h = q \qquad (2\text{-}28)$$

4) The net flowrate density into any point along a line segment of intersection is zero (except in the case of a source or sink located at the point).

As in the 2-D case, the 3-D network equations are built up by applying the Kirchhoff-type rules to each fracture intersection.

Implementations of the discrete-fracture-network concept

Various computational approaches have been used to set up and solve the equations that describe the discrete-fracture network conceptual model, including pipe networks, semi-analytical methods based on image theory, the boundary element method, and the finite-element method.

In the pipe-network approach (Cacas *et al.*, 1990a; Nordqvist *et al.*, 1992), the plate-network flow problem is reduced to a pipe-network problem composed of 1-D line segments as in the 2-D model described above, except that the pipes are connected in 3-D.

Using image theory, Long *et al.* (1985) developed an analytical solution for the

steady-state flow in a single disc-shaped fracture as a function of the average heads along a set of uniform-strength line sources/sinks. The network mass balance (Kirchhoff-type rules) leads to a set of linear algebraic equations that can be solved for the average head along each line segment of fracture intersection.

In the boundary-element approach (Shapiro and Andersson, 1985; Andersson and Dverstorp, 1987), the Laplace equation for each fracture is transformed into a boundary integral over the line segments of intersection and over the rim of the fracture, across which a no-flow condition is assumed to hold. As in the mixed analytical/numerical method, this leads to a set of linear algebraic equations in terms of the average head along each intersection segment.

The finite-element method (*e.g.*, Robinson, 1984) has proven to be the most versatile method for modeling flow in discrete-fracture networks, as it can accommodate transient flow, arbitrary fracture shapes (including nonplanar fractures), complicated boundary geometries, and mixed boundary conditions. This approach is the basis for flow modeling in commercial DFN software including FracMan/MAFIC (Dershowitz *et al.*, 1996) and NAPSAC/CONNECTFLOW (Jackson *et al.*, 2000). In this approach the fractures are divided into triangular or quadrilateral *elements*, and the unknown head field is approximated piecewise as a linear or quadratic function within each element. These piecewise functions are expressed in terms of the unknown head values (usually) at the element corners which are referred to as *nodes*. All elements adjoining a given shared edge will share the same nodes, and thus will have consistent head values, whether the edge is part of a fracture intersection or is just an internal, artificial division of a single fracture.

The partial differential equation for flow as defined on the network is transformed into a linear algebraic equation in terms of the unknown nodal heads by an integration over the domain, *e.g.* by integrating the squared approximation error over each elements and requiring that the sum over all elements be minimized. Other finite-element formulations such as the Galerkin formulation may be used. For the transient case, usually the transient portion of the problem is treated separately by use of time-stepping methods. Alternatively, time-continuous solutions can be used as presented later in this thesis.

Flow through a discrete-fracture network in a permeable matrix

Fully coupled matrix flow or matrix/fracture fluid exchange (as in the dual-porosity model of Warren and Root, 1963) can be built into the models in various fashions:

- Full discretization of the matrix blocks as a fully 3-D finite-element submodel, which is coupled to the finite-element model for the fracture network by shared nodal heads (Miller et al., 1994). In practice discretization of 3-D matrix blocks for an arbitrary fracture network has proven to be very difficult, but models developed for relatively simple geometries can be used as a check on other methods. Clemo (1994) and others have used this approach for 2-D fracture/matrix flow problems.
- Representation of matrix blocks as "storage volumes" of simple geometry (*e.g.* spheres or slabs) which take up or release fluid to an adjacent fracture but do not act as conductive pathways between fractures (Miller *et al.*, 1994).
- Boundary-element formulation for flow through a homogeneous matrix coupled with a finite-element formulation of the DFN flow problem (Shapiro and Andersson, 1985). This approach has the advantage that matrix discretization is not necessary, but is restricted to the case of steady-state flow and a homogeneous matrix.

In practice, the discrete approach leads to very large computational problems involving up to millions of fractures for large-scale problems. Clemo (1994) and Lee *et al.* (2001) have proposed approaches for upscaling of fracture networks respect to flow properties. The transport properties of these upscaling methods have not yet been fully explored.

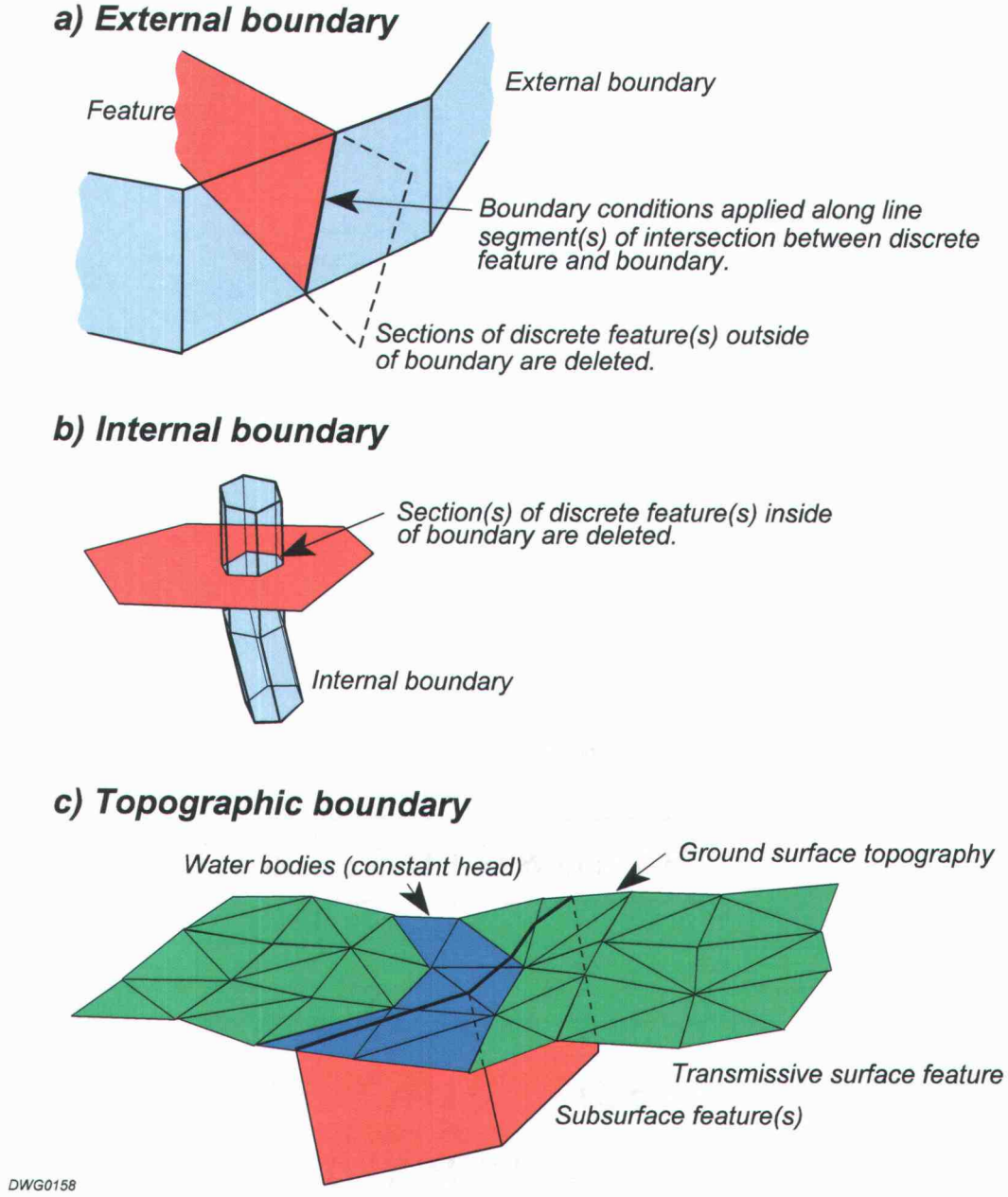

Figure 2-7. Example of implementation of boundary conditions in a discrete network model using the finite element approach (from Geier, 1996).

Stochastic fracture-network modeling

Most applications of discrete-fracture-network models have been stochastic models based on probabilistic description of fracture populations (Wilson, 1970; Long *et al.*, 1982; Robinson, 1984; Endo *et al.*, 1984; Dershowitz, 1984; Long and Witherspoon, 1985; Cacas *et al.*, 1990ab; Stratford *et al.*, 1990; Dershowitz *et al.*, 1991; Herbert *et al.*, 1991; Dverstorp *et al.*, 1992; Geier *et al.*, 1992; Geier, 1996; Bour and Davy, 1997). In these models, fractures are described in terms of a stochastic process for fracture location, intensity measures (*e.g.*, fracture spacing), and probability distributions for fracture properties such as size, orientation, aperture, transmissivity, storativity, and possibly additional mechanical or transport properties depending on the specific type of model.

Statistics to characterize the stochastic process for fracture location and probability distributions for fracture property are obtained by statistical analysis of data from mapping on outcrops and/or in underground tunnels, drill core or borehole mapping, and hydraulic tests in boreholes. Statistical methodologies for estimation of these properties from field data have evolved as a major subdiscipline within the field of fractured rock hydrogeology (*e.g.*, Dershowitz *et al.*, 1996).

Most network-modeling studies have considered the behavior of random networks in which fracture location is described by a 2-D or 3-D Poisson process. That is, the center of each fracture is a point $\boldsymbol{x}$ with uniformly random component coordinates $x_i \sim U(a_i,b_i)$, where a_i and b_i are the maximum and minimum coordinates in the ith dimension. A Poisson-process model is thus a spatially homogeneous stochastic process which tends to produce uniformly scattered fractures rather than clusters. Thus it does not mimic the concentration of fractures typically seen in the damage zones of fault zones.

Network models mimicking fault-zone concentrations of fractures

A number of attempts have been made to mimic concentrations of fractures, such as occur in proximity to fault zones, within fracture network models. The common property of these models is that fracture location is a spatially heterogeneous stochastic process, in contrast with the spatially homogeneous process (*i.e.*, simple Poisson process) models.

The tendency of fractures to occur in clusters related to larger fractures was recognized by Billaux *et al.* (1989), who proposed a "parent-daughter" model to account for geostatistical correlations between secondary and primary fractures in a network. The complexity and number of parameters of this model limited its use in site-specific applications.

Lee (1988) proposed a set of fracture-zone mimicking models based on (1) a fractal clustering algorithm based on a Lévy flight (fractional Brownian motion) process for fracture location, (2) a compound Poisson process in which the intensity of fractures in the nth set decays exponentially with distance from the "nearest neighbor" fracture in the $(n-1)$th set, and (3) a compound Poisson process in which intensity of the nth set of fractures is increased within overlap zones between fractures in the $(n-1)$th fracture set.

The Lévy-flight model produces fracture swarms which tend to be amorphous. The "nearest-neighbor" model produces concentrations of fractures similar to that seen in the damage zone around faults. The third model produces elevated fracture intensity in distinct tabular zones similar to the stepovers in en échelon zones. Analysis of fracture data from granitic rock at Stripa, Sweden in terms of these models was presented by Geier *et al.* (1988), and subsequently these models were implemented in a commercial FracMan code for modeling stochastic fracture populations (Dershowitz *et al.*, 1996).

The nearest-neighbor model of Lee (1988) was applied to granitic rock at Finnsjön, Sweden (Geier *et al.*, 1992). Analysis of fracture intensity adjacent to borehole radar reflectors showed that fracture intensity decreased exponentially with distance from the reflectors, which Geier *et al.* interpreted as representing sub-kilometer-scale fracture zones. The influence of these structures on the spatial correlation of effective permeability and anisotropy was evaluated by simulation of flow through rock blocks on scales of 15 m to 40 m (Geier and Hässler, 1992), but no specific analysis was made of the correlation structures within the fracture zones themselves.

A power-law distribution of fracture size l (*i.e.*, length in 2-D models or disc radius in 3-D models) has a probability density function of the form:

$$f(l) = Cl^{-a}$$

where C is a constant and $0 < a < 3$ for physically realistic situations (Renshaw, 2000). A power-law distribution is more likely to produce extensive single fractures that connect over

large scales, in comparison with more conventional distributions such as lognormal and exponential distributions. Thus it has the capacity to represent large-scale connections due to fault zones which may appear as single lineaments in larger-scale mapping.

Power-law scaling of fracture size was recognized in granitic rocks in the Sierra Nevada (Segall and Pollard, 1983) and in volcanic rocks at Thingvellir, Iceland (Gudmundsson, 1987). The 3-D model of Geier *et al.* (1992) also incorporated a power-law distribution for fracture size, based on an integrated interpretation of fracture maps from a range of scales. Power-law scaling was also deduced from analysis of fracture maps in granitic rock at Äspö, Sweden (Geier and Thomas, 1996) and in sandstones in western Norway (Odling, 1997).

A systematic study of the connectivity properties of fracture networks with a power-law size distribution was conducted by Bour and Davy (1997), using a 2-D network model in numerical experiments. They confirmed that such networks have significantly different percolation properties than models based on finite-variance size distributions, and developed rules relating network properties to the exponent of the power-law distribution. De Dreuzy *et al.* (2001a,b) extended this analysis to consider power-law distribution with correlations between fracture size and aperture. Renshaw (2000) further discusses the connectivity properties of power-law networks near the percolation threshold.

For a model of granitic rock at the Stripa site, Sweden (Dershowitz *et al.*, 1991), fracture zones were represented in a discrete-fracture network model as simple tabular zones of elevated fracture intensity relative to the protolith, and with distinct fracture population statistics. The models were used for simulation of in-situ tracer experiments as part of a validation exercise for the discrete-fracture-network concept, but were not further analyzed in terms of the role of fault-zone architecture for flow and transport.

Fracture network models have been used more recently by Caine (1999) to explore the flow behavior of fault-zone end members including single-fracture, distributed deformation, localized deformation, and composite deformation models. Hicks *et al.* (2000) have also used network models to explore the flow behavior of en échelon zones. Findings from this investigations are discussed later in this chapter.

2.2.6 Solute transport in fracture networks

Solute transport in a discrete fracture network entails at least three main categories of transport phenomena (Figure 2-8):

- Advective-dispersive transport within a given fracture.
- Exchange of solute species with the wall rock, *e.g.* by sorption and/or matrix diffusion.
- Mixing at fracture intersections.

The first two of these categories have been discussed with respect to single fractures, in the preceding sections. The third category, mixing at fracture intersections, is unique to the problem of network-scale transport. Relevant results of past research are reviewed in this section, prior to a review of how these phenomena are combined in transport models.

Additional phenomena that might affect particular problems include:

- Solute decay (radioactive or biological).
- Chemical reactions (among multiple solute species and/or minerals in the wall rock).

These phenomena are highly dependent on the particular chemical species considered and the detailed hydrogeochemistry. Hence these are mainly outside of the focus of this investigation which is focused on more general effects of fault-zone geometry on flow and transport.

However, radioactive decay should be mentioned in one respect important for the practical significance present study: When considering safety of a repository, radioactive decay can make the difference between retardation and retention of radionuclides within the bedrock. The rate of decay to daughter products is proportional to the number of atoms N of the radionuclide present at a given time:

$$\frac{dN}{dt} = -\lambda N \qquad (2\text{-}30)$$

where λ is the decay constant for the given species. This implies an exponential reduction in the mass $m(t)$ of a given radioactive species with time t.

$$m(t) = m(t_0)e^{-\lambda(t-t_0)} \qquad (2\text{-}31)$$

transport in a network. Slower transport of radionuclides by advection and longer retardation by processes such as sorption and matrix diffusion lead to decay of more radionuclides before

they discharge from the fracture network into the surface environment. Thus the process of radioactive decay has the possibility to increase the significance of other phenomena that retard the transport of radionuclides.

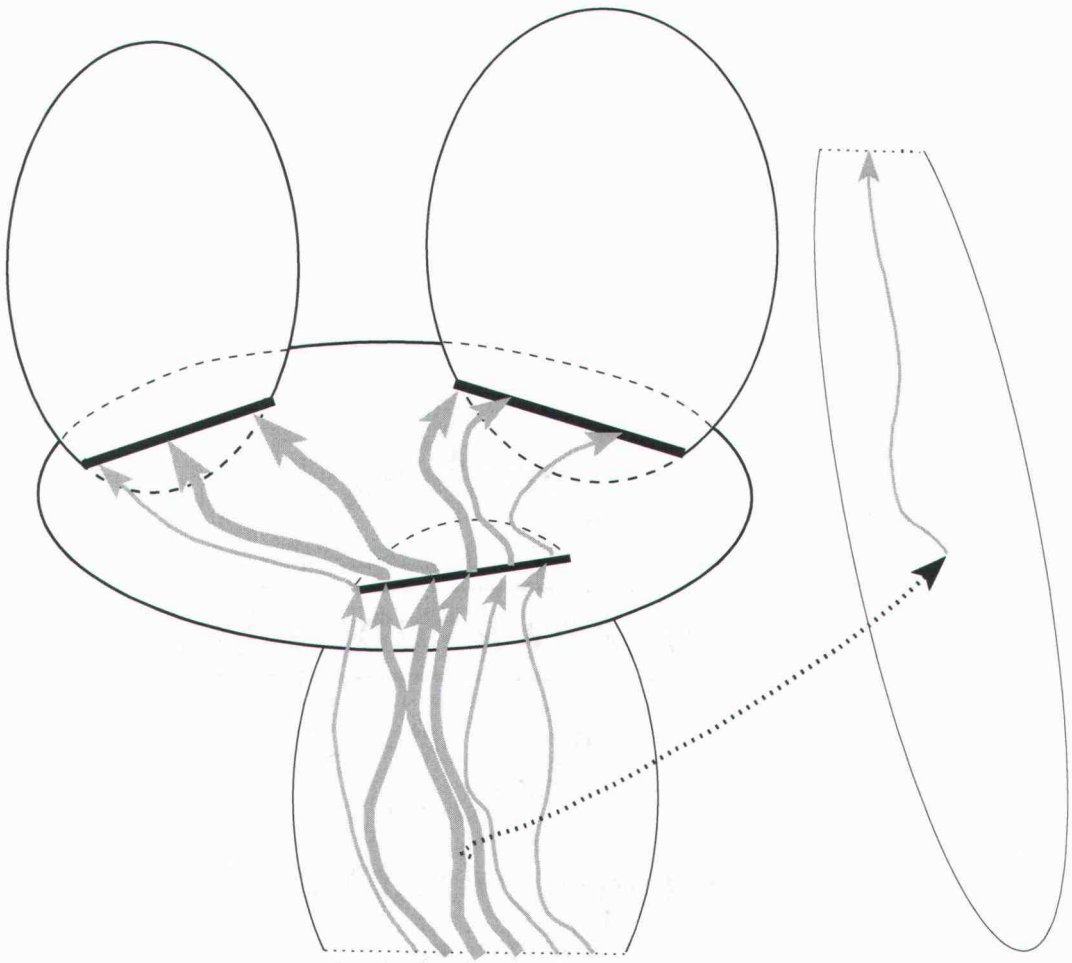

Figure 2-8. Schematic illustration of processes affecting transport in a fracture network. Solute moves by advection along streamlines in what may be heterogeneous flow fields in a given fracture, with dispersion due to velocity variations in combination with diffusion both parallel to and transverse to the local flow direction . Solute may interact with the adjacent rock by sorption and/or by diffusion into the matrix, possibly even transferring via the matrix between fractures that are not otherwise directly connected.

Mixing of solute in fracture intersections in a network

Mixing at fracture intersections is unique to the problem of network-scale transport. However it can be viewed as analogous to a mixing process that acts in porous media, when the porous medium is viewed on the pore scale as a network of distinct conduits (as in the model of de Josselin de Jong, 1958). There are three basic possibilities (Figure 2-9):

- No mixing
- Perfect mixing
- Partial mixing

As discussed by Endo *et al.* (1984), the experimental evidence for mixing at fracture intersections is mixed. An experimental study by Krizek *et al.* (1972) showed that complete mixing occurs between streamlines that originate from different branches of the fracture network, even under laminar flow conditions. Other experiments by Wilson (1970), as well as later work by Robinson and Gale (1990) indicated the opposite: Virtually no mixing takes place under laminar conditions. To reconcile these contradictory conclusions, more fundamental analysis of the processes governing mixing at intersections is needed.

Mixing at an idealized fracture intersection could occur either by pure molecular diffusion or, if turbulence is present, by a combination of molecular and turbulent diffusion across the mean streamlines. For most situations of concern in fracture networks (excepting very high gradients induced at the wellbore during well tests), flow is laminar so the process of concern is molecular diffusion as expressed by Fick's law.

For the case of pure molecular diffusion in a laminar flow field, intuitively the degree of mixing in an intersection is governed by whether the transit time for fluid passing through the intersection is large or small relative to the time scale of diffusion. The fluid transit time is on the order of b/v, where b is the fracture aperture and v is the mean fluid velocity. The time scale for diffusion across a distance of half the aperture, on the other hand, is on the order of b^2/D_d, where D_d is the coefficient of molecular diffusion. The ratio of diffusion time to fluid transit time is thus on the order of:

$$\frac{b^2/D_d}{b/v} = \frac{vb}{D_d} = \mathrm{Pe} \qquad (2\text{-}32)$$

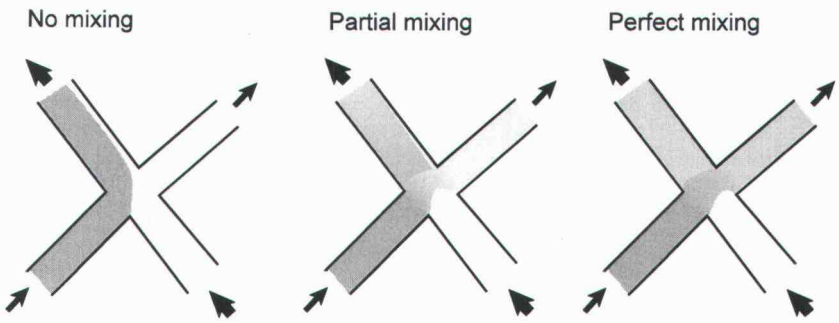

Figure 2-9. Qualitative illustration of different types of mixing at intersections in a fracture network model. Size of arrows indicates magnitude of flow through each branch; shading indicates concentration of solute entering or leaving the intersection in each branch.

where *Pe* is a Peclet number. When Pe $\gg$ 1 the transit of fluid is rapid relative to diffusion, and no mixing should be expected. When Pe $\ll$ 1, the time scale of diffusion is large relative to the fluid transit time, and a high degree of mixing should occur.

For reasonable values of b = 0.1 mm (10^{-4} m) and $D_d \approx 10^{-9}$ m^2/s, Pe > 1 when $v > 10^{-5}$ m/s, which is about 3.6 cm/hr or about 0.3 km/yr. Thus we would expect to see little or no mixing in laboratory experiments with v on the order of 1 cm/min or 1 cm/s. On the other hand, for flow through fractures within a radioactive-waste repository, v can be on the order of 1 m/yr or less, and a significant degree of mixing might be possible at fracture intersections.

Berkowitz *et al.* (1994) modeled this situation using an advective-diffusive particle-tracking technique in combination with an analytical solution for streamlines through an idealized intersection (as given by Philip, 1988). They found that mixing was in fact negligible (less than 5%) for Pe > 0.1, but increased to 34% as Pe decreased to 0.0001. Thus complete mixing was not obtained even for this low Peclet number, which corresponds to $v \approx$ 3 cm/yr in a 0.1 mm fracture. However, these results confirm that mixing at intersections

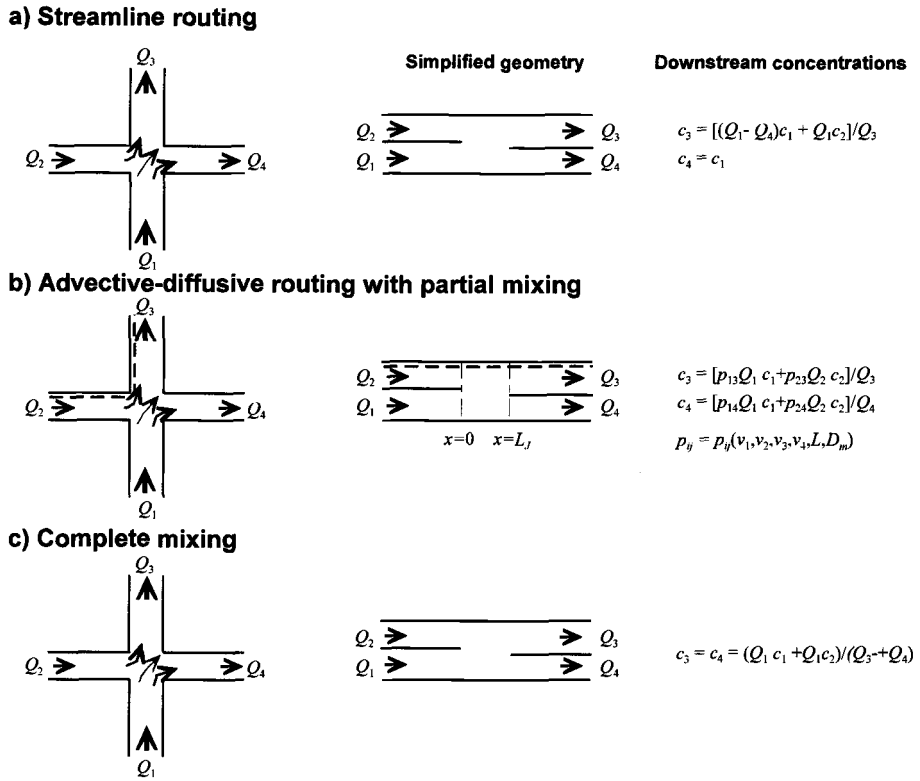

Figure 2-10. Alternative rules for routing of solute at four-branch junctions in a 2-D fracture network, with equivalents in terms of simplified geometry proposed by Park and Lee (1999).

would not be negligible for advective velocities on the order of 30 m/yr or less.

The position of the streamlines within the intersection are needed in order to model solute transfer due to diffusion across streamlines within the junctions. In detailed studies of individual junctions this problem has been addressed by numerical solution of the Navier-Stokes equation (Berkowitz *et al.*, 1994) or lattice-gas simulation (Stockman *et al.*, 1997).

Park and Lee (1999) proposed modeling advective-diffusive transport through junctions based on a simplified, "folded-up" geometry as depicted in Figure 2-10. With this simplification, they derived an analytical solution for solute transfer probabilities at 2-D intersections as a function of the fluid velocities and size of fractures entering and leaving an intersection. This 2-D solution does not easily generalize to a 3-D case, where a component of flow can occur along the fracture intersections (possibly a preferred direction for flow), leading to longer distances over which solute exchange can occur across streamlines belonging to different fractures. The result is also singular for stagnant branches of

intersections, which will exist in networks with dead-end fractures.

Detailed modeling of flow and transport through fracture intersections (Berkowitz *et al.*, 1994; Stockman *et al.*, 1997; Park and Lee, 1999; Park *et al.*, 2001) has shown that the degree of mixing is related to the Peclet number $Pe = av/D_m$ where v is the fluid velocity and a is a characteristic length for the intersection. For high Pe the rate of diffusion across streamlines is small relative to the advective velocity, and streamline routing (Figure 2-10a) may be a better approximation. For low Pe the rate of diffusive transport across streamlines is large relative to the rate of advection, and complete mixing (Figure 2-10c) may be a good approximation. At intermediate values of Pe, intermediate forms of routing may occur (Figure 2-10b). Thus for a fixed geometry, the degree of mixing for flow through the intersection varies with the fluid velocity.

Continuous-concentration models for solute transport in fracture networks

The assumption of complete mixing at fracture intersections may not apply for all flow situations of practical concern in modeling granitic rock. However, the results of Berkowitz *et al.* (1994) and of Park *et al.* (2001) suggest that this assumption may be reasonable for low flow velocities such as are expected to prevail in areas of low topographic relief under natural gradients (*e.g.*, post-closure conditions at a repository in the Fennoscandian Shield).

In such cases, adoption of a complete-mixing rule at fracture intersections allows construction of continuous-concentration models based on Kirchhoff-type laws of continuity and conservation of flux at intersections, analogous to those invoked for network flow models. We need only substitute concentration c for head h, substitute mass flux q for flowrate intensity q, and replace the transient flow equation by the advective-dispersive equation, possibly with terms for sorption, matrix diffusion, decay, *etc.* Thus the rules 2-4 for the fluid-flow models are replaced by following:

1) Each fracture (or segment thereof, for heterogeneous fracture models) is treated as a conduit of appropriate dimension (1-D for a 2-D network model composed of linear fracture segments, or 2-D for a 3-D network model composed of plate-like fractures).
2) At any point along the line segment of intersection between two fractures, there is a single value of concentration c_i which is common to both fractures

(complete mixing assumption).

3) The spatial and temporal derivatives of concentration at any point within a fracture satisfy the AD equation (with terms as appropriate for sorption, matrix diffusion, radioactive decay *etc.*):

4) The net mass flux into any point along a line segment of intersection is zero (except in the case of a solute source or sink located at the point).

Thus the problem of solute transport through a fracture network, with or without coupled diffusion through the matrix rock, is analogous to the corresponding cases of transient groundwater flow.

In principle, network models for solute transport can be constructed by applying the finite-element method to the network transport equations in exactly the same manner as we saw in the case of flow. However, severe practical difficulties arise in the form of numerical dispersion effects at the solute front. Refinements such as adaptive gridding that are used to control these effects in continuum models are more difficult to implement in the complex geometry of a DFN model.

One method used to mitigate numerical dispersion effects is the Laplace transform Galerkin (LTG) finite-element method (Sudicky, 1989). In the LTG approach one uses the finite-element method to solve the Laplace transform of the network transport equations, and then performs the inverse Laplace transform by a numerical algorithm to obtain solutions to the transport problem at any chosen point in time. Sudicky and McLaren (1992) applied the LTG method to model fully coupled fracture/matrix transport of a contaminant downward through fractured clay. They used a 2-D model with a relatively simple fracture geometry (orthogonal fracture sets), which allowed for simple mesh generation. However, in principle the technique can be applied to 3-D network models of arbitrarily complex geometry (as developed in this dissertation).

Matrix diffusion is usually included in fracture network models by means of idealized geometries. Sudicky and Frind (1982) presented an analytical solution for advective-diffusive transport with matrix diffusion in a system of parallel fractures. Moreno and Neretnieks (1991; 1993) developed a channel-network model based on a regular grid of 1-D channels (effectively pipes, but intended to represent a variety of actual channel geometries) with variable properties between channel junctions.

Particle-tracking methods for modeling solute transport in fracture networks

Due to questions about the degree of mixing at intersections, as well as problems of numerical dispersion in continuous-concentration models, most attempts to model solute transport in discrete fracture networks have used particle-tracking approaches (*e.g.*, Cacas *et al.*, 1990ab; Nordqvist *et al.*, 1992; Dershowitz *et al.*, 1991; Geier, 1996). Advective-dispersive transport within a 3-D fracture network can be modelled by the discrete-parcel random walk (DPRW) method (Ahlstrom *et al.*, 1977). This approach represents local, 2-D advective-dispersive transport within each fracture plane. Alternatively it may be used to represent 1-D advective-dispersive transport within a fracture segment, for the simpler case of a 2-D network model. Network dispersion, due to the interconnectivity among discrete features, arises as the result of local dispersion in combination with mixing across fracture intersections.

In the DPRW method, the motion of a particle within a fracture element is modelled as a random walk of appropriate dimension. In the random walk, each step $\Delta \boldsymbol{x}$ consists of a deterministic, advective component plus a random, dispersive component. The advective component of $\Delta \boldsymbol{x}$ is $\boldsymbol{u}\Delta t$, where $\boldsymbol{u}$ is the (local) fluid velocity calculated from the local head gradient ∇h and hydrologic properties as:

$$\boldsymbol{u} = -\frac{T}{b_T}\nabla h \tag{2-33}$$

and Δt is a locally-specified time step. In order to account for linear instantaneous, reversible sorption, the retarded velocity $\boldsymbol{u}' = \boldsymbol{u}/R$ is used in place of $\boldsymbol{u}$ in calculating the advective component, where $R = 1 + a_w K_a$ is the retardation factor as defined for surface sorption.

The random, dispersive component $\boldsymbol{r}$ is calculated as the vector sum of components representing longitudinal and (in the 2-D case) transverse dispersion (Figure 4-11). The longitudinal component (parallel to the local velocity) is generated from the normal distribution with zero mean and variance:

$$\sigma^2 = 2D_L\Delta t \tag{2-34}$$

where D_L is the longitudinal dispersion coefficient. The transverse component (perpendicular to the local velocity, and in the plane of the element) is generated from the normal distribution

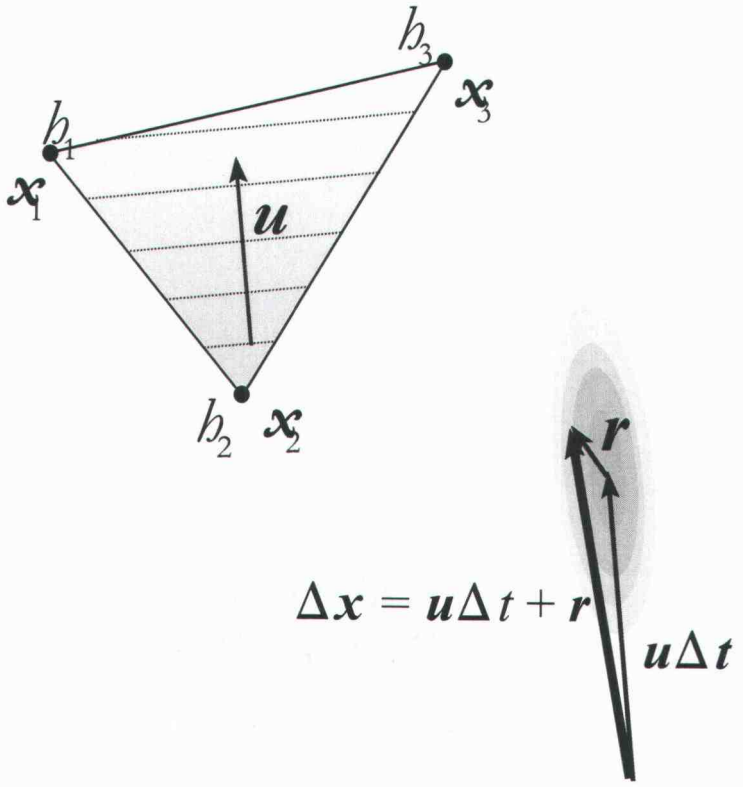

Figure 2-11. Particle-tracking algorithm for advective-dispersive transport within a 2-D triangular element of a fracture.

with zero mean and variance:

$$\sigma^2 = 2D_T\Delta t \tag{2-35}$$

where D_T is the transverse dispersion coefficient. The local dispersion coefficients depend on the magnitude of the local velocity as:

$$\begin{aligned} D_L &= \alpha_L |\boldsymbol{u}| + D_m \\ D_T &= \alpha_T |\boldsymbol{u}| + D_m \end{aligned} \tag{2-36}$$

where α_L and α_T are the longitudinal and transverse dispersivities, respectively, within a given fracture.

Extensions of the DPRW method have been developed to account explicitly for Taylor-Aris dispersion due to diffusion in combination with in-plane fluid velocity variations plus the variation of velocity across the aperture of a single fracture (Detwiler *et al.*, 2000; Bruderer and Bernabé, 2001). A similar algorithm has been applied to examine the role of macrodispersion vs. Taylor dispersion in variable-aperture fractures by Wörman *et al.* (2004).

In these approaches, the dispersivities α_L and α_T in the above equations are set to zero so that only diffusion contributes to the random component of motion $\boldsymbol{r}$ in the plane of the fracture. The particle is also assume to move randomly due to diffusion in the direction perpendicular to the plane. The fluid velocity is assumed to have a parabolic profile across the aperture (as calculated from the assumptions of Poisieulle flow and no-slip boundary conditions, in the derivation of the cubic law), so as the particle moves across the aperture its motion is affected by lower or higher velocities depending on the distance from the fracture wall.

Application of the DPRW model in a network requires rules for transferring particles at fracture intersections. To date, applications have made use of one of the two end-member assumptions, either complete mixing or pure streamline routing, described as follows.

The complete-mixing assumption has been used in conjunction with particle tracking in several applications of DFN models to transport problems (Miller *et al.*, 1994; Dershowitz *et al.*, 1991; Geier, 1996). When a particle arrives at an intersection edge, the particle is randomly assigned to one of the elements sharing that edge. The probability of assignment to the *i*th connected element is:

$$P[i] = Q_i / \sum_e Q_e \qquad (2\text{-}37)$$

where Q_e is the inflow to the *e*th connected element along the edge (zero if there is outflow), and the summation is taken over all elements connected to the edge. This reassignment technique does not allow for particles to move between adjacent elements in the absence of net advection. Hence the model will under-represent the actual diffusion and/or transverse dispersion (due to small-scale heterogeneity within fracture planes) that takes place in the physical system.

For incomplete mixing or no mixing, streamlines must be determined at intersections. This has been done explicitly in 2-D studies (*e.g.*, Endo *et al.*, 1984; Bruderer and Bernabé, 2001), but becomes computationally difficult in 3-D. Nordqvist *et al.* (1992) resolved this problem in an approximate way by routing the particle to the outflowing branch that is closest to the inflowing branch (the branch via which the solute particle arrived). In case of a tie in proximity between two or more outflowing branches, the particle is randomly allocated to a branch with probability proportional to the fluid flux. The particle-tracking implicitly assumes

instantaneous, complete mixing immediately after the particle enters an outflowing branch; as noted by Nordqvist *et al.* (1992) this results in an artificial transverse dispersion.

Matrix diffusion can be modeled explicitly with the DPRW method by advective-diffusive tracking of particles through the matrix, although this requires either a discretization of the matrix or algorithms for finding intersections between particle trajectories in an undiscretized matrix and fractures. Either of these two approaches can be computationally intensive in 3-D meshes.

Dershowitz and Miller (1995) and Tsang and Tsang (2001) have presented efficient analytical solutions for particle tracking with diffusion into finite matrix blocks adjacent to fractures. In both approaches the matrix blocks are assumed to have idealized geometries, and the results are obtained in terms of a time delay for particles passing through the adjoining fracture. The principal advantage is an efficient way for accounting for matrix diffusion in particle-tracking models. A limitation of both approaches is that they treat matrix diffusion as effectively a 1-D process out of and back into a single fracture. Thus neither approach takes into account the possibility of fracture-to-fracture transfer or movement of solute along a fracture via the matrix. This distinction may not be significant for cases in which advective transport within the fractures is rapid relative to the velocity of the diffusion front in the adjoining matrix. However, for low advective velocities and networks near the percolation threshold (where inter-fracture diffusion across small gaps in the network may be critical), this simplification might need to be examined. Recently Tsang and Doughty (2003) have extended the particle-tracking approach to account for multi-stranded flow in complex fractures with variable properties, presenting results for realizations of a single, complex fracture with stochastic properties.

Delay and Bodin (2001) presented a time-domain random walk method for simulating advection-dispersion and matrix diffusion in networks composed of fractures idealized as 1-D "bonds" (line segments). This method is based on calculating the transit time distribution for particles to traverse each bond in the network, with or without diffusion into and out of the wall rock. The method for incorporating diffusion into the wall rock assumes that an infinite depth is available for matrix diffusion. The method appears to be more efficient than standard Lagrangian particle-tracking methods such as the DPRW method which require multiple leaps through each "bond," but has not yet been generalized to networks composed of 2-D elements. The authors note that their method is singular for $u = 0$ (stagnant fluid).

2.2.7 Modeling studies of impact of fault-zone architecture on fluid flow

Forster and Evans (1991) modeled a permeable thrust fault overlying crystalline basement, accounting for anisotropy of fault properties by reducing the permeability of a sliver of the fault overlying the more permeable damage zone. This produced increased flow above this fault core, but had little effect on the overall distribution of fluid pressure and temperature in their model. Effects of heterogeneity were also explored and found to have a strong impact on flux through the fault, but little impact on pressure and temperature overall.

Exploratory models of the effects of hydrologic heterogeneity within fracture zones on transport parameters (López and Smith, 1996; Tsang *et al.*, 1996; Geier, 1996) has demonstrated that fracture-zone heterogeneity characterized by correlation scales of 100 m to 300 m (for models on the scale of a few kilometers) can significantly affect groundwater flow patterns, local heat flux, and solute transport times, due to large-scale channeling of flow within these structures. To date, such modeling has been based on hypothetical geostatistical models for the spatial correlation of hydrologic parameters.

As part of the SKI SITE-94 project (SKI, 1996), Tsang *et al.* (1996) used a stochastic-continuum representation to model flow on the scale of 1 km at a hypothetical radioactive-waste repository in granitic rocks at the site of the Äspö Hard Rock Laboratory in SE Sweden. The heterogeneity of permeability in the model was produced by an indicator simulation technique which allowed the specification of different correlation lengths for different classes of hydraulic conductivity K. By introducing a hypothetical, large-scale correlation for the highest-K class, Tsang *et al.* were able to produce a model with heterogeneous, tabular, high-K regions resembling fracture zones as had been deduced from the structural geological interpretation. This type of model was found to predict significantly faster radionuclide times (for release from the repository to the surface environment) than stochastic-continuum models without such structures, due to large-scale channeling effects within the heterogeneous structures.

Also in the SKI SITE-94 Project, Geier (1996) modeled the influence of fracture zones by modeling them as a network of extensive, planar conductors referred to as "discrete features," analogous to single fractures or tabular aquifers. This type of model also predicted relatively fast transport of radionuclides, in comparison with the more homogeneous types of continuum models. This study considered 25 variational cases to evaluate the impact of

various assumptions regarding unconstrained aspects of the model. In one such case, fracture zones were represented as heterogeneous by using a geostatistical model for spatial correlation of transmissivity within each discrete feature. This was found to be one of the most significant variational cases in terms of effective parameters for radionuclide transport.

In the models of Tsang *et al.* (1996) and Geier (1996), the large-scale correlation structure for the hydraulic properties in the features representing fracture zones was simply assumed. The use of hypothetical rather than data-based geostatistical models is largely due to practical limits on the density of subsurface hydrologic measurements, which can make it impossible to discriminate among alternative geostatistical models based purely on point measurements of permeability (Tsang *et al.*, 1996).

Detailed-scale models of fracture zones and fault zones

Zhang and Sanderson (1996) modeled the effects of fault slip on fluid flow around extensional faults, using a distinct element model to account for the dilation resulting from fault slip in a normal fault with dilational and anti-dilational fault jogs adjoining a fractured layer above a basement block.

Caine and Forster (1999; also Chapter 2 of Caine, 1999) presented a series of 3-D discrete-fracture network models using representative field data to represent each of four fault-zone architectural styles defined by Caine *et al.* (1996): single-fracture fault (SFF), localized deformation zone (LDZ), distributed deformation zone (DDZ) and composite deformation zone (CDZ). Numerical simulations of flow in response to hydraulic gradients parallel and perpendicular to the fault plane and slip direction were used to illustrate the effects of the different fault-zone geometries on large-scale directional permeability.

In Caine and Forster's models, stochastic realizations of fractures were generated using the Enhanced Baecher model (Dershowitz *et al.*, 1996), a model which represents the fractures as being located according to a Poisson process but with probabilistic termination of fractures at intersections, in tabular domains with different fracture intensity and other fracture population statistics to represent protolith, damage zones, and fault cores. The LDZ model is essentially equivalent to the type of model employed by Dershowitz *et al.* (1991). In the SFF and DDZ cases, offsets were introduced along the main fault slip planes, to represent

the disruption in connectivity that can occur due to relative displacement of conductors in the protolith.

Within each tabular domain, the fracture population was treated as statistically homogeneous. Thus the models of Caine and Forster (1999) did not directly address the type of heterogeneity within fault zones that could result from large-scale structural variation along the faults. However, effects of fault evolution were addressed by modeling an increase in fracture aperture to represent opening during fault failure (or reactivation) episodes, and reduction of aperture to represent subsequent, gradual sealing of fractures by mineralization. These variations were used to examine changes in fault-zone hydrologic behavior during and after a failure or reactivation episode.

Odling (2001) presented a simple parallel-conductor model for scaling of hydraulic conductivity in multi-stranded fracture zones. Applying this model to data from fractured sandstones in Norway, Odling developed scaling rules for fracture-zone hydraulic properties in relation to length. Hicks *et al.* (2000) proposed a model of en échelon zones modeled as simple planar fractures linked either by fractured zone in a fault jog (similar to the "war zone" model of Geier *et al.*, 1988; Dershowitz *et al.*, 1996) or by single fractures parallel to the direction of the fault jog. They present an illustrative calculation cases for a fault with a single jog, using fracture hydrologic parameters based on representative values from the Borrowdale Volcanic Group at the Sellafield site, UK. The authors considering the effect of different transmissivity contrasts between the fractures within the jog and the main fault. As the ratio of these transmissivities increases, the fault jog becomes the dominant conduit, with reduction in breakthrough times for particles representing a conservative tracer, which are released from a point at depth.

Hicks *et al.* (2000) also produced illustrative calculations for a distributed-damage zone model similar to the DDZ model of Caine and Forster (1999), and presented breakthrough curves for particles representing a conservative tracer, for several different degrees of hydrologic property contrasts and sedimentary cover-rock permeability.

The models of Hicks *et al.* (2000) for both cases incorporate stress-field dependence, in the form of relationships for dependence of fracture hydrologic properties on the far-field stress field and local pore pressure. The effective transmissivity of a given fracture is dependent on an effective stress $\sigma_n - p$ where σ_n is the component of the far-field stress acting normal to the fracture plane, and p is the fluid pressure within the fracture. The shear stability

of each fracture is also assessed relative to the far-field stresses and local pore pressure, using a Coulomb failure criterion, and the aperture is increased if shear failure is inferred to occur, following the empirical model of Barton *et al.* (1985).

2.2.8 Synthesis

Review of laboratory and field studies leads to basic conceptual models for fault-zone evolution and scaling relationships. Key architectural elements that emerge from this survey are en échelon fractures and échelon steps, splays and other secondary fractures, fault breccias, and fault gouge.

A general conceptual model emerges of fracture zones as zones of localized brittle failure that have developed to accommodate strain during regional deformation. Early stages of inelastic deformation (small regional strains) are accommodated by diffuse fracturing throughout the protolith, with extension, interaction and linkage among fractures in en échelon arrangements. Thus en échelon zones may be the main type of large-scale structure seen in regions which have undergone relative small regional strains, or internal to rock blocks which have been shielded from larger strains by localization of strain along their boundaries.

Continued deformation is accommodated by increasing localization of strain within zones of relatively intense fracturing, leading to development of shear faults. In regions that have undergone large strains, such faults may typify boundaries of rock blocks.

Nucleation and growth of a fault is preceded by and/or accompanied by development of a process zone or "halo" of smaller-scale fracturing and faulting in the vicinity of the propagating fault. With continued deformation, strain becomes increasingly localized within a distinct fault core of highly fractured rock and/or breccia (high permeability), while growth of fractures in the halo largely ceases.

Continued deformation is accommodated within the fault core by regular shear fracture arrays within the breccia. Intense comminution (grain size reduction) along these shear fractures may produce low-permeability lenses of gouge (ultracataclasite) within the core, although in very low-permeability granitic rock the gouge may be significantly more permeable than the protolith. Strain gradually shifts to shear fractures aligned nearly parallel to the macroscopic fault plane, often at one or both boundaries between the fault core and the surrounding fracture halo. Reactivation of fault zones is usually along pre-existing planes of weakness within the fault cores.

This conceptual model has implications for groundwater flow and radionuclide transport. First, it implies that flow properties within fracture zones will be heterogeneous and

anisotropic. Fracture halo and breccia zones may be favorable to flow along the fracture zone. Flow paths through the fracture halo may be irregular due to fracture network effects. Highly comminuted gouge along shear fractures may act as barriers to flow across the fracture zone. Relative proportions of different structural elements (fracture halo, breccia, and gouge) may vary with position along the fault.

This conceptual model also implies that transport properties will be more complex than in a simple, equivalent porous continuum model of a fracture zone. Scale-dependent macrodispersion may result from heterogeneous flow through a network in the fracture halo. Contrasts in mean advective velocities between breccia, fracture halo, and gouge may result in anomalous transport influenced by diffusion between relatively mobile and relatively immobile portions of the groundwater in the fracture zone. Matrix diffusion into fragments of variable size in breccia may result in anomalous transport which is mathematically equivalent to multiple-rate matrix diffusion, as shown by Cunningham and Roberts (1998). Alteration or precipitation of minerals within fault-zone fractures and breccia may produce further heterogeneity with respect to flow and transport properties (including effective partitioning coefficients for sorbing species).

Finally, several studies suggest that fault-zone architecture may have similar geometric characteristics across a large range of scales. From this, we may expect that the effects of fault zone architecture on heterogeneous fluid flow and solute transport will also be manifested on a wide range of scales. Furthermore, this suggests the usefulness of field studies of fault-zone geometry on scales that are relatively convenient to observe in outcrop, for developing improved conceptual models of fault-zone networks on larger scales. Among the key architectural elements of fault zones, fractures and fault breccias appear to be particularly important elements of pathways for fluid flow and solute transport granitic rock. An extensive body of research has developed on the flow and transport properties of individual fractures (including hydromechanical effects) and their aggregate behavior in networks.

The variation of aperture within single fractures, and its effects on flow and transport, has been studied in great detail both experimentally and using numerical models. Less is known about variability of properties that may govern mass transfer with the wall rock of fractures (matrix diffusivity, matrix connectivity, fracture mineralogy and sorption coefficients) although the work of Xu *et al.* (2001) provides both data on limited scales, and a

theoretical exploration of the results. Recognition of the complexity of natural fractures and minor faults as potentially multi-stranded features with variable constituent properties (alteration zones, multiple strands, gouge, *etc.*) has grown in recent years, notably with the work of Mazurek *et al.* (1996; 2003) and Tsang and Doughty (2003).

Capabilities of modeling network flow and transport in large populations of fractures have also advanced greatly in recent decades, as well as methods for up-scaling of flow properties. Much of this development continues to be in terms of fracture populations defined in terms of idealized statistical measures (Poisson, geostatistically correlated or fractal models for fracture location; lognormal or power-law distributions of fracture size and aperture; independent random variables describing properties of individual fractures or simple models of correlation). Relatively little research has examined the significance of structural complexity along fault zones which might not be well described by these types of statistical models. Notable exceptions are the work of Caine (1999) and Hicks *et al.* (2000) who have explored the consequences of more complex fault-zone structural models using discrete-fracture network simulations. These efforts mainly considered flow properties, with less attention to transport properties of the fault zones considered (although Hicks *et al.* investigated the advective trajectories of particles representing conservative tracers).

Network effects on solute transport have mainly been investigated in terms of idealized 2-D networks, at a high level of abstraction. This work has yielded theoretical insights into topics such as macrodispersion in networks near the percolation threshold, and the relative importance of intrafracture and network heterogeneity for macrodispersion. However, questions can be raised as to whether complex natural fracture and fault systems are adequately described by the idealized models employed in these types of studies.

Similarly, developments of mass-transfer theory for granular media of variable size have likewise provided valuable theoretical insights. However, in applying these results to complex structures in fractured rock, questions remain as to the consequences of interplay between spatial variability on different scales, *e.g.*, particle-size variability or network response of microfractures in the matrix over a few cm in a complex fracture *vs.* channeling effects over scales of decimeters to meters, and larger-scale network connectivity effects. An outstanding question is whether the methods for description of heterogeneity on these various scales capture the most important properties for aggregate behavior of the system.

The research presented in the following chapters of this dissertation aims to address

some of the gaps identified in this literature survey, by exploring the consequences of complex fault-zone geometry based as nearly as possible on direct observations in the field.

3. METHODS

The methods of investigation for this study comprise three main steps:

- digital mapping of fracture zones,
- statistical analysis of the resulting fracture trace maps, and
- flow and transport simulations in models based on the maps and statistics.

These steps are outlined briefly in the following paragraphs, with details given in the sections of this chapter which follow.

To prepare the digital maps, examples of fracture zones were mapped by systematic photography of outcrops and road cuts. Fracture traces were identified by marking points on computer displays of the images thus obtained. The resulting fracture trace maps were rectified with respect to points of manually measured coordinates in each image.

Analysis of the digital maps focused on the connectivity properties of the mapped fractures in and adjacent to the fracture zones, which are of key importance for hydrologic and transport behavior. An interactive computer program developed as part of this investigation was used to calculate statistics with respect to primary fractures, which were identified by inspection. Statistics of fracture traces that connected to the primary fractures were calculated to characterize the frequency, length and relative orientation of connected, secondary fractures (referred to herein as branches), as well as the depth or block-size distribution of unfractured rock adjacent to these branches. This analysis was repeated for successive orders of secondary fractures to characterize the fractures that connect to the primary fractures, either directly or indirectly, in terms of the statistics of branched network structures and the adjacent matrix.

Modeling of groundwater flow in networks with statistics similar to the hierarchical structures in the maps was done by discrete-fracture network modeling techniques, based on the finite-element method. Solute transport was modeled by a particle-tracking technique developed as part of this work. Details of these components of the methodology are described in the following sections of this chapter.

3.1 Field Mapping

Two types of fracture zones were chosen for detailed study. The first type, addressed in this thesis, is a set of N to NNW-trending, near-vertical zones that are expressed on surface outcrops as en échelon fractures linked by step-over zones (duplexes). In terms of the fault-zone architectural styles proposed by Caine (1999), these structures can be viewed as a fault of single-fracture type (the discrete segments), punctuated by zones of localized-deformation type (the duplexes).

The N to NNW trending, en échelon zones are interesting from a hydrological perspective since the main fractures strike at a low angle to the regional maximum compressive stress. This increases the likelihood that these fractures are transmissive. In combination with a low ratio of fracture surface area to water volume, because these zones are dominated by single, discrete fractures, this could give the fractures a high potential for rapid transport of radionuclides to the environment from a repository, for radioactive-waste disposal,

A second type of fault zone important for the hydrogeology of this site is exemplified on Äspö by the broad, NE-SW trending deformation zone that divides the island. Following the nomenclature of Caine (1999), this can be described as a composite-deformation zone. The hydrologic behavior of this second type of fault zone was investigated in this study by considering the hydrologic behavior of an idealized fracture-zone model with the same variation of fracture intensity vs. distance from the main slip surfaces, as in the mapped zone.

Fracture zones and exposures for study at Äspö were chosen based on consideration of past geological studies, including fracture mapping on outcrops (Ericsson, 1987; Talbot and Munier, 1989), and reconnaissance of the island. Detailed data on the geometric configuration of fractures in the chosen fracture zones were obtained by photographic and direct mapping during a field visit May 1999, and by subsequent computer analysis of the photographic images.

A N-striking en échelon fracture zone exposed on one outcrop on SW Äspö was mapped in detail on a 1:10 scale by a photographic mapping procedure (Figure 3-1) which is described in detail in Appendix A. The detailed maps thus developed account for a total length along strike of about 15 m. A survey of N to NNW-trending en échelon zones in the vicinity of this outcrop was also made, to obtain estimates of the spacing and geometry of

stepovers along this set of fracture zones. A 20 m transect across a major NW trending fracture zone was also photographed systematically using the same methods as for the en échelon zone examples, but analysis of these data was not completed.

The N to NNW trending fracture zone represents a distinctive family of structures found on Äspö, which are composed of extensive (up to 10 m in length), simple fractures arranged *en échelon* , with complex duplex structures connecting between the overlapping ends of these fractures. This family of structures is expected to be of hydrologic significance, especially for radionuclide transport, due to several factors:

- Orientation nearly perpendicular to the direction of regional minimum horizontal stress, which means that the extensive simple fractures are less subject to stress-induced closure, and thus are expected to be more transmissive than fractures in other orientations.
- Connections between extensive, simple fractures (joints or simple faults) via the intensely fractured duplex structures result in well-connected, discrete structures that may extend for hundreds of meters.
- Low specific wetted surface area in the simple fractures implies relatively poor radionuclide retention properties for these structures.

The NW trending fracture zone (in EW-1) represents a second, more complex type of hydrologically significant fracture zone that is found on Äspö. This particular zone is interpreted as part of a regional-scale structure which divides the northern block of Äspö from the southern block. Results of hydrologic interference (pumping) tests that were carried out on Äspö during the pre-investigation phase for the Äspö Hard Rock Laboratory suggest that there is a hydrologic boundary between the northern and southern blocks, which might be explained by a high-transmissivity zone that acts effectively as a constant-head boundary with respect to pumping tests in either block.

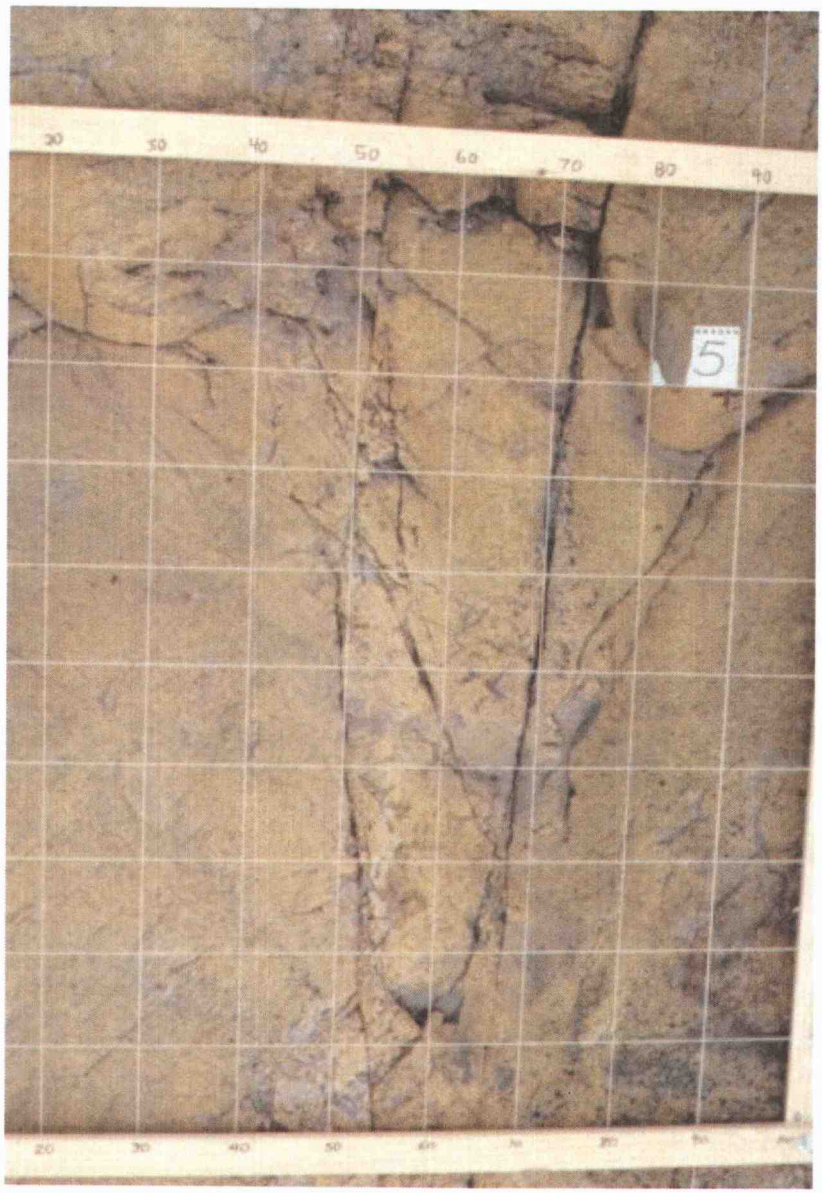

Figure 3-1. Example of photographic mapping method using a grid. This is one of the approximately 45 photographs making up the photographic mosaic of the exposure on Äspö. The spacing between grid lines (strings visible as white lines in the photo) is 10 cm.

The mapping at Ekolsund was carried out in September, 2001. The mapping method was adapted for the mainly vertical exposures at this site. A single fracture zone showing geometric characteristics of an en échelon fault zone, which was mappable across all four vertical exposures at the site, was chosen for detailed mapping. The en échelon zone chosen for detailed analysis was named "MY-1" in part for the proximity of its projection to an "M" road sign on the one-lane access road to the north side of the site (indicating "*möteplats*" or "meeting place" for cars to yield to oncoming traffic) and partly as a whimsical reference. Other zones showing more distributed deformation analogous to the EW zone on Äspö were mapped in detail as part of the same project, but the data have not yet been fully analyzed.

3.2 Geometrical Analysis

Digital maps of fracture traces were analyzed in terms of geometric characteristics that could affect flow and transport through the fracture zones. In addition to more basic fracture statistics, characteristics that were analyzed included:

- hierarchical branching structures,
- spatial correlations among fractures of different order,
- block size distributions as a function of fracture order, and
- breccia (highly fragmented) zones.

The analysis in terms of hierarchical branching structures is inspired in part by concepts of fractal geometry and analysis of stream/drainage networks of different orders. The use of the term "branches" in this context follows Moody and Hill (1956), who noted a similarity relationship of subsidiary faults to dominant faults in wrench-fault systems.

Fracture order and branching structures (represented as groups of polylines, *i.e.,* open polygons or connected line segments) are defined with respect to *primary fractures* which are identified interactively, by inspection (Figure 3-2). The program then identifies *first-order branches* as the fracture traces that connect to the primary fractures at one end. *Second-order branches* are identified as fractures that connect to first-order branches at one end, and so on until no further branching fractures can be found.

For convenience we introduce the notation ψ_i to denote a set of branches of order I pertaining to a structure defined in terms of a given set of primary fractures, which are denoted ψ_0. A *branching structure* of a given order I is defined here as consisting of the primary fractures and all branches up to and including the ith-order branches. The notation Ψ_i is used here to denote a branching structure of order I. Thus:

$$
\begin{aligned}
&\Psi_0 = \psi_0 \\
&\Psi_1 = \Psi_0 \cup \psi_1 = \psi_0 \cup \psi_1, \\
&\Psi_2 = \Psi_1 \cup \psi_2 = \psi_0 \cup \psi_1 \cup \psi_2, \\
&\cdot \\
&\cdot \\
&\cdot \\
&\Psi_N = \Psi_{(-1)} \cup \psi_N = \psi_0 \cup \psi_1 \cup \ldots \cup \psi_N,
\end{aligned}
\qquad (3\text{-}1)
$$

where N is the highest order for which the set ψ_N is not empty. In other words Ψ_N consists of all fracture traces (within the resolution of the map) that connect to the primary fractures ψ_0,

either directly or indirectly via other fracture traces. For the sake of brevity, we will refer to this as an *N*th-order branching structure or *entire* branching structure.

Assuming all fractures to be water-conducting, the fractures in Ψ_N would be accessible to solute moving through the primary fractures, by some combination of advection and diffusion through the network of connected fractures.

The entire branching structure Ψ_N is found by iteratively identifying the branching structures of successive order *I* until the set ψ_{i+1} is empty.

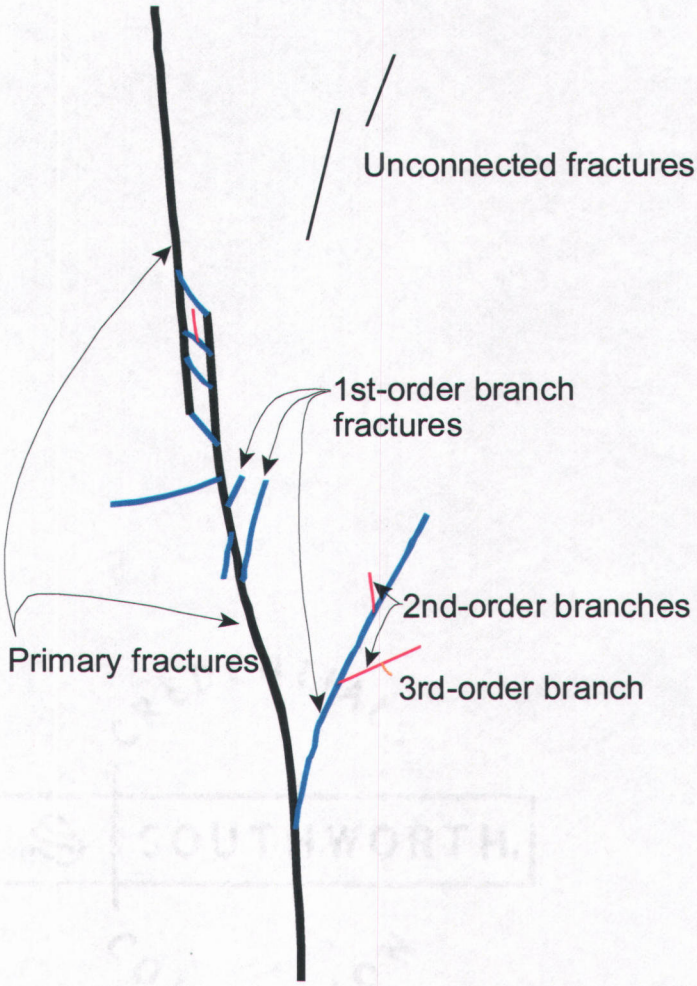

Figure 3-2. Definition of different orders of branch fractures, relative to primary fractures. Unconnected fractures which do not connect to the primary fractures, either directly or indirectly, are treated as a separate class of fractures.

Matrix volume within a given distance of a branching structure

Following Neretnieks and Rasmuson (1984), the volume of matrix within a given distance of fractures can be regarded as a measure of the volume available for matrix diffusion with a given depth of penetration from the relatively mobile zone in the fractures. With this in mind, we define $V_i(s)$ as the volume of matrix within a given distance s of any fracture in the ith-order branching structure Ψ_i. This volume is very difficult to characterize in natural fracture systems, without knowing the detailed, 3-D configuration of fractures.

However, a corresponding region $\Omega_i(s)$, defined as the region of a map within distance s of any fracture trace belonging to Ψ_i, can be drawn directly on a map of fracture traces (Figure 3-3). If all fractures are perpendicular to the map section, $\Omega_i(s)$ is equivalent to $\delta V_i(s)$, the intersection of $V_i(s)$ with the plane of the map.

In general, additional fractures belonging to Ψ_i may be parallel to or oblique to the plane of the cross section, without appearing as traces on the map. Some of these fractures may come within a distance s of points that are within $\Omega_i(s)$. Thus $\Omega_i(s)$ includes some portion of the map that does not belong to $\delta V_i(s)$. On the other hand, if a fracture that appears as a trace is inclined relative to the plane of the map, the area that it contributes to $\Omega_i(s)$ is decreased relative to its contribution to $\delta V_i(s)$, in proportion to $\sin(\phi)$ where ϕ is the angle between the plane of the fracture and the plane of the map.

Here we assume that the differences between $\Omega_i(s)$ and $\delta V_i(s)$ are approximately offsetting, and thus we use the area of $\Omega_i(s)$:

$$A_i(s) = \left|\Omega_i(s)\right| = \int_{\Omega_i(s)} dA \qquad (3\text{-}2)$$

as a two-dimensional estimator of $V_i(s)$ for a unit thickness of the rock. We adopt a 2-D analysis of this area in order to characterize the potential volume available for matrix diffusion as a function of diffusion depth, for a 2-D representation of en échelon zones in which all fractures are assumed to be perpendicular to the section studied.

The area $A_i(s)$ can be evaluated over the irregular region $\Omega_i(s)$ by Monte Carlo integration. The basic concept of Monte Carlo integration for irregular regions is described by Press *et al.* (1986). In this case, to estimate $A_i(s)$ a large number of points are generated with

x and y coordinates uniformly random in the plane of the map. For each point $\boldsymbol{x}_j$ within the map boundaries, the distance s_j to $\boldsymbol{\Psi}_i$, (defined as the distance between $\boldsymbol{x}_j$ and the nearest point on any segment of any fracture trace belonging to $\boldsymbol{\Psi}_i$) is calculated.

Following the general procedure of Press *et al.* (1986) for Monte Carlo integration (with an integrand $f(\boldsymbol{x}_j) = 1$ for all $\boldsymbol{x}_j \in \boldsymbol{\Omega}_i(s)$), the area is estimated by:

$$A_i(s) = \frac{N_i(s)}{N} A \qquad (3\text{-}3)$$

where $N_i(s)$ is the number of points $\boldsymbol{x}_j$ for which $s_j \leq s$, N is the total number of points, and A is the area of the map. In the present analysis, 10,000 uniformly random points are used to evaluate $A_i(s)$ to a precision of about 10 cm^2 over a 10 m^2 map.

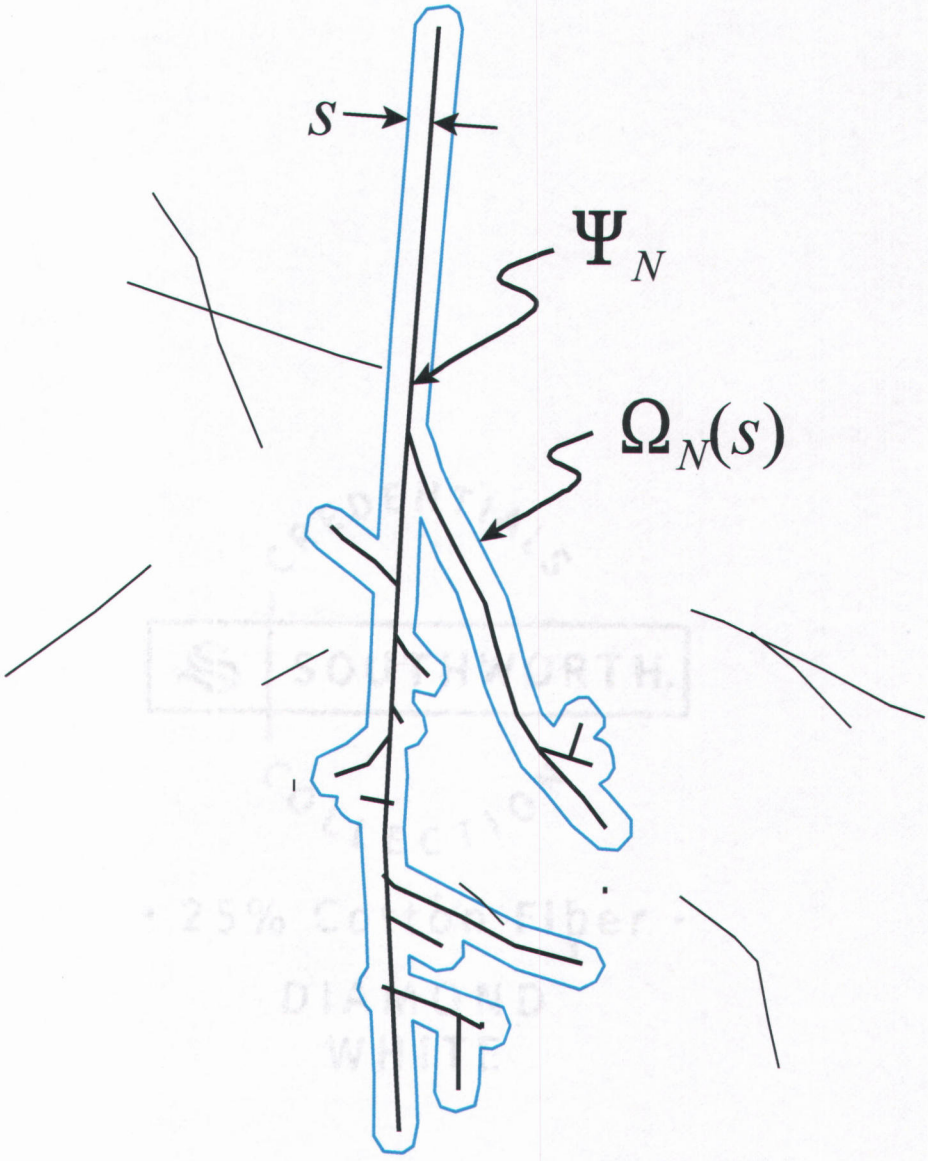

Figure 3-3. Definition of the map region $\Omega_N(s)$ within a distance s of an entire branching structure Ψ_N (indicated as the area outlined in blue). Note that additional fractures that are not part of Ψ_N do not affect $\Omega_N(s)$ and may even intersect it.

Fracture intensity as a function of distance from a branching structure

The intensity of fracturing adjacent to a branching structure Ψ_i is a measure of the damage zone around the structure, as a function of the distance s. This measure is calculated in terms of trace length per unit area on a trace map, as follows.

First, let Ξ be the set of all fracture traces on the map, and let Ξ_i be the complement of Ψ_i for the trace map, that is, the set of all fracture traces on the map that do not belong to Ψ_i. Thus for any i:

$$\Xi = \Xi_i + \Psi_i \tag{3-4}$$

The fracture traces belonging to Ξ_i may or may not connect with each other to form branching structures or other types of networks. If Ψ_i is not an entire branching structure, then some of the traces in Ξ_i (but not necessarily all) are branches of Ψ_i. If Ψ_i is an entire branching structure, then none of the traces in Ξ_i are linked to Ψ_i.

Second, define the incremental map region $\delta\Omega_i(s)$ as:

$$\delta\Omega_i(s) = \Omega_i(s+\delta s) - \Omega_i(s-\delta s)$$

with corresponding incremental area:

$$\delta A_i(s) = |\delta\Omega_i(s)| = A_i(s+\delta s) - A_i(s-\delta s)$$

where δs is some fixed increment of s. This incremental area is evaluated directly as the difference between $A_i(s)$ for different values of s, as described above.

Next, consider the intersection of the two sets $\Xi_i \cap \delta\Omega_i(s)$. This is the set of all points on fracture traces that do not belong to Ψ_i, but lie within the distance interval $s \pm \delta s$ of Ψ_i. Denoting the total length of fracture-trace segments composed of points in $\Xi_i \cap \delta\Omega_i(s)$ as:

$$\delta L_i(s) = \left|\Xi_i \cap \delta\Omega_i(s)\right| = \int_{\Xi_i \cap \delta\Omega_i(s)} dL \tag{3-5}$$

we note that the 2-D intensity of fractures belonging to Ξ_i within the incremental region $\delta\Omega_i(s)$, using the conventional definition as trace-length per unit map area (Dershowitz, 1984; Dershowitz and Herda, 1992) is then:

$$P_{21}(s\pm\delta s) = \delta L_i(s)/\delta A_i(s) \tag{3-6}$$

The notation P_{21} follows the convention for a unified set of fracture intensity measures, based on the dimensions of the observations (Dershowitz and Herda, 1992). In this case the observations are taken over a 2-D sample (area map) and the observed entities (the fracture trace lengths) are 1-D.

The length measure $\delta L_i(s)$ is obtained by another Monte Carlo integration, here taken on the set $\Xi_i \cap \delta\Omega_i(s)$. In this case random points $\boldsymbol{x}_j$ are generated with uniform distribution on the set of all fracture traces in Ξ_i. The length measure $\delta L_i(s)$ is estimated by:

$$\delta L_i(s) = \frac{M_i(s)}{M} L_i \tag{3-7}$$

where $M_i(s)$ is the number of random points $\boldsymbol{x}_j \in \Xi_i \cap \delta\Omega_i(s)$, and which $s_j \le s$, M is the total number of random points generated on Ξ_i, and L_i is the total length of fracture trace segments in Ξ_i.

The random points on Ξ_i are generated by the following subsidiary algorithm: A fracture trace (polyline) k is selected randomly from Ξ_i, with probability equal to l_k/L_i where l_k is the length of the kth trace. The random point $\boldsymbol{x}_j$ is then chosen as uniformly randomly distributed along the polyline k.

Matrix volume within a given distance of any fracture

The distribution of unfractured block sizes is characterized by the distribution of incremental map area:

$$\delta A(s) = A(s+\delta s) - A(s-\delta s) \tag{3-8}$$

as a function of the distance s to the nearest fracture trace Ξ (*i.e.* the entire map). The algorithm is identical to that for calculating $\delta A_i(s)$, as described above, except that distances are measured with respect to Ξ rather than Ψ_i.

While only an approximate measure of actual block sizes, $\delta A(s)$ is closely related to the potential for dissolved contaminants traveling through the fracture network to be retarded by diffusion into the rock matrix. For vanishingly small δs the function $\delta A(s)$ equals the derivative $A'(s)$. This can be thought of physically as the incremental amount of rock matrix that will be available for diffusion on successively longer time scales, if all fractures participate in transport.

Breccia zones

Breccia zones were defined by inspection, by interactively marking out areas within which intense fracturing has resulted in clusters of fragments on a scale of 0.5 cm or less. The fabric of these zones is more easily described in terms of a granular medium than a fractured rock.

Analysis of the internal fabric of these zones is limited by the resolution of the photographic mapping technique, and by a tendency for these zones to be obscured by soil development and/or past erosion by glaciers and surface water. However, in most cases the boundaries of the breccia zones and the larger fragments within them can be discerned, so that the configurations of these zones relative to larger-scale fractures can be evaluated. Past investigations at Äspö have found a strong correlation between high-flow zones in boreholes and breccia zones in core (Voss *et al.*, 1996).

Implementation of algorithms

The geometric analysis algorithms described above are implemented in the interactive graphical code named *splinter* which was developed in the course of this research. Appendix A gives a general description of the code and its application in this research . The C-language source and Linux executable version for *splinter* are included on the CD-ROM that accompanies this dissertation.

The interactive graphical portion of the *splinter* code is based on the GTK+ open-source toolkit for GNU software development (http://www.gtk.org, 1991), which provides functions for window, menu, and mouse management, and a set of graphical primitives. The remainder of *splinter* was developed within this research project; this includes functions for managing geometric objects on trace maps, for geometric calculations, and algorithms for identification of branching structures.

The numerical portion of the code is based on geometrical objects which are built up of points, line segments, polylines, and polyline groups, in succession. Algorithms for calculating lengths and areas of geometric objects, and for performing the Monte Carlo integrations described above, were verified by hand calculations for simple test cases. The algorithms for identification of branching structures Ψ_i of successive order were checked by

visual confirmation of the operations in test cases. The graphical nature of the code provides for highlighting of the Ψ_i for each order I, and visual confirmation both that all branching fractures are connected to the Ψ_N structures and that fractures that do not connect remain in the complementary set Ξ_i.

3.3 Hydrogeological Modeling

Flow and transport was modeled by a discrete-fracture network approach. The discrete-fracture network approach represents individual fractures as discrete conductors surrounded by a rock matrix which may or may not be treated as impermeable. A review of past applications of the method is given in Sections 2.2.5 and 2.2.6.

A new program for modeling flow and transport in a discrete-fracture network was developed as part of this research. The *dfm* (for "discrete-feature model") code was written in C. Source code, Linux executable version, and verification cases are included on the CD-ROM that accompanies this dissertation. The code is designed as a general-purpose modeling program for fractured granitic rock, and includes a number of capabilities that were not used in this research.

The rock matrix is treated as effectively impermeable for flow between fractures, *i.e.* flow via the matrix is considered to be insignificant in comparison with flow via the fractures. For the fine scale of representation of fractures in the present study, this approximation is reasonable given the very low permeability of granitic rock excluding macroscopic fracturing.

The mathematical representation of the discrete-fracture network used in this work is based on the finite-element method. A fracture is represented as a planar or piecewise-planar surface, described at each point ξ on its surface by effective 2-D parameters of transmissivity $T(\xi)$, storativity $S(\xi)$, and transport aperture $b(\xi)$. In the simplest case, these parameters are taken to be uniform over all segments of a given fracture. Alternatively the properties may vary with position in each fracture.

The boundaries of a discrete-fracture network model take the form of arbitrary polyhedra. In general these may include an external boundary, which bounds the domain to be modeled, and an arbitrary number of internal boundaries which represent tunnels, segments of borehole, *etc*. Boundary conditions are imposed at intersections between discrete features and the external or internal boundaries. In the present research only very simple configurations of boundaries (rectilinear external boundaries) have been used.

Groundwater flow and transport through the discrete-fracture network are specified by 2-D equations that apply locally within each planar segment, by conditions of continuity which apply at the intersections between segments, and by the external and internal boundary conditions. The groundwater flow field is defined only on this network, and boundary

conditions are specified only along the intersections between the network and the internal and external boundaries.

Model for groundwater flow

Within each planar segment of a feature, groundwater flow is governed by the 2-D transient flow equation:

$$S\frac{\partial h}{\partial t} - \nabla\cdot(T\nabla h) = q(\xi) \tag{3-9}$$

where S and T are respectively the local storativity and transmissivity, h is hydraulic head, t is time, and q is a source/sink term which is zero everywhere except at the specified boundaries. In the present work, S and T are assumed to be homogenous within a given triangular segment. Conservation of mass and continuity of hydraulic head are required between segments, and at intersections between features.

In the case of steady-state flow, the time derivative is zero and the local flow equation simplifies to

$$\nabla\cdot(T\nabla h) = -q(\xi) \tag{3-10}$$

To solve the flow equations for a given realization of a discrete-fracture network model, the network is discretized to form a computational mesh, which consists of 2-D, triangular finite elements that interconnect in 3-D. The head field is calculated by the Galerkin finite-element method.

For the case of steady-state flow this leads (Appendix B) to a system of linear algebraic equations:

$$\mathbf{A}\boldsymbol{h}(t)\big|_{t=\infty} = \boldsymbol{q}(t)\big|_{t=\infty} \tag{3-11}$$

where $\mathbf{A}$ is a sparse, diagonally dominant, banded matrix depending only upon the transmissivity and geometry of each triangular element, $\boldsymbol{h}(t)$ is a column vector of head values

as a function of time t at the element vertices, and $\boldsymbol{q}(t)$ is a column vector of unbalanced flux values at the vertices, equal to zero except at physical boundaries. In the steady-state case these functions are only evaluated for the limit $t = \infty$ and thus may be considered as constants in the above equation.

Features that are not connected to a specified-head boundary (either directly or indirectly via connections with other features and/or net-specified-flux boundaries) are indeterminate and are not represented in the matrix equations. These features constitute hydraulically isolated networks

For transient flow the Galerkin finite-element method is applied after application of the Laplace transform to the transient flow equation, giving a system of linear algebraic equations:

$$[s\mathbf{D} - \mathbf{A}]\bar{\boldsymbol{h}}(s) = \bar{\boldsymbol{q}}(s) + \mathbf{D}\boldsymbol{h}(t)\big|_{t=0} \qquad (3\text{-}12)$$

where overbars denote Laplace transforms with respect to t, and s is the Laplace transform variable, and $\mathbf{D}$ is a sparse, diagonally dominant, banded matrix depending only upon the storativity and geometry of each triangular element.

Solutions to the systems of linear algebraic equations for the steady-state and transient cases given above are obtained using standard sparse-matrix methods. The transient solution for head is obtained from the Laplace-domain solution by the algorithm of de Hoog *et al.* (1982).

Spatially continuous model for solute transport

The Laplace-transform Galerkin finite-element approach of Sudicky (1989) can also be used to formulate a model for 3-D solute transport in terms of concentration $c(\boldsymbol{x},t)$, with the assumption of complete mixing. The local equation for advective-dispersive transport with linear, reversible equilibrium sorption in a 2-D steady-state flow field in the plane of a fracture can be written as:

$$R\frac{\partial c}{\partial t} + \boldsymbol{v}\cdot\nabla c - \nabla\cdot(\boldsymbol{D}\nabla c) = q_c \qquad (3\text{-}13)$$

where R is the retardation due to sorption, $\boldsymbol{v}$ is the 2-D vector of local water velocity, $\boldsymbol{D}$ is the local dispersion tensor in the plane of the fracture (regarded as a 2-D tensor function of the local velocity vector), and q_c is a source term (zero except on boundaries where solute is being added or removed from the system). The formulation developed for this research did not take into account matrix diffusion, which could be included as a source-sink term in the above equation.

As shown in Appendix B, the Laplace-transform Galerkin method combined with an assumption of continuity *of* $c(\boldsymbol{x},t)$ at element edges (equivalent to the assumption of complete mixing at fracture intersections) leads to a linear system of equations in terms of the Laplace transform of concentration at nodes of the finite-element mesh:

$$[s\mathbf{B} - \mathbf{U}]\bar{\boldsymbol{c}}(s) = \mathbf{B}\boldsymbol{c}(0) - \bar{\boldsymbol{q}}_c(s) \qquad (3\text{-}14)$$

where **B** is a matrix with coefficients depending only on the interpolation functions and the local retardation factor, **U** is a matrix depending on the interpolation functions, local groundwater velocities (assumed to be steady with respect to time), and the dispersion tensor, and $\boldsymbol{c}(t) = [c_j(t)]^T$ and $\boldsymbol{q}_c(t) = [q_{ci}(t)]^T$ are 1xN column vectors. See Appendix B for full definitions of these terms. The Laplace-transform variable s is in general a complex number, so this system of linear equations must be solved with complex arithmetic.

As noted in the literature review (Section 2.2.6) the validity of the assumption of complete mixing at fracture intersections can be questioned. Partly for this reason, and partly due to practical (numerical) difficulties in solving the above set of equations in the complex domain, this approach was not relied on for the transport modeling results presented in this thesis.

Instead, modeling of solute transport is based on a particle-tracking algorithm that can account for variable mixing by diffusion across streamlines at intersections, including possible stagnant branches. This algorithm, although limited to 2-D networks, is a significant extension over previous algorithms for particle-tracking in such networks, and is described in detail in the following sections.

Simulation of advective-diffusive transport in fracture segments

Transport of solute through the fracture network and in the adjoining rock (matrix) is simulated by an advective-dispersive particle-tracking method. The method for tracking particles through fracture intersections is inspired by the conceptualization of Park *et al.* (1999), but the algorithm used here permits diffusion into stagnant branches.

Within a given 1-D fracture segment, advective transport with Taylor dispersion is modeled by a discrete-parcel random walk algorithm, following the general approach of the algorithm for advective-dispersive particle tracking by Ahlstrom *et al.* (1977), but similar to recent extensions of the method by Detwiler *et al.* (2000) and Bruderer and Bernabé (2001) which account for fluid velocity variations and diffusion across the aperture by tracking particles in this dimension as well. A similar algorithm has also been applied to examine the role of macrodispersion vs. Taylor dispersion in variable-aperture fractures by Wörman *et al.* (2004).

Each discrete parcel or "particle" represents a fixed mass m_p of solute, which moves through the network and/or matrix as a random walk. A particle's displacement during a single step of the random walk, representing a time interval Δt, is the sum of an advective component and a dispersive component. Using a local system of coordinates with x parallel to a fracture segment and z perpendicular (Figure 3-4), the diffusive component of particle motion for a given step has x and z components:

$$\Delta x_d \sim N(0, \sqrt{(2D_m \Delta t)}) \qquad (3\text{-}15)$$
$$\Delta z_d \sim N(0, \sqrt{(2D_m \Delta t)})$$

where D_m is the coefficient of molecular diffusion and $N(\mu,\sigma)$ indicates a normally distributed variate with mean μ and standard deviation σ. The advective component of particle motion is:

$$\Delta x_a = \bar{v}\ \Delta t \qquad (3\text{-}16)$$

where $\bar{v}_{\Delta t}$ is the mean aperture along the particle's trajectory during the interval Δt:

$$\bar{v}_{\Delta t} = \frac{\sum_i \int_{z_i}^{z_{i+1}} v(z)|dz|}{\sum_i |z_{i+1} - z_i|} \qquad (3\text{-}17)$$

where z_1, z_2, ...z_2 are the z coordinates of the successive endpoints of segments of the particle's advective-diffusive motion during the time interval Δz (including possible "bounces" as described below) .

If the Δz_d component is large enough to cause the particle to move beyond the boundaries of the fracture segment (*i.e.* the fracture walls), the particle may either enter the adjoining matrix with probability P_m, or else "bounce" off the fracture wall, continuing its motion with the residual component of the x-direction motion $\Delta x_a + \Delta x_d$, and the residual component of Δz_d with sign reversed.

The local velocity $v(z)$ at a given height z above the median surface within a given fracture segment is assumed to follow the parabolic velocity profile for Poiseuille flow with no-slip conditions at the fracture walls:

$$v(z) = \frac{Q}{b}\left[\frac{3}{2} - \frac{6z^2}{b^2}\right] \tag{3-18}$$

where Q is the flow through the fracture segment per unit thickness (obtained from the finite-element solution) and b is the local value of fracture aperture.

The size of the time steps Δt within a given fracture segment is limited to 100 s to ensure that the step size is sufficiently small relative to the segment length. Trial simulations indicate that results are not sensitive to step size, for steps equal to or smaller than prescribed by this formula, for the range of flow conditions modeled in this work.

Two fracture segments connecting end-to-end may have different apertures, for example if a fracture is modeled as having stepwise variable aperture along its length. When a particle moves from a segment of aperture b_1 to a segment of different aperture b_2, its vertical position is in the new segment is set to $z_2 = (b_2/b_1)z_1$, where z_1 was the vertical coordinate in the first segment. Thus the particle position is mapped onto the corresponding streamline in the second segment. This neglects the complicated hydrodynamics that would occur at an abruptly changing aperture; however, it should be noted that the abrupt aperture transition is an artifact of the finite discretization of the flow model, rather than something to be expected in nature.

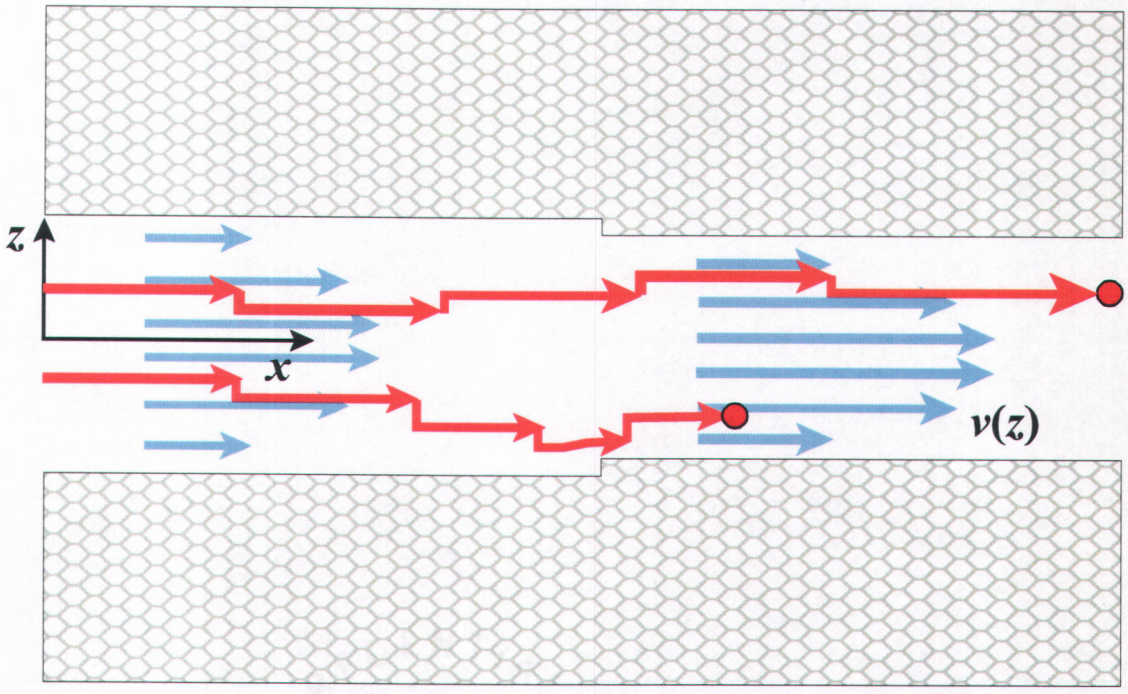

Figure 3-4. Schematic illustration of advective-diffusive particle-tracking algorithm, showing particle motion in a cross-section with coordinate x chosen parallel to the direction of the local fluid velocity v, and z coordinate parallel to the aperture direction. The magnitude of velocity $v(z)$ as indicated by the blue arrows is assumed to follow the parabolic profile calculated for Poisieulle flow with no-slip boundary conditions at the fracture walls. A particle moves through the fracture in a series of steps, with each step being the sum of random (diffusive) components in the x and z directions, and an advective component calculated directly from the average $v(z)$ over the range of z spanned by the diffusive step. In the case of variable-aperture fractures as shown, the z coordinate of the particle is adjusted when passing between segments of different aperture, in proportion to the ratio of apertures between the two segments.

Routing and mixing of solute at junctions between fracture segments

Models of solute transport in fracture networks have been based mainly on either of two end-member models for routing of solute at intersection: streamline routing with no mixing across streamlines (Figure 3-5a) or complete mixing (Figure 3-5c).

Detailed modeling of flow and transport through fracture intersections (Berkowitz *et al.*, 1994; Park *et al.*, 2001) has shown that the degree of mixing is related to the Peclet number $Pe = av/D_m$ where v is the fluid velocity and a is a characteristic length for the intersection. For high Pe the rate of diffusion across streamlines is small relative to the advective velocity, and streamline routing (Figure 3-5a) may be a better approximation. For low Pe the rate of diffusive transport across streamlines is large relative to the rate of advection, and complete mixing (Figure 3-5c) may be a good approximation. At intermediate values of Pe, intermediate forms of routing may occur (Figure 3-5b). Thus for a fixed geometry, the degree of mixing for flow through the intersection varies with the fluid velocity.

Types of junctions

We consider partitioning of solute at junctions with three, four, or more branches. For brevity, we use the notation J_I to denote the class of junctions with I branches, so a J_3 junction has three branches, a J_4 junction has four branches, *etc.*

If one fracture terminates at its intersection against another fracture (a common case in natural fracture networks as pointed out by Dershowitz 1984), the junction is of type J_3. The distinction between streamline-routing and complete-mixing rules is irrelevant for a J_3 junction, if all three branches are non-stagnant and if the branches are longer than the mixing length L_{mixing} at which the solute is fully mixed across the aperture. Either the solute flux from one well-mixed inlet branch is divided according to the flow ratio between two outlet branches, or the solute fluxes from two inlet branches are combined in one outlet branch, and become well-mixed at distance L_{mixing} along that branch. However, when one branch of a J_3 junction is stagnant, solute enters and exits that branch only by diffusion, and this process must be accounted for in the mixing rule for the junction.

A J_4 junction results whenever two fractures intersect each other and both fractures

are through-going. Junctions of higher order (J_5, J_6, *etc.*) require a larger number of fractures to share a common intersect, but are occasionally found in nature as well as in synthetic, stochastically generated fracture networks.

Approximation for streamline positions through a flowing junction

When all branches of a J_4 or higher-order junction are non-stagnant, streamlines entry and exit points from a junction can be defined by considering the branches in cyclic order (either clockwise or counterclockwise).Topological constraints in a two-dimensional network model, where flow is driven by potential gradients, ensure that all branches of a junction with positive inflow lie to one side of all branches with positive outflow, when the branches are placed thus in cyclic order (Bruderer and Bernabé, 2001).

Finding the inlet and outlet streamline locations is then straightforward: starting from a neighboring pair of inlet and outlet branches, the streamlines must pass through points that bound an equal fraction of the inflow and outflow. The position of the streamlines within the intersection are needed in order to model solute transfer due to diffusion across streamlines within the junctions. In detailed studies of individual junctions this problem has been addressed by numerical solution of the Navier-Stokes equation (Berkowitz *et al.*, 1994) or lattice-gas simulation (Stockman *et al.* 1997), but such detailed sub-models are not practical for network-scale problems.

Park and Lee (1999) proposed modeling advective-diffusive transport through junctions based on a simplified, "folded-up" geometry, as depicted in the right-hand side of Figure 3-5. Park and Lee gave analytical solutions for the probabilities p_{ij} for a particle to pass from inlet branch I to outlet branch j, as functions of the inlet/outlet flowrates and velocities J_4. These solutions are singular for the case of stagnant branches, so not applicable for the general case we consider, but they are useful for verifying the particle-tracking algorithm for

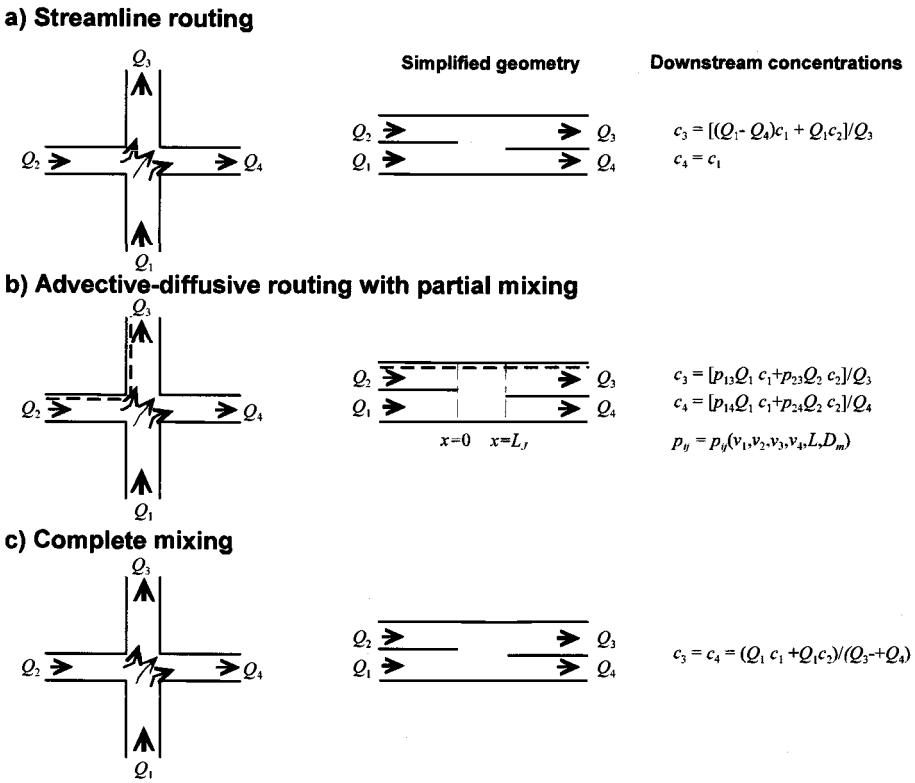

Figure 3-5. Alternative rules for routing of solute at four-branch junctions in a 2-D fracture network.

non-stagnant cases.

Here we follow the conceptual approach of Park and Lee (1999) by modeling transport through an idealized junction of simplified geometry, but in place of their analytical solutions we use explicit advective-diffusive particle-tracking through the simplified junctions, in order to address the additional complication of diffusion into and out of stagnant branches.

We order branches in clockwise cyclic sequence according to the angles at which they radiate from the junction, and identify each branch as inflowing, outflowing, or stagnant based on the direction and magnitude of flow in each branch. Following Park and Lee (1999), we represent the multiple branches are represented in a simplified geometric arrangement as in the right-hand side of Figure 3-5, with all inflowing branches on the left-hand side, and all outflowing branches on the outflow side. We note that Park and Lee's simplified geometric scheme is applicable to J_3, J_5, and higher-order junctions as well as the J_4 junctions that they explicitly considered.

Junction coordinates in the simplified representation

For the effective width of the junction (the vertical scale over which diffusion transverse to streamlines takes place in the simplified geometry) we use the average of the total inlet and outlet branch apertures:

$$b_J = \tfrac{1}{2}\left(\sum_{in} b_i + \sum_{out} b_i\right) \tag{3-19}$$

where the sums are taken over the inlet and outlet branch apertures, respectively. Note that b_J can be less than half the total aperture of branches that connect to the junction, if one or more of the branches are stagnant. Use of a single, average value of b_J is a further geometrical simplification to avoid the complication of tracking particles in diverging or converging streamlines.

The initial z coordinate as a particle enters the junction at $x = 0$ is calculated as:

$$z_{in} = b_J \psi_{in} \tag{3-20}$$

where ψ_{in} is the dimensionless stream function coordinate at which the particle enters the junction from the inlet branch ($\psi = 0$ corresponds to the bottom of the lowermost inlet branch in the simplified geometry, and $\psi = 1$ corresponds to the top of the uppermost inlet branch). As a particle exits the junction at an outlet branch, it is assigned an outlet stream function coordinate:

$$\psi_{out} = \frac{z_{out}}{b_J} \tag{3-21}$$

where z_{out} is the vertical position as the particle reaches the outlet. A particle may occasionally move counterflow due to diffusive steps (especially if the velocity is very low), in which case it may cross these interfaces in the reverse direction; in that case the inverse versions of the above formulae are used. For the length of the junction, we choose:

$$L_J = \max_i(b_i) \tag{3-22}$$

as the representative length over which diffusion takes place across the (possibly curved) interface between streamlines from different branches of the junction. Given that the exact length over which interaction takes place is not known without a more detailed submodel for viscous flow through the junction – besides that the geometry shown in the left side of Figure

3-5 is an idealization of natural fracture intersections – any single value chosen for L_J is necessarily an approximation. Choosing L_J by the rule above, the value is unlikely to be in error by more than a factor of 2, for a wide variety of conceivable cases.

One problem inherent to the simplified geometry is that streamlines that flow directly around a corner in the physical geometry are in effect "stretched" by the mapping to the simplified geometry. Consider, for example, the streamline shown as a dashed line in Figure 3-5b, which enters the junction near the top edge of Branch 2, and exits near the left edge of Branch 3. In the simplified geometry this streamline is represented by a straight line. The distance this line traverses through the simplified representation of the junction, L_J, is much greater than the distance this streamline traverses in the physical junction.

Thus the simplified geometry will exaggerate the time for (and hence the degree of) diffusive exchange across such streamlines. In order to reduce this bias, the following heuristic correction is used. The basis for this correction can be seen by re-folding the idealized, "unfolded" geometry of Park and Lee (1999) but conserving the length of the upper and lower sides of junction, so that these become imaginary pleats folded inward into the junction. Solute intersecting one side of such a pleat should pass through to the corresponding point on the opposite side. Mathematically this is accomplished by specifying that particles colliding with upper or lower junction boundary are reflected across the junction midline $x = L/2$ and re-enter the junction at the corresponding point on the other side of this line. In other words, a particle that collides with the upper boundary $z = b_J$ at $x = x_p$ is transferred to the reflected point $x' = L - x_p'$, $z' = b_J$; similarly a particle that collides with the lower boundary $z = 0$ at $x = x_p$ is transferred to the reflected point $x' = L - x_p'$, $z' = 0$.

Representation of stagnant branches

Stagnant branches can occur at any position around a junction. This is obvious if one considers the case of a short, dead-end fracture emanating from a junction, between any two branches of intersecting, flowing fractures. Hence, unlike the case with flowing inlet and outlet branches, stagnant branches cannot be segregated to a particular position in the cyclic order.

We represent the interface between a given stagnant branch and a junction are represented in the idealized junction as interfaces of infinitesimal thickness (Figure 3-6b-d). In a real junction, the mouth of each stagnant branch is a zone of interaction with flowing water. Diffusive transfer takes place across some curved surface which spans the aperture of the stagnant branch. For a viscous fluid and laminar-regime flow, in reality this is a gradational rather than distinct interface. As a key approximation in our idealized model for junctions with stagnant branches, we idealize this zone of interaction as an abrupt interface, with length equal to the aperture of the stagnant branch.

If the trajectory of a solute particle undergoing advective-diffusive motion in the flowing part of the junction happens to intersect this interface, the particle enters the corresponding stagnant branch with residual motion equal to the residual component of transverse diffusion.

Within the stagnant branch, the particle moves by purely diffusive motion as described above until it either interacts with the matrix or returns to the mouth of the stagnant branch. In the latter case, the particle will re-enter the flowing portion of the junction, via the same interface but in the reverse direction. The coordinates of the particle as it re-enters the junction are obtained by mapping its position within the stagnant-branch aperture onto the corresponding position on the interface representing the branch in the idealized junction.

Figure 3-6 shows how stagnant branches are represented for a few examples of the cases that arise in 2-D fracture network models. In the simplest cases where the stagnant branch or branches lie between the inlet and outlet branches (*e.g.*, the cases shown in Figure 3-6a or 3-6b), the interfaces to the stagnant branches are placed at the top or bottom of the junction, depending on the cyclic order. Note that in such cases the problem of "stretched" streamlines (mentioned above) disappears or is reduced, depending on whether the stagnant-branch aperture is or is not equal to L_j.

When a stagnant branch lies between two branches with the same sense of flow (both inlets or both outlets), the interface to the stagnant is placed within the junction. Figure 3-6c shows an example for the case of a stagnant zone between two outlet branches. The interface extends only a distance of $L_J/2$ (halfway) across the junction, since one side of the interface interacts with the adjacent streamlines in the clockwise direction, and the other side interacts with the adjacent streamlines in the counterclockwise direction. Together these add up to a total interface length of L_J.

Entirely stagnant junctions (Figure 3-6d) are handled as a special case since there is no logical basis for the left-hand to right-hand arrangement used for flowing junctions. For this case, all stagnant branches are aligned on the left-hand side of the junction, in cyclic order (but with an arbitrary starting point). The junction has an effective aperture:

$$b_J = \sum_{stagnant} b_i \tag{3-23}$$

and a reflecting boundary at x = L_J. Also, to represent that the bottom branch in the simplified geometry is physically adjacent to the top branch, a particle that collides with the lower boundary of the junction at $x = x_p$, $z = 0$ continues (with reversed vertical and horizontal components of motion) from the corresponding point on the upper boundary at $x = x_p$, $z = b_J$, and vice versa if the particle collides with the upper boundary.

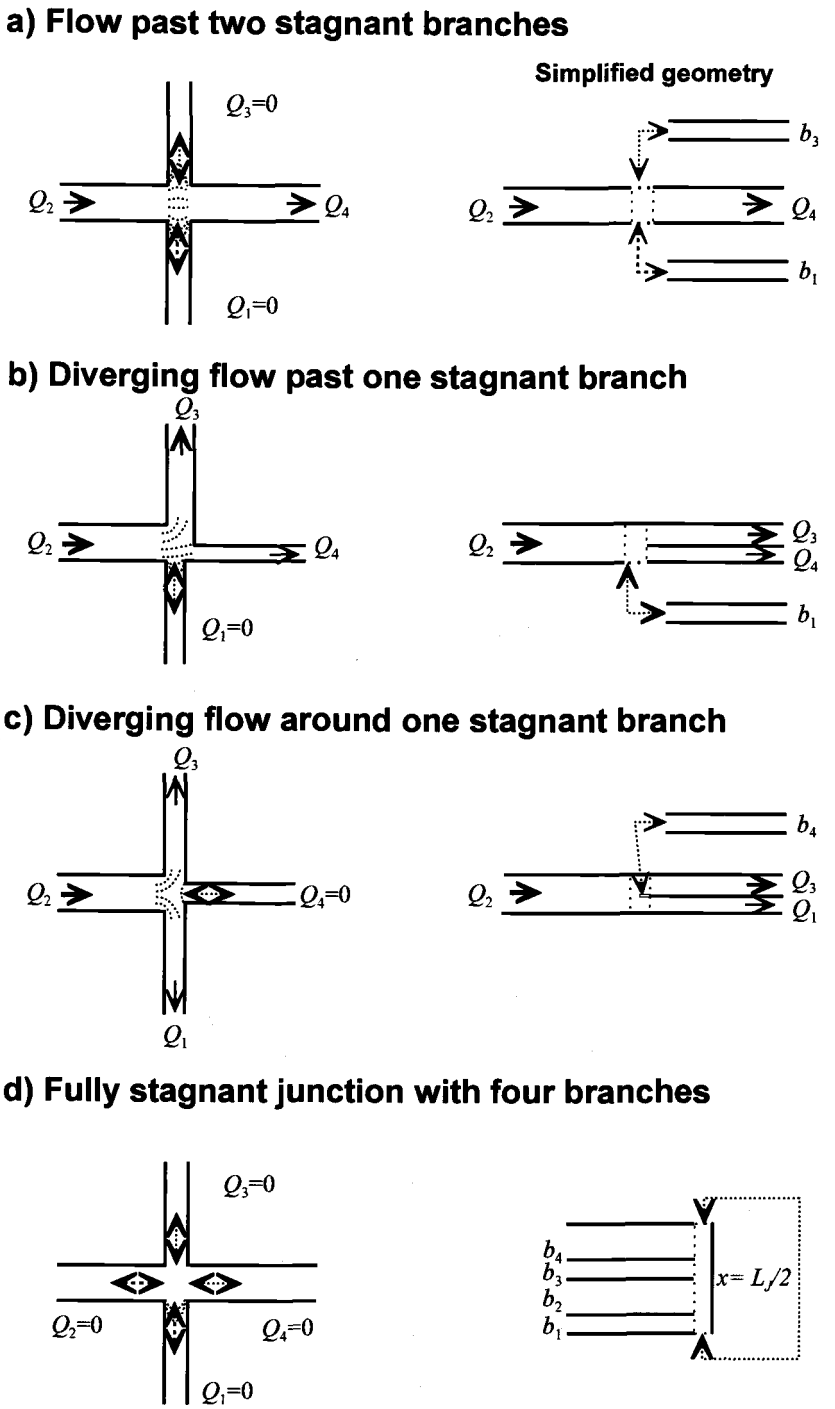

Figure 3-6. Examples of junctions with stagnant branches, and their simplified geometric representation.

Simulation of diffusive transport in the matrix

The probability P_m of a particle entering the matrix pore space on a given collision with a fracture wall is assumed to be $P_m = A_p/A_t$, where A_p is the cross-sectional area of open pore space (including grain boundaries and microfractures in granitic rock) within a given area A_t of the fracture wall. For an isotropic matrix, the ratio A_p/A_t is equal to the local matrix porosity θ_m.

For the sake of simplicity in the present study, matrix porosity is assumed to be uniform and isotropic, so $P_m = \theta_m$ with θ_m specified as a single value throughout the model. This idealization is adopted in order to focus on the role of en échelon zone and secondary fracture geometry, as the main topic of investigation for this study. Experimental data exist to support more heterogeneous models of matrix porosity (Xu *et al.*, 2001) which could be considered with minor modifications of the algorithm.

Transport for particles in the matrix is simulated in the same way as transport in the fracture, except that an effective matrix diffusivity D_p is used in place of D_m. advection in the matrix is assumed to be negligible, so only the diffusive component of particle motion is modeled. In the type of rocks considered here, the hydraulic conductivity of macroscopically unfractured matrix is on the order of 10^{-13} m/s, and due to the well-connected nature of the en échelon fracture system, local hydraulic gradients are on the order of 1 or less. For a porosity of 0.005 as used here, this implies advective velocities through the matrix on the order of $2x10^{-11}$ m/s, as compared with advective velocities on the order of 10^{-6} m/s in the fractures.

At each time step for a particle in the matrix, a check is made of whether the particle motion intersects the wall of any fracture segment. If so the particle motion through the matrix is truncated at the fracture wall, and the particle moves into the fracture segment. This segment need not belong to the same fracture or fracture segment from which the particle initially entered the matrix.

Thus the method explicitly accounts for the variable, finite size of matrix blocks within the en échelon zone, and allows through-diffusion of particles from one fracture to another, even if the fractures are not directly connected. This contrasts with algorithms of Dershowitz and Miller (1995) and of Tsang & Tsang (2001) which treat diffusion as an effectively 1-D process out of and back into a single given fracture.

The matrix is not discretized, and particles are free to move arbitrarily long distances

from the fractures. Thus in effect the matrix on either side of the en échelon zone is treated as semi-infinite , although in practice the particles rarely travel more than a few centimeters from the en échelon zone, for the time scales considered here.

With a computer implementation of this algorithm, the finite precision of floating point representation imposes a computational limit on diffusion distances into the matrix, *i.e.* the magnitude of the absolute coordinates become so large that the magnitude of the smallest digit approaches the standard deviation of the diffusive steps. For the double-precision arithmetic used in the implementation, and for the time steps used in the present study, this numerical limit is not reached until the magnitude of the absolute coordinates exceeds 10^{11} m. Hence this computational limit is not significant for problems of any realistic scale.

4 ANALYSIS OF SPATIAL VARIABILITY IN EN ÉCHELON FAULT ZONES

Abstract

Fracture zones (active or relict fault zones) in granitic rocks have characteristic internal architectures which influence their hydrologic behavior. Detailed mapping and geometric analysis of échelon-type fracture zones in granitic rock at two sites in southern Sweden, Äspö (e. Götaland) and Ekolsund (s. Uppland), provides a basis for quantitative analysis of spatial variability of fracture intensity within these zones.

Variability of fracture intensity within and adjacent to these zones implies anisotropic and heterogeneous permeability, with preferential directions at a high angle to the slip direction, and dependent on whether the step-over is synthetic or antithetic to the sense of slip.

Fracture intensity shows an anisotropic variability which is correlated over scales of several meters along strike, corresponding to the length of, and recurrence interval between the step-over zones that were mapped. This study did not find evidence for correlations of fracture intensity along strike, over larger scales of 50 to 150 meters. Previous modeling studies have shown that correlations on such scales, if they exist, would have significant consequences for large-scale transport and retention of radionuclides.

Intensity of fracturing in the wall rock shows an approximately exponential decrease with distance from the central deformation zone (fault core), as has been commonly observed in other fault zones.

Within step-over zones, smaller-scale en échelon structures are observed which suggest a degree of self-similarity, implying that the characteristics identified may be manifested on a range of scales. The variability of fracture intensity also implies heterogeneous, anisotropic and correlated properties for solute transport, in particular the pore volume and surface available for sorption.

4.1 Introduction

Fracture zones, including active and relict fault zones, can be important conduits for groundwater flow and contaminant transport in granitic rock. Fracture zones often have complex internal structures in which fracture intensity and connectivity vary from place to place (Committee on Fracture Characterization and Fluid Flow *et al.*, 1996, p. 58). Field studies show that transmissivity and porosity can vary by orders of magnitude along an individual fracture zone (*e.g.*, Andersson *et al.*, 1989a,b). Results of numerical modeling using assumed models for large-scale spatial correlation of properties within fault zones (López and Smith, 1996; Tsang *et al.*, 1996; Geier 1996) show that this can be significant for predictions of flow and transport.

Different forms of hydrologic heterogeneity can occur in fracture zones with different structural characteristics. Structural types that have been identified by investigations at research sites in shield settings in Sweden and Canada include simple and compound fracture zones, diffuse fracture swarms, en échelon fractures, and reactivated mylonite zones characterized by anastomosing fractures (Tirén *et al.*, 1996; Martel, 1990; Andersson *et al.*, 1989b; Davison and Kozak, 1988). Mazurek *et al.* (2003) suggest that in some cases a single fault zone may appear as a number of these different structural types depending on the location along the fault zone.

This paper examines the structural character of en échelon fracture zones at two sites in granitic rock in the Swedish portion of the Fennoscandian shield: Äspö (eastern Götaland) and Ekolsund (southern Uppland). The first site provides good exposures of en échelon zone segments on single, horizontal outcrops, over scales of 1 m to 15 m. The second site provides a unique possibility to study fault zones in multiple vertical and horizontal exposures, over distances of 30 m to 150 m along strike. Thus the two sites provide complementary information on structural correlations on different scales.

Detailed maps of the fracturing within well-exposed examples of en échelon zones are analyzed in terms of internal architecture and fracture geometric properties that are postulated to be of significance for fluid flow and solute transport. The fracture intensity along these zones is analyzed to provide quantitative evidence regarding spatial correlation of structure along strike. Effective transmissivity is also evaluated for one of these zones by use of a numerical flow model, to evaluate the consequences of the observed structural

heterogeneity in terms of hydrologic heterogeneity.

This paper represents the first part of a broader investigation which evaluates the influence of échelon-zone architecture on groundwater flow and contaminant transport. Companion papers examine the significance of secondary-fracture geometry in these structures for providing solute access to the matrix (Chapter 5), and present results of fracture groundwater flow and transport modeling to examine the significance of stagnant porosity and compartmentalized flow within these structures (Chapter 6).

4.2 Site descriptions

Äspö, eastern Småland

Äspö is an island in the archipelago along Sweden's southeastern Baltic coast (Figure 4-1). The island and its vicinity have been a focus of intensive geoscientific investigations over the past 15 years, as the site of the Äspö Hard Rock Laboratory which extends to a depth of 450 m below the surface. The bedrock on Äspö is predominantly a suite of 1.81 Ga to 1.76 Ga old plutonic rocks associated with the Transscandinavian Igneous Belt, with modal compositions ranging from monzodiorite to quartz monzodiorite and quartz monzonite to monzogranite and granite (Wahlgren *et al.*, 2003; SKB, 2004). Contacts between these rock types are locally gradational or migmatitic, and are not always discernible in the field (Tirén, 1996). These plutonic rocks intrude older metavolcanics (2.0 Ga), and are in turn intruded by aplite dikes (1.8 to 1.35 Ga). The Äspö region subsequently underwent multiple orogenic and rifting episodes (Larsson and Tullborg, 1993) which produced multiple sets of fracture zones. Many of the fracture zones have been reactivated in a different sense of shear in the later deformation episodes, in response to changes in the direction of maximum compressive stress (Tirén, 1997).

The glaciated upper surface of the bedrock is well exposed on numerous outcrops, particularly around the shoreline of the island and on a set of transects where the late Holocene soil cover was removed for geologic mapping. These outcrops and cleared areas provide continuous horizontal exposures on scales of up to 15 m. However vertical exposures are sparse, with the exception of the underground tunnels where only a few meters are visible within a given structure, and correlation of structures through the rock between different points in the tunnels is difficult.

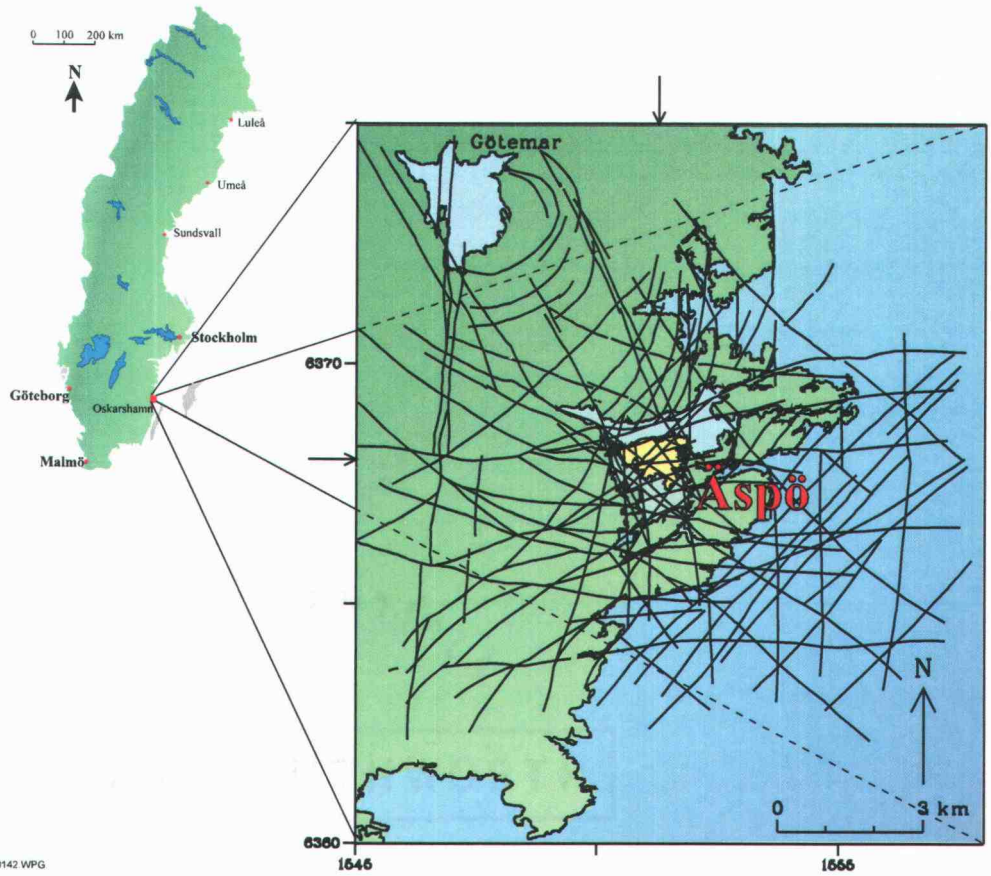

Figure 4-1. Location and regional structural setting of the Äspö Hard Rock Laboratory site, Sweden. Äspö is the island in the center of the inset box, highlighted in yellow. Lines show the pattern of regional lineaments interpreted as fracture zones, based on elevation, geophysical and remote-sensing data (Tirén *et al.*, 1996).

Ekolsund, southern Uppland

The Ekolsund study site is in southern Uppland, on the west side of Ekolsundsvik, an inlet of Lake Mälaren, between Stockholm and Enköping. This site has not been studied as intensively as Äspö 300 km to the south, but offers certain advantages in terms of the scale and configuration of exposures. The site has been the focus of a study sponsored by the Swedish Nuclear Power Inspectorate since 2001, with a primary aim of verifying methods for lineament interpretation based on remote sensing.

The bedrock at Ekolsund is granodiorite to diorite, with a weak foliation over most of the study site. Gneiss and mylonite occur just outside the mapping area at the eastern edge of the study site, adjacent to Ekolsundsvik. The composition and age of the local rocks have not been studied but the locality falls within a region of early to late Svecofennian granitoids (1.9-1.77 Ga) of the Transscandinavian Igneous Belt, according to the lithostratigraphic map of Larsson and Tullborg (1993). The regional tectonic history affecting the site over the last 1.2 Ga is similar to that of Äspö in general terms.

A unique aspect of the Ekolsund site is that two nearly parallel road cuts along a motorway provide a set of four near-vertical exposures 5 to 10 m in height, with a 30 m to 80 m spacing between exposures along strike of N- to NNW-striking structures. Adjoining horizontal exposures where soil cover was removed along the tops of the road cut further reveal the 3-D character of the structures.

Using aerial photographs and detailed topographic data from the highway construction, as well as very low frequency (VLF) electromagnetic surveys and ground mapping, it has been possible to establish the continuity of several structures in this family, between and across the road cuts. Thus the Ekolsund site provides exposures that allow examination of structural correlations within en échelon zones, on larger scales than is provided by natural and/or underground exposures at Äspö.

The N to NNW trending sets of en échelon fracture zones at both sites represent a class of features that may be significant for local hydrogeology and radionuclide transport, due to (1) their orientation conjugate to the direction of regional maximum horizontal stress, (2) the apparent connections between extensive, simple fractures via duplex structures at

en échelon steps, and (3) the small amount of wetted surface area in the simple fractures, which implies relatively a low potential for radionuclide retention by matrix diffusion and sorption, relative to fracture zones with more distributed deformation.

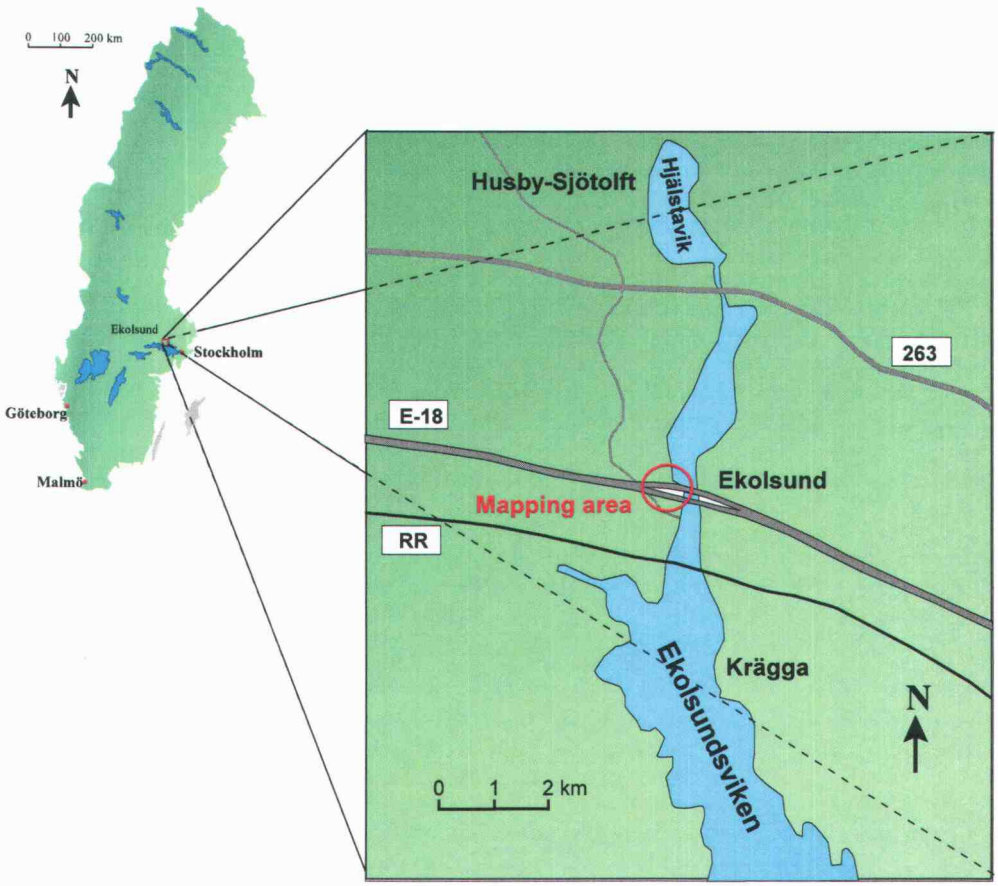

Figure 4-2. Location of the Ekolsund site, southern Uppland, Sweden.

4.3 Methods

This paper investigates the heterogeneity of fracture intensity of the en échelon zones studied, and the consequences of fracture intensity and geometry for effective transmissivity.

The primary data for this investigation are rectified digital (vector) maps of selected en échelon zones at the Äspö and Ekolsund sites. The maps were analyzed in terms of two-point correlation functions for fracture intensity as a function of distance along and perpendicular to the main en échelon fault segments. Simulations of groundwater flow through the fracture network represented by one of the maps were used to evaluate the variability and spatial correlation of effective transmissivity along the fault zone.

The detailed maps were prepared following the methods described by Geier (2004 [Section 2.2.1]). Briefly the approach was to was to photograph the exposures along with a fixed grid of points that were marked on the exposures, to digitize fracture traces from the photographic images, and convert these to detailed trace maps.

Fracture traces were digitized from the photographic images thus produced, and converted to true coordinates after using the known coordinates of the fixed points to correct for moderate obliqueness of the photographs. In the case of Äspö, fracture traces were identified directly from the digital images, although a 1 m^2 section of the 15 m^2 mapping area was also mapped by hand sketching using the grid of fixed points, as a check on the accuracy of the digitization. In the case of Ekolsund, the digital images were printed onto laminated sheets which were then used as base maps for sketching the fracture traces while at the exposure. Corrections for obliqueness and conversion of the digitized traces to natural coordinates were performed using the *splinter* program (Section 2.2.2). At both sites, 3-D orientations of selected fractures were measured by hand compass for a selection of fractures, to allow for conventional structural analysis.

The map for Äspö (Figure 4-3) is a plan-view map of a 15 m long section of a subvertical, northward striking en échelon zone, mapped with a resolution of 1 cm for a width of 1 m along most of this zone, and along a 4 m section of a second, east-west striking fracture zone that intersects the first. The northward striking zone consists of five en échelon segments which overlap in four step-over zones of lengths 0.5 to 3.5 m.

The exposure in the map area is mainly horizontal with undulating relief of less than 1 m within the map area. An impression of the structural character in the third dimension is provided by a small vertical exposure at the south end of this structure (Figure 4-4). This exposure suggests that the extent of secondary fractures in the vertical dimension may be limited, but also that secondary fractures which appear as separate fractures in the mapping plane may connect directly to the main en échelon segment in the vertical direction.

The map includes over 1200 fracture traces, many of which cannot be shown on the scale of this figure. A digital version of the map, giving coordinates to the full resolution, is included on CD-ROM accompanying this dissertation.

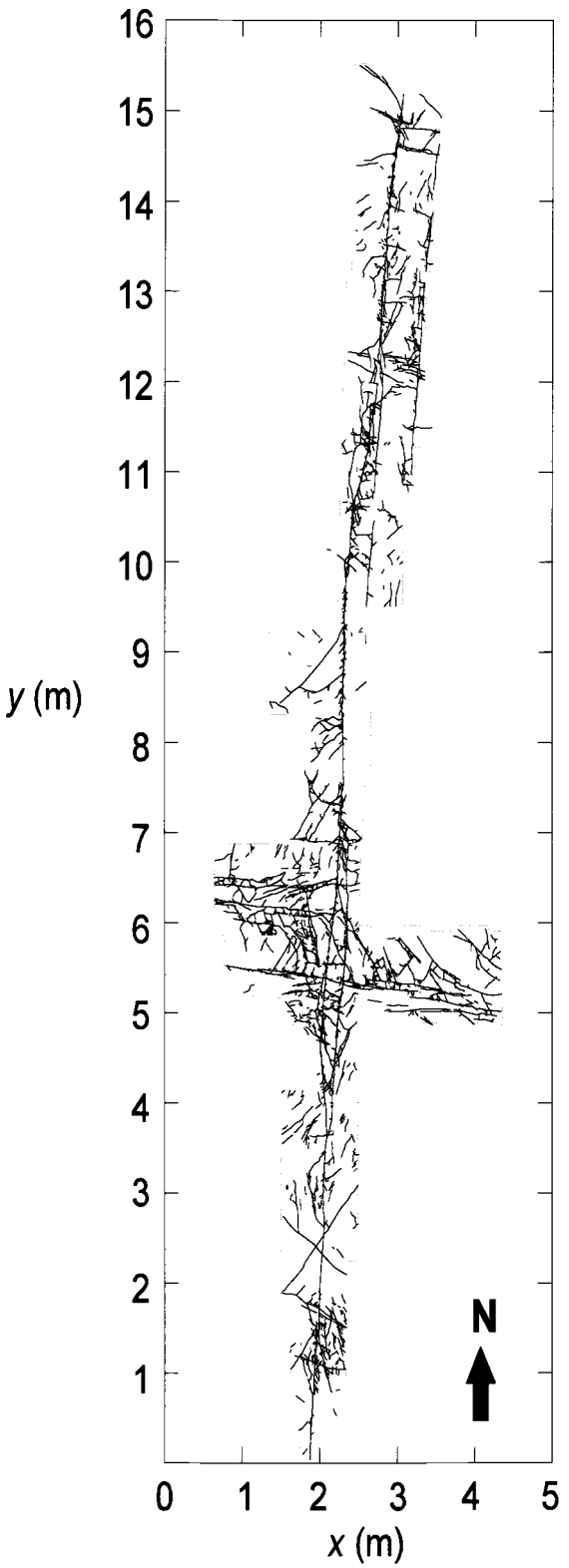

Figure 4-3. Rectified plan-view map of en échelon zone on southern Äspö [digital vector version available on CD accompanying dissertation].

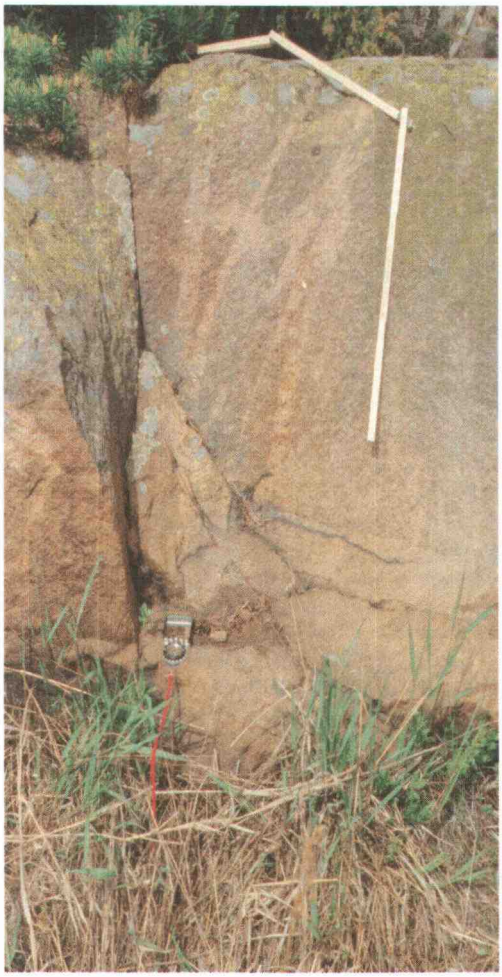

Figure 4-4. Vertical exposure of Äspö structure, approximately 5 m south end of horizontal exposure mapped in Figure 4-3 (coordinates of approximately $x = 2$ m and $y = -5$ m in the grid used in Figure 4-3), showing pattern of steeply dipping splays fanning from the main en échelon segment. Straight segment of measuring stick hanging down from top of exposure is 0.6 m long.

Ekolsund maps

The maps for Ekolsund (Figure 4-5) describe four vertical exposures, of heights ranging from 3.5 m to 7 m, spaced 54 to 57 m apart over a total horizontal distance of 165 m. Small horizontal exposures at the tops of two of the vertical exposures were also mapped, to give a 3-D perspective. Figure 4-5 includes an isometric view of the four vertical exposures, to illustrate the scale of the maps relative to the separation between exposures. As in the case of the Äspö map, the level of detail in the Ekolsund maps exceeds what can be plotted on this scale. Digital versions of these maps are also included in the CD-ROM accompanying this dissertation.

One noticeable feature of this structure is that the dip varies along strike. The dip in the two more northern exposures is about 80-85° W, while in the two more southern exposures the dip is 85- 90° E, with variability of dip apparent within the largest of the exposures.

Within single exposures in the vertical direction, zones of relatively intense fracturing, with vertical extent of up to 2m, are apparent on spacings of 2 m to 8 m. Fan-shaped arrangements of steeply dipping splays, similar to that seen in the vertical exposure of the Äspö zone, are evident in several of the vertical exposures at Ekolsund. The upper part of the tallest exposure (left-hand side of Figure 4-5) shows a fractured section bounded by convergent and divergent fans, above and below.The fracture intensity in maps from the two sites was calculated in terms of the measure $P_{21}(\boldsymbol{y})$, defined as the total fracture length per unit area, calculated for a square section of the map centered at the point $\boldsymbol{y}$.

The coordinates $\boldsymbol{y}$ are defined with respect to distance from and along the median surface of the fault zone (that is, a non-planar surface connecting the primary fractures and brecciated fault core in each exposure). The components of the coordinate vector $\boldsymbol{y}$ are:

$$\boldsymbol{y} = (y_a, y_b, y_n) \tag{4-1}$$

where y_a is the horizontal coordinate measured along the median surface of the zone (*i.e.* following the local strike direction), y_b is the coordinate perpendicular to this in the local dip direction, and y_n is the coordinate perpendicular to the local tangent plane to the zone.

Geostatistics are calculated in terms of the logarithm of local fracture intensity:

$$p(\mathbf{y}) = \log_{10}\{\max[P_{21}(\mathbf{y}),1\ \mathrm{m}^{-1}]\}, \tag{4-2}$$

The statistics and geostatistics of $p(\mathbf{y})$ are calculated for each class I_k, where I_k contains all data points $\mathbf{y}_i$ with normal component y_n in the range $n_{\min,k} \le y_n < n_{\max,k}$. If the analysis is symmetric about the median plane, points are assigned to the class for which $n_{\min,k} \le |y_n| < n_{\max,k}$. For each class I_k, the mean and variance of fracture intensity are calculated as:

$$\overline{p}_k = \frac{\sum_{\mathbf{y}_i \in I_k} p(\mathbf{y}_i)}{N_k} \tag{4-3}$$

$$\sigma_{p_k} = \frac{\sum_{\mathbf{y}_i \in I_k} [p(\mathbf{y}_i) - \overline{p}_k]}{N_k} \tag{4-4}$$

where N_k = the number of data pairs in the class I_k. For each pair of points in a given class, the isotropic lag (separation) in the $\mathbf{y}$ coordinate system is calculated as:

$$h_{ij} = \sqrt{(a_i - a_j)^2 + (b_i - b_j)^2 + (n_i - n_j)^2} \tag{4-5}$$

The variogram is then calculated as:

$$C[I_k(h)] = 1 - \frac{\sum_{y_i, y_j \in I_k(h)} [p(\mathbf{y}_i) - \overline{p}_k][p(\mathbf{y}_j) - \overline{p}_k]}{N_k \sigma_{p_k}^{\ 2}} \tag{4-6}$$

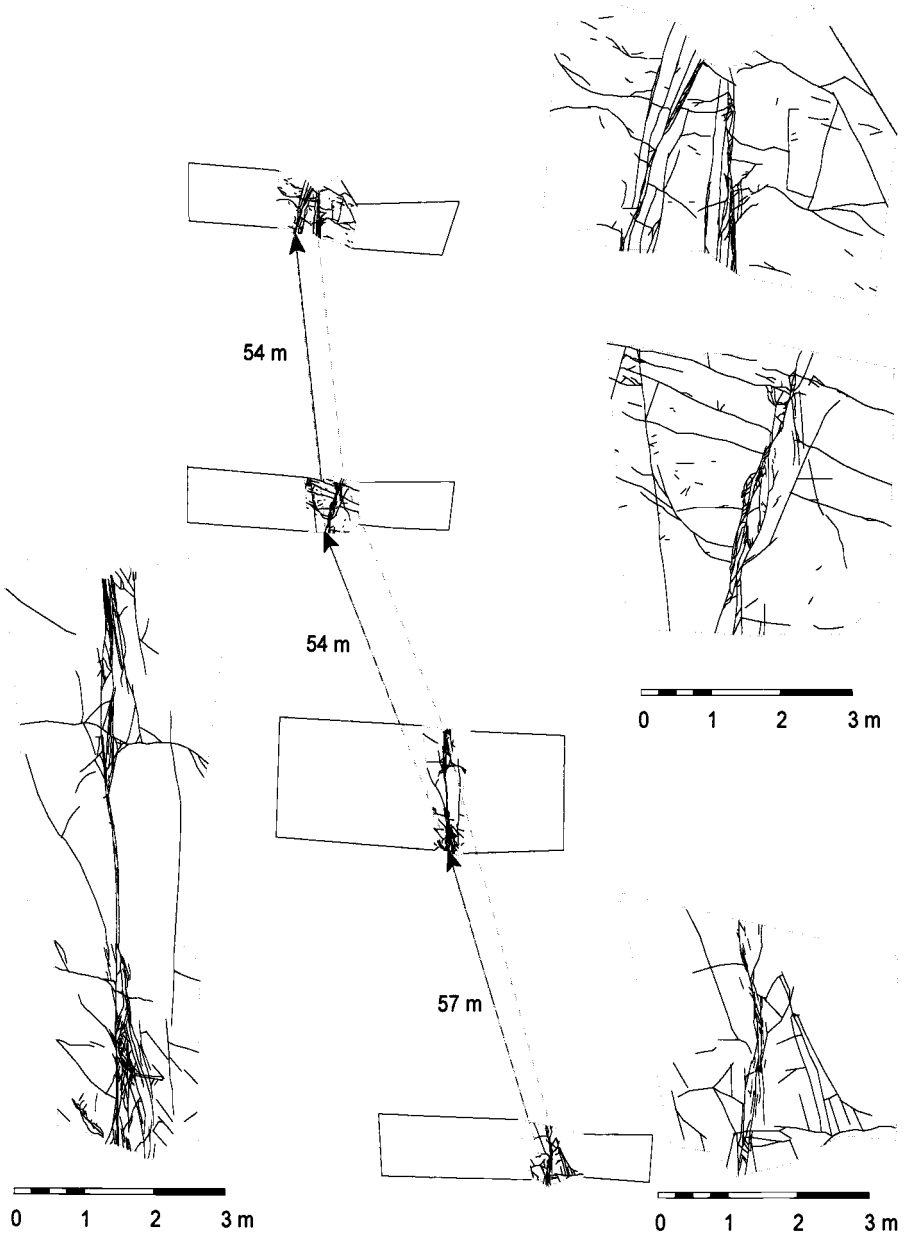

Figure 4-5. Fracture maps of four vertical exposures along a single interpreted, N-trending fracture zone at the Ekolsund site. Overview in center of plot is isometric view of the four exposures, viewed in the direction N15E and 20 degrees downward from horizontal. The median surface of the zone is indicated by the dashed lines connecting between panels. Note fractures were mapped only for the portions of the panels as shown; the larger panels are shown only to convey a sense of the scale of the exposures relative to the distance between exposures.

Flow through the horizontal section represented by the Äspö map, and through the vertical section represented by the largest of the Ekolsund maps, was modeled by the discrete-fracture network method, using the *dfm* code described by Geier (2004 [Section 3.2]). Fixed-head boundary conditions were imposed at the ends of the respective map sections for the assumed distribution of transmissivity (uniform value or lognormal depending on the calculation case), and the steady-state flow solutions were calculated. Effective section transmissivities $T(y_a)$ or $T(y_b)$ depending on the orientation of the section)for fixed-length increments of the map sections were calculated as the ratio of the net flux to average head gradient across each increment, and geostatistics calculated as for the P_{12} data above. We note that for the normalized variograms reported here, the results are independent of the specific values of head and fracture transmissivity values (for the uniform-value case).

4.4 Analysis

The analysis of data from the two sites begins with a general description in terms of fracture orientations in relation to the primary fractures (the main en échelon segments). This is followed by an analysis of heterogeneity in fracture intensity.

General description of fracture orientations

The distribution of fracture strike directions for the Äspö map (Figure 4-6a) shows two dominant directions, one nearly N-S which is parallel to the primary fractures, and the second WNW to E-W. A minor peak corresponds to NE striking fractures. Complete 3-D fracture orientations were measured only for a 2 m^2 section of the map. A stereonet plot of the fracture poles (Figure 4-6b) for this section shows clusters of near-vertical fractures corresponding to the first two sets, plus a cluster of WNW to NW striking, near-vertical fractures that are not evident in the trace-length-weighted strike distribution.

The distribution of fracture strike directions for a sample of 166 fractures on the Ekolsund maps (Figure 4-7a) shows a dominant direction NNW, parallel to the main structure. A second set striking WNW to E-W is at a slightly more acute angle with respect to the primary fractures, than in the case of the Äspö map. Minor, indistinct peaks in the NE-SW quadrant may correspond to the third set seen in the Äspö map.

A stereonet plot of the fracture poles for the Ekolsund zone (Figure 4-7b) shows clusters of near-vertical fractures corresponding to the first two sets, plus a cluster of horizontal to gently N-dipping fracture. This cluster represents a set of orientations that are not well sampled on the nominally horizontal mapping surface at Äspö.

a) Strike direction of traces b) Fracture poles (equal area plot)

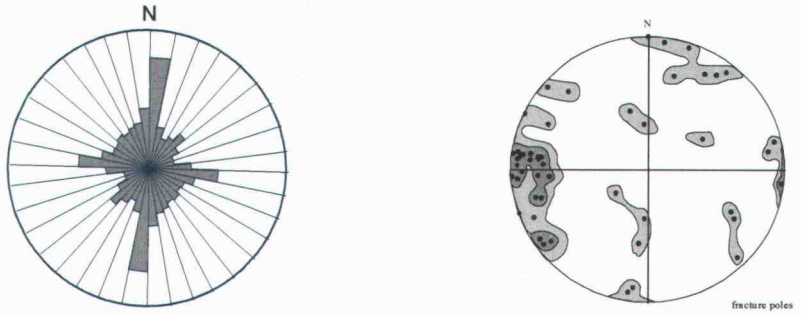

Figure 4-6 a) Distribution of fracture strike directions on the Äspö map, weighted with respect to trace length (note that this plot emphasizes the longer fractures). b) Equal-area stereonet plot of fracture poles in a 2 m^2 section of the Äspö map, lower hemisphere projection, not corrected for bias due to orientation of sampling surface.

a) Strike direction of all fracture traces b) Fracture poles (equal area plot)

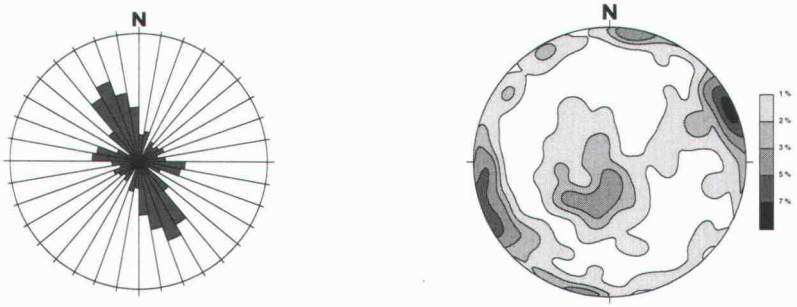

Figure 4-7 a) Distribution of strike directions for sample of 166 fractures on the Ekolsund maps, not weighted with respect to trace length. b) Equal-area stereonet plot of fracture poles for the same fractures, lower hemisphere projection, not corrected for bias due to orientation of sampling surfaces.

Variability and spatial correlation of fracture intensity

As seen in Figure 4-8, the fracture intensity in the Ekolsund maps decays in a roughly exponential fashion with distance from the median surface. This type of decay with distance is commonly observed in other fault zones. This fracturing in the damage zone is found by further analysis (Chapter 5) to be systematically related to the main slip surfaces as a branching pattern of splays of different orders.

A plot of the sample variogram of fracture intensity in the Äspö fracture zone map (Figure 4-9) shows a variability which is significantly correlated over scales at least up to 8 m along strike. The variogram (for mathematical definition and restrictions see for example, de Marsily, 1986) represents the degree to which values of fracture intensity differ between points, as a function of the separation distance between points.

The general trend of the variogram of fracture intensity is one of continuously evolving heterogeneity, from a "nugget effect" (non-zero value of variogram at zero distance) which accounts for about half of the variance, up to a scale of 10 m or more. Beyond 12 m the number of data pairs to support points on the variogram becomes small, and thus the variogram may not be reliable.

On closer inspection, the variogram has a stepped appearance, with apparent plateaus for separation ranges of roughly 2- 4 m, 6- 8 m , and 10-12 m along strike. These ranges correspond to the extent of and distances between different en échelon steps in the map.

Whether these plateaus would be expected in a variogram of a longer section of the zone would depend on whether there is a tendency for certain discrete step lengths and distances between steps, or whether the distribution of these distances is continuous. If the latter, the variogram for a larger-scale map would have a more continuous slope over this range of distances.

Besides fracture intensity, other factors that may affect spatial correlation of hydraulic properties with in a fracture zone, include variation in fracture hydraulic properties and variable connectivity due to structural patterns in the zone.

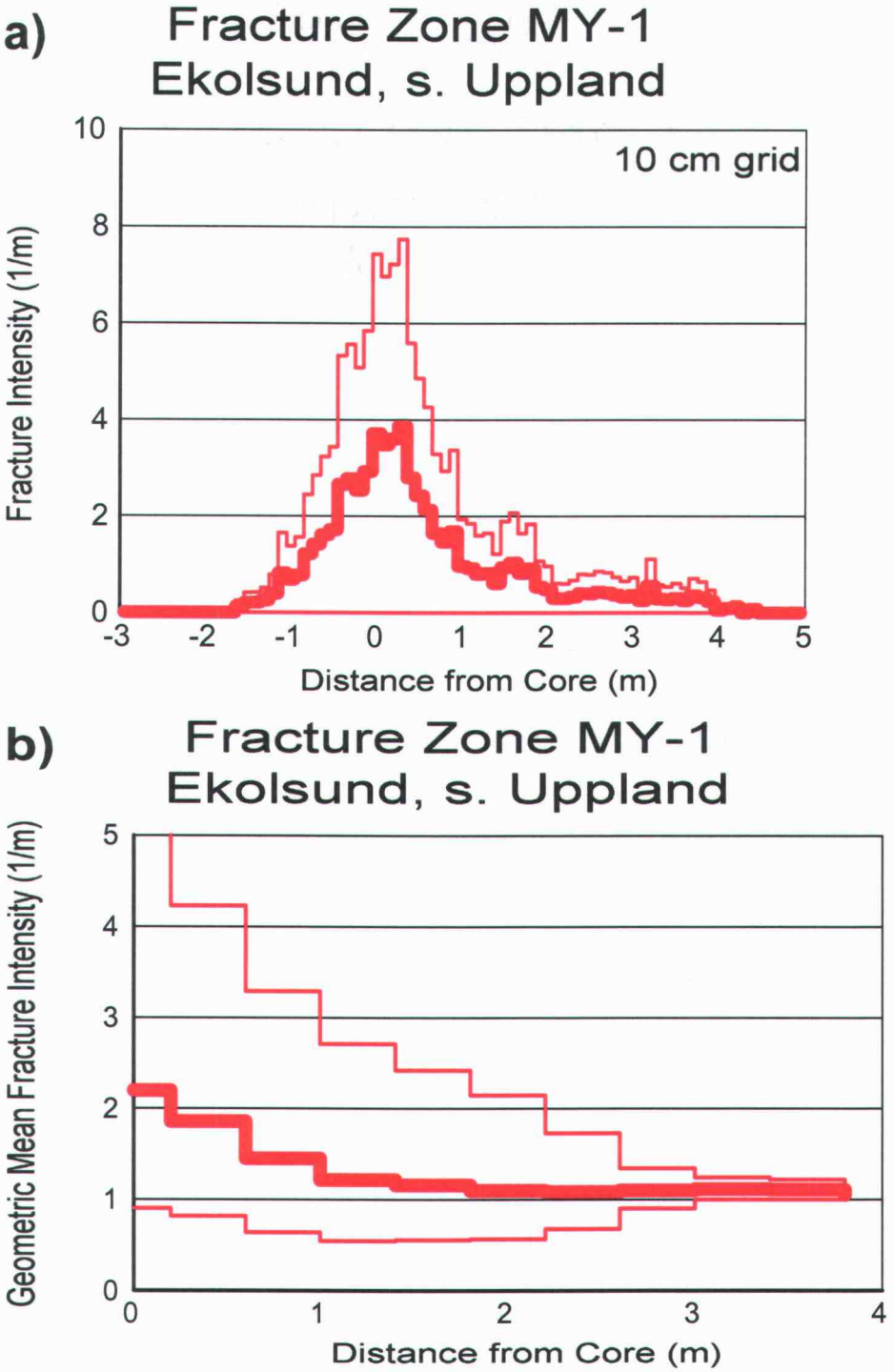

Figure 4-8. Variation of fracture intensity with distance from the median surface, in the Ekolsund maps, (a) plotted across the en échelon zone, showing asymmetry in terms of mean fracture intensity and 90th percentile upper and lower bounds, and (b) as geometric mean of fracture intensity with distance from the median plane (on either side).

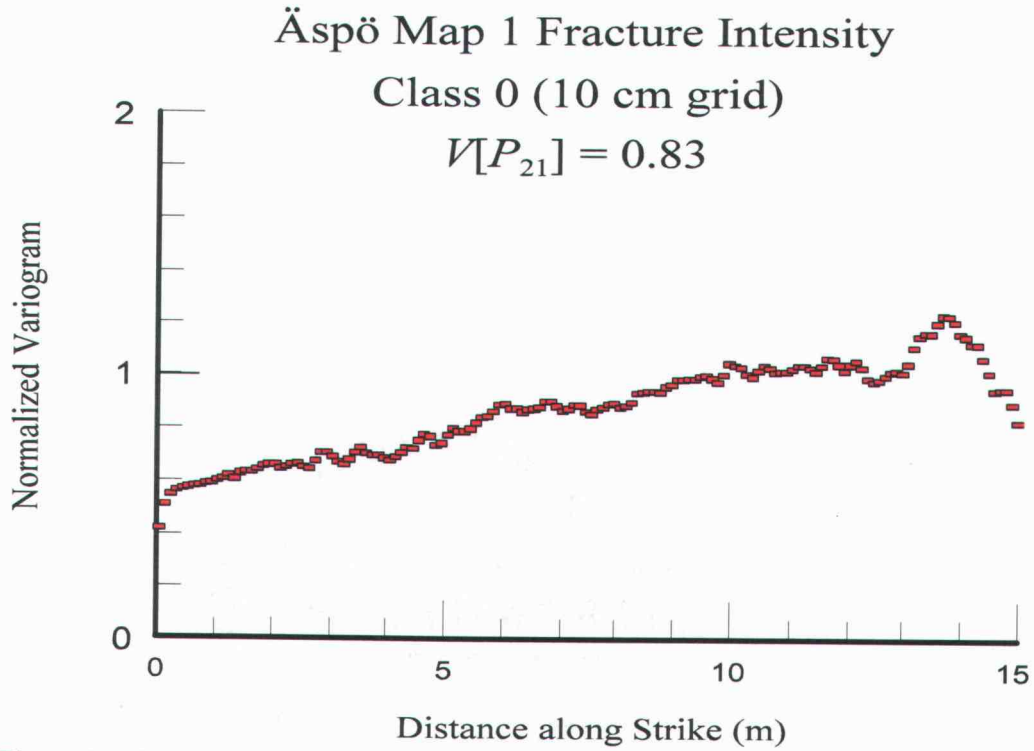

Figure 4-9. Variogram of fracture intensity in Äspö map.

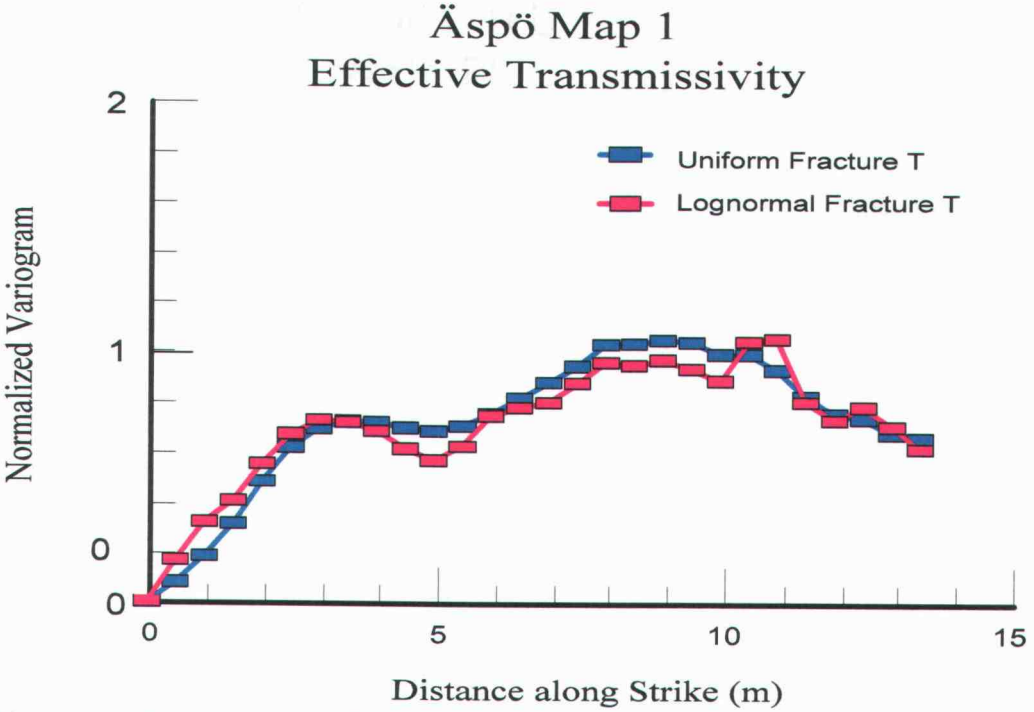

Figure 4-10. Variograms of effective transmissivity based on simulation of flow through the fracture geometry in the Äspö map, using assumptions of uniform vs. lognormally random transmissivity in the individual fracture segments.

For the zone shown in Äspö Map 1 (Figure 4-3), the hydraulic properties of the fractures were not known. The effects of connectivity variations due to structural relations among fractures were assessed by simulating flow through the 2-D network of the map, assuming either uniform or randomly lognormal transmissivity of the fracture segments. The head and flow fields predicted for the uniform case are shown in Figure 4-11

For the lognormal case, a unit variance in log transmissivity was assumed (*i.e.*, a standard deviation of one order of magnitude). The flow simulations were accomplished with the discrete-feature modeling code which is described in further detail by Geier (2004ab). Effective transmissivity values were calculated by dividing the simulated flux by the mean hydraulic gradient over each 0.5 m section of the map (along strike).

Variograms of the calculated effective transmissivity for both cases (Figure 4-10). show a significant correlation of effective transmissivity over scales of up to 8 m. A step with a slight "hole effect" (a decrease in the variogram at a finite distance, which can indicate periodicity) is evident in the range 3 m to 6 m, and is more pronounced for the lognormal case.

The two-dimensional simulations of flow cannot represent additional connections that might exist among fractures in the third dimension. Since a high percentage of the fractures on the map terminate at intersections with (or branch from) other fractures, it can be argued that the 2-D network connects most of the fractures intersecting this plane that would be connected directly or indirectly in 3-D. This contrasts with the well-known result for random (unstructured) fracture networks, where significant differences in 3-D vs. 2-D connectivity and percolation thresholds have been predicted by network models.

Additional connections could exist via unmapped fractures that are parallel to the plane of the map, or between fractures that are only indirectly connected in the map view, but which converge to form direct connections out of the map plane. The small vertical exposure at the south end of this map (Figure 4-4) indicates that such out-of-plane convergence occurs. These factors could affect the efficiency of the network and hence the quantitative results in Figure 4-10.

Convergence of secondary fractures in the vertical direction is also indicated by exposures at the Ekolsund site. Simulated flows for the Ekolsund site (Figure 4-12) illustrate the patterns that could be expected for vertical flow through such a flow, based on a 2-D analysis. 3-D network simulations would be needed to investigate the significance of the 3-D

connectivity structure implied by these two sets of exposures, taken together. Such simulations would require speculative assumptions about the 3-D connections.

Figures 4-13a-d show the variograms of fracture intensity for the Ekolsund maps, over separation distances of decimeters to 160 m. Plots are given for different classes of distance from the median surface (normal distances of 0-0.2 m, 0.2-0.6 m, and 0.6-1.0 m). Note the separation distances are plotted on a logarithmic scale to better display the smaller scales. The data support (number of data pairs) for each point on the semivariograms is also indicated; note that the more erratic points are associated with points with relatively few data.

Solid lines in the figures represent best fits for spherical variogram models. A spherical model is used simply because this is one of the simplest types of variogram which is capable of representing the data. Other variogram models such as an exponential model could perhaps give fits of similar quality.

Due to the limited support for separation distances in the range from map scale (<10 m) to the distance between exposures (roughly 50 m), little can be said about possible correlations on scales from 10 m to 50 m. The data show little if any significant correlation at 10 m separations, and no significant correlation for the longer separations in excess of 50 m.

Thus these results show no support for speculative models of fracture intensity correlations along strike, over larger scales of 50 to 150 meters. Previous modeling studies (Tsang *et al.*, 1996; Geier, 1996), have shown that correlations on such scales, if they exist, would have significant consequences for large-scale transport and retention of radionuclides, due to channelization in the heterogeneous flow fields within large-scale structures.

Significant correlations are indicated only on the scale of the individual stepovers that are seen on single exposures. The variability of fracture intensity in the direction normal to the median surface (as shown in Figure 4-8 above) is the dominant component of variability in this zone.

In interpreting these results, the limitations of a variogram analysis should be considered. Small-scale correlations of fracture intensity within and between en échelon steps could be masked by variability in the lateral extent and spacing of the en échelon steps. Although the simple geostatistical model represented by the variogram does not capture this type of structural variability, models for en échelon zone heterogeneity might usefully be constructed based on a more explicit representation of the observed structural characteristics. This type of model is explored in a companion model (Chapter 6).

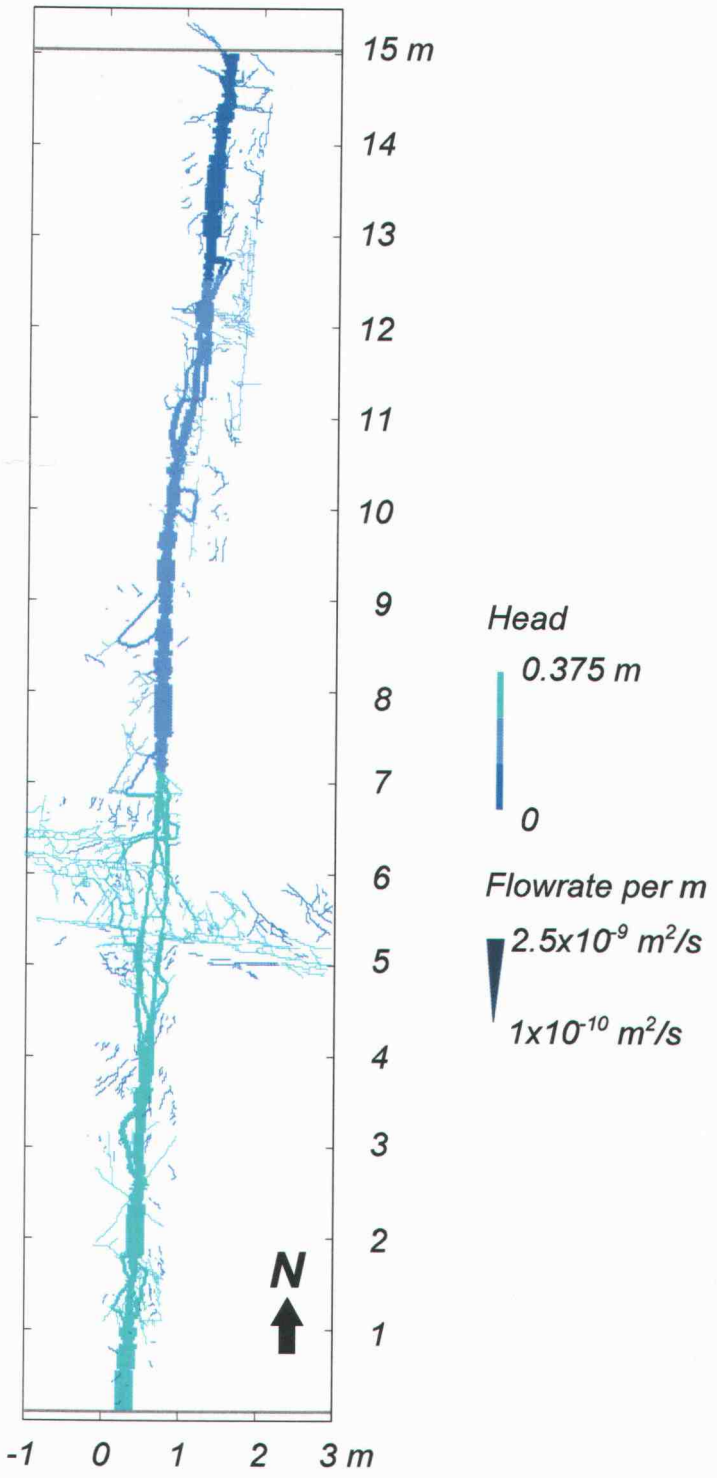

Figure 4-11. Head and flow field calculated for 2-D fracture network defined by Äspö en échelon zone map, for 0.375 m differential head applied south to north. Head in fractures is indicated by color scale. Flow rate is proportional to line width (except for stagnant fractures which are represented by the narrowest lines).

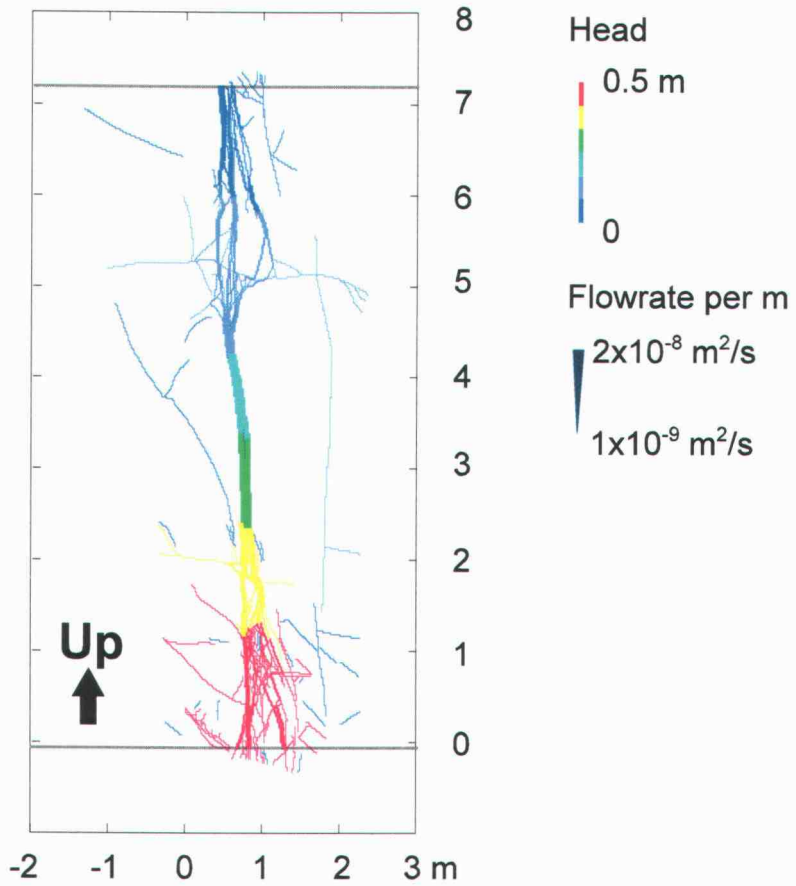

Figure 4-12. Head and flow field calculated for 2-D fracture network defined by Ekolsund map SRNC, for a 0.5 m gradient applied south to north. Head in fractures is indicated by color scale. Flow rate is proportional to line width (except for stagnant fractures which are represented by the narrowest lines). Note non-connected fractures have head set to 0 m.

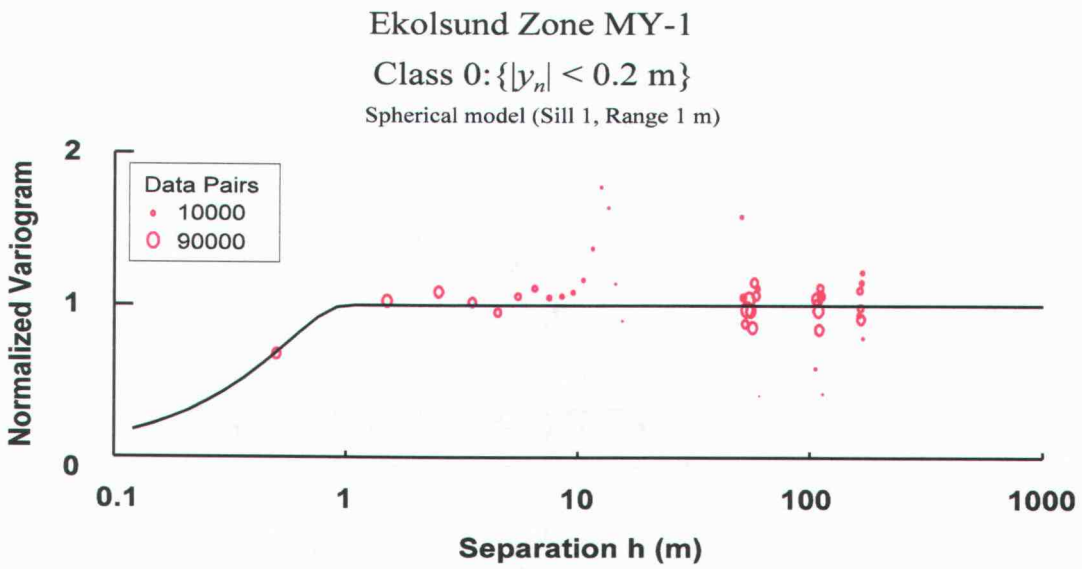

Figure 4-13a. Normalized variogram of fracture intensity $P_{21}(y)$ for the Ekolsund site, for Class 0 representing rock within 0.2 m of the median surface of the zone MY-1. Size (area) of symbols is proportional to the number of supporting data pairs.

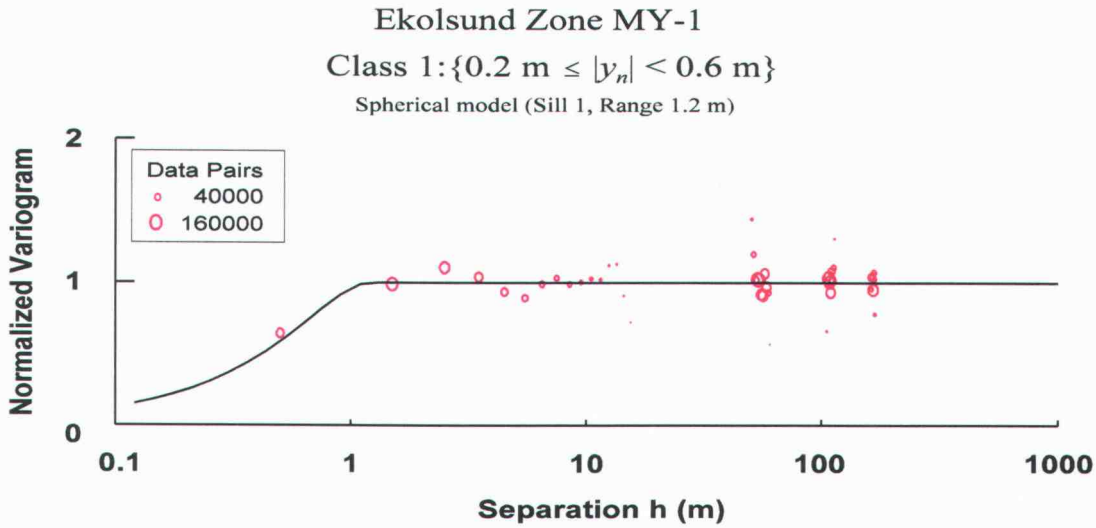

Figure 4-13b. Normalized variogram of fracture intensity $P_{21}(y)$ for the Ekolsund site, for Class 2 representing rock 0.2 m to 0.6 m from the median surface of the zone MY-1. Size (area) of symbols is proportional to the number of supporting data pairs.

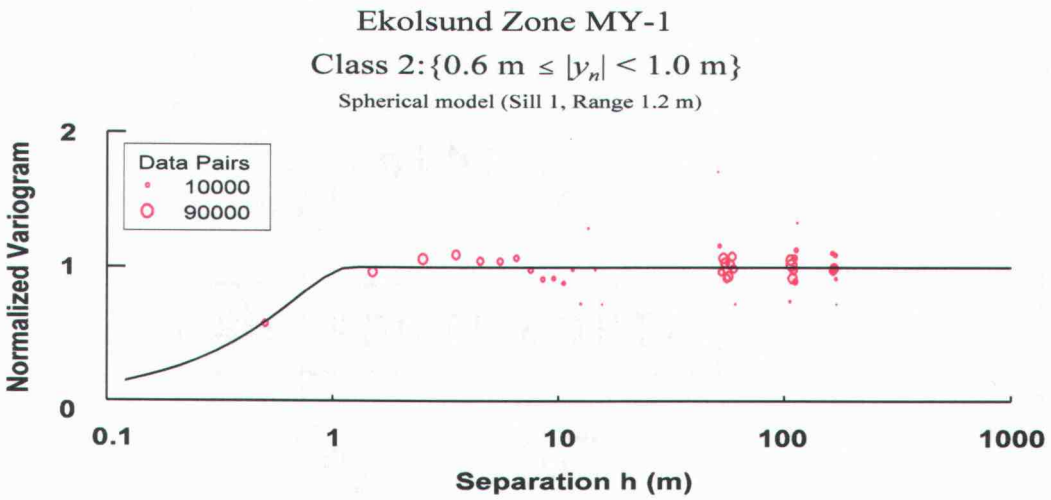

Figure 4-13c. Normalized variogram of fracture intensity $P_{21}(y)$ for the Ekolsund site, for Class 2 representing rock 0.6 m to 1.0 m from the median surface of the zone MY-1. Size (area) of symbols is proportional to the number of supporting data pairs.

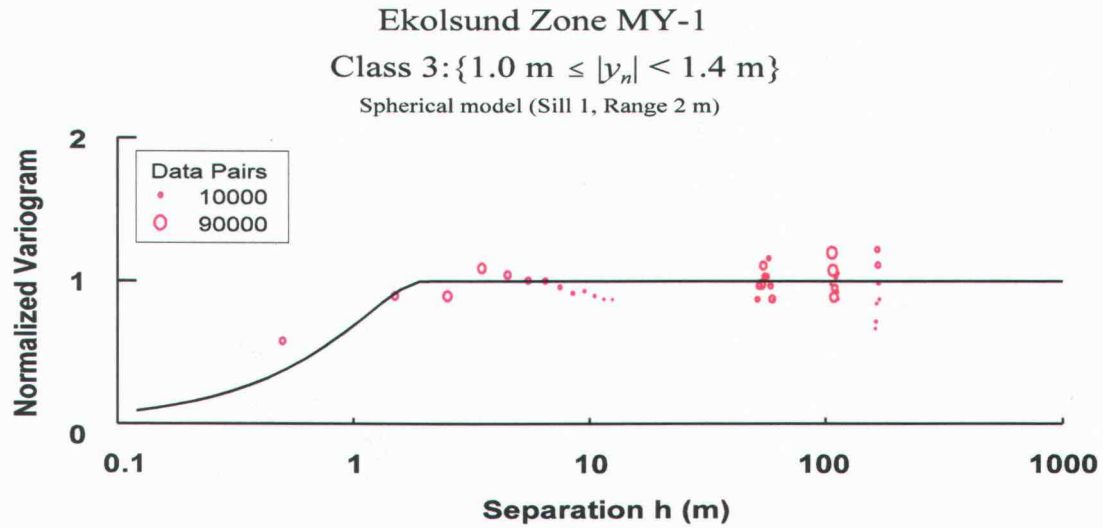

Figure 4-13d. Normalized variogram of fracture intensity $P_{21}(y)$ for the Ekolsund site, for Class 2 representing rock 1.0 m to 1.4 m from the median surface of the zone MY-1. Size (area) of symbols is proportional to the number of supporting data pairs.

Connectivity as a function of sense of en échelon offsets in the Äspö map

The en échelon structure in the Äspö map is interpreted as left-lateral fault zone based in part on the NW-directed regional maximum horizontal stress which is likely to have been fairly consistent over the past 60 Ma (Stephansson *et al.*, 1991), and in part on the orientation of secondary fractures interpreted as pinnate fractures. Markers to confirm this sense of offset are difficult to find, due in part to the obscuring effect of the weathered and largely lichen-

Figure 4-14. Detailed photograph from Äspö mapping area showing apparent left-lateral separation of about 3 cm of two fragments of an oblong, leucocratic inclusion which is cut by one of the main en échelon segments. The inclusion fragments are outlined by red dashed lines. The spacing between strings on the grid is 10 cm. North is upward in the photo, parallel to the reference line which passes through the 40 cm marks on the frame. The branching fracture which bifurcates from the main segment in the lower left corner, dips at low angle toward the SE. Note the point of bifurcation is from a bend in the main segment (interpreted as a compressional bend) from which fragmented material has apparently been weathered and eroded away.

covered bedrock surface. A leucocratic inclusion which was apparently cut by one of the primary échelon segments (Figure 4-14) shows a horizontal separation of about 3 cm relative between the apparently matching fragments. Two glacial striae crossing the trace show possible left-lateral offsets of up to 1 cm, as indicated in Figure 4-15, suggesting that a fraction of the inferred left-lateral slip may have occurred during or after glaciation. Other striae show no perceptible offset, indicating that any such slip would need to have been synglacial. Interpretation of striae as markers for offset on this small scale (1 cm) is uncertain due to the typical irregularities along individual striae.

Figure 4-15. Detailed photograph from Äspö mapping area showing glacial striae crossing one of the main en échelon segments. The stria (outlined in red) below the compass appears to show no offset. Two striae above the compass show possible left-lateral offsets of up to 1 cm, although these apparent offsets might alternatively be explained as irregularities in the striae. The spacing between strings on the grid is 10 cm. North is upward (parallel to the grid lines) in the photo. The dark band crossing the lower right-hand corner of this photo is a shadow.

Both left-hand and right-hand steps, interpreted as extensional and contractional (as defined in Figure 4-16) based on the interpretation of left-lateral slip, are seen between fracture segments. There is a distinct contrast between extensional and contractional steps, in terms of the degree of fracturing and connectivity of fractures within the stepover zones.

In the left-hand (extensional) step between y = 3.7 m and y = 7.2 m (Figure 4-17a) , the end of each en échelon segment curves toward and connects with the other segment. Numerous secondary fractures within the stepover, many sub-parallel to the curved ends of the segments, provide additional connections between the en échelon segments. These secondary fractures strike NW, and thus are oriented parallel to the current direction of maximum compressive stress.

This portion of the map also shows a swarm of E-W striking fractures which appear to be of the same age or younger based on termination relationships, which have the

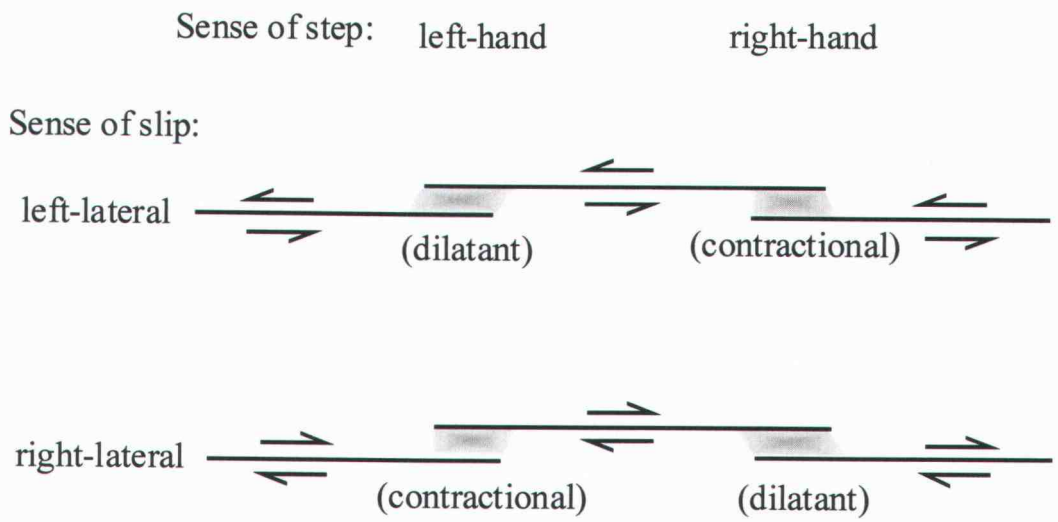

Figure 4-16. Definition of left-hand and left-hand steps for en échelon zones with left-lateral and right-lateral senses of slip.

appearance of a crossing, en échelon structure. The limited extent of the exposure in this direction restricts the possibility to interpret this apparent crossing structure. Considering the regional stress field, a right-lateral sense of slip across this structure would be expected, but no markers were found to confirm this.

In terms of the potential for fluid flow, the extensional type of step seen in the main structure in Figure 4-17a in should provide good connectivity from one en échelon segment to the next. Considering their orientation relative to the stress field, the secondary fractures within these zones are more likely than fractures in other orientation to have high transmissivity. Such a step might provide a favorable path for vertical flow along the fault band, particularly in the third dimension (vertical).

The right-hand (contractional) step between $y = 10.5$ m and $y = 12.3$ m (Figure 4-17b) shows a very different configuration of fractures. The ends of the main segments bypass each other without connecting directly. The end of one segment (on the left-hand side) apparently bifurcates around $y = 10.5$ m, with one branch growing away from the next segment, and one branch growing closer to but roughly parallel to the next segment. Small fractures striking at nearly right angles to the main segments form irregular connections between the en échelon segments, but the segments do not directly connect to each other. This type of step is likely to be less conducive to fluid flow that the extensional step.

Examples of extensional and contractional steps exposed on outcrops nearby on Äspö show similar patterns. Within stepovers, smaller-scale en échelon structures are also observed, suggesting a degree of self-similarity in the geometry of the networks. The variability of fracture intensity within and adjacent to these zones implies anisotropic and heterogeneous permeability, with preferential directions at a high angle to the slip direction, and dependent on whether the step-over is synthetic or antithetic to the sense of slip.

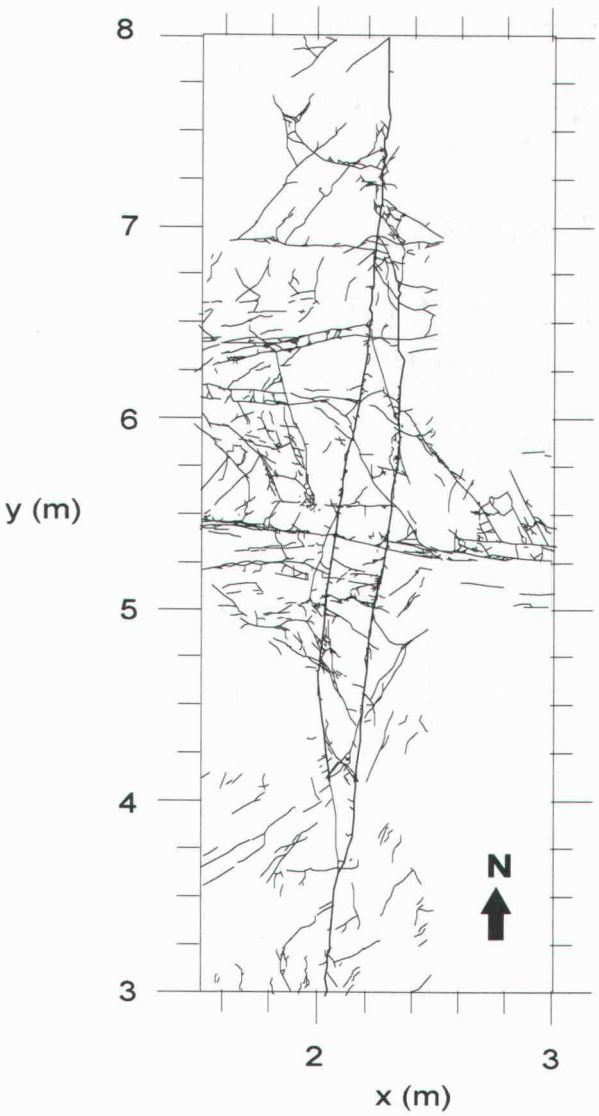

Figure 4-17a. Detail of en échelon zone map on southern Äspö showing left-stepping stepover between y = 3.7 m and y = 7.2 m. The N-S striking zone is intersected in this interval by an E-W structure which may also be an en échelon fault zone (rightward-stepping and possibly right-lateral), although the exposure in this direction is limited.

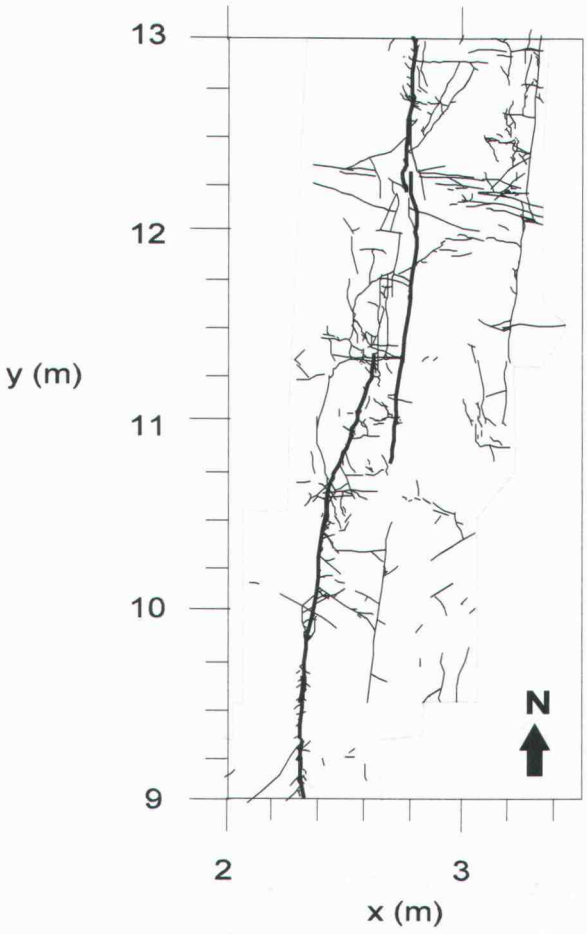

Figure 4-17b. Detail of en échelon zone map on southern Äspö showing right-stepping (antithetic) stepover.

4.5 Conclusions

The en échelon structures mapped at Äspö and Ekolsund show an anisotropic and heterogeneous permeability, with preferential directions parallel to the strike of the zones along which slip is inferred. Detailed configurations of stepovers in the horizontal exposure at Äspö show marked differences in connectivity, depending on whether the sense of step is synthetic or antithetic to the sense of slip. Intensity of fracturing in the wall rock shows an approximately exponential decrease with distance from the central deformation zone (fault core), as has been commonly observed in other fault zones.

Geostatistical analysis of fracture intensity for both sites shows an anisotropic variability which is correlated over scales of several meters along strike, corresponding to the length of, and recurrence interval between the step-over zones that were mapped. Effective transmissivity of the structure at Äspö, based on network flow simulations using assumptions of either uniform transmissivity or lognormally varying transmissivity (with an order of magnitude standard deviation) among individual fractures, show similar correlation lengths.

This study considered exposures which gave the possibility to test for correlations across separations along strike of 50 to 150 m. Results did not provide positive support for correlation of fracture intensity at these scales. This finding is significant in view of previous modeling results which indicated correlation on such scales, if they exist, could be significant for flow, solute transport, and heat transfer in fault zones.

A caveat on this result is that the observed small-scale correlations of fracture intensity may be masked by variability in the lateral extent and spacing of the en échelon steps. Thus although a simple geostatistical model does not capture this type of structural variability, models for en échelon zone heterogeneity might usefully be constructed based on a more explicit representation of these structural characteristics. This type of model is explored in a companion paper (Chapter 6).

Within stepovers, smaller-scale en échelon structures are observed which suggest a degree of self-similarity, implying that the characteristics identified may be manifested on a range of scales. The variability of fracture intensity also implies heterogeneous, anisotropic and correlated properties for solute transport, in particular the pore volume and surface available for sorption.

5. HIERARCHICAL STRUCTURE AND IMPLICATIONS FOR RADIONUCLIDE TRANSPORT

Abstract

Detailed mapping and geometric analysis of en échelon-type fracture zones in granitic rock at two sites in southern Sweden, Äspö (e. Götaland) and Ekolsund (s. Uppland), reveal characteristics of significance for groundwater flow and solute transport.

A companion paper (Chapter 4) examines heterogeneity and anisotropy of fracture intensity in these fracture zones. This paper considers implications of the apparent hierarchical structure within these zones, for transport including mass transfer between the relatively mobile water in the main fracture zone and relatively immobile water in the secondary fractures and adjacent matrix.

Splay fractures along the main fractures also contribute to the surface area that is available for sorption. A hierarchical pattern of splays in the damage zone implies a systematic, possibly fractal increase in the amount of surface area and pore volume that solute can access by diffusive mass transfer, with increasing distance from the fault core.

Analysis of the function $A'(s)$ representing the incremental matrix volume versus distance s from fractures in this hierarchical structure shows an approximately log-linear slope. Comparison with fractal models of block-size distribution indicate these are consistent with a log-linear slope of $A'(s)$.

These aspects of en échelon zone architecture suggest a need for more complex representation in hydrologic models, than as simple, planar conductors with or without heterogeneous properties, or as zones of increased but unstructured fracturing. These implications are evaluated by means of numerical modeling in a companion paper (Chapter 6).

5.1 Introduction

Radionuclides from a spent nuclear fuel repository in granitic rock will most likely travel along fracture zones (active or relict fault zones). The transport characteristics of fracture zones are therefore of primary interest in assessing the potential for retention of radionuclides as they migrate through these features, or conversely the risk of radiation release to the surface environment via these features.

For most radionuclides of concern, the principal mechanism for retention of radionuclides within granitic rock is the process known as matrix diffusion. When radionuclides spend time on excursions into regions of the rock where, because of low permeability and correspondingly low fluid velocities, transport is mainly by diffusion, this allows a fraction of the radionuclides to decay. Therefore properties governing the time radionuclides may spend on these diffusive excursions into the matrix are significant for evaluating the risk of radiation release to the surface environment.

Matrix diffusion in granitic rock is conventionally idealized in terms of a binary model, in which water and solute are either in a mobile zone (often referred to as "the fractures") or an immobile zone (referred to as "the matrix"). In such a model, rock properties that govern matrix diffusion include (1) the amount of surface area over which relatively mobile water in the fracture zones comes into contact with relatively immobile water in the rock matrix, and (2) the availability of matrix volume as a function of the diffusion distance into the matrix. Matrix diffusion is assumed to act in macroscopically unfractured granite as well as fault-zone rock, although the potential extent of matrix diffusion into macroscopically unfractured granite is a topic of ongoing research (Ohlsson and Neretnieks, 1995; Jakob, 2004).

Neretnieks and Rasmuson (1984) noted that fracture zones have a large capacity for matrix diffusion due to the large contact area between mobile and immobile zones, or "flow wetted surface," per unit bulk volume, but that this capacity is limited by the finite size of the rock fragments within the fracture zones. Using hypothetical cases with different fragment sizes, they demonstrated how the distribution of fragment size can influence the retention of radionuclides within fracture zones.

Cunningham and Roberts (1998) demonstrated a mathematical equivalence between matrix diffusion in the case of a variable fragment-size distribution, and the multi-rate mass

transfer model of Haggerty and Gorelick (1995), which postulates that fine-scale heterogeneity of matrix properties affecting diffusion can be described by a distribution of effective mass-transfer rate coefficients between the mobile zone and immobile zone. Thus results of in-situ tracer experiments in fracture zones which can be described in terms of a distribution of rate coefficients using the multi-rate mass transfer model could equivalently be interpreted in terms of a distribution of rock fragments in the fracture zone.

As tracer experiments convolute the effects of multiple processes and heterogeneous properties into a set of observations at a few discrete points (*i.e.* sampling intervals in boreholes), there is inherent nonuniqueness in their interpretation. Hence interpretations need to be grounded in an understanding of the physical structure of the geologic medium in which they are conducted. The physical structure of the medium may also be significant for evaluating the binary mobile/immobile model which has been the basis for most mathematical development to date.

This paper examines the structural character of one type of fracture zone, en échelon zones, which are potentially significant in terms of providing pathways for radionuclide migration from a repository in granitic bedrock, in terms of centimeter- to decimeter-scale geometric properties that relate to potential for retention of radionuclides by matrix diffusion. Companion papers (Chapters 4 and 6) examine larger-scale structural heterogeneity in terms of fracture intensity, as indicative of the heterogeneity in the capacity for different portions of these fracture zones to conduct water.

5.2 Background

The data for this analysis come from detailed mapping of en échelon zones at two locations in granitic rock in the Swedish portion of the Fennoscandian shield: Äspö (eastern Småland) and Ekolsund (southern Uppland). Locations of these sites are shown in Figure 5-1. More detailed maps are given in Chapter 4 and Section 2.1.

N to NNW trending sets of en échelon fracture zones at both sites represent a class of features that may be significant for local hydrogeology and radionuclide transport, due to (1) their orientation conjugate to the direction of regional maximum horizontal compressive stress, (2) the apparent connections between extensive, simple fractures via duplex structures at en échelon steps, and (3) the small amount of wetted surface area in the simple fractures, which implies a relatively low potential for radionuclide retention by matrix diffusion and sorption relative to fracture zones with more distributed deformation.

Site descriptions

Äspö is an island in the archipelago along Sweden's southeastern Baltic coast. The island and its vicinity have been a focus of intensive geoscientific investigations over the past 15 years, as the site of the Äspö Hard Rock Laboratory which extends to a depth of 450 m below the island. The bedrock on Äspö is predominantly a suite of 1.81 Ga to 1.76 Ga old plutonic rocks associated with Transscandinavian Igneous Belt, with modal compositions ranging from monzodiorite to quartz monzodiorite and quartz monzonite to monzogranite and granite (Wahlgren *et al.*, 2003; SKB, 2004). These plutonic rocks intrude older metavolcanics (2.0 Ga), and are in turn intruded by aplite dikes (1.8 to 1.35 Ga).

The Äspö region since undergone multiple orogenic and rifting episodes (Larsson and Tullborg, 1993) which have produced multiple sets of fracture zones. Many of the fracture zones have been reactivated in a different sense of shear in the later deformation episodes, in response to changes in the direction of maximum compressive stress (Tirén *et al.*, 1996).

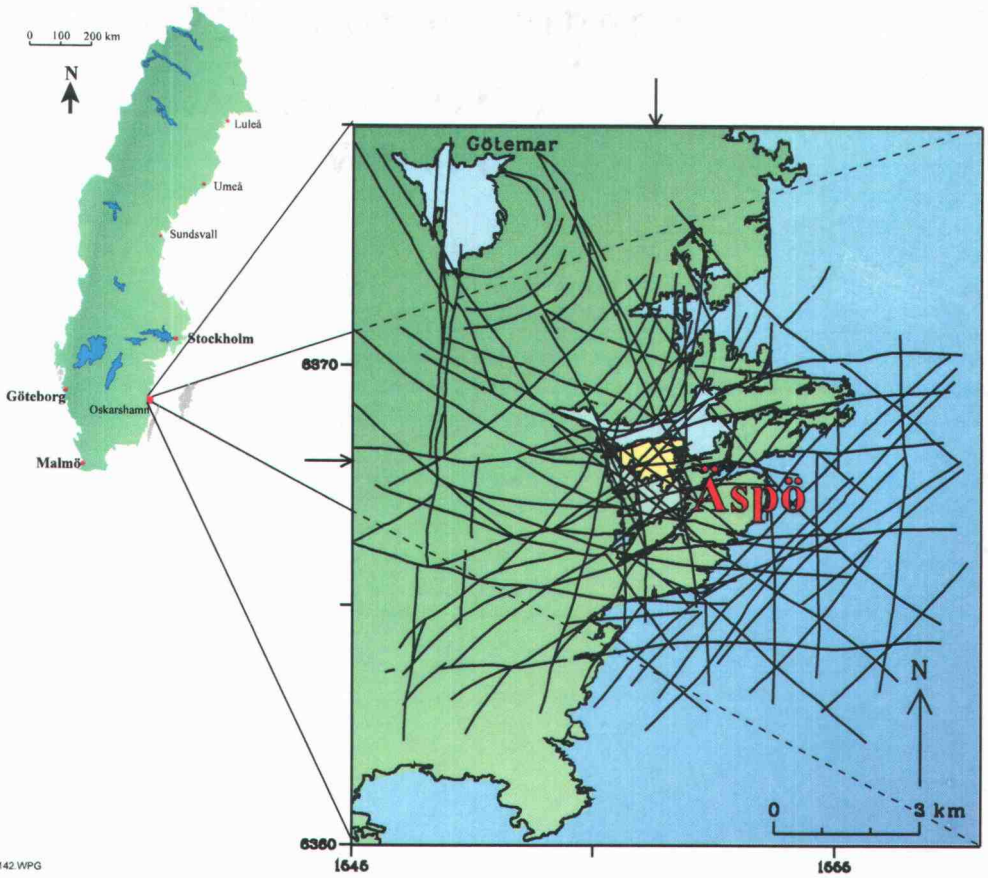

Figure 5-1a. Location and regional structural setting of the Äspö Hard Rock Laboratory site, Sweden. Äspö is the island in the center of the inset box. Lines show the pattern of regional lineaments interpreted as fracture zones, based on elevation, geophysical and remote-sensing data (Tirén *et al.*, 1996).

The Ekolsund study site is in southern Uppland, on the west side of Ekolsundsvik, an inlet of Lake Mälaren, between Stockholm and Enköping. This site has not been studied as intensively as Äspö 300 km to the south, but offers certain advantages in terms of the scale and configuration of exposures. The site has been the focus of a study sponsored by the Swedish Nuclear Power Inspectorate since 2001, with a primary aim of verifying methods for lineament interpretation based on remote sensing data.

The bedrock at Ekolsund is granodiorite to diorite, with a weak foliation over most of the study site. Gneiss and mylonite occur just outside the mapping area at the eastern edge of the study site, adjacent to Ekolsundsvik. The composition and age of the local rocks have not been studied but the locality falls within a region of early to late Svecofennian granitoids (1.9-1.77 Ga) of the Transscandinavian Igneous Belt, according to the lithostratigraphic map of Larsson and Tullborg (1993). The regional tectonic history affecting the site over the last 1.2 Ga is similar to that of Äspö in general terms.

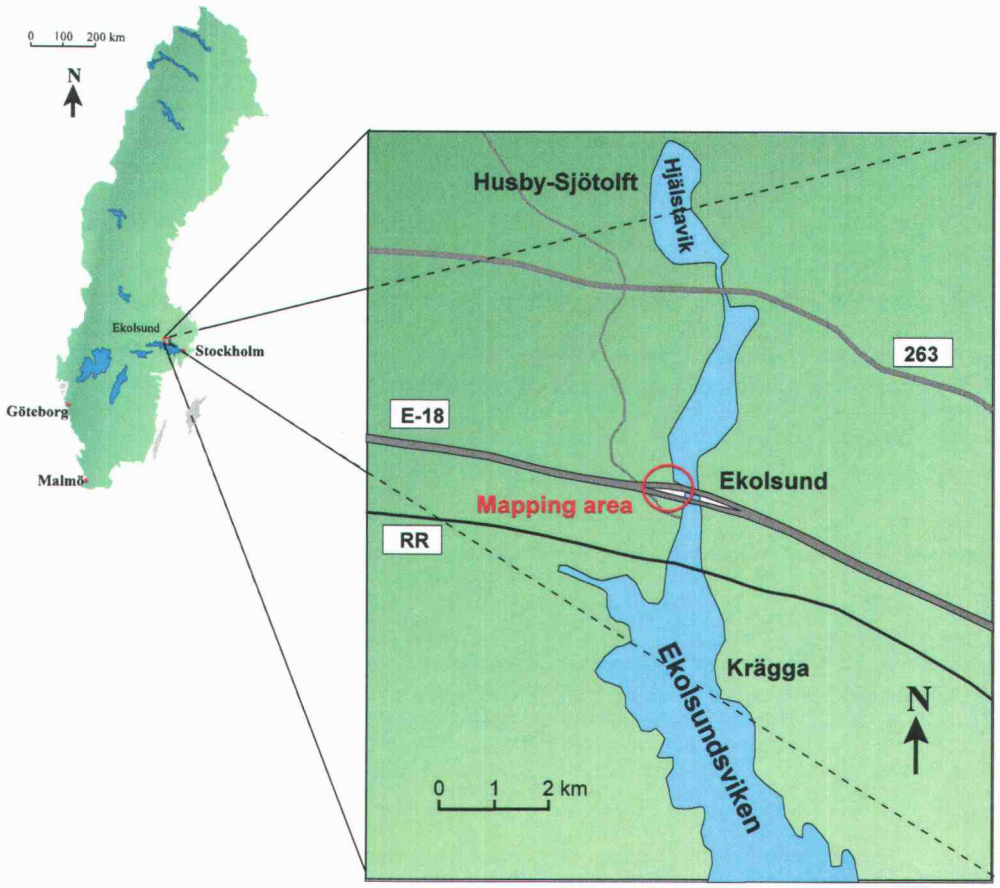

Figure 5-1b. Location of the Ekolsund site, southern Uppland, Sweden.

Source data for analysis

The basic data used in this analysis are detailed maps of N to NNW striking, subvertical en échelon zones from the two sites. The map for Äspö (Figure 5-2) is a plan-view map of a 14.5 m long exposure of a subvertical en échelon zone, mapped with a resolution of 1 cm for a width of 1 m along most of this zone. The maps for Ekolsund (Figure 5-3) describe four vertical exposures, of heights ranging from 5 m to 12 m, over an approximately 160 m horizontal extent. Small horizontal exposures were also mapped at the tops of two of the vertical exposures, to give a 3-D perspective. Figure 5-3 includes an isometric view of the four vertical exposures to illustrate the scale of the maps relative to the separation between exposures. Details of the preparation of these maps are given in Section 3.1 and Chapter 4.

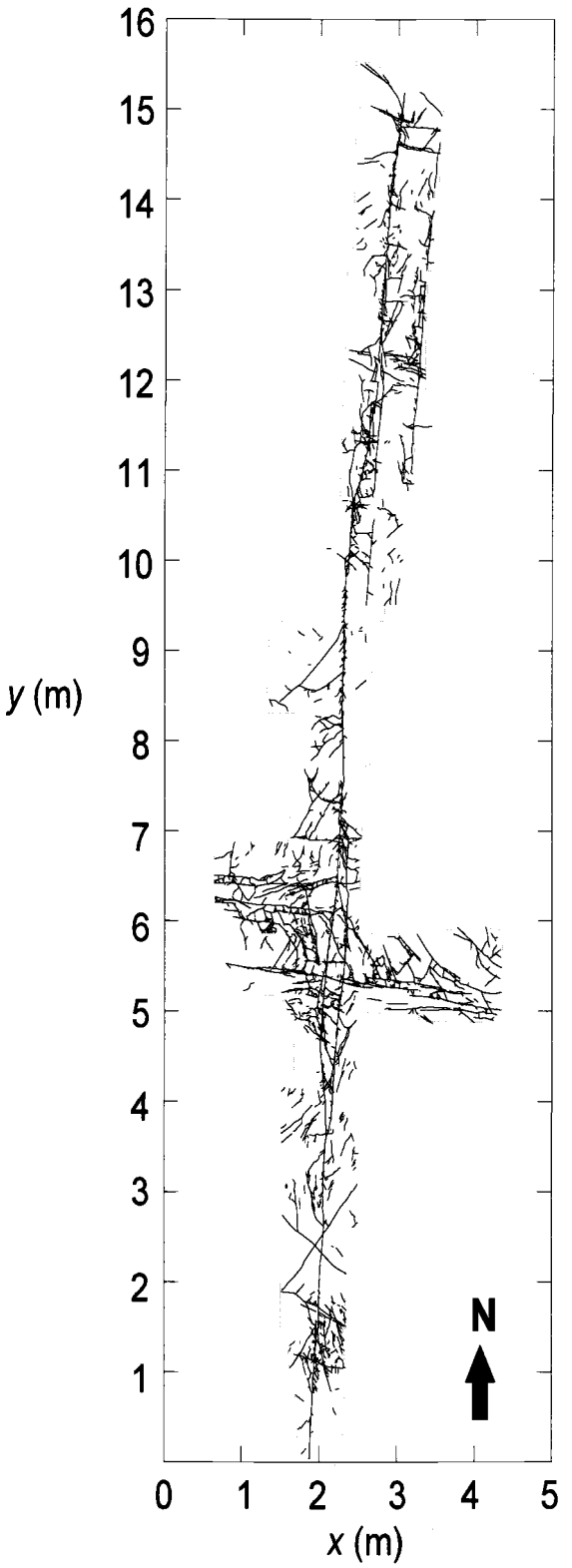

Figure 5-2. Rectified plan-view map of en échelon zone on southern Äspö [digital vector version available on CD accompanying dissertation].

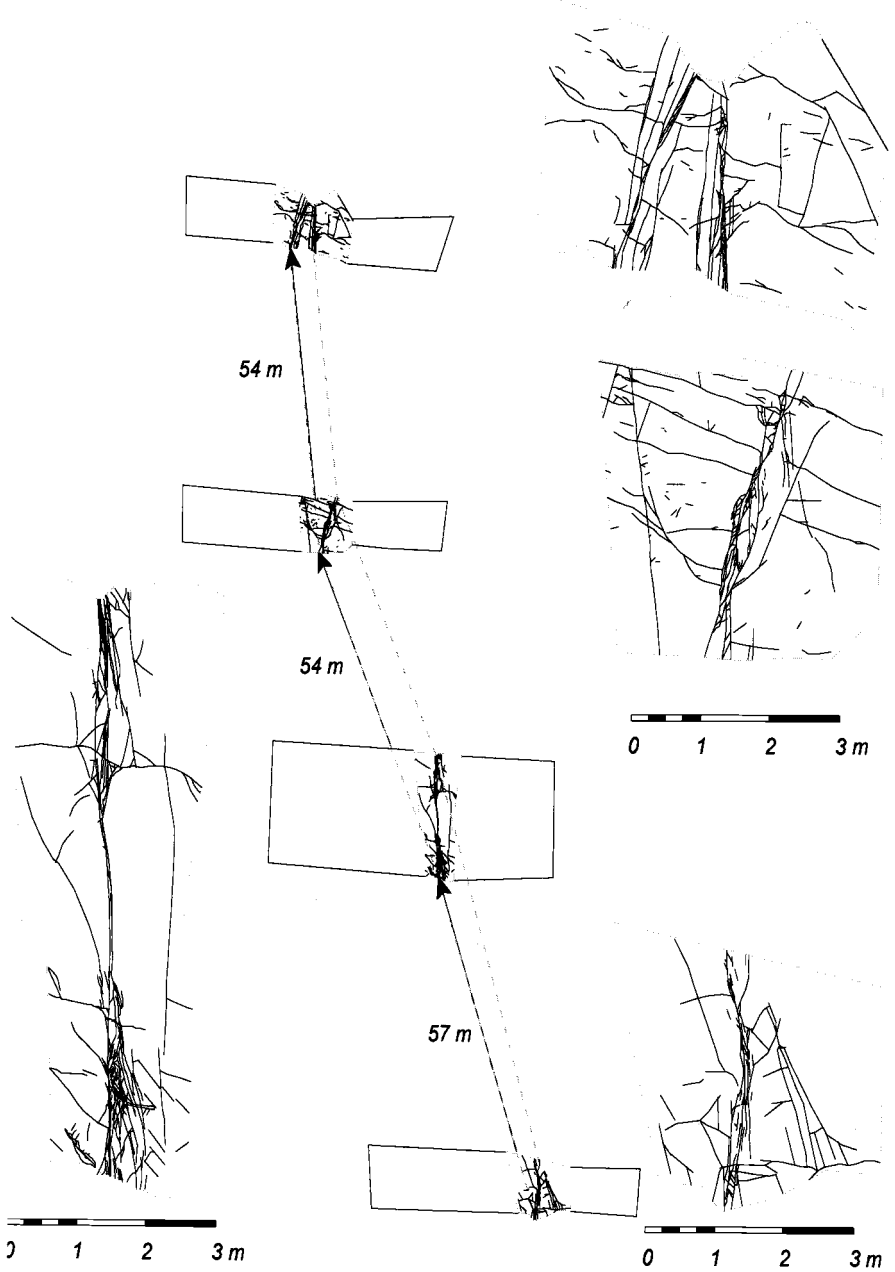

Figure 5-3. Fracture maps of four vertical exposures along a single interpreted, N-striking fracture zone at the Ekolsund site. Overview in center of plot is isometric view of the four exposures, viewed in the direction N15E and 20 degrees downward from horizontal. The median surface of the zone is indicated by the dashed lines connecting between panels.

Geometrical analysis

Branch fractures are defined in this analysis as fractures for which the traces in map view connect to a longer fracture trace at one or both ends. Fracture order and branching structures (represented as groups of polylines, *i.e.* open polygons or connected line segments) are defined with respect to *primary fractures* (Figure 5-4). The nomenclature developed here is similar to that of Moody and Hill (1956), who noted a similarity relationship of "subsidiary" or second-order faults to "dominant" or first-order faults in wrench-fault systems.

For convenience we introduce the notation ψ_i to denote a set of branches of order I pertaining to a structure defined in terms of a given set of primary fractures, which are denoted ψ_0. A *branching structure* of a given order I is defined here as consisting of the primary fractures and all branches up to and including the ith-order branches. The notation Ψ_i is used here to denote a branching structure of order I. Thus:

$$\begin{aligned}
&\Psi_0 = \psi_0 \\
&\Psi_1 = \Psi_0 \cup \psi_1 = \psi_0 \cup \psi_1, \\
&\cdot \\
&\cdot \\
&\cdot \\
&\Psi_N = \Psi_{(-1)} \cup \psi_N = \psi_0 \cup \psi_1 \cup \ldots \cup \psi_N,
\end{aligned} \tag{5-1}$$

where N is the highest order for which the set ψ_N is not empty. In other words Ψ_N consists of all fracture traces (within the resolution of the map) that connect to the primary fractures ψ_0, either directly or indirectly via other fracture traces. For the sake of brevity, we will refer to this as an Nth-order branching structure or *entire* branching structure.

We may note that referring to Ψ_N as an "entire" branching structure implies that the branching process terminates at some order N. In the case of the following geometrical analysis, this may be due to the finite resolution of the map rather than a termination of the physical branching process. If the branching structure were a true fractal in the mathematical sense, the entire branching structure would only be encompassed by Ψ_N for infinite N. Presumably constraints such as grain size impose a physical limit on the maximum order of branching.

Geometrical analysis of the fracture trace maps was carried out using the interactive map-analysis program *splinter* (Section 2.2), which performs geometrical calculations with

geometric objects defined in terms of individual line segments, polylines (open polygons composed of line segments), or groups of polylines. In this analysis, simple fracture traces are represented as polylines. Primary fractures comprising Ψ_0 are identified interactively, by inspection. The *splinter* program then identifies the branching structures Ψ_1, Ψ_2, ... Ψ_N by iteratively extending the branching structures of successive order I until the set ψ_{i+1} is empty, *i.e.* no further branch fractures can be found.

Assuming all fractures to be water-conducting, the fractures in an entire branching structure Ψ_N would be accessible to solute moving through the primary fractures, by some combination of advection and diffusion through the network of connected fractures.

The volume of matrix $V(s)$ within a given distance s of fractures in a branching structure Ψ_i of a given order I is a measure of the volume available for matrix diffusion with a given depth of penetration from the relatively mobile zone in the macroscopic fractures, following the approach of Neretnieks and Rasmuson (1984).

With this in mind, we define $V_i(s)$ as the volume of matrix within a given distance s of any fracture in the ith-order branching structure Ψ_i. This volume is very difficult to characterize in natural fracture systems without knowing the detailed, 3-D configuration of fractures. However, a corresponding region $\Omega_i(s)$, defined as the region of a map within distance s of any fracture trace belonging to Ψ_i, can be drawn directly on a map of fracture traces (Figure 3-3). If all fractures are perpendicular to the map section, $\Omega_i(s)$ is equivalent to $\delta V_i(s)$, the intersection of $V_i(s)$ with the plane of the map.

Here we assume that $\Omega_i(s)$ and $\delta V_i(s)$ are approximately equivalent (an approximation discussed further by Geier (2004, Chapter 3), and use the area of $\Omega_i(s)$:

$$A_i(s) = \left|\Omega_i(s)\right| = \int_{\Omega_i(s)} dA \tag{5-2}$$

as a two-dimensional estimator of $V_i(s)$ for a unit thickness of the rock. We adopt a 2-D analysis of this area in order to characterize the potential volume available for matrix diffusion as a function of diffusion depth, for a 2-D representation of en échelon zones in which all fractures are assumed to be perpendicular to the section studied. The area $A_i(s)$ is evaluated by Monte Carlo integration as described by Geier (2004, Chapter 3), to a precision of about 10 cm^2 over a 10 m^2 map.

The functions $V_i(s)$ and $A_i(s)$ are related to the size distribution of rock fragments within and adjacent to the branch networks, noting that such fragments need not be completely separated from other portions of the rock matrix. In this regard, the present analysis follows the stochastic geometric definition of rock block size distributions for jointed rock, as advanced by Dershowitz (1984).

The intensity of fractures adjacent to a branching structure Ψ_i is a measure of the damage zone around the structure, as a function of the distance s. This measure is calculated for a given distance increment δs as:

$$P_{21}(s \pm \delta s) = \delta L_i(s) / \delta A_i(s) \tag{5-3}$$

where $\delta L_i(s)$ is the fraction of the total trace length of fractures not belonging to Ψ_i that are within the incremental region $\delta \Omega_i(s) = \Omega_i(s+\delta s) - \Omega_i(s-\delta s)$, and $\delta A_i(s)$ is the area of $\delta \Omega_i(s)$. Details of the calculation are described in Chapter 3. The notation P_{21} follows the convention for a unified set of fracture intensity measures, based on the dimensions of the observations (Dershowitz and Herda, 1992). In this case the observations are taken over a 2-D sample (area map) and the observed entities (the fracture trace lengths) are 1-D.

5.3 Observational Results

Interpretation of branch fractures in Äspö map

The distribution of fracture azimuth, for first-order branches of the main fractures in Äspö Map 1 (Figure 5-2) is shown as a rosette diagram in Figure 5-5a. The main peaks in frequency correspond to the expected directions of pinnate fractures and conjugate faults, based on interpretation of the main en échelon segments as part of a left-lateral fault band. The arrows show the approximate, present-day orientation of the principal compressive stress σ_1.

Figure 5-5b shows a histogram for the branching angle between first-order branch fractures and the primary fractures. The sign of a branching angle is taken as positive if the branch fracture bifurcates rightward, for an observer standing on the primary fracture that the branch starts from. Note that branching angles of +90 deg and -90 deg are equivalent. Three

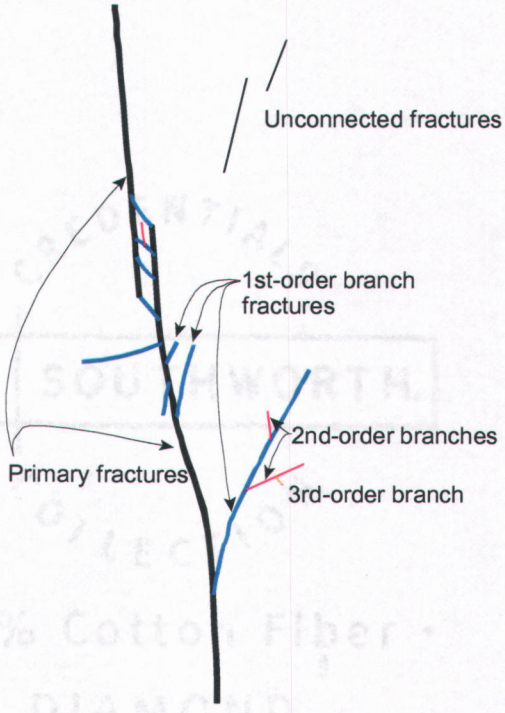

Figure 5-4. Definition of different orders of branch fractures, relative to primary fractures. Unconnected fractures which do not connect to the primary fractures, either directly or indirectly, are treated as a separate class of fractures.

dominant directions are evident in the rosette diagram, and are represented schematically by the fractures in the cartoon.

A peak in branch azimuths from N45W to N20W (branching angle -35 to -60 deg) can be explained in terms of pinnate fractures consistent with left-lateral slip along the primary fractures, and bridging fractures within duplexes (termed α and β fractures by Lin and Logan, 1991) . Some of these bridging fractures can be interpreted as R1 fractures in terms of the Riedel shear fracture array. These fractures are nearly parallel to the present-day direction of maximum compressive stress, and are hence are more likely to be dilatant than fractures in other orientations.

A second peak at N75W (branching angle +80 deg) is consistent with the expected orientation of R2 shear fractures in the Riedel array. On the map this orientation is exemplified by the second fracture zone which crosses the main structure around Y=5.2 m.

A peak at N35W to N50W (branching angle +35 to +50 deg) cannot be explained in terms of the Riedel array. In the map, many of these fractures appear to form bridges between the primary fractures and R2 fractures, or small breakouts between the primary fractures and pinnate fractures. Interpretation of these fractures in terms of the current stress regime is unclear.

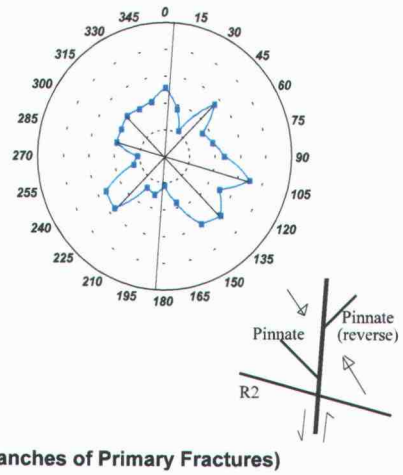

Figure 5-5a. Distribution of branch fracture azimuths, for first-order branches of the primary fractures in Äspö Map 1. Cartoon shows possible interpretations of the main peaks in frequency as pinnate fractures and conjugate faults, based on tentative interpretation of the main en échelon segments as part of a left-lateral fault band. Arrows show the approximate, present-day orientation of the principal compressive stress.

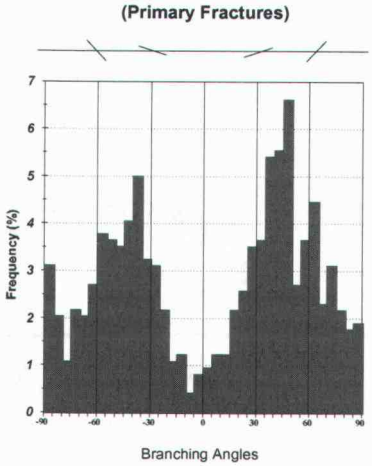

Figure 5-5b. Histogram of branch fracture frequency as a function of branching angle. Branching angle is defined as positive for branch fractures that bifurcate rightward, when viewed from the side of the main fracture opposite the branch fracture, and negative if the branch fracture bifurcates leftward. The angles represented in this plot are measured between the mean direction of the main fracture and the mean direction of the branch fracture.

Branched networks

Fractures that connect to the primary en échelon segments, either directly or indirectly via other fractures, account for 63% of the total trace length on the Äspö map. Statistical summaries of these fractures, as given in Tables 5-1 and 5-2, show how the number of branches and their total trace length varies as successively higher orders of branches are taken into account

Both the number of branches and the number of branches per unit length of the parent network decrease with the order of branches considered. Thus a higher density of branches is found along the primary fractures than along the first-order branches, and a progressively lesser density is found along the higher-order branches.

The average trace length of the branches also shows a slight decrease with increasing order. The net effect is a pronounced decrease with order, in the incremental fracture intensity that is associated with the branches of a given order.

The reduction of branching frequency with branch order may be partly an effect of the limited resolution of the maps. Since branches tend to be smaller than their parent fractures, and trace length tends to decrease with branch order, the effects of limited resolution will tend to be stronger for higher-order branches. However, in going from 1st order to 3rd order branches, the average branch length decreases only slightly if at all (only a 22% reduction in the case of the Äspö map, and an insignificant increase in the case of the Ekolsund maps) while the branching frequency decreases by 89% to 93%. This indicates that a large component of the observed reduction in branching frequency is real, rather than an artifact of the map resolution.

A speculative physical explanation for the reduction in branching frequency with order could be that the main locus of strain in this fault zone was along the primary en échelon segments, and that higher-order branches experienced successively lesser degrees of strain. Insofar as branch fractures provide a mechanism for accommodation of deformation, fewer would be induced by the smaller strains along the higher-order branches.

Table 5-1. Statistics of fracture trace networks formed by including progressively higher orders of branches, for the detailed fracture map from Äspö shown in Figure 5-2.

Order	Total Length (m)	Intensity (m/m^2)	Branches	Branching Frequency (per m)	Total length of branches (m)	Intensity (m/m^2)	Average length of branches (m)
1	20.37	1.123	740	36.3	48.19	2.656	0.065
2	68.56	3.779	516	7.53	31.29	1.725	0.061
3	99.85	5.504	242	2.42	12.35	0.679	0.051
N	133.90	7.381					

Table 5-2. Statistics of fracture trace networks formed by including progressively higher orders of branches, for the detailed fracture map from Ekolsund shown in Figure 5-3.

Order	Total Length (m)	Intensity (m/m^2)	Branches	Branching Frequency (per m)	Total length of branches (m)	Intensity (m/m^2)	Average length of branches (m)
1	24.46	0.31	182	7.44	59.64	0.76	0.33
2	84.10	1.07	174	2.07	62.66	0.80	0.36
3	146.76	1.87	119	0.81	41.58	0.53	0.35
4	188.34	2.40	61	0.32	27.79	0.35	0.16
N	232.85	2.97					

Branch fractures have the potential to affect solute transport through an en échelon zone by providing access to additional rock surface area for sorption, or more rock volume for matrix diffusion. Figures 5-6 shows rock volume (represented as area in the plane of the map) as a function of distance to the nearest fracture, for networks in which different orders of branch fractures are included, based on the Äspö map.

While only 20% of the rock within the Äspö map area is within 10 cm of one of the primary fractures, and less than 5% in the case of the Ekolsund map, 60% to 80% is within the same distance of the connected network formed by primary and higher-order branches of these fractures. As noted above, the branch fractures also increase the surface area over which water can come into contact with the rock, by nearly an order of magnitude.

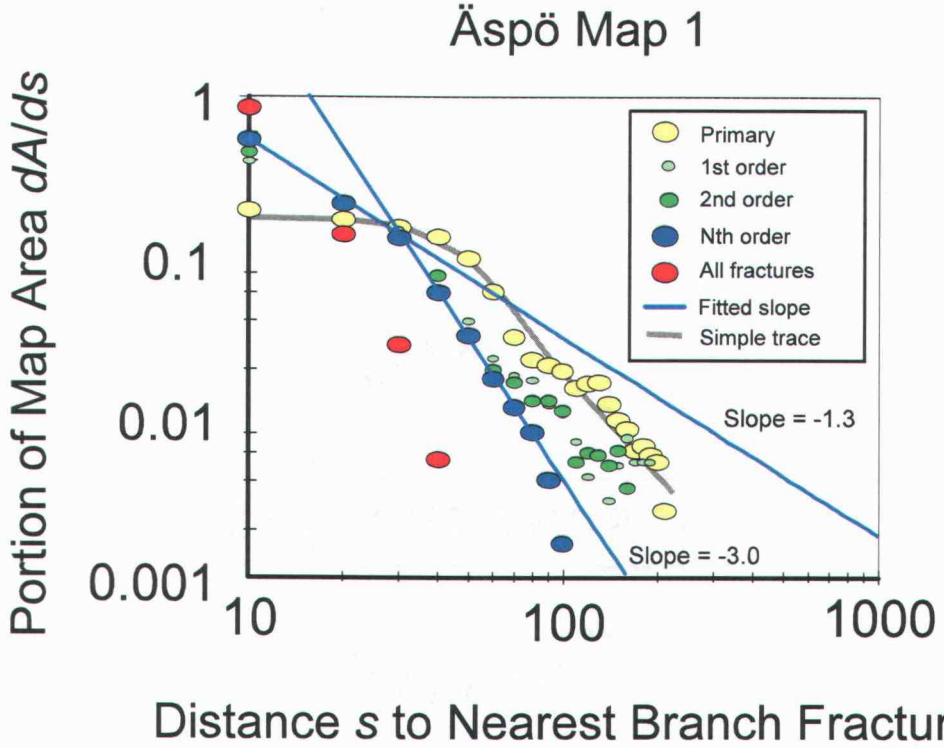

Figure 5-6. Variation of incremental map area $A_i'(s) = dA_i/ds$ as a fraction of the distance s to the nearest fracture on the Äspö en échelon zone map, for different orders i of branching structures Ψi. Yellow symbols are for the primary en échelon segments (Ψ_0) which show nearly constant $A_0'(s)$ up to about s = 50 cm, at which distance truncation effects are seen due to the finite map size (as shown by the gray line showing incremental area *vs.* distance to a single, simple trace). Green symbols show $A_i'(s)$ for the first- and second-order branching structures (Ψ_1 and Ψ_2). Blue symbols show $A_N'(s)$ for the entire branching structure (Ψ_N). A log-linear fit to the data for $s \leq 30$ cm yields a slope of -1.3. The data for $s > 30$ cm show a steeper slope, due to truncation effects by the finite map. Red symbols show $A'(s)$ for the set of all fractures on the map, including fractures that are not connected to Ψ_N.

When plotted on a log-log scale as here, the combined data for $A_N'(s)$ for the Ekolsund site (Figure 5-7) show a negative log-linear slope of –1.07 over the range 10 cm to 200 cm, above which scale the effects of the finite size of the map are seen. The individual exposures have less well-defined log slopes ranging from –1.93 to –0.83, indicating a potentially large variation of this measure between exposures.

The data for the single exposure in the Äspö map (Figure 5-6) do not show a well-defined log-slope for $A_N'(s)$, due at least in part to truncation effects which are evident from the $A_0'(s)$ for $s \geq 50$ cm. The data for $s \leq 30$ cm yield a log-slope of –1.3. The slope for larger distances time is steeper (–3.0) but this is likely affected by truncation effects. A log-linear regression over the range from 10 cm to 80 cm gives a slope of –2.07, but this yields a poor fit to the data.

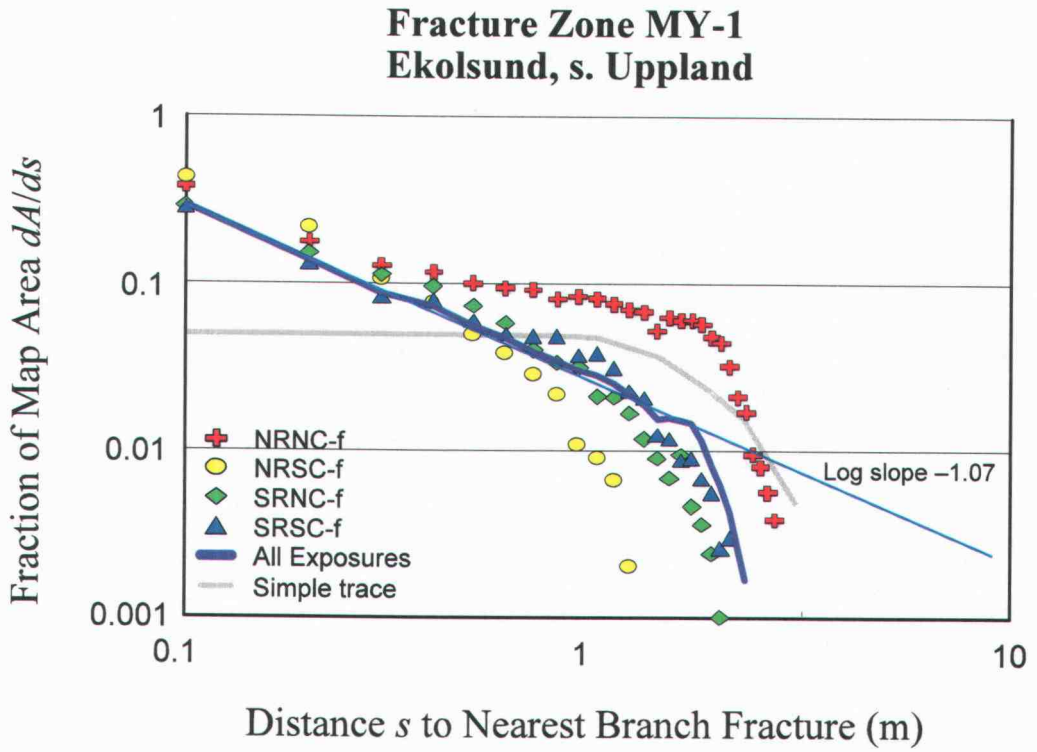

Figure 5-7. Variation of incremental map area $A_i'(s) = dA_i/ds$ as a fraction of the distance s to the nearest fracture on the Ekolsund maps. Each set of colored symbols (red, yellow, green and blue) represents $A_i'(s)$ for the entire branching structure (Ψ_N) on a given vertical exposure (NRNC = north roadway, north cut; NRSC = north roadway, south cut; SRNC = south roadway, north cut; SRSC = south roadway, north cut). The purple line gives the composite $A_i'(s)$ for all four exposures. A log-linear fit to the data for $s \leq 2$ m yields a slope of –1.07. The gray line shows incremental area *vs.* distance to a single, simple trace on each exposure. The distance at which this line deviates from a level line is the point at which map truncation effects begin to occur.

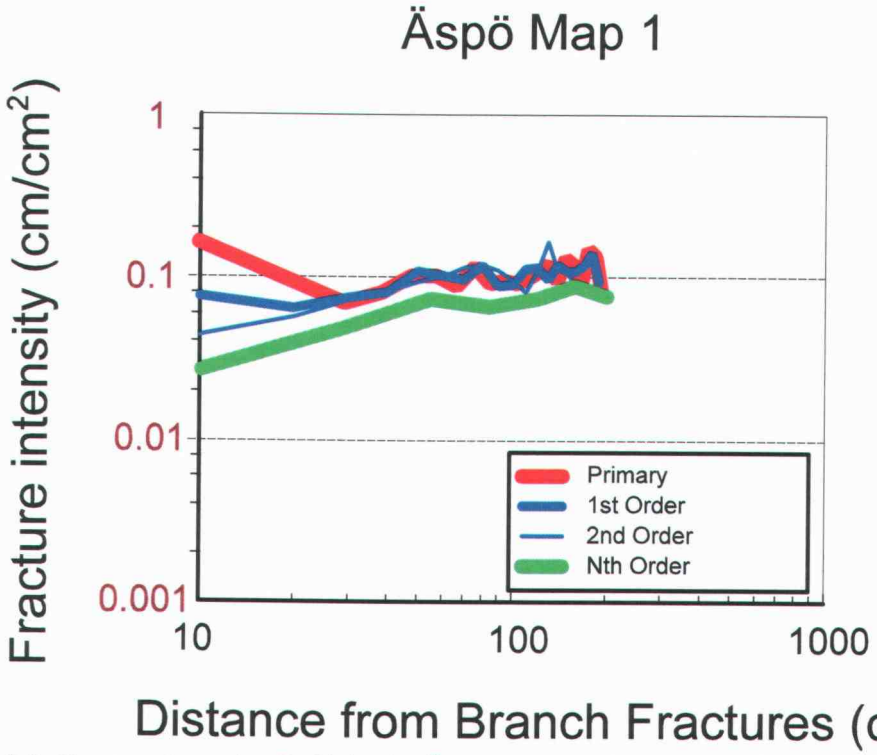

Figure 5-8. Fracture intensity $P_{21}(s)$ in the Äspö map as a function of distance s from the nearest point on a fracture belonging to branching structure of a given order (Ψ_0, Ψ_1, Ψ_2, and Ψ_N). The factor-of-two decrease of $P_{21}(s)$ in the range $s \leq 30$ cm for the primary fractures (Ψ_0) indicates a zone of elevated fracture intensity adjacent to these fractures, beyond which the fracture intensity increases slightly to background levels for s ≥60 cm. In contrast, $P_{21}(s)$ with respect to the entire branching structure Ψ_N shows a continuous, factor-of-three increase over the same range. The difference indicates a tendency of fractures in the vicinity of the structure to belong as a branch of the structure, while random (uncoordinated) fractures are more sparse.

A scaled exponential distribution arising from an exponential distribution of fragment size (derived in Appendix C) was also considered. However, this type of distribution gave very poor fits to the data from both sites, and is not further considered.

Fracture intensity in the damage zone

Analysis of neighboring fracture intensity as a function of distance from branch networks of different order (Figure 5-8) shows that the fractures that are close to the branch network tend to be a connected part of the structure. Fracture intensity at a distance of 10 cm from the primary fractures (shown as the "primary" curve in this plot) is elevated above background

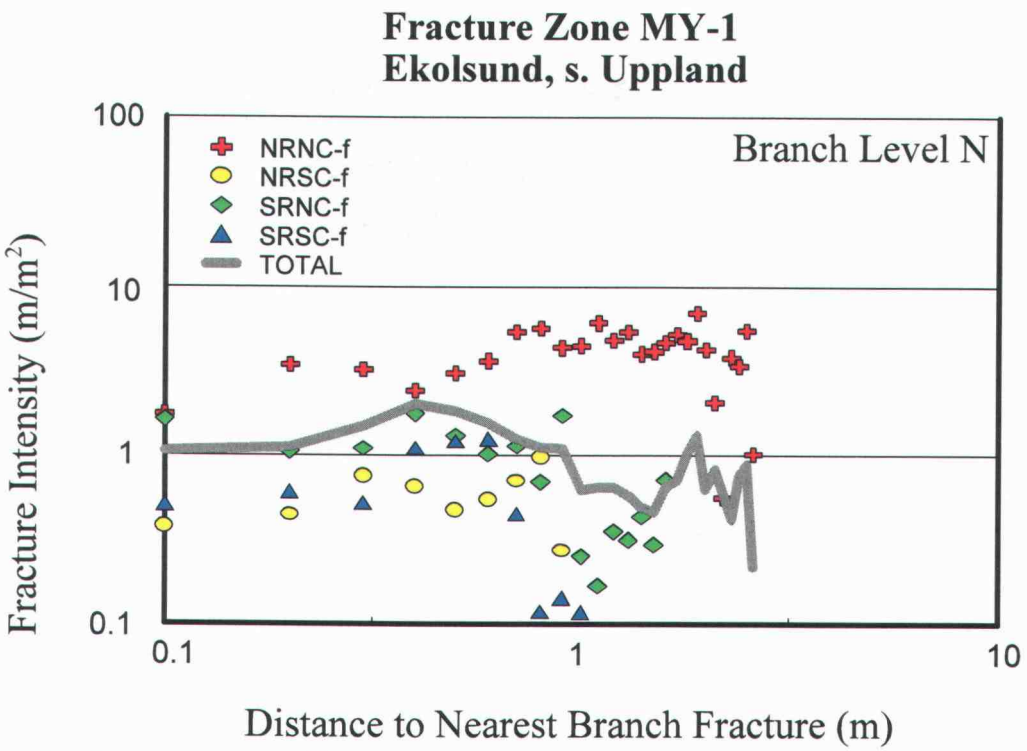

Figure 5-9. Fracture intensity $P_{21}(s)$ in the Ekolsund maps as functions of distance s from the nearest point on a fracture belonging to entire branching structures (Ψ_N). The general tendency seen is for $P_{21}(s)$ for fractures that do not belong to the structure to be decreased within the first 40-50 cm from the structure. Patterns at larger distances are irregular .

levels, by up to a factor of two. However, when branch fractures are included as part of the structure (as in the "Nth order" curve) the remaining fractures within a distance of 10 cm have a fracture intensity only about 1/3 of the background level.

Thus branch fractures account for a strong majority of the fractures in the rock adjacent to the primary fractures. Thus these fractures are more well-connected than would be the case in a randomly fractured medium. A model of fault zones that simply represents the damage zone as having an elevated intensity of random fractures would not represent this characteristic found in these examples.

5.4 Discussion

The results in Tables 5-1 and 5-2 illustrate the significance of branch fractures for solute retention, as they provide greater potential area for interchange of solute between the relatively mobile zone (fractures) and the relatively immobile zone (rock matrix). With the conventional assumption (*e.g.*, Neretnieks and Rasmuson, 1984) that flow wetted surface in a fracture zone is proportional to fracture intensity, the *N*th order branch network in these maps provide close to 7-10 times the wetted surface for interchange that is provided by the primary fractures alone.

The actual increase in area for interchange may depend on the nature and extent of the damage zones adjacent to the branches of different orders. If higher-order branches tend to have thinner damage zones than lower-order branches (as seems likely based on consideration of how fault zones are understood to develop, as reviewed in Chapter 2), the proportional contribution of wetted surface by the higher-order branches may be less. Differences in damage-zone thickness between higher-order and lower-order branches are at least partly accounted for in the foregoing analysis, since the branches of a given order N represent the macroscopic features of the damage zones for the branches of order $N-1$.

To understand the matrix diffusion properties of a medium with a penetration depth-area relationship as suggested by Figures 5-6 and 5-7, comparison can be made to an idealized assemblage of spherical particles with the same characteristics.

As derived in the Appendix D, an assemblage of particles that displays a log-linear distance-area relationship has a power-law size distribution of the form:

$$f(r) = Ar^{-D} \tag{5-4}$$

where A is a normalization constant and $p = 2\text{-}D$ (so $D = 2\text{-}p$), where p is the fitted log slope of the distance-area plot. Thus the geometric data obtained here, within the range of scales covered by the map, are approximately equivalent to an assemblage of spheres with this power-law distribution.

Whether or not this relation applies over a wider range of scales, it provides a conveniently simple model for discussing the expected consequences of the observed penetration depth-volume relationship in terms of matrix diffusion. The matrix-diffusion properties of a power-law particle-size distribution are discussed by Haggerty (2001) who

showed that this type of distribution leads to a power-law distribution of solute residence times:

$$g^*(t) \sim t^{1-k} \tag{5-5}$$

where $D = 2k - 3$, so $k = (D+3)/2$ and the term $1-k = -(D+1)/2$.

The Ekolsund data gave $p = -1.93$ to -0.83, with a combined-average value $p = -1.07$. The corresponding ranges are $D = 3.93$ to 2.83 and $1-k = -2.47$ to -1.92, with combined-average values $D = 3.07$ and $1-k = -2.04$. The Äspö data gave $p = -1.3$, with corresponding values $D = 3.3$ and $1-k = -2.15$. We note that the conversion here from p to D involves an extrapolation beyond the range of applicability of the fractal fragmentation model that was used to derive the relationship $D = 2-p$, which we will return to below.

In-situ experiments using non-sorbing tracers in a discrete structure in the Äspö Hard Rock Laboratory (Path I in the TRUE Block Scale experiments described by Winberg *et al.*, 2002) yielded log-linear late-time slopes of $1-k \approx -2.2$, based on graphical analysis of the published breakthrough curves (Figure 5-10). Thus these experiments yielded similar late-time slopes, to what could be expected based on the geometrical analysis described above. This experiment was conducted over a nominal transport distances of 14 m in a NW-trending structure, similar to the length of the en échelon zone map presented here, at a depth of about 350 m below the bedrock surface and a similar distance NW of the mapping location.

The late-time slopes in the TRUE Block Scale experiments were observed over time scales of $\tau = 20$ to 200 hours. The corresponding scale for diffusive transport can be estimated as $a = \sqrt{(\tau D_a)}$ where $D_a \approx 2\text{x}10^{-11}$ m/s^2 is a representative value for molecular diffusion in water. This yields a in the range of 0.12 to 0.4 cm, which is at most less than half the 1 cm resolution of the detailed maps. Thus application of these results to tracer breakthrough, on time scales of the TRUE experiments, requires an assumption that the hierarchical scaling of branch fractures on these maps persists to smaller scales, although possibly as little as an order of magnitude. Such scales should be practical for higher-resolution mapping over smaller portions of an en échelon zone than were mapped for this study.

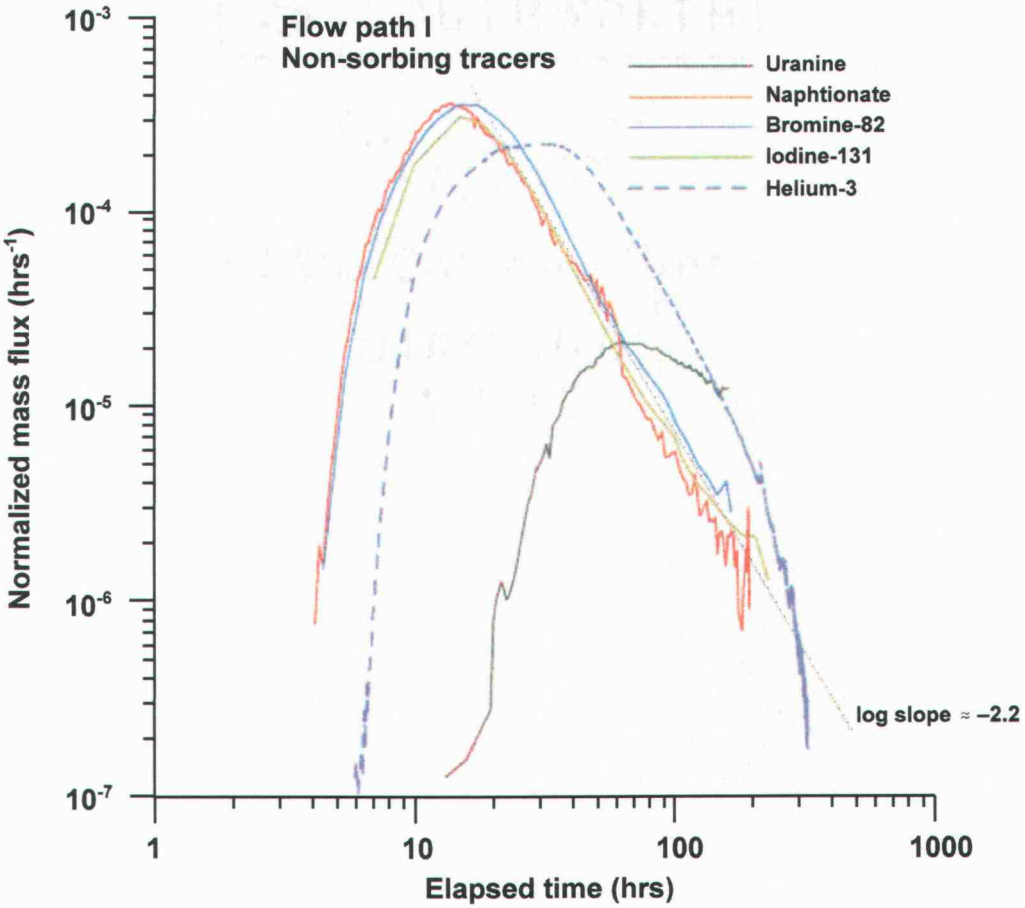

Figure 5-10. Normalized breakthrough curves for conservative tracers in Flow Path I during the TRUE Block Scale experiments in the Äspö Hard Rock Laboratory, showing graphical estimate of late-time log slope (modified from Winberg *et al.*, 2002).

The values of k extrapolated from analysis of the map in this study ($k = 2.92$ to 3.47) are very high relative to values that have been reported for fragmented materials. Turcotte (1986) reported a range $k = 0.72$ to 1.77 for a range of fragmented materials. Marone and Scholz (1989) found stable values of $D = 2.6 \pm 0.15$ for natural and synthetic fault gouges subjected to shear, corresponding to $k \sim 1.8$. Similar results were reported by Biegel *et al.* (1989).

The large discrepancy might be explained by the fact that the rock analyzed here is not completely fragmented into discrete particles, as in the media considered by those authors, but rather is cracked by a branched network of fractures. The "fragments" in this case are not completely bounded by the fractures. Consideration of the fractal cube model shows that D

values obtained by this extrapolation cannot correspond to a space-filling distribution of particles. The value of D obtained here is therefore to be considered as an abstraction, the physical implications of which need to be further explored by network models.

On the other hand, these results suggest that data such as from Path I in the TRUE Block Scale experiment are better explained in terms of branching network models than space-filling particle distributions.

5.5 Conclusions

The en échelon zones analyzed here display a hierarchical structure which is described in terms of branch networks of different orders. This characteristic is potentially important for solute transport because the higher-order branches potentially provide up to an order of magnitude more fracture interfacial area (depending on the nature of the damage zones adjacent to the different orders of branches). This means an increased area over which mass transfer can take place between mobile water moving through the primary fractures, and the relatively immobile water in the rock matrix.

The hierarchical pattern of splays in the damage zone implies a systematic, possibly power-law increase in the amount of pore volume that solute can access by diffusive mass transfer, with increasing distance from the fault core. The incremental matrix area versus distance from fractures belonging to these hierarchical structures is approximately log-linear over length scales of up to 30 to 50 cm (depending on the truncation limit of the maps). The log-linear slopes are in the range –1.93 to –0.83, with best estimates of –1.07 and –1.3 for the Ekolsund and Äspö data, respectively. These correspond to fractal block-size distribution with dimensions $D = 3.07$ and 3.3, respectively, by extrapolation from a fractal fragmentation model given in Appendix D.

This extrapolation leads to predicted late-time log slopes in solute breakthrough curves of –2.04 and –2.15, which compare well to observed late-time slopes of –2.22 in in-situ tracer experiments in a single NW-trending structure over a similar scale at the Äspö site. This extrapolation goes beyond the range of applicability of fractal fragmentation model. We suggest this may be understood in terms of the rock around this structure being a partially cracked solid, rather than a fragmented medium.

These aspects of en échelon zone architecture suggest a need for more complex representation in hydrologic models, than as simple, planar conductors with or without heterogeneous properties, or as zones of increased but unstructured fracturing. These implications are evaluated by numerical modeling in a companion paper (Chapter 6).

6. Role of Secondary Fractures for Solute Transport in en Échelon Fault Zones

Abstract

Solute transport in hierarchical fracture networks associated with en échelon structures is investigated using a numerical model for network flow and advective-diffusive transport. Results are presented for cases that account for diffusion into both stagnant branch fractures and macroscopically unfractured matrix. Cases that are analyzed include both a deterministic geometry taken directly from a detailed fracture map from a site in southern Sweden, and a synthetic geometry based on statistics of maps.

For both cases, diffusion into stagnant branches increases retardation of solute, relative to simple advective-diffusive transport through the main en échelon segments in the absence of matrix diffusion. The retardation is less than for an equivalent two-domain model with equilibrium mass transfer between flowing and stagnant domains. Branch fractures thus may act as an additional type of immobile domain, beyond other hypothesized types of domains such as stagnant pools in channelized fractures or stagnant zones in gouge.

In cases with uniform fracture properties, stagnant branches increase the retardation of solute due to matrix diffusion, and the degree of late-time tailing. However, matrix diffusion is the dominant effect in terms of median arrival times for solute mass, for conditions representative of a repository in granitic rock. When fracture properties are heterogeneous, branch fractures can in some cases yield slightly lower net retardation when combined with matrix diffusion. This surprising result is interpreted as due to the interaction of flow-field heterogeneity and through-diffusion across fracture blocks. Where through-diffusion occurs, in some instances branch fractures may act as relatively rapid paths for solute to return to the flowing fractures.

From a practical standpoint in the context of a radioactive-waste repository, these results suggest that secondary fractures in en échelon structures are of net benefit in terms of radionuclide retention, but not sufficiently so to mitigate the otherwise poor retention characteristics of these structures. The effect of branch fractures on tailing of breakthrough curves may be important to recognize in analysis of in-situ tracer experiments, to avoid incorrect assessment of parameters for matrix diffusion models that will be applied over longer time scales.

6.1 Introduction

Groundwater flow in granitic rock is typically restricted to discrete fractures and fault zones. The flow and transport properties of these features are of concern, given proposals in several countries to build high-level radioactive-waste repositories in granitic rock (McCombie, 1997).

A generally understood principle of repository design in granitic rock is to avoid the fault zones on the larger scales likely to be encountered at a site (1 km to 10 km), which are likely to carry relatively high flows and to pose engineering difficulties for the underground construction process. The largest such zones are usually detectable by geophysical methods and borehole investigations, and hence they can usually be accounted for in the design process. However, blocks between such zones are commonly found to contain lesser-order fault zones, which are more difficult to detect prior to underground investigations, and which may therefore need to be accounted for in repository designs.

In this paper we consider the transport properties of a particular type of fault zone, which consists of discrete fractures arranged en échelon with linking fractures at stepovers. En échelon zones are of interest as one of the main types of hydraulically transmissive features that might be expected in a rock volume considered for a repository.

Field investigations (Martel *et al.*, 1988) indicate that en échelon zones represent an early stage of fault zone development, for low degrees of regional strain. Such a situation may be expected for rock volumes which are bounded by larger-scale fault zones that accommodate the major portion of regional strain. Thus en échelon zones are expected in volumes of sparsely fractured rock with a low degree of brittle deformation, which are sought as repository locations.

Field investigations at granitic sites in Sweden, including the present study, confirm that en échelon zones are found in rock volumes bounded by fault zones with more extensive brittle deformation, and that these en échelon zones can be traced over distances of up to tens of meters. Some of these zones are aligned nearly normal to the minimum principal compressive stress, and are hence likely to be transmissive in the present time.

En échelon zones may also have a relatively low potential for retardation of radionuclides leaking from a repository, in comparison with more extensively sheared fault zones. Matrix diffusion is the most significant mechanism for retention of radionuclides

leaking from a repository in granitic rock (Jakob, 2004), and is controlled by the interfacial area. In comparison with zones of more extensive brittle deformation, en échelon zones have relatively small interfacial area for matrix diffusion over most of their length (*i.e.* within the discrete en échelon segments).

However, detailed mapping of en échelon zones (Chapter 4) reveals a large number of small secondary fractures branching from the main en échelon segments, as well as intense fracturing within stepover zones. This is also predicted by theoretical models of compressive shear fault development (*e.g.*, Schulson *et al.*, 1999). These secondary fractures provide additional interfacial area via which diffusion into the matrix can take place. In this paper we explore the quantitative significance of secondary fractures for increasing the degree of radionuclide retardation along en échelon zones.

6.2. Method

To evaluate the potential effects of secondary fractures on solute transport through en échelon zones, we simulate flow and transport through deterministic and statistical, two-dimensional models. Steady-state flow through the models is computed by the finite-element method. Solute transport, including diffusion into stagnant branches and/or the rock matrix, is modeled by an advective-diffusive particle tracking algorithm described below. Comparison of cases with and without diffusion into stagnant secondary fractures, and cases with and without matrix diffusion, are used to evaluate the relative significance of these phenomena, as well as their combined effects.

Deterministic and statistical models of en échelon zones

The deterministic and statistical models are both based on detailed mapping of en échelon structures in granitic sites. The deterministic 2-D models are produced directly from a detailed map of an en échelon zone at the Äspö site in SE Sweden, as described by Geier *et al.* (2004). The statistical models were based on statistics from the Äspö site maps.

The deterministic model based on the Äspö map reproduces a 15 m long portion of a N-striking en échelon zone, in horizontal section. The map is adapted for numerical simulations (to simplify calculations of matrix diffusion) by conversion to a network of rectilinear segments (Figure 6-1). The model thus obtained has the advantage of not being filtered by any particular statistical model, and preserving details of architecture which may be overlooked in formulating a conceptual model for such zones.

The deterministic model has two main drawbacks for understanding the large-scale behavior of single en échelon zones. First it spans scales of only 15 m, and includes only a few stepovers, so does not represent averaging effects over longer transport distances involving multiple stepovers. Second, interpretation of the model results is complicated by the particular features such as the intersection with an ENE-striking feature of comparable order (between $y = 5$ m and $y = 6$ m in Figure 6-1). A model that represents a single en échelon zone in isolation, and at a higher level of abstraction, may be helpful for clarification of the main effects.

A statistical model was therefore constructed by statistical simulation of a 40 m long

en échelon zone based on analysis of branching and stepover statistics from the Äspö site, including observations from the zone mapped in detail as well as similar structures in the vicinity. Key components of the model which are described in terms of probability distributions include: length of en échelon segments, the length of the stepovers, block size distribution within stepovers, and frequency and length of branch fractures of different orders (using the definition of branch order given in Section 3.2).

Outcrop mapping does not yield data on hydrologic properties (transmissivity or effective transport aperture). While apertures could be observed in a few of the fractures, here we take the view that apertures measured under stress-relieved and weathered conditions on bedrock outcrops are not a reliable indicator of apertures at depth. Instead, representative transmissivity values are chosen based on previous analyses of borehole data from Äspö (Geier *et al.*, 1995; Geier and Thomas 1996).

Uniform transmissivities are used for a given order of fractures. Field evidence suggests that the most realistic model would be one that includes variability of transmissivity both between and within individual fractures. However, variable-transmissivity models add additional degrees of complexity and uncertainty in the parameters, apart from the geometric properties which are the main focus of this study. Therefore we use a simplified representation of transmissivity in these models, recognizing that this is an idealization the implications of which could be explored through further analysis.

Effective apertures for transport are also assigned based on uniform, representative values for a given class of fractures. As with transmissivity, effective transport aperture are likely to be variable. The nature of this variation under in situ conditions is poorly known, due to the difficulty of performing in situ transport experiments with unequivocal interpretations. For the present study, representative values were chosen based on results of past investigations of single-fracture transport properties in similar geologic settings, as reviewed in Chapter 2.

The statistical distributions used to generate the network models are summarized in Table 6-1. Examples of stochastic realizations are shown in Figure 6-2, which may be compared with the actual outcrop map in Figure 6-1.

The simulated en échelon zone in Figure 6-2 is an abstraction in several respects. A rectilinear configuration of segments is used to simplify the problem of computing fracture intersections, and to reduce the chance of the numerical difficulties in the flow and solute

transport computations due to an ill-conditioned finite-element mesh. The complex architecture of fracturing within the stepovers between en échelon segments is idealized as a simple, hierarchical fragmentation process. Intersecting fracture zones such as those seen on the outcrop are excluded, to focus on the transport properties of a single en échelon zone.

Despite these idealizations, the models reproduce approximately the geometric properties observed on the outcrop that were anticipated to be key for transport, as discussed in the foregoing paper. These aspects are (1) the length distribution of the main en échelon segments, (2) the frequency of branching secondary fractures (such as splays or pinnate fractures) of various orders, (3) the length distributions for different orders of branches, and (4) the block size distribution and fracture intensity within the stepovers between en échelon segments.

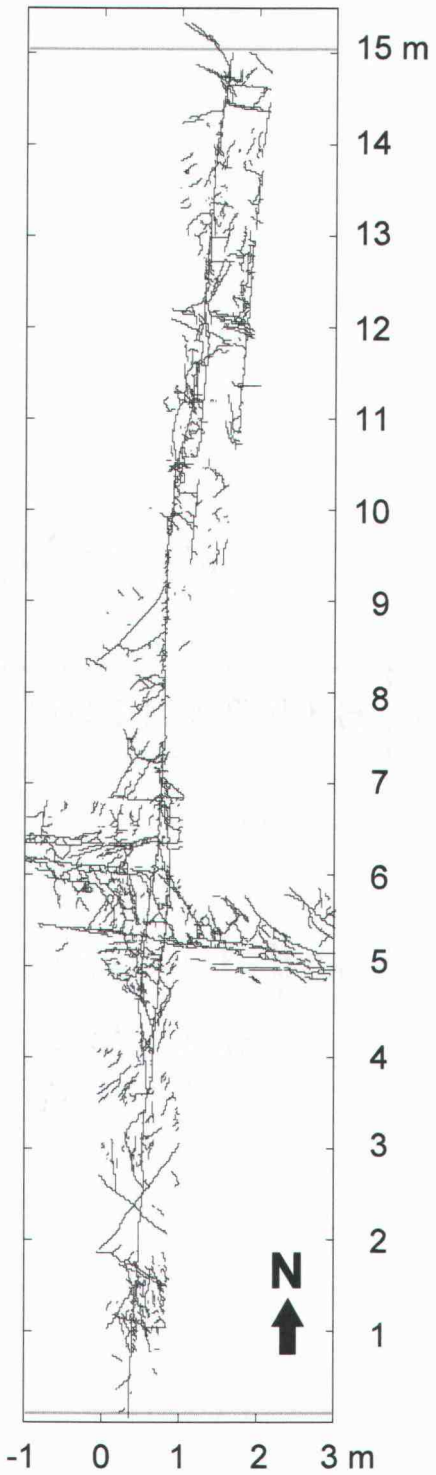

Figure 6-1 Rectilinear network model for flow and transport simulations, based on detailed en échelon zone map from Äspö site, using a discretization level of 2 cm.

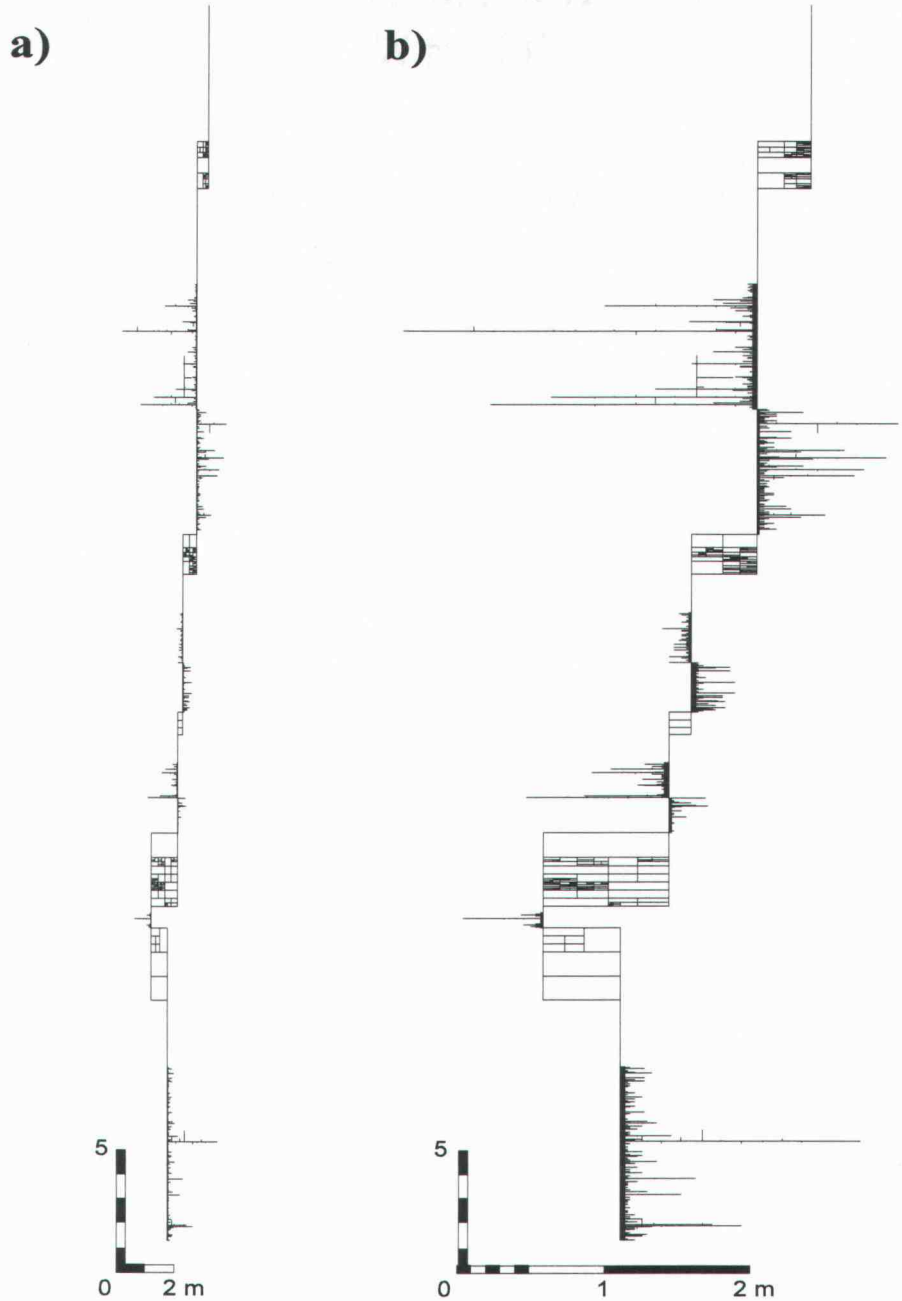

Figure 6-2. A single realization of a 40 m long section of en échelon zone simulated based on a rectilinear statistical model (revised version)for stepovers and branch fractures in en échelon zones on Äspö, shown (a) with equal scales in horizontal (E-W) and vertical (N-S) directions, and (b) with horizontal (E-W) scale exaggerated by a factor of 5 to show frequency of small wing/pinnate fractures.

Table 6-1: Parameters and statistical models for en échelon fracture zones

1. Deterministic model:		
Segment transmissivity T_{seg}		$1x10^{-7}$ m^2/s
Segment transport aperture b_{seg}		0.5 mm
2. Stochastic geometric model		
Length of en échelon segments L_0:		U[5 m, 15 m]
Length of en échelon segment overlaps (stepovers):		U[0.5m, 2.5 m]
Aspect ratio of stepovers:		U[3,5]
Sense of step-overs:		P[right-stepping] = 0.8;
		P[left-stepping] = 0.2
Branch fracture frequency f_i (I = order of branch):	f_1	36.3 per m
	f_2	7.53 per m
	f_3	2.42 per m
Branch length distribution L_i (I = order of branch):	L_1	P_L(2.75,0.02 m)
	L_2	P_L(2.55,0.02 m)
	L_3	P_L(2.75,0.02 m)
Stepover fragmentation fractal dimension	D_f = 1.5	
Transmissivity (heterogeneous case)	T_0	$1x10^{-7}$ m^2/s
(T_i, I = order of branch)	T_1	$2x10^{-8}$ m^2/s
	T_2	$1x10^{-8}$ m^2/s
	T_3	$1x10^{-9}$ m^2/s
Transmissivity (uniform case)	T_i	$1x10^{-7}$ m^2/s
Transport aperture (heterogeneous case)		b_0 0.5 mm
	b_1	0.2 mm
	b_2	0.1 mm
	b_3	0.05 mm
Transport aperture (uniform case)	b_i	0.5 mm

$U[x_{min}, x_{max}]$ = uniform distribution of the parameter x in the range $x_{min} \le x \le x_{max}$

$P_L[D, x_{min}]$ = power-law distribution of the parameter x with exponent D and minimum value x_{min}.

Simulation of groundwater flow

Steady-state flow of groundwater through the en échelon-zone models is calculated using the *dfm* finite-element code as described by Geier (2004). The steady-state flow is a function of the fracture transmissivities and the imposed head gradient between the end points along strike.

Values of transmissivity are assigned choosing representative values of single-fracture transmissivity based on past analyses of hydraulic test data at Äspö (Geier *et al.* 1995; Geier and Thomas 1996). For the deterministic case, the same uniform value was assigned to all fracture segments. For the synthetic model, two separate cases were used, one with uniform hydraulic properties and the other with heterogeneous properties (values depending on the order of branch fractures in the model).

A hydraulic gradient of 0.025 was imposed by assigning a head differential of 0.375 m across the 15-m length of the Äspö map. A 1 m head differential was applied to the 40 m long synthetic model, to give the same hydraulic gradient for all cases. A hydraulic gradient of 0.025 is at the high end of the range of gradients that can reasonably be expected for a repository in granitic rock in Sweden (Dverstorp *et al.*, 1996).

Gradients of this magnitude are of practical concern for a high-level radioactive-waste repository in granitic rock. In low-relief regions of granitic bedrock such as southern Sweden, head differentials on the order of 1 m over a 40 m scale are most likely to occur in relatively "good" rock which has low fracture intensity and low effective hydraulic conductivity. Current repository siting concepts for granitic rocks favor locating radioactive wastes in such blocks (*e.g.*, SKB, 1999). In such a block, an en échelon zone consisting of a small number of favorably connected fractures could act as a discrete flow path through an otherwise low-conductivity block of rock.

The variation of hydraulic head and groundwater flow rates in the deterministic network and in the synthetic network model are illustrated in Figures 6-3 and 6-4, respectively. The synthetic zone carries a groundwater flow per 1 m thickness (in the vertical direction) of 5.3×10^{-10} m^3/s (1.92 ml/hr or 16.8 liters per year). The corresponding advective velocity in the main en échelon segments, for an assumed mean aperture of 0.2 mm, is 2.7×10^{-6} m/s (9.6 mm/hr or 84 m/yr). The mean advective velocity along the entire zone, based on the median water-residence time determined by advective-diffusive particle tracking, is 1.95×10^{-6}

m/s (7.0 mm/hr or 61 m/yr). The mean velocity is lower than the velocity within the main en échelon segments, due to slower passage through the stepover zones, where the high fracture intensity implies larger pore volumes per unit distance along strike.

The mean velocity of 61 m/yr is on the high end of what is typically considered a reasonable range for repository conditions, but probably on the low end for in-situ tracer tests.

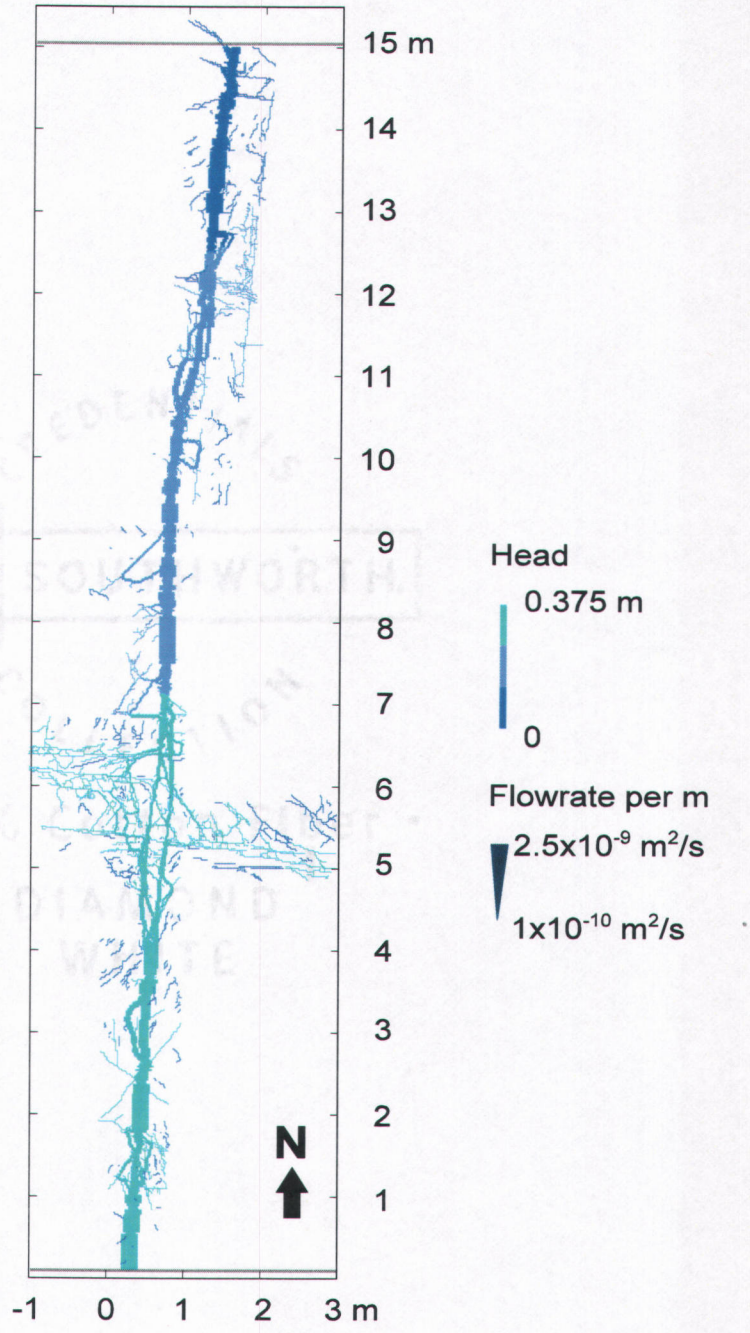

Figure 6-3. Head and flow field calculated for 2-D fracture network defined by Äspö en échelon zone map, for 1 m gradient applied south to north. Head in fractures is indicated by color scale. Flow rate is proportional to line width (except for stagnant fractures which are represented by the narrowest lines). A digital version of this plot which can be viewed at higher resolution is provided in the electronic supplement.

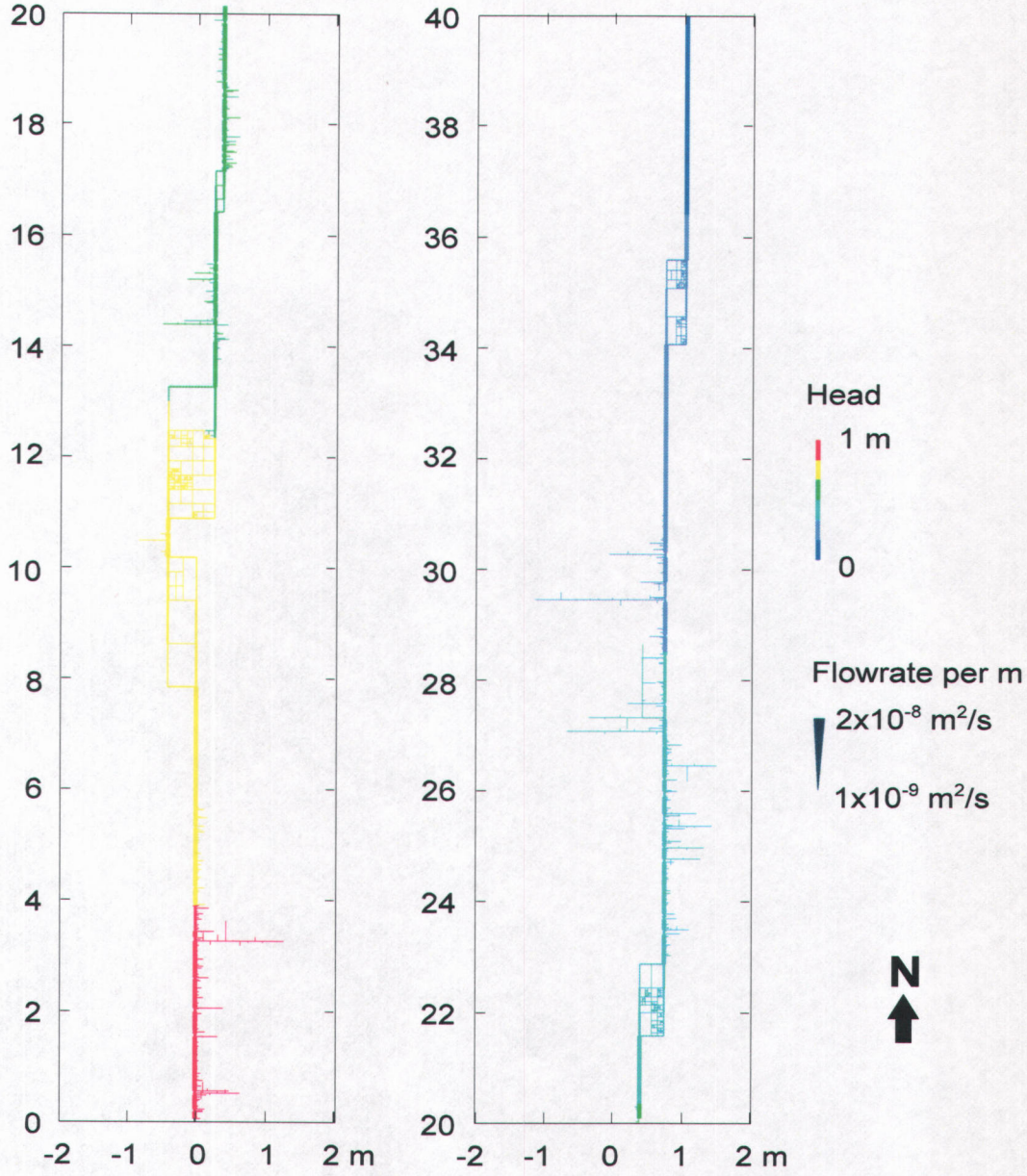

Figure 6-4. Head and flow field calculated for 2-D synthetic en échelon zone, for 1 m gradient applied south to north. Head in fractures is indicated by color scale. Flow rate is proportional to line width (except for stagnant fractures which are represented by the narrowest lines). Note the plot has been split into two sections to allow plotting at a larger scale on the page. A digital version of this plot which can be viewed at higher resolution is provided in the electronic supplement.

Simulation of advective-diffusive transport in fracture segments

Transport of solute through the fracture network and in the adjoining rock (matrix) is simulated by an advective-diffusive particle-tracking method. The method for tracking particles through fracture intersections is inspired by the conceptualization of Park *et al.* (1999), but the algorithm used here permits diffusion into stagnant branches. The following is a brief summary; full details of the method are given in Chapter 3.

Within a given 1-D fracture segment, advective-dispersive transport is modeled by a discrete-parcel random walk algorithm (Ahlstrom *et al.*, 1977), following the suggestion of Detwiler *et al.* (2000) and Bruderer and Bernabé (2001) to account for Taylor dispersion resulting from diffusion in combination with velocity variations across the aperture, by tracking particles in this dimension (here denoted z).

Each discrete parcel or "particle" represents a fixed mass m_p of solute, which moves through the network and/or matrix as a random walk. A particle's displacement during a single step of the random walk, representing a small time interval Δt, is the sum of a random, diffusive component $(\Delta x_d, \Delta z_d)$ and an advective component Δx_a which is equal to Δt times the average velocity over the diffusive trajectory during the time interval, taking into account possible "bounces" off the fracture wall as described below.

If the Δz_d component is large enough to cause the particle to move beyond the boundaries of the fracture segment (*i.e.* the fracture walls), the particle may either enter the adjoining matrix with probability P_m, or else "bounce" off the fracture wall with reflected motion. The local velocity $v(z)$ at a given height z above the median surface within a given fracture segment is assumed to follow the parabolic velocity profile for Poiseuille flow with no-slip conditions at the fracture walls:

$$v(z) = \frac{Q}{b}\left[\frac{3}{2} - \frac{6z^2}{b^2}\right] \tag{6-1}$$

where Q is the flow through the fracture segment per unit thickness (obtained from the finite-element solution) and b is the local value of fracture aperture.

Routing and mixing of solute at junctions between fracture segments

Routing of solute at junctions between fracture segments is modeled by an explicit algorithm for diffusion across streamlines within the junctions, with the simplifying assumption of an idealized junction geometry as suggested by Park and Lee (1999).

Models of solute transport in fracture networks have commonly been based on either of two end-member assumptions for routing of solute at intersections: streamline routing with no mixing across streamlines or complete mixing. Detailed modeling of flow and transport through fracture intersections (Berkowitz *et al.*, 1994; Park *et al.*, 2001) has shown that the degree of mixing is related to the Peclet number $Pe = av/D_m$ where v is the fluid velocity and a is a characteristic length for the intersection. For high Pe the rate of diffusion across streamlines is small relative to the advective velocity, and streamline routing may be a better approximation. For low Pe the rate of diffusive transport across streamlines is large relative to the rate of advection, and complete mixing may be a good approximation. At intermediate values of Pe, intermediate forms of routing may occur. Thus for a fixed geometry, the degree of mixing for flow through the intersection varies with the fluid velocity.

We consider partitioning of solute at junctions with three, four, or more branches. For brevity, we use the notation J_I to denote the class of junctions with I branches, so a J_3 junction has three branches, a J_4 junction has four branches, *etc.*

If one fracture terminates at its intersection against another fracture (a common case in natural fracture networks as pointed out by Dershowitz 1984), the junction is of type J_3. The distinction between streamline-routing and complete-mixing rules is irrelevant for a J_3 junction, if all three branches are non-stagnant and if the branches are longer than mixing length L_{mixing} at which fully mixing across the aperture can be assumed. Either the solute flux from one well-mixed inlet branch is divided according to the flow ratio between two outlet branches, or the solute fluxes from two inlet branches are combined in one outlet branch, and become well-mixed at distance L_{mixing} along that branch. However, when one branch of a J_3 junction is stagnant, solute enters and exits that branch only by diffusion, and this process must be accounted for in the mixing rule for the junction.

A J_4 junction results whenever two fractures intersect each other and both fractures are through-going. Junctions of higher order (J_5, J_6, *etc.*) require a larger number of fractures to share a common intersection, but are occasionally found in nature as well as in synthetic,

stochastically generated fracture networks.

When all branches of a J_4 or higher-order junction are non-stagnant, the entry and exit points of streamlines from a junction can be defined by considering the branches in cyclic order (either clockwise or counterclockwise). Topological constraints in a two-dimensional network model, where flow is driven by potential gradients, ensure that all branches of a junction with positive inflow lie to one side of all branches with positive outflow, when the branches are placed thus in cyclic order (Bruderer and Bernabé, 2001). Finding the inlet and outlet streamline locations is then straightforward: starting from a neighboring pair of inlet and outlet branches, the streamlines must pass through points that bound an equal fraction of the inflow and outflow.

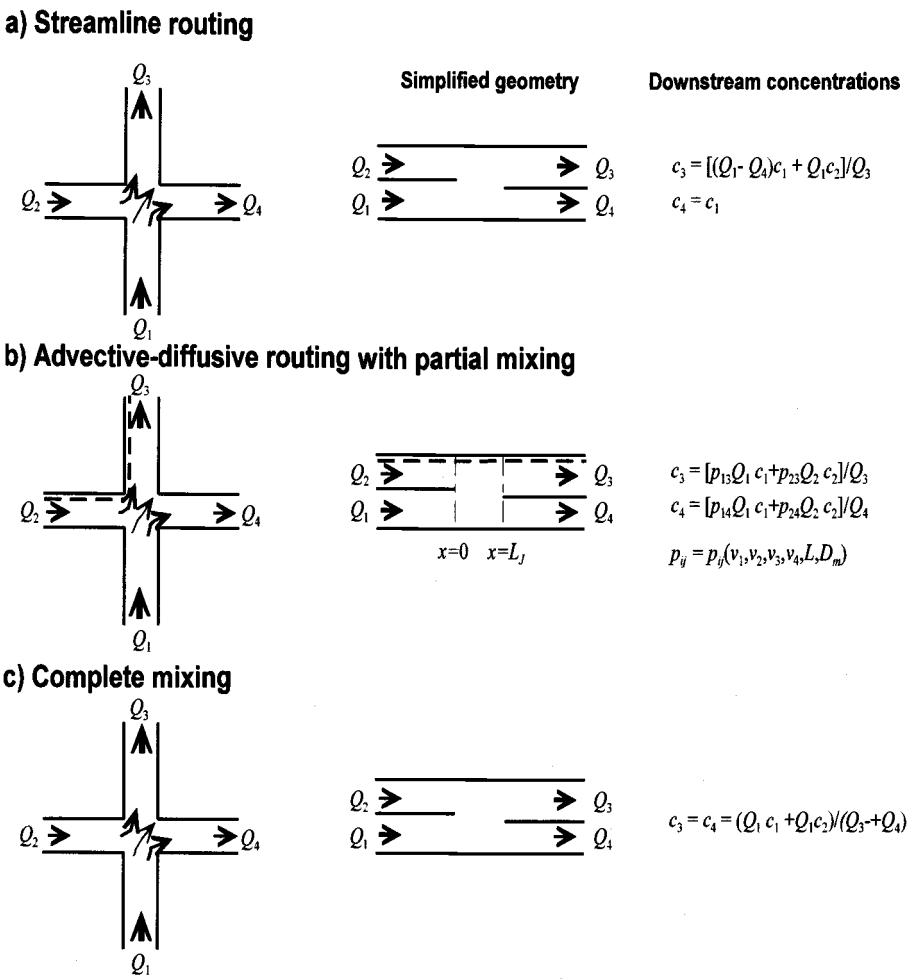

Figure 6-5. Alternative rules for routing of solute at four-branch junctions in a 2-D fracture network.

The position of the streamlines within the intersection are needed in order to model solute transfer due to diffusion across streamlines within the junctions. In detailed studies of individual junctions this problem has been addressed by numerical solution of the Navier-Stokes equation (Berkowitz *et al.*, 1994) or lattice-gas simulation (Stockman *et al.* 1997), but such detailed sub-models are not practical for the network-scale problems we address here.

Park and Lee (1999) proposed modeling advective-diffusive transport through junctions based on a simplified, "folded-up" geometry, as depicted in the right-hand side of Figure 6-4. Park and Lee gave analytical solutions for the probabilities p_{ij} for a particle to pass from inlet branch I to outlet branch j, as functions of the inlet/outlet flow rates and velocities J_4. These solutions are singular for the case of stagnant branches, so not applicable for the general case we consider, but they are useful for verifying the particle-tracking algorithm for non-stagnant cases.

Here we follow the conceptual approach of Park & Lee (1999) by modeling transport through an idealized junction of simplified geometry, but in place of their analytical solutions we use explicit advective-diffusive particle-tracking through the simplified junctions, in order to address the additional complication of diffusion into and out of stagnant branches.

Representation of stagnant branches

We represent the interface between a stagnant branch and a junction as an interface of infinitesimal thickness, with position depending on the cyclic position of the stagnant branch relative to the flowing branches (Figure 6-6a through 6-6d). In a real junction, the mouth of each stagnant branch is a zone of interaction with flowing water. Diffusive transfer takes place across some curved surface which spans the aperture of the stagnant branch. For a viscous fluid and laminar-regime flow, in reality this is a gradational rather than distinct interface. As a key approximation in our idealized model for junctions with stagnant branches, we idealize this zone of interaction as an abrupt interface, with length equal to the aperture of the stagnant branch.

If the trajectory of a solute particle undergoing advective-diffusive motion in the flowing part of the junction happens to intersect this interface, the particle enters the corresponding stagnant branch with residual motion equal to the residual component of transverse diffusion.

Within the stagnant branch, the particle is postulated to move by purely diffusive motion as described above until it either interacts with the matrix or returns to the mouth of the stagnant branch. In the latter case, the particle will re-enter the flowing portion of the junction, via the same interface but in the reverse direction. The coordinates of the particle as it re-enters the junction are obtained by mapping its position within the stagnant-branch aperture onto the corresponding position on the interface representing the branch in the idealized junction.

Simulation of diffusive transport in the matrix

An explicit particle-tracking algorithm is used to represent diffusion in the matrix. More efficient methods of simulating matrix diffusion with particle-trackers have been presented, for example, by Dershowitz and Miller (1995), Delay and Bodin (2001), and Tsang and Tsang (2001). All of these make use of idealizations regarding the geometry and extent of the matrix volume into which solute diffuses, and assume that solute eventually returns to the same fracture from which it enters the matrix. Delay and Bodin (2001) also note that their method is singular for the case of stagnant fluid in the fracture.

Here we use an computationally expensive but explicit method, which accounts for both the finite depth of matrix available for diffusion (depending on fragment size), and the possibility that solute may diffuse from one fracture to another. For the results presented here, over 10% of solute diffusing into the matrix from a given fracture was found to re-emerge in a different fracture. This indicates that transfer of mass by diffusion between fractures may be significant for the network geometries and time scales considered here.

The probability P_m of a particle entering the matrix pore space on a given collision with a fracture wall is assumed to be equal to the local matrix porosity θ_m. Matrix porosity is assumed to be uniform and isotropic. This idealization is adopted in order to focus on the role of en échelon zone and secondary fracture geometry, as the main topic of investigation for this study. Experimental data exist to support more heterogeneous models of matrix porosity (Xu *et al.*, 2001) which could be considered with minor modifications of the algorithm.

Transport for particles in the matrix is simulated in the same way as transport in the fracture, except that random diffusive motions are proportional to the square root of effective matrix diffusivity D_p, rather than of the molecular diffusion coefficient D_m. Advection in the

matrix is assumed to be negligible, so only the diffusive component of particle motion is modeled. In the type of rocks considered here, the hydraulic conductivity of macroscopically unfractured matrix is on the order of 10^{-13} m/s, and due to the well-connected nature of the en échelon fracture system, local hydraulic gradients are on the order of 1 or less. For a matrix porosity $\theta_m = 0.005$ as used here, this implies advective velocities through the matrix on the order of $2x10^{-11}$ m/s, as compared with advective velocities on the order of 10^{-6} m/s in the fractures.

At each time step for a particle in the matrix, a check is made of whether the particle motion intersects the wall of any fracture segment. If so the particle motion through the matrix is truncated at the fracture wall, and the particle moves into the fracture segment. This segment need not belong to the same fracture or fracture segment from which the particle initially entered the matrix.

Thus the method explicitly accounts for the variable, finite size of matrix blocks within the en échelon zone, and allows through-diffusion of particles from one fracture to another, even if the fractures are not directly connected. This contrasts with algorithms of Dershowitz and Miller (1995) and of Tsang & Tsang (2001) which treat diffusion as an effectively 1-D process out of and back into a single given fracture.

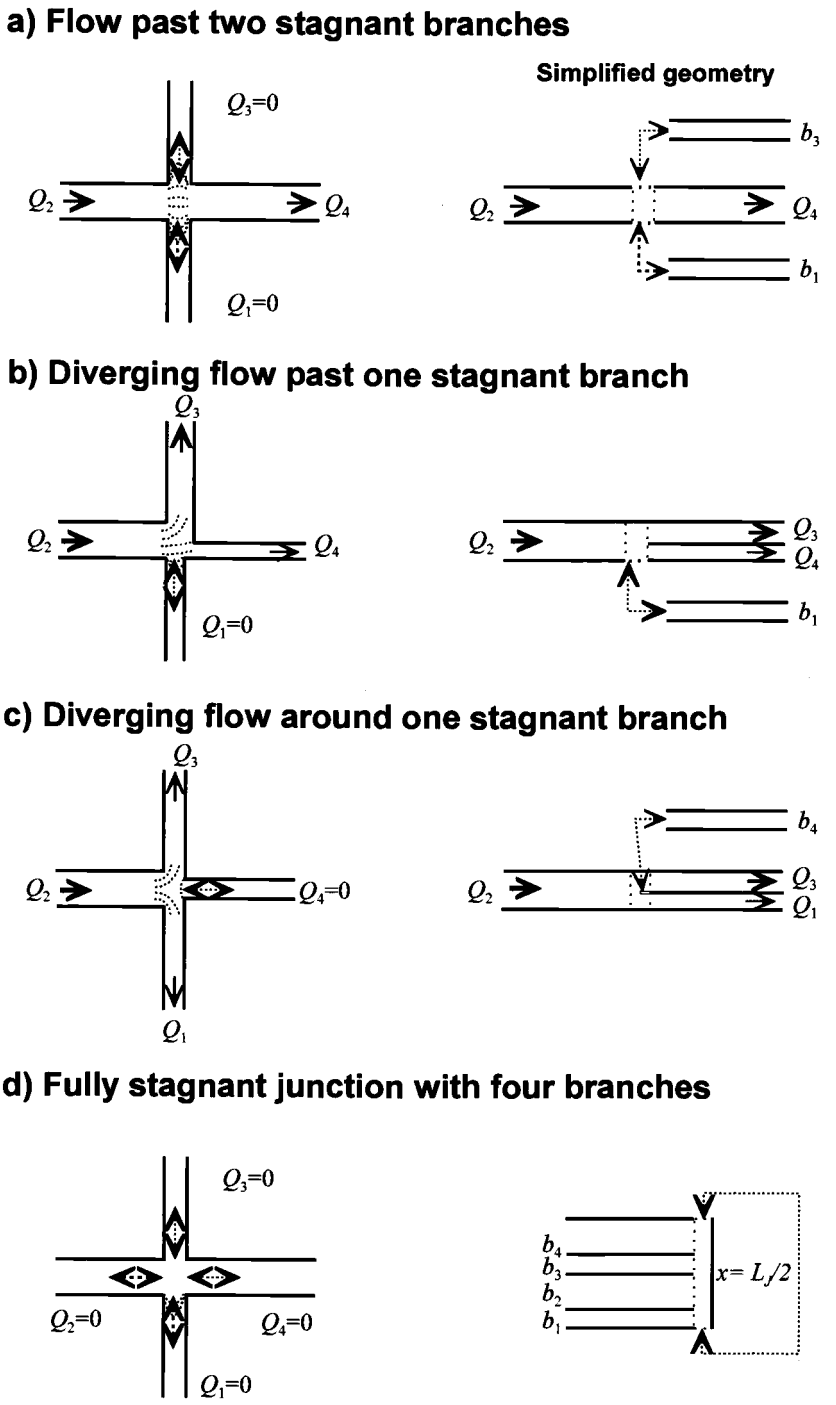

Figure 6-6. Examples of junctions with stagnant branches, and their simplified geometric representation.

Simulations of network-scale transport

For the present study, the algorithms described above have been implemented in a C language program, *meshtrak2d*, and verified with respect to a set of simple test networks for which the results could be predicted analytically. Further documentation of this program including source code and results of verification cases are provided as an electronic appendix by Geier (2004).

Simulations of the following cases were conducted to assess the relative effects of stagnant branches and matrix diffusion in terms of solute break-through:

Case AD: Advective-diffusive transport in the flowing fractures (the network backbone), with no diffusion into stagnant branches or into the matrix.

Case ADB: Advective-diffusive transport in flowing fractures and diffusion into stagnant branches, but no matrix diffusion.

Case ADM: Advective-diffusive transport in flowing fractures and matrix diffusion, but no diffusion into stagnant branches.

Case ADBM: Advective-diffusive transport in flowing fractures with diffusion into both stagnant branches and the matrix.

For the last two cases matrix properties were assumed to be uniform. Sorption was not included in any of the runs, nor was radioactive decay. For the cases with matrix diffusion, values of matrix diffusivity $D_p = 2\text{x}10^{-11}$ m^2/s and matrix porosity $\theta_m = 0.005$ were assumed based on recommended values for Swedish granitic rock from Ohlsson & Neretnieks (1995).

For each case, 1000 particles, each representing an arbitrary fixed mass of solute m_p, were released at the inflowing edge of the network (the southern end) at time t=0 and tracked until they emerged at the outflowing edge (the northern end). Thus the input was in the form of a Dirac delta pulse of mass $1000m_p$.

At each end, only one fracture (a main en échelon segment) intersected the boundary, so nearly all particles entered and left the simulated network via these fractures. For the cases that included matrix diffusion, a small number of particles (less than 1%) exited the 40 m long section while diffusing through matrix adjacent to the main en échelon segment, after entering the matrix a few millimeters from the upstream or downstream boundary.

6.3 Results and Analysis

Figure 6-7 through 6-9 show the solute breakthrough curves for the deterministic and synthetic cases, each comparing the four cases of simple advection-diffusion without and with diffusion into stagnant branches (Cases AD and AD+B, respectively), and the same cases including matrix diffusion (Cases AD+M and AD+B+M). The accompanying tables (Tables 6-2 through 6-4) give transport statistics in terms of the temporal moments at the outlet defined as (*e.g.*, Cunningham and Roberts, 1998):

$$m_n = \int_0^\infty t^n c_o(t) dt \tag{6-2}$$

where $c_o(t)$ is the concentration at the outlet as a function of time t, and in terms of the percentiles t_p representing the times at which p percent of the mass has arrived at the outlet, for a Dirac delta pulse release at the inlet.

Comparison of the first two cases (AD and AD+B) shows that the effect of branch fractures in retarding solute transport is less than would be expected from simple consideration of the ratios of stagnant to mobile water volumes along the en échelon zones. To quantify this effect, we define the retardation factor due to branch fractures as:

$$R_B = \frac{v_{AD}}{v_{AD+B}} = \frac{m_{1(AD+B)} / m_{0(AD+B)}}{m_{1(AD)} / m_{0(AD)}} \tag{6-3}$$

where v_{AD} is the mean nominal velocity of solute (transport distance divided by the mean transport time which is equal to m_1/m_0) in Case AD, and v_{AD+B} is the corresponding mean nominal velocity for Case AD+B.

If the branch fractures acted as stagnant volumes in equilibrium with the flowing water, we would expect the value of R_B to be simply the ratio of the total pore volume (flowing fractures and stagnant branches) to the flowing fracture volume. For the deterministic case, this ratio is 6.6 based on the values in Table 6-1. For the synthetic case, this ratio is 3.4.

The actual values of R_B obtained from the solute transport modeling are lower for the cases with uniform fracture hydraulic properties, with $R_B = 1.44$ in the deterministic case and $R_B = 2.2$ in the synthetic case. A higher retardation $R_B = 4.0$ is obtained for the heterogeneous case of the synthetic model.

In both homogeneous cases, the retardation in the models is less than the estimate from a simple calculation of the volume ratios. This is expected since a given first-order branch is guaranteed to be in equilibrium with the mobile water only at the end connecting from the fracture. Other portions of the branch (as well as higher-order branches) have a time-dependent response, so the actual R_B is only a fraction of the potential R_B as estimated from the volume ratios. The difference between actual and potential R_B can be expected to decrease with decreasing v_{AD}, as the time scale for advection along the flowing fractures approaches the time scale for diffusion into the branches.

Stagnant volumes connected to flowing areas of fractures have been invoked as an explanation for tracer residence times longer than expected based on aperture measurements, in in-situ experiments in granitic rock (Abelin *et al.*, 1985; Abelin *et al.*, 1990; Poteri *et al.*, 2002). Hypotheses have included stagnant "pools" within channelized fractures (Abelin *et al.*, 1990) as well as immobile water within gouge and breccias in complex fractures (Mazurek *et al.*, 2003; Poteri *et al.*, 2002). The results given here indicate possible significance of an additional type of immobile domain due to secondary (branch) fractures, supported by geometric evidence from detailed mapping. This additional type of immobile domain need not preclude other hypotheses that have been proposed, and indeed may well occur alongside of the other types of domains which have not been considered here.

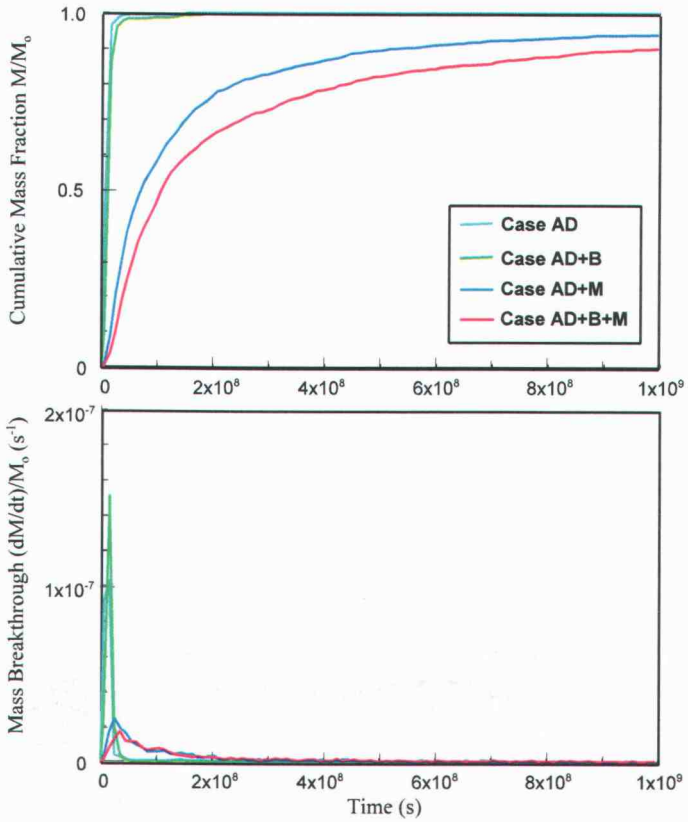

Figure 6-7 Solute breakthrough curves at north end of deterministic model with $D_p = 2x10^{-11}$ m^2/s, $\theta_m = 0.005$, $N_p = 1000$. Cases as defined in text.

Table 6-2. Moments and percentiles of solute breakthrough times for deterministic model. Statistics are given for $t' = t/(1x10^7\ s)$ where t is the breakthrough time for a given mass of solute. Moments M_1, M_2, and M_3 are normalized with respect to M_0, the total solute mass (equal to the number of particles N times the solute mass per particle, which is arbitrary).

Case	N	M_1/M_0	M_2/M_0	M_3/M_0	t'_{05}	t'_{10}	t'_{25}	t'_{50}	t'_{75}	t'_{90}	t'_{95}
AD	1000	1.19	2.19	0.122	0.80	0.83	0.90	1.03	1.23	1.56	1.79
AD+B	1000	1.71	6.03	62	0.93	1.00	1.15	1.38	1.75	2.2	2.7
AD+M	996	27	560	$2.4x10^6$	1.57	2.1	3.5	7.5	19	52	120
AD+BM	997	60	$2.1x10^5$	$2.0x10^9$	2.3	3.0	5.1	11.2	33	99	193

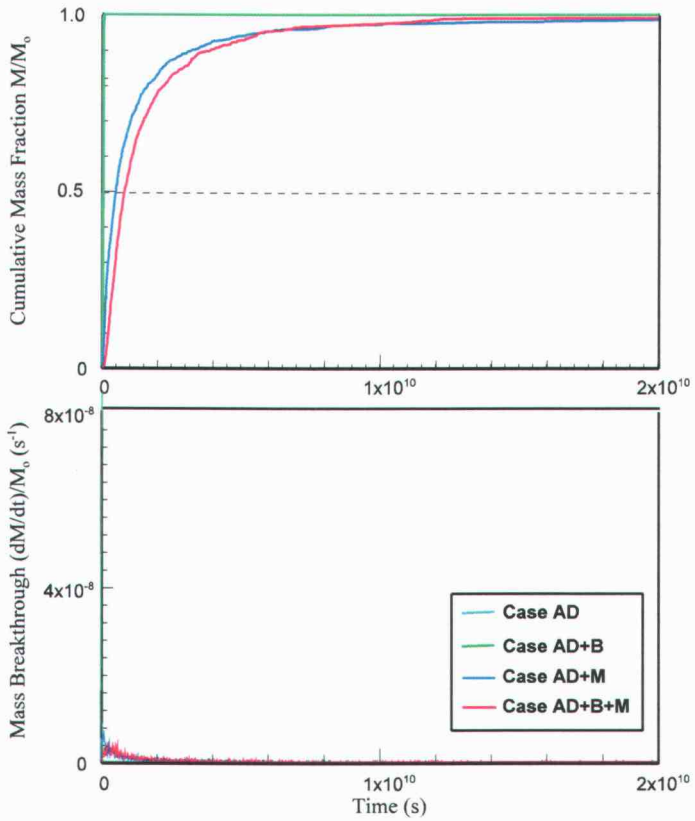

Figure 6-8 Solute breakthrough curves at north end of synthetic model (uniform hydraulic properties in all fracture segments) with $D_p = 2x10^{-11}$ m^2/s, $\theta_m = 0.005$, $N_p = 1000$.

Table 6-3. Moments and percentiles of solute breakthrough times for synthetic model (uniform hydraulic properties). Statistics are given for $t' = t/(1x10^7$ s) where t is the breakthrough time for a given mass of solute. Moments M_1, M_2, and M_3 are normalized with respect to M_0, the total solute mass as in Table 6-2.

Case	N	M_1/M_0	M_2/M_0	M_3/M_0	t'_{05}	t'_{10}	t'_{25}	t'_{50}	t'_{75}	t'_{90}	t'_{95}
AD	1000	1.67	2.9	5.5	1.45	1.49	1.56	1.64	1.74	1.84	1.90
AD+B	1000	3.7	13.9	55	2.5	2.7	3.1	3.6	4.1	4.6	4.9
AD+M	991	177	$3.5x10^5$	$1.70x10^9$	5.1	8.1	16.6	49	129	320	590
AD+BM	997	184	$1.79x10^5$	$5.13x10^8$	15.5	23	42	80	181	390	580

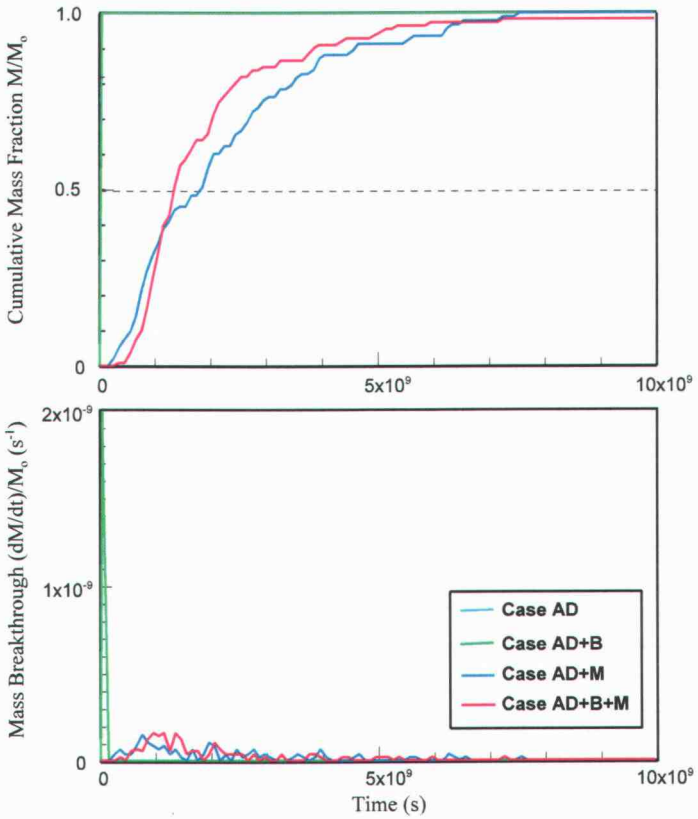

Figure 6-9 Solute breakthrough curves at north end of synthetic model (heterogeneous hydraulic properties) with $D_p = 2x10^{-11}$ m^2/s, $\theta_m = 0.005$, $N_p = 100$ (Cases AD+M and AD+B+M) to 1000 (Cases AD and AD+B).

Table 6-4. Moments and percentiles of solute breakthrough times for synthetic model (heterogeneous hydraulic properties). Statistics are given for $t' = t/(1x10^7$ s) where t is the breakthrough time for a given mass of solute. Moments M_1, M_2, and M_3 are normalized with respect to M_0, the total solute mass as in Tables 6-2 & 6-3.

Case	N	M_1/M_0	M_2/M_0	M_3/M_0	t'_{05}	t'_{10}	t'_{25}	t'_{50}	t'_{75}	t'_{90}	t'_{95}
AD	1000	2.3	5.4	13.4	2.1	2.1	2.1	2.2	2.3	2.5	2.7
AD+B	1000	9.2	86	830	7.0	7.4	8.1	9.0	10.0	11.0	11.6
AD+M	93	2200	$8.0x10^6$	$3.7x10^{10}$	360	600	870	1870	3000	4600	6200
AD+BM	111	1990	$6.7x10^6$	$3.7x10^{10}$	670	860	1030	1400	2300	3900	5100

Non-equilibration between branch fractures and the mobile fractures is also indicated by skewed breakthrough curves, with heavier late-time tails than the Gaussian curve expected for simple advection with Taylor dispersion through the flowing fractures. In terms of the random-walk model of diffusion processes, this may be understood as longer residence times for the fraction of particles that happen to enter stagnant fractures, with variable stagnant-fracture residence times related to the length of the stagnant branches and depth of the stagnant network.

Matrix diffusion either without or without stagnant branches (Cases AD+M and AD+B+M) produced a much larger retardation than stagnant branches alone. We define retardation factors for these two cases as:

$$R_M = \frac{v_{AD}}{v_{AD+M}} = \frac{m_{1(AD+M)} / m_{0(AD+M)}}{m_{1(AD)} / m_{0(AD)}} \tag{6-4}$$

$$R_{BM} = \frac{v_{AD}}{v_{AD+B+M}} = \frac{m_{1(AD+B+M)} / m_{0(AD+B+M)}}{m_{1(AD)} / m_{0(AD)}} \tag{6-5}$$

where v_{AD+M} and v_{AD+B+M} are the median nominal velocities of solute for Cases AD+M and AD+B+M respectively.

For the case of matrix diffusion from flowing fractures without stagnant branches (Case AD+M), the values of R_M are 23 and 106 for the deterministic and synthetic (uniform) cases, respectively, and $R_M = 960$ for the synthetic, heterogeneous case. Thus the retardation due to ordinary matrix diffusion, ignoring the branches, is much greater than that due to stagnant branches, for the representative values of head gradient, matrix porosity, and matrix diffusivity considered here. The breakthrough curves for these cases are also skewed.

When diffusion into stagnant branches is included along with matrix diffusion (Case AD+B+M), the values of R_{BM} are 50 and 110 for the deterministic and synthetic (uniform) cases, respectively, and R_{BM} = 865 for the synthetic, heterogeneous case. Thus in the deterministic case, the additional access to the matrix provided by the stagnant branches enhances the retardation due to matrix diffusion by roughly a factor of two. For the synthetic model, the relative significance of the branch fractures is lower, even in the case with uniform hydraulic properties.

The effects of stagnant branches and heterogeneity on retardation in the respective cases are illustrated by the plots of solute distribution in Figures 6-10 through 6-14. All of these plots represent cases in which matrix diffusion is included. In the pairs of synthetic-model figures representing the uniform case (6-11 & 6-12) and heterogeneous case (6-13 & 6-14), the second figure pair includes diffusion into stagnant branches. The synthetic model results are plotted for longer time scales to show the late-time behavior, particularly for the heterogeneous case which produces markedly greater retardation.

The results at late time show that the solute diffusing into the matrix adjacent to the flowing fractures (Figures 6-11 & 6-13) penetrates only a short distance as the main solute pulse passes. Therefore this solute returns to the flowing fractures relatively rapidly. Solute that enters the stagnant branches (Figure 6-12 & 6-14) and then diffuses into the adjoining matrix takes longer to return to the flowing fractures.

In the synthetic case with heterogeneous properties, the network with stagnant branch fractures actual produces less net retardation, when matrix diffusion is included, than when branch fractures are excluded. The percentiles in Table 6-4 show that the earliest 25% of mass arrival is retarded relative to the same mass fraction in the case without stagnant branches. However, later-arriving fractions of the mass are apparently less strongly retarded in the case that includes stagnant branches. This surprising behavior may be explained by the role of heterogeneity and its interaction with matrix diffusion.

In the heterogeneous version of the synthetic model that the fractures in the en échelon steps have lower transmissivity than the en échelon segments, but the pore volume per transport distance is higher than in en échelon segments. The result is that the stepovers become low-velocity zones relative to the en échelon segments.

The lower advective velocity implies more time for interaction with the matrix, and hence greater depths of matrix diffusion occur adjacent to these segments. This is seen in

Figures 6-13 and 6-14 as clouds of red dots representing solute in the matrix adjoining the stepovers. In Case AD+M (no branch fractures), this solute only returns to the flowing fractures by backward diffusion. However, in Case AD+B+M (with branch fractures), favorably positioned branch fractures provide additional pathways by which solute can return to the flowing fractures, downstream of the low-velocity steps.

These branch fractures are stagnant but have large pore volumes and high diffusivities relative to the matrix. Hence they can act as additional low-concentration boundaries for leaching of solute from the matrix just downstream of echelon steps, after the peak concentration has passed via the mobile water (flowing fractures). Since the flow past these branches is relatively rapid, they have less impact as paths for diffusion into the matrix, than as paths for release of solute that entered the matrix from adjoining, low-velocity portions of the network.

The net effect is marginal, since in either case retardation is dominated by the slow rate of diffusion into and out of matrix adjoining low-velocity portions of the network. However, for some fraction of the mass, this can reduce the delay due to matrix diffusion. Short-circuiting of the network by through-diffusion only occurs for the mass fraction of solute that experiences relatively large diffusion depths, and hence larger retention times. Hence the "accelerating" effect of through-diffusion to favorably located branch fractures is only seen in the later-arriving mass fraction (exemplified by t_{50} and higher percentiles). The mass fraction that experiences smaller diffusion depths is not subject to through-diffusion. Hence the main effect of the branch fractures for this fraction (exemplified by t_{25} and lower percentiles) is additional retardation as expected in view of the additional porosity.

The longest-retained mass fraction reflects the largest diffusion depths. These depths are attained by diffusion nominally perpendicular to the strike of the echelon zone, since solute can diffuse for effectively unbounded distances in this direction, without encountering branch fractures of the flowing network. Long branch fractures perpendicular to the strike of the zone can accentuate the retardation of the longest-retained mass fraction, by acting, in effect, as sources for radial-geometry diffusion into the matrix far from the main echelon segments. In contrast, solute traveling through a network without such fractures can only reach this region by slab-geometry diffusion. Thus the tails of the breakthrough curve (represented by t_{95} and higher percentiles) are retarded more for the case with branches than without.

A corollary to the above is that densely spaced, short "comb" cracks adjoining relatively high-velocity flowing fractures have only minor effects on the breakthrough curve (for the case of a solute pulse as considered here). Diffusion depths associated with such fractures are, on average, relatively small due to rapid passage of the concentration peak in the flowing fractures. The main expected effect is a small delay at early times. At longer time scales, interference between adjacent comb cracks results leads to slab-geometry diffusion similar to that from a simple fracture without comb cracks; the only difference is the increased pore volume.

The stagnant branches may be viewed as contributing a component of porosity additional to that considered as part of the matrix porosity θ_m. For the synthetic model, the effective porosity of the first-order stagnant branches at their intersection with the flowing fractures is $\theta_B = P_{10}\, b$, where P_{10} is the one-dimensional intensity measure of branch fractures and b is the mean aperture. For these simulations $P_{10} = 36\ \mathrm{m}^{-1}$ and $b = 2\mathrm{x}10^{-4}$ m, giving $\theta_B = 0.0072$. The total effective matrix porosity seen by solute passing through the flowing fractures $\theta_m + \theta_B = 0.0122$, or a factor of 2.44 times the value of θ_m that was assumed for the matrix alone.

The applicability of standard values of matrix porosity for a model that includes centimeter-scale branch fractures might be questioned, since the length of these fractures approaches the dimension of samples used in through-diffusion experiments (*e.g.*, as reviewed by Ohlsson and Neretnieks, 1995). Conceivably some fraction of θ_B might be included in estimates of intact matrix porosity θ_m. However, core samples taken from rock that is free of through-going fractures should be mostly free of secondary fractures (given the approximately exponential decrease of secondary fracture intensity with distance from primary fractures, as noted in this research). Estimates of θ_m obtained by fitting data to in-situ tracer experiments in natural fractures are more likely to include porosity belonging to θ_B.

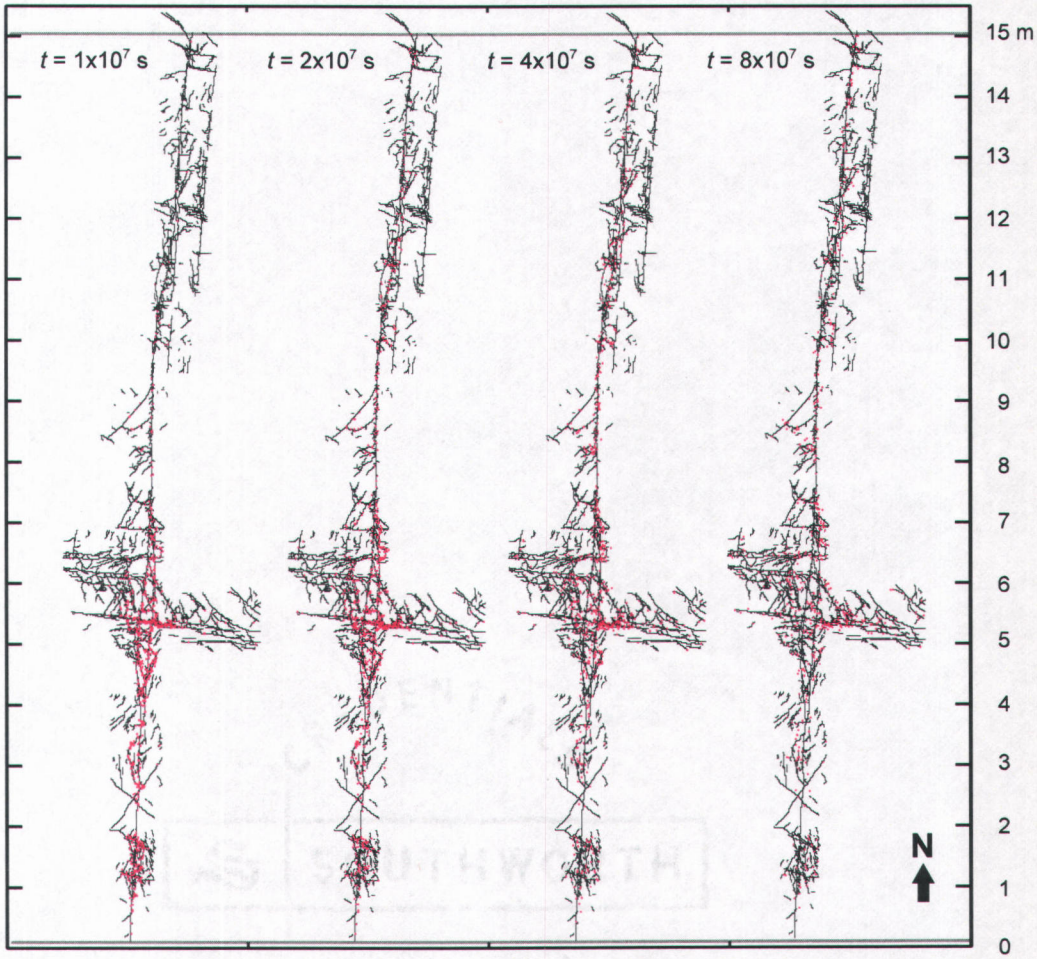

Figure 6-10. Solute distribution along 15 m long en échelon zone map at times ranging from $1x10^7$ s to $8x10^7$ s, Case ADBM (matrix diffusion with diffusion into stagnant branches). Red symbols indicate locations of particles, each representing a fixed mass of solute, at the indicated times.

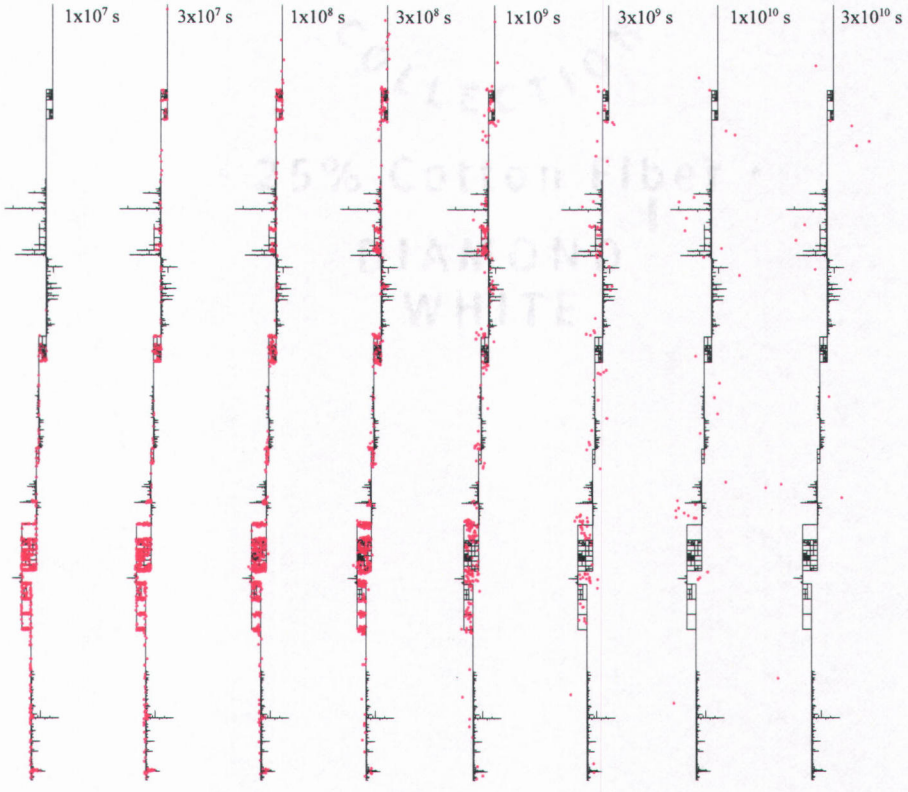

Figure 6-11. Solute distribution along 40 m long synthetic en échelon zone (uniform case) at times ranging from $1x10^7$ s to $8x10^8$ s, Case ADM (matrix diffusion without diffusion into stagnant branches). Red symbols indicate locations of particles, each representing a fixed mass of solute, at the indicated times.

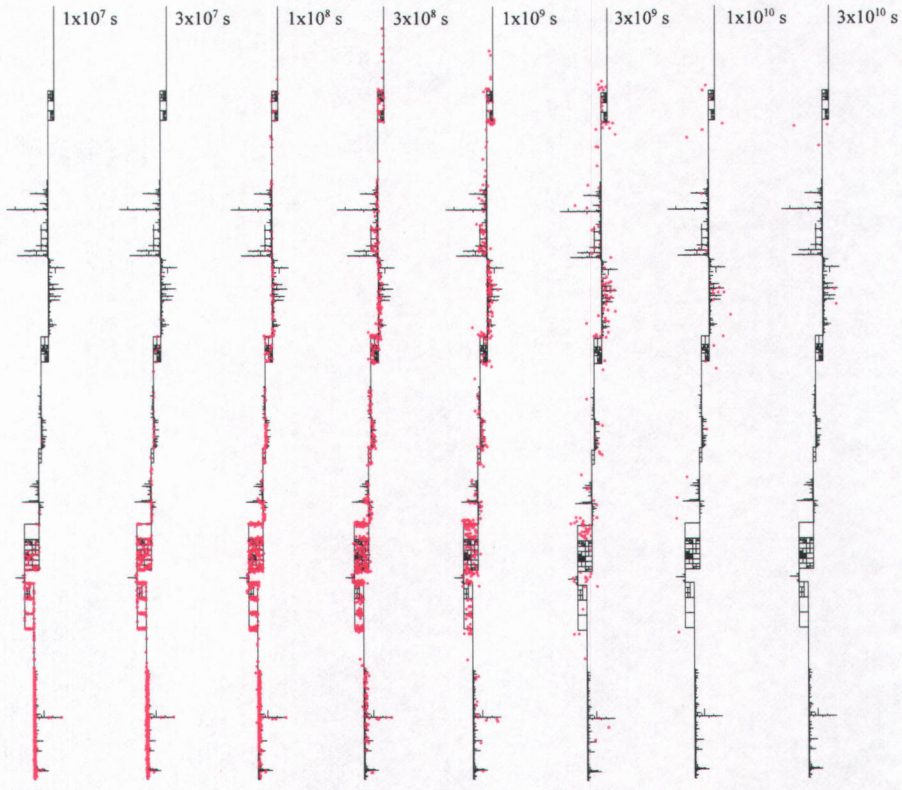

Figure 6-12. Solute distribution along 40 m long synthetic en échelon zone (uniform case) at times ranging from $1x10^7$ s to $8x10^8$ s, Case ADBM (matrix diffusion with diffusion into stagnant branches). Red symbols indicate locations of particles, each representing a fixed mass of solute, at the indicated times.

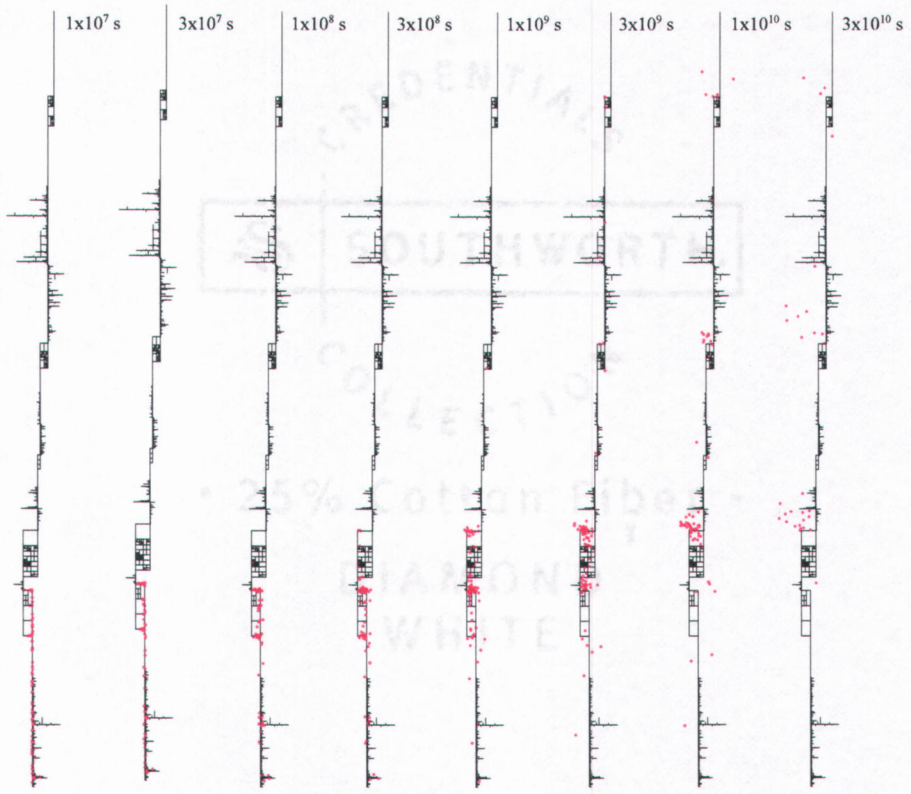

Figure 6-13. Solute distribution along 40 m long synthetic en échelon zone (heterogeneous case) at times ranging from $1x10^7$ s to $8x10^8$ s, Case ADM (matrix diffusion without diffusion into stagnant branches). Red symbols indicate locations of particles, each representing a fixed mass of solute, at the indicated times. Note that the number of particles in this simulation was about a factor of ten lower than for the corresponding (uniform) case in Figure 6-11.

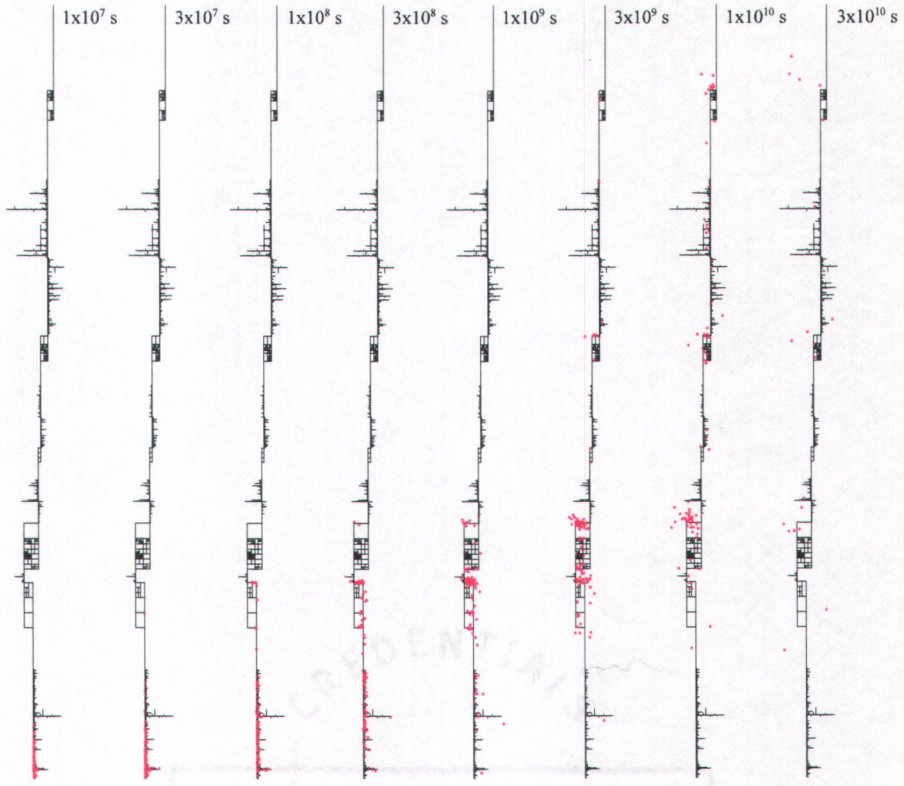

Figure 6-14. Solute distribution along 40 m long synthetic en échelon zone at times ranging from $1x10^7$ s to $8x10^8$ s, Case ADBM (matrix diffusion with diffusion into stagnant branches). Red symbols indicate locations of particles, each representing a fixed mass of solute, at the indicated times. Note that the number of particles in this simulation was about a factor of ten lower than for the corresponding (uniform) case in Figure 6-12.

6.4 Conclusions

Results are presented for models of advective-diffusive transport through en échelon fault zones, taking into account diffusion into both stagnant branch fractures and macroscopically unfractured matrix. Models analyzed include both a deterministic model based on an actual fracture map, and a synthetic model based on statistics of the 2-D geometry of en échelon zones observed at the Äspö site. The deterministic model assumes uniform hydraulic properties in all fracture segments. Two different cases of the synthetic model are analyzed, one with uniform hydraulic properties as in the deterministic model, and the second with heterogeneous properties, by which is meant lower values of transmissivity and aperture in higher-order branches.

For both models, diffusion into stagnant branches of the main en échelon segments is shown to produce up to a factor-of-two retardation of solute, relative to simple advective-diffusive transport through the main en échelon segments in the absence of matrix diffusion. The retardation is less than would be predicted by a two-domain model with equilibrium mass transfer between the flowing and stagnant domains, based on the ratio of the total pore volumes of the stagnant branch fractures and the main en échelon segments. Tailing of the simulated breakthrough curves also indicates non-equilibrium mass transfer.

The stagnant domain associated with branch fractures amounts to an additional type of immobile domain, beyond other hypothesized immobile zones (including stagnant pools in channelized fractures and stagnant fluid in gouge or breccia) which have been suggested to explain results of in situ tracer experiments. The potential for such a domain is supported by geometric evidence observed directly on outcrops.

When effects of matrix diffusion are included in the models, stagnant branches are demonstrated to enhance the retardation of solute due to matrix diffusion (in the cases with uniform hydraulic properties), and to increase the degree of late-time tailing. However, matrix diffusion is the dominant effect in terms of median arrival times for solute mass, at least for the head gradients, matrix porosities, and matrix diffusivities representative of a repository in granitic host rock that were considered in these calculations cases.

In the case with heterogeneous fracture properties, a surprising result is obtained, with branch fractures leading to slightly lower net retardation when combined with matrix diffusion. Inspection of the results indicates this may be explained as a combination of the

influence of flow-field heterogeneity on the depth of matrix diffusion, together with through-diffusion across fracture blocks. Where through-diffusion occurs, in some instances branch fractures may act as relatively rapid paths for solute to return to the flowing fractures.

From a practical standpoint in the context of a radioactive-waste repository, the principal concern with en échelon zones is that they pose a relatively well-connected, low-porosity, and potentially high-transmissivity type of pathway for transport of radionuclides, with relatively little interfacial area for exchange of solute with the matrix rock. The results presented here suggest that secondary fractures associated with such features are of net benefit in terms of radionuclide retention, but are not sufficient to mitigate those concerns significantly, either directly by providing additional immobile pore volume, or indirectly by improving access of solute to the matrix. For flow in heterogeneous networks, secondary fractures may in some circumstances accelerate breakthrough of a fraction of the solute mass by enhancing through-diffusion, although this effect is minor in the one calculation case where it is seen.

Branch fractures do apparently have the potential to affect tailing of breakthrough curves, which may be important to recognize in the interpretation of in-situ tracer experiments. If not recognized, tailing behavior due to branch fractures and branching networks of finite extent could conceivably lead to incorrect assessment of parameters for matrix diffusion models based on more simplistic diffusion geometries.

7. Significance of En échelon-zone architecture for radioactive waste disposal

Previous research reviewed here (Chapter 2) indicates that en échelon fault zones are a potentially important class of geologic features for radioactive waste disposal. As discrete structures that are well connected via more highly fractured zones at en échelon steps, they form potential flow paths over distances of tens to possibly hundreds of meters. As the en échelon segments have relatively low interfacial area, en échelon zones also have low capacity for exchange of radionuclides with the rock matrix (protolith), via matrix diffusion with or without sorption. These are the most important processes for retention of radionuclides in granitic bedrock, in the event that engineered barriers in a repository begin to leak.

The significance of en échelon zones is not strictly limited to the function of the bedrock as a barrier for radionuclides released from failed engineered barriers. A low potential for radionuclide retention due to interactions with the rock matrix also implies a relatively low potential for buffering and mixing of infiltrating groundwater of undesirable chemistry, *e.g.* oxygenated glacial meltwaters as proposed by Glynn and Voss (1996), and/or other types of groundwater that may have deleterious effects on engineered barriers such as the bentonite buffer and backfill used in the Swedish and Finnish repository concepts. These aspects have not been explored in the current dissertation. However, they may be equally important, or more important, than the properties of en échelon zones for radionuclide migration, given the importance ascribed to geochemical stability and engineered barrier longevity in recent safety assessments (SKB, 1999).

The discrete nature of en échelon segments also makes en échelon zones difficult to detect in the vicinity of a radioactive-waste repository. The anomalies for geophysical methods such as seismic reflection/refraction, magnetic, resistivity, or electromagnetic methods are likely to be less pronounced than the corresponding anomalies for distributed-deformation fault zones with high degrees of alteration. When intersected in an exploration borehole, an en échelon zone may appear to be merely a single fracture. As such it may not be recognized as a significant hydrological feature, particularly if the borehole intersects it in a relatively low-transmissivity portion of the zone.

The field investigations and analysis described in Chapters 3 and 4 provide new information on the heterogeneity of en échelon zones in granitic rock. Results suggest that a

geostatistical model may be adequate for describing the potential variation of hydraulic properties (here inferred from fracture intensity data) on scales of up to 10 m, similar to the spacing and length of en échelon steps. However, on larger scales of 50 m to 150 m, this study did not find evidence of spatial correlations in the geostatistical sense.

Systematic variations in fracture intensity correlated to structure along en échelon zones may be obscured in a geostatistical analysis, if the spacing and length of en échelon steps are variable. As a simple illustration, we may consider an ideal case in which the spacing and length of en échelon steps are constant with respect to position along strike, and fracture intensity takes on either of two values: P_1 if within one of the steps, or P_2 if between the steps. Such a model has periodic variation of fracture intensity, with period corresponding to the step spacing S, and correspondingly a decreased variogram at separation distances equal to integral multiples of S, *i.e.* what is referred to as a "hole effect" in geostatistical analysis. Next, if we consider a combined analysis of several such zones, each with a different step spacing S, we note that the variogram obtained by superposition will reflect interfering "hole effects" at the different values of S. Thus actual correlations of fracture intensity to structural features can be obscured in a conventional geostatistical analysis, if the scales of these features are variable.

To explore the consequences of systematic variations in fracture intensity correlated to structure along en échelon zones, which might not be fully characterized by a geostatistical analysis, simulations of solute transport have been performed using both actual maps and a synthetic structural model of en échelon zones. The results of these simulations are given in Chapter 6.

Analysis of detailed maps in Chapters 4 and 5 point to several characteristics that may be significant for flow and transport modeling. Fracture frequency generally decreases with distance from the median surface defined by the main en échelon segments, a characteristic common to other types of fault zones as reviewed in Chapter 2. This implies that effective hydraulic conductivity is not uniform across the nominal thickness of such zones. This has potential consequences for solute transport in that zones of varying mobility may occur in parallel within the zone. The need for more complex models to represent transport in such features in granitic rock has been recognized in recent years (Poteri *et al.*, 2002; Tsang and Doughty, 2004).

Secondary fractures (here treated as a non-genetic category encompassing splays,

wing cracks, pinnate fractures, comb cracks, *etc.*) are found to have a hierarchical branching structure, which accounts for a major portion of the elevated fracture intensity near the median surface. Thus the elevated fracture frequency adjacent to the main slip surfaces, as noted above, is not haphazardly random, but rather is organized in structural patterns that may have consequences for transport (as explored in Chapters 5 and 6).

In terms of repository safety, observations of hierarchical branches of en échelon zones pose a particular concern with respect to the concept of "respect distances" for waste emplacement. Branch fractures may provide direct connections to flowing fault zones that may not readily be recognized by methods for checking the suitability of emplacement locations. The branching structures identified here are of modest extent, and may not be of great concern in themselves. However, in view of observations such as by Kim *et al.* (2004) of structural similarity of fault zones over a very large range of scales, the possibility of large-scale branching structures than observed here should be considered.

Branch fractures in an en échelon zone could potentially act as positive attributes for repository safety. They potentially provide access to a much larger volume of rock that can react with radionuclides traveling along the zone, than would be the case for zone composed only of the primary fractures. This would imply a greater capacity for a retardation of solutes due to matrix diffusion and sorption.

A major aim of the numerical simulations in Chapter 6 was to evaluate the potential significance of branch fractures in this respect. Results indicate that, at best, branch fractures provide an additional degree of retardation which is minor relative to the effect of matrix diffusion. Their influence in this respect appears to be sensitive to groundwater velocities and heterogeneity of hydraulic properties within the fractures comprising the en échelon zone.

A surprising result of network simulations in Chapter 6 was that, in some circumstances, branch fractures apparently reduce the net retardation. This appears to be a consequence of branch fractures, in conjunction with through-diffusion under conditions of diffusion-dominated transport. Under these circumstances, branch fractures may provide relatively high-diffusivity paths by which solute can exit the immobile zone (matrix) after passage of the peak concentration. This effect is, at most, a minor factor relative to the dominant process of matrix diffusion.

The overarching conclusion, with regard to secondary fractures of en échelon zones, is that these do not provide significant additional retardation capacity, for transport scenarios

representative of post-closure repository conditions. Branching structures do not significantly mitigate the concern that en échelon zones will act as pathways with relatively low capacity for radionuclide retention in the bedrock. Thus en échelon zones must still be regarded as features with potentially negative consequences for repository safety.

On the other hand, branching structures are shown to affect the shape of solute breakthrough curves, particularly tailing phenomena. The effects of en échelon zone structure may be important for interpreting tracer tests that are conducted as part of site characterization for repositories. As shown in Chapter 5, late-time tails observed in tracer tests in-situ at the Äspö Hard Rock Laboratory can be explained in terms of diffusion into hierarchical branching structures, as mapped on an outcrop within half a kilometer of the in-situ experiments.

An important caveat on all of these conclusions is that they rely primarily on fracture geometry as observed in the plane of the given cross-sections, and on an assumption that water and solutes have equal access to all of the fractures. In reality some fractures may be entirely sealed by fracture mineralization, and other fractures are likely open to flow and solute transport over only a fraction of their extent. The three-dimensional nature of en échelon zones is evident in some of these exposures, but has not been addressed quantitatively. Gouge, fracture mineralogy, microstructure, and other properties not explored here may also affect échelon-zone transport properties. This research effort has aimed to investigate the flow and transport consequences of échelon-zone geometry, as revealed by (mainly) 2-D exposures. Other aspects of these structures certainly warrant further research.

BIBLIOGRAPHY

Note: This bibliography follows American conventions for alphabetical order, treating letters with diacritical marks (ä, å, and ö) as equivalent to the letters without such marks. The author apologizes for any inconvenience to readers who may expect to find these letters alphabetized after z.

Abelin, H., L. Birgersson, H. Widén, T. Ågren, L. Moreno, and I. Neretnieks, 1990. Channeling Experiment, Stripa Project Technical Report 90-13, Swedish Nuclear Fuel and Waste Management Co., Stockholm.

Abelin, H, I. Neretnieks, S. Tunbrant, and L. Moreno, 1985. Final report of the migration in a single fracture - Experimental results and evaluation, Stripa Project Technical Report 85-03, Swedish Nuclear Fuel and Waste Management Co., Stockholm.

Ahlstrom, S. W., Foote, H. P., Arnett, R. C., Cole, C. R., and Serne, R.J., 1977. Multicomponent mass transport model. Theory and numerical implementation (discrete parcel random walk version), Battelle report BNWL for ERDA, Columbus, Ohio.

Anderson, J. G. C., 1978. *The Structure of Western Europe*, Pergamon Press, Oxford, 250 p.

Anderson, L. J., Osborne, R. H., and Palmer, D. F., 1983. Cataclastic rocks of the San Gabriel fault – An expression of deformation at deeper crustal levels in the San Andreas fault zones. *Tectonophysics*, v. 98, p. 209-251.

Andersson, J-E, L. Ekman, E. Gustafsson, R. Nordqvist, and S. Tirén, 1989a. Hydraulic interference tests and tracer tests within the Brändan area, Finnsjön study site -- The Fracture Zone Project -- Phase 3, SKB Technical Report 89-12, Swedish Nuclear Fuel and Waste Management Co., Stockholm.

Andersson, J-E, L. Ekman, R. Nordqvist, and A. Winberg, 1989b. Hydraulic testing and modeling of a low-angle fracture zone at Finnsjön, Sweden. In SKB Technical Report 89-19, Swedish Nuclear Fuel and Waste Management Co., Stockholm

Andersson, J-E, Nordqvist, R, Nyberg, G, Smellie, J, and Tirén, S, 1991. Hydrogeological conditions in the Finnsjön area: Compilation of data and conceptual model, SKB Technical Report 91-24, Swedish Nuclear Fuel and Waste Management Co., Stockholm.

Andersson, J., and Dverstorp, B., 1987. Conditional simulations of fluid flow in three-dimensional networks of discrete fractures. *Water Resources Research*, v. 23, p. 1876-1886.

Antonellini, M. and Aydin, A., 1994. Effect of faulting on fluid flow in porous sandstones: Petrophysical properties. *American Association of Petroleum Geologists Bulletin*, v. 78, p. 355-377.

Aris, R., 1956. On the dispersion of solute in a fluid moving through a tube. *Proceedings of the Royal Society of London Ser. A*, v. 235, p. 67-77.

Aydin, A., 1978. Small faults formed as deformation bands in sandstone. *Pure Appl. Geophysics* v. 116:913-930.

Aydin, A., and Nur, A., 1985. The types and role of stepovers in strike-slip tectonics. *Society of Economic Paleontologists and Mineralogists Special Publication No. 37*, p. 35-44.

Aydin, A. and Schultz, R.A., 1990. Effect of mechanical interaction on the development of strike-slip faults with echelon patterns. *Journal of Structural Geology*, v.12, p.123-129.

Bäckblom, G., and Karlsson, F., 1990. Swedish programme for disposal of radioactive waste – geological aspects. *Geologiska Föreningens I Stockholm Förhandlingar*, v. 112, p. 307-315.

Bandis, S., A.C. Lumisden, and N.R. Barton, 1981. Experimental studies of scale effects on the shear behaviour of rock joints, *Int. J. Rock Mechanics, Mining Science and Geomechanics Abstracts* v. 18, p. 1-21.

Bandis, S., A.C. Lumisden, and N.R. Barton, 1983. Fundamentals of rock joint deformation, *Int. J. Rock Mechanics, Mining Science and Geomechanics Abstracts* v. 20, p. 249-268.

Barton, C.A., Zoback, M.D. and Moos, D., 1995. Fluid flow along potentially active faults in granitic bedrock. *Geology*, v. 23, p. 683-686.

Barton, N., Bandis, S., and Bakhtar, K., 1985. Strength, deformation and conductivity coupling of rock joints. *International Journal of Rock Mechanics, Mineral Science and Geomechanics Abstracts*, v. 22, p.121-140.

Bates, R.L. and Jackson, J.A., eds., 1984. *Dictionary of Geologic Terms*, 3rd edition, American Geological Institute.

Bear, J., 1993. Modeling flow and contaminant transport in fractured rocks. *In* Bear, J., Tsang, C-F, and de Marsily, eds., *Flow and Contaminant Transport in Fractured Rock*, Academic Press, San Diego, p. 1-35.

Bergman, T., Isaksson, H., Johansson, R., Lindén, A. H., Lindgren, J., Lindroos, H., Rudmark, I., and Wahlgren, C.-H.., 1998. *Förstudie Oskarshamn. Jordarter, bergarter och deformationszoner* (Pre-study Oskarshamn: Soil types, rock types, and deformation zones), SKB Report R-98-56, Swedish Nuclear Fuel and Waste Management Co., Stockholm.

Berkowitz, B., Nauman, C., and Smith, L., 1994. Mass transfer at fracture intersections: An evaluation of mixing models. *Water Resources Research*, v. 30, p. 1765-1773.

Biegel, R. L., Sammis, C. G., and Dieterich, J. H., 1989. The frictional properties of simulated fault gouge having a fractal particle distribution. *Journal of Structural Geology*, v. 11, p. 827-846.

Billaux, D., Chiles, J. P., Hestir, K., and Long, J. C. S., 1989. Three-dimensional statistical modeling of a fractured rock mass – an example from the Fanay-Augeres Mine. *International Journal of Rock Mechanics, Mining Science and Geomechanics Abstracts*, v. 26, p.281-299.

Bjarnasson, B. and Stephansson, O., 1988. Hydraulic fracturing stress measurements in the borehole Fi 06, Finnsjön. SKB Working Report R&D 88-54, Swedish Nuclear Fuel and Waste Management Co., Stockholm.

Bour, O. and Davy, P., 1997. Connectivity of random fault networks following a power law length distribution, *Water Resources Research*, v. 33, p. 1567-1583.

Bourke, P. T., 1987. Channeling of flow through fractures in rock, *in* Proceedings of the GEOVAL-87 International Symposium, Stockholm, April 7-9, 1987.

Brace, W.F., 1960. An extension of Griffith theory of fracture to rocks, *Journal of Geophysical Research*, v. 65, p. 3477-3480.

Brown, A., Everitt, R.A., Martin, C.D., and Davison, C.C., 1995. Past and future fracturing in AECL research areas in the Superior province of the Canadian Precambrian Shield, with emphasis on the Lac du Bonnet Batholith. Atomic Energy of Canada Ltd. Report AECL-11214, COG-94-528, Whiteshell Laboratories, Pinawa, Manitoba.

Brown, S. R., 1987. Fluid flow through rock joints: The effect of surface roughness, *Journal of Geophysical Research*, v. 92, 1337-1347.

Brown, S. R., Kranz, R. L. and Bonner, B. P. 1986. Correlation between the surfaces of natural rock joints, *Geophysical Research Letters*, v. 13, p. 1430-1434.

Brown, S. R. and Scholz, C. H., 1985. Broad bandwidth study of the topography of natural rock surfaces, *Journal of Geophysical Research,* v. 90, p. 12,575-12,582.

Brown, S. R. and Scholz, C. H., 1986. Closure of rock joints, *Journal of Geophysical Research,* v. 91, p. 4939-4948.

Brown, S.R., Stockman, H.W., and Reeves, S. J., 1995. Applicability of the Reynolds equation for modeling fluid flow between rough surfaces, *Geophysical Research Letters*, v. 22, p. 2537-2540.

Bruderer, C. and Bernabé, Y., 2001. Network modeling of dispersion: Transition from Taylor dispersion in homogeneous networks to mechanical dispersion in very heterogeneous ones. *Water Resources Research*, v. 37, p. 897-908.

Bruhn, R. L., Yonkee, W. E., and Parry, W. T., 1994. Structural and fluid-chemical properties of seismogenic normal faults, *Tectonophysics*, v.175, p.139-157.

Byerlee, J., 1993. Model for episodic flow of high-pressure water in fault zones before earthquakes. *Geology*, v. 21, p. 303-306

Cacas, M. C., Ledoux, E., de Marsily, G., Tillie, B., Barbreau, A., Durand, E., Fuega, B. and Peaudecerf, P., 1990a. Modeling fracture flow with a stochastic discrete fracture network: Calibration and validation, 1, The flow model. *Water Resources Research*, v. 26, p. 479-489.

Cacas, M.C., Ledoux, E., de Marsily, G., Barbreau, A., Calmels, P., Gaillard, B. and Margritta, R., 1990b. Modeling fracture flow with a stochastic discrete fracture network: Calibration and validation, 2, The transport model. *Water Resources Research*, v. 26, p. 491-500.

Caine, J. S., 1999. The architecture and permeability structure of brittle fault zones. Ph.D. thesis, Department of Geology and Geophysics, University of Utah, 134 p.

Caine, J. S., Coates, D. R., Timoffeef, N. P., and Davis, W. D., 1991. Hydrogeology of the Northern Shawangunk Mountains. New York State Geological Survey Open-File Report 1g806, 72 p. and maps.

Caine, J. S., Evans, J. P., and Forster, C. B., 1996. Fault zone architecture and permeability structure, *Geology*, v. 24, p. 1025-1028.

Caine, J. S. and Forster, C. B., 1999. Fault zone architecture and fluid flow: Insights from field data and numerical modeling. In Haneberg, W.C., Mozley, P.S., Moore, J.C., and Goodwin, L.B., *Faults and Subsurface Fluid Flow in the Shallow Crust*, AGU Geophysical Monograph, v. 113, p. 107-127.

Carlsson, A., and Olsson, T., 1986. Large scale in-situ tests on stress and water flow relationships in fractured rock. RD&D report, Vattenfall AB, Vällingby, Sweden.

Chester, F. M. and Chester, J.S., 1998. Ultracataclasite structure and friction processes of the Punchbowl fault, San Andreas system, California. *Tectonophysics*, v. 295, p.199-222.

Chester, F. M., Evans, J. P., and Beigel, R. I., 1992. Internal structure and weakening mechanisms of the San Andreas Fault. *Journal of Geophysical Research*, v. 98, p.778-786.

Chester, F. M. and Logan, J. M., 1986. Composite planar fabric of gouge from the Punchbowl fault, California. *Journal of Structural Geology*, v. 9, p. 621-634.

Childs, C., Nicol, A., Walsh, J. J., and Watterson, J., 1996a. Growth of vertically segmented normal faults. *Journal of Structural Geology*, v. 18, p.1389-1397.

Childs, C., Watterson, J., and Walsh, J. J., 1996b. A model for the structure and development of fault zones. *J. Geological Society*, v. 153, p. 337-340.

Clemo, T., 1994. Dual permeability modeling of fractured media. Ph. D. thesis, University of British Columbia, Vancouver.

Committee on Fracture Characterization and Fluid Flow, U.S. National Committee for Rock Mechanics, and Geotechnical Board, Board on Energy and Environmental Systems, Commission on Engineering and Technical Systems, National Research Council, 1996. *Rock Fractures and Fluid Flow*, National Academy Press, Washington D.C., 551 p.

Cooke, M. L., 1997. Fracture localization along faults with spatially varying friction. *Journal of Geophysical Research*, v. 102(B10), p. 22,425-22,434.

Cruikshank, K. M., Zhao, G., and Johnson, A. M., 1991a. Analysis of minor fractures associated with joints and faulted joints. *Journal of Structural Geology*, v.13(8), p.865-886.

Cruikshank, K. M., Zhao, G., and Johnson, A. M., 1991b. Duplex structures connecting fault segments in Entrada sandstone. *Journal of Structural Geology*, v.13(8), p.1185-1196.

Cunningham, J. A. and Roberts, P. V., 1998. Use of temporal moments to investigate the effects of nonuniform grain-size distribution on the transport of sorbing solutes. *Water Resources Research*, v. 34(6), p.1415-1425.

Davison, C. C. and Kozak, E. T., 1988. Hydrogeologic characteristics of major fracture zones in a large granite batholith of the Canadian shield. In *Proceedings of the 4th Canadian-American Conference on Hydrogeology*, Banff, June 1988. Published by National Ground Water Association, Dublin, Ohio.

Delay, F. and Bodin, J., 2001. Time domain random walk method to simulate transport by advection-dispersion and matrix diffusion in fracture networks. *Geophysical Research Letters*, v. 37(10) p. 2503-2512.

Di Pietro, L. B., 1996. Application of a lattice-gas numerical algorithm to modeling water transport in fractured media, *Transport in Porous Media*, v. 22, p. 307-325.

Dershowitz, W. S., *Rock Joint Systems*, Ph.D. dissertation, Massachusetts Institute of Technology, 1984.

Dershowitz, W. S. and Herda, H. H., 1992. Interpretation of fracture spacing and intensity. In Tillerson, J.R. and Wawersik, W.R. (eds.), *Rock Mechanics: Proceedings of the 33rd U.S. Symposium*, Santa Fe, New Mexico 3-5 June 1992, Balkema, Rotterdam, p. 757-766.

Dershowitz, W. S., Lee, G., Geier, J., Foxford, T., LaPointe, P., and Thomas, A., 1996. FracMan™: Interactive discrete feature data analysis, geometric modeling, and exploration simulation: User Documentation, Version 2.5, Golder Associates Inc., Redmond, Washington.

Dershowitz, W. S. and Miller, I., 1995. Dual porosity fracture flow and transport, *Geophysical Research Letters*, v. 22, p. 1441-1444.

Dershowitz, W. S., Wallman, P., and Kindred, S., 1991. Discrete fracture modeling for the Stripa site characterization and validation experiment. Stripa Project Technical Report 91-16, Swedish Nuclear Fuel and Waste Management Co., Stockholm.

Detwiler, R. L., Rajaram, H., and Glass, R. J., 2000. Solute transport in variable-aperture fractures: An investigation of the relative importance of Taylor dispersion and macrodispersion, *Water Resources Research* v. 36(7), p. 1611-1625.

de Dreuzy, J.-R., Davy, P., and Bour, O., 2001a. Hydraulic properties of two-dimensional fracture networks following a power law length distribution: 1. Effective connectivity. *Water Resources Research*, v. 37(8), p. 2065-2078.

de Dreuzy, J.-R., Davy, P., and Bour, O., 2001b. Hydraulic properties of two-dimensional fracture networks following a power law length distribution: 2. Permeability of networks based on a lognormal distribution of apertures. *Water Resources Research*, v. 37(8), p. 2079-2095.

Du, Y., and Aydin, A., 1991. Interaction of multiple cracks and formation of echelon crack arrays, *International Journal of Numerical and Analytical Methods in Geomechanics*, v. 15(3), p. 205-218.

Du, Y. and Aydin, A., 1993. The maximum distortional strain energy density criterion for shear fracture propagation with applications to the growth paths of *en échelon* faults, *Geophysical Research Letters*, v. 20(11), p.1091-1094.

Dverstorp, B., Andersson, J., and Nordqvist, W., 1992. Discrete fracture network interpretation of field tracer migration in sparsely fractured rock, *Water Resources Research*, v. 28(9), p. 2327-2343.

Dverstorp, B., Geier, J., and Voss, C., 1996. Simple evaluation of groundwater flow and radionuclide transport at Äspö. SKI Report 96:14, Swedish Nuclear Power Inspectorate, Stockholm.

Elsworth, D., and Doe, T. W., 1986. Application of nonlinear flow laws in determining rock fissure geometry from single borehole pumping tests. *Int. J. Rock Mech. Min. Sci. & Geomech. Abstr.*, v. 23(3), p. 245-254.

Endo, H. K., Long, J. C. S., Wilson, C. R., and Witherspoon, P. A., 1984. A model for investigating mechanical transport in fracture networks. *Water Resources Research*, v. 20(10), p. 1390-1400.

Ericsson, L. O., 1987. Fracture mapping on outcrops. Äspö. SKB Swedish Hard Rock Laboratory Progress Report 25-87-05, Swedish Nuclear Fuel and Waste Management Co., Stockholm.

Evans, J. P., Forster, C. B., and Goddard, J. V., 1997. Permeability of fault-related rocks and implications for hydraulic structure of fault zones. *Journal of Structural Geology*, v. 19(11),p. 1393-1404.

Fairley, J., Heffner, J., and Hinds, J., 2003. Geostatistical evaluation of permeability in an active fault zone. *Geophysical Research Letters*, v. 30(18), 1962, doi:10.1029/2003GL018064.

Falconer, K., 1990. *Fractal Geometry: Mathematical Foundations and Applications.* Wiley & Sons, Chichester, UK, 288 p.

Fischer, U., Kulli, B., and Flühler, H., 1998. Constitutive relationships and pore structures of undisturbed fracture zone samples with cohesionless fault gouge layers. *Water Resources Research*, v. 34(7), p. 1695-1701.

Forster, C. B., and Evans, J. P. 1991. Impact of a permeable thrust fault on thermal and hydrologic regimes: Regional-scale numerical modeling results. *GSA Abstracts with Programs*, p. A104.

Forster, C. B., Evans, J. P., Tanaka, H., Jeffreys, R., and Nohara, T., 2003. Hydrologic properties and structure of the Mozumi Fault, central Japan. *Geophysical Research Letters*, v. 30(6), 8010, doi:10.1029/2002GL014904.

Fossen, H., and Rykkelid, E., 1992. Postcollisional extension of the Caledonide orogen in Scandinavia: Structural expressions and tectonic significance. *Geology*, v. 20, p. 737-740.

Gale, J. E., 1987. Comparison of coupled fracture deformation and fluid flow models with direct measurements of fracture pore structure and stress-flow properties. Proceedings of the 28th U.S. Rock Mechanics Symposium, Tucson, Arizona, June 29 - July 1, 1987.

Gale, J. E. and Raven, K. G., 1980. Effects of sample size on the stress-permeability relationship for natural fractures. Report LBL-11865/SAC-48/UC-70, Swedish-American Cooperative Program on Radioactive Waste Storage in Mined Caverns in Granitic Rock, Swedish Nuclear Fuel and Waste Management Co., Stockholm.

Ge, S., 1997. A governing equation for fluid flow in rough fractures. *Water Resources Research*, v. 33, p. 53-61.

Geier, J.E., 1996. Discrete-feature modelling of the Äspö site: 3. Predictions of hydrogeological parameters for performance assessment (SITE-94), SKI Report 96:7, Swedish Nuclear Power Inspectorate, Stockholm.

Geier, J.E., Axelsson, C.-L., Hässler, L., and Benabderrahmane, A., 1992. Discrete-fracture network modelling of the Finnsjön rock mass: Phase 2. SKB Technical Report 92-07, Swedish Fuel and Waste Management Co., Stockholm.

Geier, J. E., Doe, T. W., Benabderrahman, A., and Hässler, L., 1995. Generalized radial flow interpretation of well tests for the SITE-94 project. SKI Technical Report 96:4, Swedish Nuclear Power Inspectorate, Stockholm.

Geier, J. E. and Hässler, L., 1992. Scale effects in estimating fractured rock block conductivity from packer tests. In Tillerson, J.R. and Wawersik, W.R. (eds.), *Rock Mechanics: Proceedings of the 33rd U.S. Symposium*, Santa Fe, New Mexico 3-5 June 1992, Balkema, Rotterdam, p. 551-560.

Geier, J. E., Lee, K., and Dershowitz, W. S., 1988. Field validation of conceptual models for fracture geometry. American Geophysical Meeting Poster Session Abstract H12A-10 1605, *EOS*, v. 69(44), p.1177.

Geier, J. E., and Thomas, A. L., SITE-94: Development of discrete-fracture network models for repository-scale flow and transport. SKI Technical report 96:5, Swedish Nuclear Power Inspectorate, Stockholm, 1996.

Geier, J. (ed.), Tirén, S., Dverstorp, B., and Glynn, P., 1996. SITE-94: Site-specific base data for the performance assessment. SKI Report 96:10, Swedish Nuclear Power Inspectorate, Stockholm.

Gelhar, L. W., 1987. Applications of stochastic models to solute transport in fractured rocks. SKB Technical Report 87-05, Swedish Nuclear Fuel and Waste Management Co., Stockholm.

Gentier, S., 1986. Morphologie et comportment hydromechanique d'une fracture naturelle dans une granite sous constrainte normale. Ph. D. dissertation, L'Universite d'Orleans.

Gentier, S., Billaux, D., and van Vliet, L., 1989. Laboratory testing of the voids of a fracture, *Rock Mechanics and Rock Engineering*, v. 22, p. 149-157.

Glynn, P. and Voss, C., 1996. Geochemical characterization of ground waters near the Äspö Hard Rock Laboratory, Simpevarp Region, Sweden. SKI Technical Report 96:29, SKI, Stockholm.

Gorbatschev, R., 1980. The Precambrian development of southern Sweden, *Geologiska Föreningens I Stockholm Förhandlingar*, v.102, p.129-136.

Gorbatschev, R., Lindh, A., Solyom, Z., Laitikari, I., Aro, K., Lobach-Zhuchenko, S.B., Markov, M.S., Ivliev, A.I., and Brynhi, I., 1987. Mafic dyke swarms of the Baltic shield. In Hall and Fahrig (eds.), *Mafic Dyke Swarms*, GAC Special Paper 34.

Gudmundsson, A., 1987. Tectonics of the Thingvellir fissure swarm, SW Iceland, *Journal of Structural Geology*, v. 9, p. 61-69.

Gustafson, G. 1990. Identification and nomenclature of fracture zones. In *Proceedings of the 3rd NEA/SKB Symposium on In Situ Experiments Associated with the Disposal of Radioactive Waste*, Stockholm, 3-4 October 1989, p. 218-222. Organization for Economic Cooperation and Development, Paris.

Gustafsson, E. and Nordqvist, R., 1993. Radially converging tracer test in a low-angle fracture zone at the Finnsjön site, central Sweden. The Fracture Zone Project -- Phase 3. SKB Technical Report 93-25, Swedish Nuclear Fuel and Waste Management Co., Stockholm.

Gutfraind, R. and Hansen, A.,1995. Study of fracture permeability using lattice gas automata, *Transport in Porous Media*, v. 18, p. 131-149.

Haggerty, R., 2001. Matrix diffusion: Heavy-tailed residence-time distributions and their influence on radionuclide retention, in *Radionuclide Retention in Geologic Media*, Workshop Proceedings, Oskarshamn, Sweden, 7-9 May 2001. Radioactive Waste Management GEOTRAP Project, Organization for Economic Cooperation and Development, p. 81-90.

Haggerty, R., Fleming, S. W., Meigs, L. C., and McKenna, S. A., 2001. Tracer tests in a fractured dolomite: 2. Analysis of mass transfer in single-well injection-withdrawal tests. *Water Resources Research*, v. 37(5), p. 1129-1142.

Haggerty, R. and Gorelick, S. M., 1995. Multiple-rate mass-transfer for modeling diffusion and surface reactions in media with pore-scale heterogeneity, *Water Resources Research*, v. 36(12), p. 3467-3479.

Hakami, E., 1989. Aperture measurements and flow experiments using plastic resin replicas of rock joints.

Hartikainen, J., Hartikainen, K., Hautojärvi, A., Kuoppamäki, K., and Timonen, J., 1996. Helium gas methods for rock characteristics and matrix diffusion. Posiva Oy, Helsinki, 55 p.

Hazzard, J. F. and Mair, K., 2003. The importance of the third dimension in granular shear. *Geophysical Research Letters*, v. 30(13),1708 doi:10.1029/2003GL017534.

Heath, M. J., 1984. Solute migration experiments in fractured granite, South West England, *in* Design and Instrumentation of In Situ Experiments in Underground Laboratories for Radioactive Waste Disposal; Proceedings of a Joint CEC-NEA Workshop, Brussels, May 15-17, 1984.

Herbert, A. W., Gale, J. E., Lanyon, G. W., and MacLeod, B., 1991. Modeling for the Stripa site characterization and validation drift inflow prediction of flow through fractured rock. Stripa Project Technical Report 91-35, Swedish Nuclear Fuel and Waste Management Co., Stockholm.

Hestir, K., Martel, S. J., Yang, J., Evans, J. P., Long, J. C. S., D'Onfro, P., and Rizer, W. D., 2001. Use of conditional simulation, mechanical theory, and field observations to characterize the structure of faults and fracture networks. *In* Evans, D.D., Nicholson, T.J., and Rasmussen, T.C., *Flow and Transport Through Unsaturated Fractured Rock*, Geophysical Monograph 42, 2nd Edition, American Geophysical Union, Washington, D.C..

Hicks, T., Wickham, S., Bruel, D., Jeong, W.-C., Connolly, P., Goelke, M., Podlachikov, Y., and Rodrigeus, N., 2000. Modeling the influence of fault zone heterogeneity and the hydrodynamics of fault movement in hydrogeological systems. European Commission Report EUR 19134.

de Hoog, F. R., Knight, J. H., and Stokes, A. N., 1982. An improved method for numerical inversion of Laplace transforms, *SIAM Journal of Scientific and Statistical Computing*, v. 3(3), p. 357-366.

Hopkins, D. L., Cook, N. G. W., and Myer, L. R., 1990. Normal joint stiffness as a function of spatial geometry and surface roughness. In *Rock Joints: Proceedings of the International Symposium on Rock Joints*, Loen, Norway, June 4-6, p. 203-210.

Hull, J., 1988. Thickness-displacement relationships for deformation zones. *Journal of Structural Geology*, v. 10, p. 431-435.

Itasca Consulting Group, UDEC User's guide, Version 3.1, Minneapolis, Minnesota, 2000.

Iwai, K., 1976. *Fundamental studies of fluid flow through a single fracture.* Ph.D. dissertation, University of California, Berkeley.

Jackson, C. P., Hoch, A. R., and Todman, S., 2000. Self-consistency of a heterogeneous continuum porous medium representation of a fractured medium. *Water Resources Research*, v. 36(1), p. 189-202.

Jaeger, J. C., and Cook, N. G. W., 1979. *Fundamentals of Rock Mechanics*, 3rd Edition, Chapman and Hall, London, 593 p.

Jakob, A., 2004. Matrix diffusion for performance assessment – Experimental evidence, modelling assumptions and open issues. PSI Bericht Nr. 04-08, Paul Scherrer Institut, Villigen, Switzerland.

Jakob, A., Mazurek, M., and Heer, W., 2003. Solute transport in granitic rocks at Äspö – II: Blind predictions, inverse modelling and lessons learnt from test STT1. *Journal of Contaminant Hydrology*, v. 61, p. 175-190.

Johansson, H., Siitari-Kauppi, M., Skålberg, M., and Tullborg, E.-L.,1998. Diffusion pathways in crystalline rock – examples from Äspö diorite and fine-grained granite. *Journal of Contaminant Hydrology*, v. 35(1-3), p. 41-53.

de Josselin de Jong, G., 1958. Longitudinal and transverse dispersion in granular deposits. Transactions of the American Geophysical Union, v. 39, p. 67-74.

Kearey, P., and Vine, F. J., *1990. Global Tectonics*. Blackwell Scientific Publications, Oxford, 203 p.

Keller, A. A., Roberts, P. V., and Blunt, M. J., 1999. Effect of fracture aperture variations on the dispersion of contaminants. *Water Resources Research*, v. 35(1), p. 55-63.

Kim, Y.-S., Peacock, D. C. P., and Sanderson, D. J., 2004. Fault damage zones. *Journal of Structural Geology*, v. 26, p. 503-517.

Kohl, T., Evans, K. F., Hopkirk, R. J., Jung, R., and Rybach, L., 1997. Observation and simulation of non-Darcian flow transients in fractured rock. *Water Resources Research*, v. 33(3), p. 407-418.

Kornfält, K.-A. and Wikman, H., 1987. Description to the map (No. 4) of solid rocks of three small areas around Simpevarp, Swedish Hard Rock Laboratory Progress Report 25-87-02a, Swedish Nuclear Fuel and Waste Management Co., Stockholm ,1987.

Kornfält, K-A. and Wikman, H., 1988. The rocks of Äspö Island: Description to the detailed maps of solid rocks including maps of 3 uncovered trenches, Swedish Hard Rock Laboratory Progress Report 25-88-12, Swedish Nuclear Fuel and Waste Management Co., Stockholm.

Kornfält, K.-A., Persson, P.-O., and Wikman, H., 1997. Granitoids from the Äspö area, southeastern Sweden – geochemical and geochronological data, *Geologiska Föreningens I Stockholm Förhandlingar*, v. 119, p.109-114.

Krizek, R. J., Karadi, R. M., and Socias, E., 1972. Dispersion of a contaminant in fissured rock, *Proceedings of the International Society of Rock Mechanics Symposium on Percolation through Fissured Rock*, Stuttgart, Germany.

Lagerbäck, R. and Witschard, F., 1983. Neotectonics in northern Sweden – geological investigations. SKBF/KBS Teknisk Rapport TR-83-58, Swedish Nuclear Fuel and Waste Management Co., Stockholm.

Larsson, S.-Å., and E.-L. Tullborg, 1993. Tectonic regimes in the Baltic Shield during the last 1200 Ma – A review. SKB Technical Report 94-05, Swedish Nuclear Fuel and Waste Management Co., Stockholm

Lee, J.-J. and Bruhn, R. L., 1996. Structural anisotropy of normal fault surfaces. *Journal of Structural Geology*, v. 18(8), p. 1043-1059

Lee, K., 1988. Report on development and validation of conceptual models for major fracture zones, GAI report 873-1313.011, Golder Associates Inc., Redmond, Washington.

Lee, S. H., Lough, M. F., and Jensen, C. L., 2001. Hierarchical modeling of flow in naturally fractured formations with multiple length scales. *Water Resources Research*, v. 37(3), p. 443-455.

Lidmar-Bergström, K., 1991. Phanerozoic tectonics in southern Sweden. *Zeitschrift für Geomorphologie*, v. 82,p. 1-16.

Lin, P. and Logan, J. M., 1991. The interaction of two closely spaced cracks: A rock model study. *Journal of Geophysical Research*, v. 96(B13), p. 21,667-21,675.

Löfgren, M. and Neretnieks, I., Formation factor logging in-situ by electrical methods. SKB Technical Report TR-02-27, Swedish Nuclear Fuel and Waste Management Co., Stockholm.

Logan, J. M., 1992. The influence of fluid flow on the mechanical behavior of faults. In Tillerson, J.R., and Wawersik, W.R., eds., *Rock Mechanics: Proceedings of the 33rd U.S. Symposium*, p. 141-149, Balkema, Rotterdam.

Logan, J. M., Dengo, C. A., Higgs, N. G., and Wang, Z. Z., 1992. Fabric of experimental fault zones: Their development and relationship to mechanical behavior. In *Fault Mechanics and Transport Properties of Rocks*, Academic Press.

Long, J. C. S., Gilmour, P., and Witherspoon, P. A., 1985. A model for steady fluid flow in random three-dimensional networks of disc-shaped fractures. *Water Resources Research*, v. 21(8), p. 1105-1115.

Long, J. C. S., Remer, J. S., Wilson, C. R. and Witherspoon, P. A., 1982. Porous media equivalents for networks of discontinuous fractures. *Water Resources Research*, v.18(3), p. 645-658.

Long, J. C. S. and Witherspoon, P. A., 1985. The relationship of the degree of interconnection to permeability in fracture networks. *Journal of Geophysical Research*, v. 90(B4), p. 3087-3098.

López, D. L. and Smith, L., 1996. Fluid flow in fault zones: Influence of hydraulic anisotropy and heterogeneity on the fluid flow and heat transfer regime, *Water Resources Research*, v. 32(12), p. 3227- 3235.

Louis, C., 1969. A study of groundwater flow in jointed rock and its influence on the stability of rock masses. Imperial College of Rock Mechanics Report No. 10, London.

Lyakhovsky, V., Ben-Zion, Y., and Agnon, A., 1997. Distributed damage, faulting and friction. *Journal of Geophysical Research*, v.102(B12), p. 27,635-27,649.

Makurat, A., Barton, N., Tunbridge, L., and Vik, G., 1990a. The measurement of joint properties at different scales in the Stripa project, *Rock Joints: Proceedings of the International Symposium on Rock Joints*, Loen, Norway, June 4-6, p. 541-548.

Makurat, A., Barton, N., Vik, G. and Tunbridge, L., 1990b. Site characterization and validation – Coupled stress-flow testing of mineralized joints of 200 mm and 1400 mm length in the laboratory and in situ, Stage 3. Stripa Project Technical Report 90-07, Swedish Nuclear Fuel and Waste Management Co., Stockholm.

Malowszewski, P. and Zuber, A., 1985. On the theory of tracer experiments in fissured rocks with a porous matrix, *Journal of Hydrology*, v. 79, p. 333-358.

Mandelbrot, B.B., 1982. *The Fractal Geometry of Nature*, Freeman, San Francisco.

Marone, C. and Scholz, C. H.,1989. Particle-size distribution and microstructures within simulated fault gouge, *Journal of Structural Geology*, v. 11, p. 799-814.

de Marsily, G., 1986. *Quantitative Hydrogeology: Groundwater Hydrology for Engineers*, English edition translated by Gunilla de Marsily, Academic Press, Orlando, Florida, 440 p.

Martel, S. J., 1990. Development of compound fault zones in granitic rock, Mount Abbot quadrangle, Sierra Nevada, California. *Journal of Structural Geology*, v. 12, p. 869-882.

Martel, S. J., 1997. Effects of cohesive zones on small faults and implications for secondary fracturing and fault trace geometry. *Journal of Structural Geology*, v. 19(6), p. 835-847.

Martel, S. J. and Boger, W. A., 1998. Geometry and mechanics of secondary fracturing around small three-dimensional faults in granitic rock. *Journal of Geophysical Research*, v. 103(B9), p. 21,299-21,314.

Martel, S. J., and Pollard, D. D., 1989. Mechanics of slip and fracture along fault zones in granitic rock, Mount Abbot quadrangle, Sierra Nevada, California. *Journal of Geophysical Research*, v. 94, p. 9417-9428.

Martel, S. J., Pollard, D. D., and Segall, P., 1988. Development of simple fault zones in granitic rock, Mount Abbot quadrangle, Sierra Nevada, California. *Geological Society of America Bulletin*, v.100, p. 1451-1465.

Matthäi, S. K. and Belayneh, M., 2004. Fluid flow partitioning between fractures and a permeable rock matrix. *Geophysical Research Letters*, v. 31, L0762, doi: 10.1029/2003GL019027.

Mazurek, M., Bossart, P., and Eliasson, T., 1996. Classification and characterisation of water-conducting fractures at Äspö: Results of observations on the outcrop scale. SKB International Cooperation Report ICR 97-01, Swedish Nuclear Fuel and Waste Management Co., Stockholm.

Mazurek, M., Jakob, A. and Bossart, P., 2003. Solute transport in granitic rocks at Äspö – I: Geologic basis and model calibration. *Journal of Contaminant Hydrology*, v.61, p. 157-174.

McCombie, C. Nuclear waste management worldwide. *Physics Today*, v. 50(6), p. 56-62, 1997.

McKenna, S. A., Meigs, L. C., and Haggerty, R., 2001. Tracer tests in a fractured dolomite: 3. Double-porosity, multiple-rate mass transfer processes in convergent flow tracer tests. *Water Resources Research*, v. 37(5), p. 1143-1154.

Menendez, B., Zhu, W. and Fong, T.-F., 1996. Micromechanics of brittle faulting and cataclastic flow in Berea sandstone. *Journal of Structural Geology*, v. 18(1), p.1-16.

Miller, I., Lee, G., and Sharp, G., 1994. MAFIC matrix/fracture interaction code with solute transport -- User documentation. GAI report, Golder Associates, Redmond, Washington.

Min, K.-B., 2004. Fractured rock masses as equivalent continua – a numerical study. Doctoral thesis, Department of Land and Water Resources Engineering, Swedish Royal Technical Institute.

Moody, J. D. and Hill, M. J., 1956. Wrench-fault tectonics. Geological Society of America Bulletin, v. 67, p. 1207-1246.

Moreno, L. and Neretnieks, I., 1991. Fluid and solute transport in a network of channels. SKB Technical Report 91-44, Swedish Nuclear Fuel and Waste Management Co., Stockholm.

Moreno, L. and Neretnieks, I., 1993. Fluid and solute transport in a network of channels, *Journal of Contaminant Hydrology*, v. 14, p. 163-192.

Moreno, L., Tsang, Y., Tsang, C. F. and Neretnieks, I., 1988. Flow and transport in a single fracture. A two-dimensional statistical model, SKB Technical Report 88-03, Swedish Nuclear Fuel and Waste Management Co., Stockholm.

Morgan, J. K., 1999. Numerical simulations of granular shear zones using the distinct element method. 2. Effects of particle size distribution and interparticle friction on mechanical behavior, *Journal of Geophysical Research*, v. 104(B2), p. 2721-2732.

Morgan, J. K., and Boettcher, M. S., 1999. Numerical simulations of granular shear zones using the distinct element method. 1. Shear zone kinematics and the micromechanics of localization. *Journal of Geophysical Research*, v.104(B2), p. 2703-2719.

Morrow, C. A. and Byerlee, J. D., 1989. Experimental studies of compaction and dilatancy during frictional sliding on faults containing gouge. *Journal of Structural Geology*, v. 11, p. 815-825.

Morrow, C. A., Shi, L. Q., and Byerlee, J. D., 1981. Permeability and strength of San Andreas fault gouge under high pressures. *Geophysical Research Letters*, v. 8(4), p. 325-328.

Morrow, C. A., Shi, L. Q., and Byerlee, J. D., 1984. Permeability of fault gouge under confining pressure and shear stress. *Journal of Geophysical Research*, v 89(B5), p 3193-3200.

Myers, R., and Aydin, A., 1997. The permeability structure of fault zones formed from shearing of preexisting joint zones. *GSA Abstracts with Programs*, p. A-416.

Neretnieks, I., 1980. Diffusion in the rock matrix: An important factor in radionuclide transport? *Journal of Geophysical Research*, v. 85(B8), p. 4379-4397.

Neretnieks, I., Eriksen, T. and Tähtinen, P., 1982. Tracer movement in a single fracture in granitic rock: Some experimental results and their interpretation, *Water Resources Research,* v. 18, p. 849-858.

Neretnieks, I., and Rasmuson, A., 1984. An approach to modelling radionuclide migration in a medium with strongly varying velocity and block sizes along the flow path. *Water Resources Research*, v. 20(12), p.1823-1836.

Neuzil, C. E. and Tracy, J. V., 1981. Flow through fractures, *Water Resources Research*, v. 17, p. 191-199.

Nordenskjöld, C. E., 1944. *Morfologiska studier inom övergångsområdet mellan Kalmarslätt och Tjust* (Morphological studies in the passage area between Kalmar light and Tjust), Carl Bloms Boktryckeri, Lund, 216 p.

Nordqvist, A. W., Tsang, Y. W., Tsang, C.-F., Dverstorp, B., and Andersson, J., 1992. A variable aperture fracture network model for flow and transport in fractured rocks. *Water Resources Research*, v. 28, No. 6, p. 1703-1713.

Novakowski, K. S., Evans, G. V., Lever, D. A. and Raven, K. G., 1985. A field example of measuring hydrodynamic dispersion in a single fracture, *Water Resources Research*, v. 21, No. 8, p. 1165-1174.

Odling, N., 1997. Scaling and connectivity of joint systems in sandstones from western Norway, *Journal of Structural Geology*, v. 19, p. 1257-1271.

Odling, N., 2001. The scaling of hydraulic conductivity in fracture zones. *Geophysical Research Letters*, v. 28(15), p. 3019-3022.

Ohlsson, Y. and Neretnieks, I., 1995. Diffusion data in granite - recommended values, SKB Technical Report TR-95-12, Swedish Nuclear Fuel and Waste Management Co., Stockholm.

Olson, J. E. and Pollard, D. D., 1991. The initiation and growth of en-echelon veins. *Journal of Structural Geology*, v.13, p. 595-608.

Olsson, O. (ed.), 1992. Site characterization and validation – Final report. Stripa Project Technical Report 92-22, Swedish Nuclear Fuel and Waste Management Co., Stockholm.

Osnes, J. D., Winberg, A., and Andersson, J., 1988. Analysis of well test data – Application of probabilistic models to infer hydraulic properties of fractures. Topical Report RSI-0338, RE/SPEC Inc., Rapid City, South Dakota.

Park, S. K. and Roberts, J. J., 2003. Conductivity structure of the San Andreas Fault, Parkfield, revisited. *Geophysical Research Letters*, v. 30(16), p. 1842, doi:10.1029/2003GL017689.

Park, Y. J., and Lee, K. K., 1999. Analytical solutions for solute transfer characteristics at continuous fracture junctions, *Water Resources Research*, v. 35(5), p. 1531-1537.

Park, Y. J., Lee, K. K., and Berkowitz, B., 2001. Effects of junction transfer characteristics on solute in fracture networks. *Water Resources Research*, v. 37(4), p. 909-923.

Peng, S. and Johnson, A. M., 1972. Crack growth and faulting in cylindrical specimens of Chelmsford granite. *International Journal of Rock Mechanics and Mining Science*, v. 9, p. 37-86.

Philip, J., 1988. The fluid mechanics of fracture and other junctions. *Water Resources Research*, v. 24(2), p. 239-246.

Piggott, A. R. and Elsworth, D., 1990. Laboratory studies of transport within a single rock fracture, *Rock Joints: Proceedings of the International Symposium on Rock Joints*, Loen, Norway, June 4-6.

Piper, J. D. A., 1987. *Palaeomagnetism and the Continental Crust*. Open University Press, Milton Keynes, UK.

Poteri, A., Billaux, D., Dershowitz, W., Gómez-Hernandez, J., Cvetkovic, V., Hautojärvi, A., Holton, D., Medina, A., and Winberg, A., 2002. Final report of the TRUE Block Scale project: 3. Modelling of flow and transport. SKB Technical Report TR-02-15, Swedish Nuclear Fuel and Waste Management Co., Stockholm.

Påsse, T., 2001. An empirical model of glacio-isostatic movements and shore-level displacement in Fennoscandia. SKB Report R-01-41, Swedish Nuclear Power and Fuel Co., Stockholm.

Prabhu, N. U., 1965. *Stochastic Processes: Basic Theory and Its Applications.* MacMillan Co., New York, 233 p.

Pyrak-Nolte, L. J., Myer, L. R. and Cook, N. G. W. 1985. Determination of fracture void geometry and contact area as a function of applied load, in *Earth Sciences Division Annual Report 1985*, report LBL-20450, Lawrence Berkeley Laboratory, Berkeley, California, p. 16-17.

Pyrak-Nolte, L. J., Cook, N. G. W. and Nolte, D. D., 1988. Fluid percolation through single fractures, *Geophysical Research Letters*, v. 15, p. 1247-1250.

Press, W. H., Flannery, B. P., Teukolsky, S. A., and Vetterling, W. T., 1986. *Numerical Recipes: The Art of Scientific Computing*, Cambridge University Press, Cambridge, 818 p.

Raven, K. G., Novakowski, K. S., and Lapcevic, P. A., 1988. Interpretation of field tracer tests in a single fracture using a transient solute storage model, *Water Resources Research,* v. 24, p. 2019-2032.

Renshaw, C. E., 2000. Fracture spatial density and the anisotropic connectivity of fracture networks. In Faybishenko, B., Witherspoon, P.A., and Bencon, S.M., *Dynamics of Fluids in Fractured Rock, Geophysical Monograph 122*, American Geophysical Union, Washington, D.C.

Renshaw, C.E. and Pollard, D.D., 1994. Numerical simulation of fracture set formation: A fracture mechanics model consistent with experimental observations. *Journal of Geophysical Research*, v. 99, p. 9359-9372.

Robeson, K. R. and Evans, J. P., 1997. Three-dimensional structure of a small strike slip fault zone, *Abstracts with Programs - Geological Society of America*, v. 29(6), p. 258.

Robinson, P. C., 1984. Connectivity, flow and transport in network models of fractured media. Ph. D. dissertation, St. Catherine's College, Oxford University, Oxford, England.

Robinson, J. W., and Gale, J. E., 1990. A laboratory and numerical investigation of solute transport in discontinuous fracture systems, *Ground Water*, v. 28(1), p. 25-36.

Roux, S., Plouraboue, F., and Hulin, J. P., 1998. Tracer dispersion in rough open cracks, *Transp Porous Media*, v. 32, p. 97-116.

Rudberg, S., 1954. Västerbottens berggrundmorfologi, ett för till rekonstruktions av preglaciala erosionsgenerationer I Sverige. *Geografiska skifter från Upsala Universitets Geografiska Institution*, Appelbergs Boktryckeri AB, Uppsala, 457 p.

Sahimi, M., 1995. *Flow and Transport in Porous Media and Fractured Rock: From classical methods to modern approaches*. VCH, Weinheim, Germany, 482 p..

Schrauf, T. W. and Evans, D. D., 1986. Laboratory studies of gas flow through a single fracture, *Water Resources Research*, v. 22, p. 1038-1050.

Schulson, E. M., Biescu, D., and Renshaw, C. E., 1999. On the initiation of shear faults during compressive brittle failure: A new mechanism. *Journal of Geophysical Research*, v. 104(B1), p. 695-705.

Schulz, S. E. and Evans, J. P., 1998. Spatial variability in microscopic deformation and composition of the Punchbowl Fault, southern California: implications for mechanisms, fluid-rock interaction and fault morphology. *Tectonophysics*, v. 295, p. 223-244.

Schulz, S. E. and Evans, J. P., 2000. Mesoscopic structure of the Punchbowl Fault, southern California and the geological and geophysical structure of active strike-slip faults. *Journal of Structural Geology*, v. 22, p. 913-930.

Segall, P. and Pollard, D. D., 1980. Mechanics of discontinuous faults. *Journal of Geophysical Research*, v. 85, p. 4337-4350.

Segall, P., and Pollard, D. D., 1983. Joint formation in granitic rock of the Sierra Nevada, *Geologic Society of America Bulletin*, v. 94, p. 563-575.

Shapiro, A. M., 1988. Interpretation of Tracer Tests Conducted in an Areally Extensive Fracture in Northeastern Illinois, *Symposium Proceedings of International Conference on Fluid Flow in Fractured Rocks*, Georgia State University, Atlanta, Georgia, May 15-18, p. 12-22.

Shapiro, A. M., and Anderson, J., 1985. Simulation of steady-state flow in three-dimensional networks using the boundary element method. *Advances in Water Resources*, v. 8, p. 106-110.

Sharp, J. C., 1970. Fluid flow through fissured media. Ph. D. dissertation, University of London, Imperial College of Science and Technology, London, U.K.

Sibson, R. H., 1973. Interactions between temperature and pore pressure during earthquake faulting. *Nature*, v. 243, p. 66-68.

Sibson, R. H., 1977. Fault rocks and fault mechanisms. *Geological Society of London Journal*, v. 133, p. 191-231.

Sibson, R. H. 1981. Controls on low-stress hydro-fracture dilatancy in thrust, wrench, and normal fault terrains. *Nature*, v. 289, p. 665-667.

Sibson, R. H., 1992. Implications of fault-valve behavior for rupture nucleation and recurrence. *Tectonophysics*, v. 221, p. 283-293.

Sibson, R. H., 1996. Structural permeability of fluid-driven fault-fracture meshes. *Journal of Structural Geology*, 18(8), p. 1031-1042.

SKB, 1999. SR-97 – Post-closure safety assessment. SKB Technical Report 99-06, Swedish Nuclear Fuel and Waste Management Co., Stockholm.

SKB, 2004. Preliminary site description: Simpevarp area – Version 1.1. SKB Report R-04-25, Swedish Nuclear Fuel and Waste Management Co., Stockholm.

Smith, L., Forster, C. B., and Evans, J. P., 1989. Interaction of fault zones, fluid flow, and heat transfer at the basin scale. In Neuman, S. P. and Neretnieks, I., eds., *Hydrogeology of Low Permeability Environments*. International Association of Hydrogeologists, v. 2, p. 41-67. Verlag Heinz Heise, Hannover, Germany.

Snow, D. T., 1969. Anisotropic permeability of fractured media. *Water Resources Research* 5(6):1273-1289.

Stephens, M. B., 1988. The Scandinavian Caledonides: A complexity of collisions. *Geology Today*, Jan-Feb 1988, p. 20-25.

Stephansson, O., Ljunggren, C., and Jing, L., 1991. Stress measurements and tectonic implication for Scandinavia. *Tectonophysics*, v. 189, p. 317-322.

Stockman, H. W., Li, C., and Wilson, J. L., 1997. A lattice-gas simulation and lattice-Boltzmann study of mixing at continuous fracture junctions: Importance of boundary conditions. *Geophysical Research Letters*, v. 24(12), p. 1515-1518.

Stanfors, R., Erlström, M. and Markström, I, 1991.. Äspö Hard Rock Laboratory: Overview of the investigations 1986-1990. SKB Technical Report 91-20, Swedish Nuclear Fuel and Waste Management Co., Stockholm.

Stratford, R. G., Herbert, A. W. and Jackson, C. P., 1990. A parameter study of the influence of aperture variation on fracture flow and the consequences in a fracture network, *Rock Joints: Proceedings of the International Symposium on Rock Joints*, Loen, Norway, June 4-6, p. 413-422.

Sudicky, E. A., 1989. The Laplace transform Galerkin technique: A time-continuous finite element theory and application to mass transport in groundwater. *Water Resources Research*, v. 25(8), p. 1833-1846.

Sudicky, E. A. and Frind, E. G. 1982. Contaminant transport in fractured porous media: Analytical solutions for a system of parallel fractures, *Water Resources Research*, v. 18(6), p. 1634-1642.

Sudicky, E.A. and McLaren, R.G., 1992. The Laplace transform Galerkin technique for large scale simulation of mass transport in discretely fractured porous formations. *Water Resources Research*, v. 28(2), p. 499-514.

Sultan, L., Claesson, S., Plink-Björklund, P., and Björklund, P., 2004. Proterozoic and Archaean detrital zircon ages from the Palaeoproterozoic Västervik Basin, southern Fennoscandian Shield. *Geologiska Föreningens I Stockholm Förhandlingar*, v.126, p. 39.

Switek, D. P., 1994. Faults as potential hydrocarbon barriers, Arroyo Grande, California. M.S. Thesis, Texas A & M University.

Talbot, C. J., and Munier, R., 1989. Faults and fracture zones on Äspö. SKB Swedish Hard Rock Laboratory Progress Report 25-89-11, Swedish Nuclear Fuel and Waste Management Co., Stockholm.

Taylor, G. I., 1953. Dispersion of soluble matter in solvent flowing slowly through a tube. *Proceedings of the Royal Society of London A*, v. 219, p. 186-203.

Tirén, S., 1989. Geological setting and deformation history of a low angle fracture zone at Finnsjön, Sweden, in SKB Technical Report 89-19, Swedish Nuclear Fuel and Waste Management Co., Stockholm.

Tirén, S., and Beckholmen, M., 1990. Rock block configuration in Southern Sweden and crustal deformation. *Geologiska Föreningens I Stockholm Förhandlingar*, v. 112(4), p. 361-364.

Tirén, S.A., Askling, P., and Wänstedt, S., 1999. Geologic site characterization for deep nuclear waste disposal in fractured bedrock based on 3D data visualization, *Engineering Geology*, v. 52, p. 319-346.

Tirén, S.A., Beckholmen, M., Voss, C., and Askling, P., 1996. Development of a geological and structural model of Äspö, southeastern Sweden (SITE-94), SKI Report 96:16, Swedish Nuclear Power Inspectorate, Stockholm.

Tirén, S.A., Wedholm, K., Sträng, T., and Geier, J., 2005. Field study of fracture zones exposed in two adjacent roadcuts in granitic rock. Comparison with interpreted lineaments and characterisation of internal structural variability. Ekolsund/Grillby area, Uppland, south-central Sweden. SKI Report R 05-xx [in preparation], Swedish Nuclear Power Inspectorate, Stockholm.

Tsang, C. F. and Doughty, C., 2003. A particle-tracking approach to simulating transport in a complex fracture. *Water Resources Research*, v. 37(7),1174, doi: 10.1029/2002WR001614.

Tsang, Y. W., 1984. The effects of tortuosity on fluid flow through a single fracture, *Water Resources Research,* v. 20, p. 1209-1215.

Tsang, Y. W. and C. F. Tsang, 1987. Channel model of flow through fractured media, *Water Resources Research,* v. 23, p. 467-479.

Tsang, Y. W. and Tsang, C. F., 2001. A particle-tracking method for advective transport in fractures with diffusion into finite matrix blocks. *Water Resources Research*, v. 37(3), p. 831-835.

Tsang, Y.W., Tsang, C. F., Hale, F. V., and Dverstorp, B., 1996. Tracer transport in a stochastic continuum model of fractured media, *Water Resources Research*, v. 32(10), p. 3077-3092.

Tsang, Y.W. and Witherspoon, P.A., 1981. Hydromechanical behavior of a deformable rock fracture subject to normal stress, *Journal of Geophysical Research,* v. 86, p. 9287-9298.

Tsang, Y.W. and Witherspoon, P.A., 1983. The dependence of fracture mechanical and fluid flow properties on fracture roughness and sample size, *Journal of Geophysical Research,* v. 88, p. 2359-2366.

Tullborg, E.-L., Larsson, S.-Å., and Stiberg, J.-P., 1996. Subsidence and uplift of the present land surface in the southeastern part of the Fennoscandian Shield. *Geologiska Föreningens I Stockholm Förhandlingar*, v. 118, p. 126-128.

Turcotte, D.L., 1986. Fractals and fragmentation. *Journal of Geophysical Research*, v. 91(B2), p. 1921-1926.

Voss, C., Tirén, S., and Glynn, P., 1996. Hydrogeology of Äspö Island, Simpevarp, Sweden (SITE-94), SKI Report 96:13, Swedish Nuclear Power Inspectorate, Stockholm.

Valkiainen, M., Aalto, H., Lehikoinen, J., and Uusheimo, K., 1996. The effect of thickness in the through-diffusion experiment. Technical Research Centre of Finland (VTT), Espoo, Finland, 33 p.

Waite, M. E., Ge, S., Spetzler, H. and Bahr, D.B., 1998. The effect of surface geometry on fracture permeability: A case study using a sinusoidal fracture, *Geophysical Research Letters*, v. 25(6), p. 813-816.

Wahlgren, C.-H., Persson, I., Danielsson, P. Berglund, J., Triumf, C.-A., Mattsson, H., and Thunehed, H., 2003. Geologiskt underlag för val av prioriterad plats inom området väster om Simpevarp, Delrapport 1-4, SKB P-03-06, Swedish Nuclear Fuel and Waste Management Co., Stockholm.

Wallace, R. E., 1973. Surface fracture patterns along the San Andreas fault, *in* Kovach, R.L. and Nur, A., eds., *Proceedings of the Conference on Tectonic Problems of the San Andreas Fault System*, Stanford University Publication Geological Science, v. XIII, p. 173-180.

Wang, J. S. Y. and Narasimhan, T. N., 1988. Fractal and statistical characterization of rough fracture, *Symposium Proceedings of International Conference on Fluid Flow in Fractured Rocks*, Georgia State University, Atlanta, Georgia, May 15-18, p. 220-228.

Wang, J. S. Y, Narasimhan, T. N. and Scholz, C.H., 1988. Aperture correlation of a fractal fracture, *Journal of Geophysical Research,* v. 93, p. 2216-2224.

Warren, T. E. and Root, P. J., 1963. The behavior of naturally fractured reservoirs, *Society of Petroleum Engineers Journal*, v. 3, p. 245-255.

Willemse, E. J. M., and Pollard, D. D., 1998. On the orientation and patterns of wing cracks and solution surfaces at crack tips. *Journal of Geophysical Research*, v. 103(B2), p. 2427-2438.

Wilson, C. R., 1970. An investigation of laminar flow in fractured porous rocks. Ph.D. thesis, University of California, Berkeley, 178 p.

Winberg, A., Andersson, P., Poteri, A., Cvetkovic, V., Dershowitz, W., Hermanson, J., Gómez-Hernandez, J., Hautojärvi, A., Billaux, D., Tullborg, E.-L., Holton, D., Meier, P., and Medina, A., 2002. Final report of the TRUE Block Scale project: 4. Synthesis and retention in the block scale. SKB Technical Report TR-02-16, Swedish Nuclear Power and Fuel Co., Stockholm.

Witherspoon, P.A., 1979. Observations of a potential size effect in experimental determination of the hydraulic properties of fractures, *Water Resources Research,* v. 15, p. 1142-1146.

Witherspoon, P. A., Wang, J. S. Y., Iwai, K. and Gale, J. E., 1979. Validity of cubic law for fluid flow in a deformable rock fracture, Report LBL-9557/SAC-23/UC-70, Swedish-American Cooperative Program on Radioactive Waste Storage in Mined Caverns in Granitic Rock, Swedish Nuclear Fuel and Waste Management Co., Stockholm.

Witherspoon, P. A., Wang, J. S. Y., Iwai, K. and Gale, J. E., 1980. Validity of cubic law for fluid flow in a deformable rock fracture, *Water Resources Research*, v. 16, p. 1016-1024.

Wörman, A., Geier, J., and Xu, S., 2004. Modelling of radionuclide transport by groundwater motion in fractured bedrock for performance assessment purposes. SKI Report 2004:14, Swedish Nuclear Power Inspectorate, Stockholm.

Xu, S., Wörman, A., and Dverstorp, B., 2001. Heterogeneous matrix diffusion in crystalline rock – implications for geosphere retardation of migrating radionuclides. *Journal of Contaminant Hydrology*, v. 47(2-4), p. 365-378.

Yeo, I. W. and Ge, S., 2001. Solute dispersion in rock fractures by non-Darcian flow, *Geophysical Research Letters*, v. 28(20), p. 3983-3986.

Zhang, X. and Sanderson, D.J., 1996. Numerical modelling of the effects of fault slip on fluid flow around extensional faults. *Journal of Structural Geology*, v. 18(1), p. 109-119.

Zimmerman, R. W., Chen, D. W., Long, J. C. S. and Cook, N. G. W., 1990. Hydromechanical coupling between stress, stiffness, and hydraulic permeability of rock joints and fractures, *Rock Joints: Proceedings of the International Symposium on Rock Joints*, Loen, Norway, June 4-6, p. 571-577.

Zimmerman R.W. and Bodvarsson, G.S., 1996. Hydraulic conductivity of rock fractures, *Transp. Porous Media*, v. 23, p. 1-30.

Zimmerman R. W., Kumar, S., and Bodvarsson, G. S., 1991. Lubrication theory analysis of the permeability of rough-walled fractures, *Int. J. Rock Mech. Min Sci. Abstr.*, v. 28, p. 325-331.

Zoback, M. D., Zoback, M. L., Mount, V., Eaton, J., Healy, J., Oppenheimer, D., Reasonberg, P., Jones, L., Raleigh, B., Wong, I., Scotti, O., and Wentworth, C., 1987. New evidence on the state of stress of the San Andreas fault system. *Science*, v. 238, p. 1105-1111.

APPENDICES

Appendix A Preparation of detailed maps of fracture zones

The detailed-scale mapping of the fracture zones at Äspö was carried out in May, 1999 as follows. A reference line was laid on the outcrop by compass sighting. A 1 m x 1 m square frame, with 10 cm x 10 cm grid divisions, was laid over the rock in alignment with the reference line, and moved along the reference line in overlapping increments. For each frame position, the inclination of the frame was measured along two orthogonal sides, and the rock surface was photographed from a height of about 2.5 m using a step ladder. To produce a 1:10 scale field map of the N to NNW trending zone, the fracture configuration for each frame position was sketched on 2 mm graph paper by scaling fracture traces from the 10 cm x 10 cm grid to 1 cm x 1 cm squares on the paper.

In this way a continuous photographic mosaic was produced, within which the true coordinates of points along fractures could be determined by comparison to the reference grid. The outcrops were also filmed with a hand-held video camera, to provide a continuous record of each outcrop. Photographs from this work have been stored both as the original film (slides and print negatives, giving maximum resolution) and as scanned, high-resolution digital images in JPEG format on CD-ROMs for computer analysis.

As a check on the photographic mapping method, a 1:10 scale field map was prepared for a 1 m x 6 m portion of one N-striking zone, by sketching directly from the outcrop. The fracture configuration was sketched on 2 mm graph paper by scaling fracture traces from the 10 cm x 10 cm grid to 1 cm x 1 cm squares on the paper. Fracture strikes and dips were measured on the outcrop for 48 of the most extensive fractures on this map.

Working with the digital images, the fracture traces were digitized as graphical overlays on the computer screen. Correction for photographic distortion was made by use of a digital rubber-sheeting algorithm in the *splinter* analysis program (on accompanying CD-ROM), to transform the digitized traces and grid lines so that the quadrilaterals formed by intersecting grid lines throughout the image are restored to 10 cm squares.

At the Ekolsund site, the photographic mapping procedure was modified as the 1 m square grid was not practical for use on the near-vertical, larger-scale exposures. Instead, reference points were marked on the rock face with spray paint (water-soluble so that the rock would not be permanently defaced) prior to photographing the outcrops with a digital camera. Distances between pairs of reference points were measured by tape, to allow construction of a

Euclidean distance matrix which could be used to correct for photographic distortion and large-scale nonplanarity of the exposures.

The method for mapping individual traces was also modified to allow better checking of fracture traces in the field. The digital images were printed onto A4 (30 cm x 21 cm) paper and laminated, to provide a base for sketching fracture traces at an approximately 1:10 scale, directly on the printed images, while viewing the exposure.

For the detailed mapping of fracture zones, the aim was to identify and sketch all fractures and faults longer than 10 cm, within the entire area covered by the photograph. Structural details including splays and fragmented or brecciated zones within small faults were mapped in this way to an estimated resolution of about 2 cm. Fracture orientations and directions of lineations and slickensides were measured for the larger fractures and noted on the field map.

Finally each field map (laminated image with sketched fracture traces) was scanned so that the fracture traces could be digitized and analyzed, by the same procedures used for the Äspö images. With the procedure adopted at Ekolsund, the digitization was simplified, and reliability improved, by identifying and verifying each fracture trace at the exposure, rather than only from a digital image of limited resolution.

The graphical map analysis program *splinter* (included as supplementary digital materials), was used to calculate the coordinates of the digitized fracture traces in an orthogonal coordinate system aligned with geographic north, and to correct for skewed photographic angles, lens distortion (convergence) and tilt of the reference frame. After converting the digitized fracture traces to real-world coordinates, the traces from each image were combined to produce a single map of each exposure. As a final step, the reference grid lines were removed to give a clean map.

The end product, for each exposure, is a single map that show fracture traces on scales from a few mm up to over 10 m. Thus the maps show structural details on scales that range over four orders of magnitude.

The initial digitization from photographic images was done with a commercial, computer-assisted drawing software which allowed zooming to arbitrarily fine scales and drawing of vector-format lines over a digital image. The fracture trace and grid coordinates, as digitized from the images, were stored in AutoCAD (DXF) vector format for further processing and analysis using the program *splinter*. This is an interactive, graphical code

based on the *gtk* free-software toolkit, which is supported on the Linux platform. The *splinter* code was developed as part of this research program, and included on the accompanying CD-ROM.

Corrections for skewed photographic angle, camera lens distortion, and frame tilt were made by marking "pinpoints" of known coordinates on plots of the fracture traces and reference grid lines,. Given the known coordinates of these points, and frame tilt data as measured in the field, *splinter* calculates a rotation matrix and x-y polynomial of appropriate order, to map the plotted points into the real-world coordinate system. The order of the polynomial is increased when more points are specified, to allow smooth, spatially variable transformations ("rubber-sheeting") which map each pinpoint to the exact, specified coordinates, while intervening areas of the plot may be mapped nonlinearly, *e.g.* to correct for photographic distortion.

This method does not correct for all sources of error in the photographic mapping process. Nonplanarity of the outcrop surface, in combination skewed photographic angles and lens distortion, can result in errors in the mapped positions of points, even after making the corrections described above. Such errors are minimized, but not eliminated, by photographing from an angle that is close to perpendicular to the plane of the reference frame and outcrop surface.

Comparison of corresponding points from overlapping pairs of images indicates that the magnitude of such errors is typically less than 5 mm between adjacent, 1 m square frame positions. Typical manual errors in digitization, which affect comparisons between fractures that are adjacent to each other on a single image, are estimated to be 1 mm or less.

A complete map of the outcrop was assembled by combining the trace data from adjacent, photographed panels. Small offsets between adjacent map panels, due to errors such as described above, were corrected by applying a uniform linear displacement to bring the corresponding points into alignment. The residual errors between points that could not be brought into agreement in this manner were typically 3 mm or less.

Appendix B Discrete Feature Model for flow and solute transport in fractured granitic rock

A discrete-feature modeling (DFM) code for numerical simulation of flow and transport in a network of discrete features was developed as one part of this research. The code is based on the finite-element method, and is designed for the following general conceptualization of the hydrogeological system in the bedrock.

Features are planar or piecewise-planar entities representing fractures, fracture zones, disturbed zones around tunnels, or other water-conducting elements in the rock. The geometry of the features is defined in terms of triangular elements with connections defined by nodes (vertices) that are shared between elements.

Boundaries are defined in terms of groups of element vertices which are in contact with a specific physical boundary or segment of a boundary, such as a section of a borehole, a tunnel, or the ground surface. Boundary conditions are assigned to these boundary groups for each stage of the simulation.

Fluid flow simulations are restricted to the case of a single-phase, uniform-density, Newtonian fluid, *e.g.* groundwater under conditions of complete saturation and negligible density variation.

Steady-state flow is modeled by the Galerkin finite-element method. Transient flow may be modeled either by a backward-difference scheme, or by a Laplace-transform Galerkin (LTG) formulation of the finite-element equations. In a given stage of a flow simulation, the boundary conditions at a given boundary group may be specified head, specified flux, or specified net flux.

Transport simulations are restricted to the case of a single dissolved species at dilute concentrations (*i.e.* low enough to neglect the influence of concentration on fluid density gradients), influenced by advection and diffusion (including dispersion phenomena), sorption, and matrix diffusion.

Transport is modeled either by a discrete-parcel random-walk (particle-tracking) method or by a LTG formulation of the finite-element equations for advection and dispersion. Two alternative particle-tracking algorithms are supported: 2-D advective-dispersive transport within a given element, or 3-D advective-diffusive transport with an assumed parabolic velocity profile giving rise to Taylor dispersion. In a given stage of a transport simulation, the

boundary conditions at a given boundary group may be specified concentration, specified mass flux, or specified net mass flux.

As in an ordinary 2-D, finite-element mesh, the geometry of the mesh is encoded as an ordered list of global coordinate vectors $\{\boldsymbol{x}_n, n = 1, 2, ..., N_n\}$ for each of the N_n unique nodes (element vertices) in the mesh, and as a list of N_e triangular elements, each of which is defined by a triplet of node indices $\{n_{e1}, n_{e2}, n_{e3}\}$ and by a vector of parameter values $\{S_e, T_e, b_e, ...\}$ which are derived from the parent feature of the element. The mesh differs from an ordinary 2-D mesh in that the global coordinates $\boldsymbol{x}_n$ are necessarily specified in 3-D, and in that element nodes and edges that lie along intersections between two or more different features are shared among the elements formed from the different features, to account for the hydrologic connections between features.

Four different types of boundary conditions (BCs) are employed:

Type 1: Specified head:

$$h_n(t) = \hat{h}_B(\boldsymbol{x},t)\,|_{\boldsymbol{x}=\boldsymbol{x}_n}, \qquad n \in B$$

Type 2: Specified flux:

$$Q_n(t) = \int_{A_B} \hat{q}_B(\boldsymbol{x},t)\,\psi_{B,n}(\boldsymbol{x})\,dA, \qquad n \in B$$

Type 3: Specified net flux:

$$\sum_{n \in B}^{N} Q_n(t) = \hat{Q}_B(t); \qquad h_{bn}(t) = h_B(t), \quad n \in B$$

Type 4: Specified infiltration per unit surface area:

$$Q_n(tQ_n(t)) = \sum_{e:n\subset n_e} \int_e \hat{q}_B(\boldsymbol{x},t)\,\psi_e(\boldsymbol{x})\,dA, \quad n \in B$$

where circumflexes denote specified (*i.e.* known) quantities, and where Q_n and h_n are the flux

(into the mesh) and head at a given node, $Q_B(t)$ is the specified influx (m^3/s) and h_B is the head at a given boundary B, and $\psi_{e(n)}$ is the element basis function associated with the eth element at node n.

The specified-net-flux BC is used to account for the "superconductive" connection that occurs where several features are intersected by a given borehole section. For passive monitoring sections, Q_B is set to zero, and for actively pumped sections, Q_B is set to the specified pumping rate.

Simulation sequences of arbitrary complexity can be constructed as a series of stages, within each of which flow and/or transport is simulated with respect to a specified set of boundary conditions. The results of each stage serving as the initial conditions for the next stage.

Simulation sequences are defined in input files that specify the mesh to be used, and for each stage, the boundary conditions, physical parameters, and solver options. Plain-text, free-format input based on keyword recognition (rather than order of input) is supported for straightforward checking and documentation of simulations. Boundaries can be referenced by site-specific names (*e.g.* "Borehole_KAS07" or "ground_surface"). Physical parameters can be specified in terms of units used in the field data; the code automatically checks for correct dimensionality and scales the numerical values to SI units for internal calculations.

Development and documentation of the code is ongoing in relation to other projects. A copy of the version of the source code used for this research, and current draft user documentation, are included in supplemental electronic materials with this dissertation. The code is written in standard ANSI C but has only been tested on a Linux platform using the GNU compiler.

The following sections give mathematical details of the flow and solute transport solvers.

Derivation of matrix equations for flow

At a given point $\boldsymbol{x}$ in a medium with transmissivity $T(\boldsymbol{x})$ and storativity $S(\boldsymbol{x})$, conservation of mass combined with Darcy's law yields the transient flow equation:

$$S\frac{\partial h}{\partial t} = \nabla\cdot(T\nabla h) + q_i\delta(\boldsymbol{x}-\boldsymbol{x}_i) = S\frac{\partial h}{\partial t}$$

where h is hydraulic head, t is time, and q_i is the influx (water entering the medium) from a point source at $\boldsymbol{x}_i$.

Let:

$$\hat{h}(\boldsymbol{x},t) = \sum_{j=1}^{N} h_j(t)w_j(\boldsymbol{x})$$

be a discrete approximation of $h(\boldsymbol{x},t)$, where $h_j(t)$ is the hydraulic head at the jth node, $j = 1, 2, \ldots, N$, and where $w_j(\boldsymbol{x})$ is some spatial weighting function. Substituting for h in (1) we obtain:

$$S\sum_{j=1}^{N}\frac{\partial h_j}{\partial t}w_j - \nabla\cdot\left(T\sum_{j=1}^{N}h_j\nabla w_j\right) + q_i\delta(\boldsymbol{x}-\boldsymbol{x}_i) = -S\sum_{j=1}^{N}\frac{\partial h_j}{\partial t}w_j 0$$

or:

$$\sum_{j=1}^{N}\nabla\cdot(T\nabla w_j)h_j - \sum_{j=1}^{N}Sw_j\frac{dh_j}{dt} + q_i\delta(\boldsymbol{x}-\boldsymbol{x}_i) = 0$$

Requiring orthogonality with respect to the weighting functions, and choosing weighting functions that are defined piecewise on individual element areas A^e, so that $w_i = 0$ for $\boldsymbol{x}_i \notin A^e$, gives:

$$0 = \int_A \left\{ \sum_{j=1}^{N} h_j \nabla\cdot(T\nabla w_j) - \sum_{j=1}^{N} \frac{dh_j}{dt} S w_j + q_i \delta(\boldsymbol{x} - \boldsymbol{x}_i) \right\} w_i dA$$

$$= \sum_{j=1}^{N} \left[h_j \sum_e \int_{A^e} w_i \nabla\cdot(T\nabla w_j) dA - \frac{dh_j}{dt} \sum_e \int_{A^e} w_i S w_j dA \right] + \sum_e \int_{A^e} q_i \delta(\boldsymbol{x} - \boldsymbol{x}_i) w_i dA$$

where the summation over e is understood to indicate summation over all elements e.

If node locations are chosen such that any source/sink term q_i coincides with a node at $\boldsymbol{x}_i$, then:

$$\sum_e \int_{A^e} q_i \delta(\boldsymbol{x} - \boldsymbol{x}_i) w_i dA = q_i$$

since $w_i = 1$ at $\boldsymbol{x}_i$. Defining:

$$d_{ij}^e = \int_{A^e} S w_i w_j dA$$

$$a_{ij}^e = \int_{A^e} w_i \nabla\cdot(T\nabla w_j) dA$$

and defining the NxN matrices $\mathbf{A} = [\sum a^e_{ij}]$ and $\mathbf{D} = [\sum d^e_{ij}]$ and the 1xN column vectors $\boldsymbol{h}(t) = [h_j(t)]^T$ and $\boldsymbol{q}(t) = [q_i(t)]^T$, the preceding equation may be written as:

$$\mathbf{A}\boldsymbol{h}(t) - \mathbf{D}\frac{d\boldsymbol{h}}{dt} = -\boldsymbol{q}(t) + \mathbf{D}\boldsymbol{h}(0)$$

or by rearranging we obain the general matrix equation for transient flow:

$$\mathbf{D}\frac{d\boldsymbol{h}}{dt} - \mathbf{A}\boldsymbol{h}(t) = \boldsymbol{q}(t)$$

Steady-state flow

For steady-state flow, $d\boldsymbol{h}/dt = 0$ and the finite-element equation is simply:

$$\mathbf{A}\boldsymbol{h}(t_\infty) = -\boldsymbol{q}(t_\infty)$$

Laplace-Galerkin formulation for transient flow

In the following, the Laplace transform with respect to t of a given function $f(t)$ will be denoted by an overbar, *i.e.*:

$$\mathcal{L}[f(t)] = \int_0^\infty f(t)\mathrm{e}^{-st}dt = \bar{f}(s)$$

From the properties of the Laplace transform, $\mathcal{L}[d\boldsymbol{h}/dt] = s\mathcal{L}[\boldsymbol{h}(t)] - \boldsymbol{h}(0)$. Substituting this relationship into the Laplace transform of the general matrix equation for transient flow gives:

$$\mathbf{D}[s\bar{\boldsymbol{h}}(s) - \boldsymbol{h}(0)] - \mathbf{A}\bar{\boldsymbol{h}}(s) = \bar{\boldsymbol{q}}(s)$$

or:

$$[s\mathbf{D} \mp \mathbf{A}]\bar{\boldsymbol{h}}(s) = \bar{\boldsymbol{q}}(s) + \mathbf{D}\boldsymbol{h}(0)$$

Backward-difference formulation for transient flow

The backward-difference approximation of the time derivative is:

$$\left(\frac{d\boldsymbol{h}}{dt}\right)_{t=t_{n+1}} \approx \frac{\boldsymbol{h}(t_{n+1}) - \boldsymbol{h}(t_n)}{t_{n+1} - t_n} = \frac{\boldsymbol{h}_{n+1} - \boldsymbol{h}_n}{\Delta t_{n+1}}$$

Substituting this approximation for the time derivative in the general matrix equation for transient flow:

$$\frac{1}{\Delta t_{n+1}}\mathbf{D}[\boldsymbol{h}_{n+1} - \boldsymbol{h}_n] - \mathbf{A}\boldsymbol{h}_{n+1} = \boldsymbol{q}_{n+1}$$

or:

$$\left[\frac{1}{\Delta t_{n+1}}\mathbf{D}\boldsymbol{h}_{n+1}] - \mathbf{A}\right]\boldsymbol{h}_{n+1} = \boldsymbol{q}_{n+1} + \frac{1}{\Delta t_{n+1}}\mathbf{D}\,\boldsymbol{h}_n$$

which can be solved stepwise for the head vectors $\boldsymbol{h}_i = \boldsymbol{h}(t_i)$, i=1,2, ..., given the initial head vector $\boldsymbol{h}_0 = \boldsymbol{h}(t_0)$.

Finite element coefficients

Case 1: $S(\boldsymbol{x})$ and $T(\boldsymbol{x})$ piecewise constant

If $S(\boldsymbol{x})$ and $T(\boldsymbol{x})$ are constant within each element, *i.e.* $S(\boldsymbol{x}) = S_e$ and $T(\boldsymbol{x}) = T_e$, then $\nabla T = 0$ and:

$$d_{ij}^e = \int_{A^e} S_e w_i w_j dA = S_e \int_{A^e} w_i w_j dA$$

$$a_{ij}^e = \int_{A^e} w_i \nabla (T_e \nabla w_j) dA = T_e \int_{A^e} w_i \nabla^2 w_j dA$$

$$= T_e \left[\int_{A^e} \nabla \cdot (w_i \nabla w_j) dA - \int_{A^e} \nabla w_i \cdot \nabla w_j dA \right]$$

$$= T_e \left[\int_{\partial A^e} w_i \nabla w_j \cdot \boldsymbol{n}\, ds - \int_{A^e} \nabla w_i \cdot \nabla w_j dA \right]$$

by Gauss' divergence theorem.

Case 2: $S(\boldsymbol{x})$and $T(\boldsymbol{x})$ piecewise linear

If $S(\boldsymbol{x})$and $T(\boldsymbol{x})$ are taken to be piecewise linear within each element:

$$T(\boldsymbol{x}) = \sum_{k \in e} T_k w_k(\boldsymbol{x}) = \sum_{k \in e} T_k w_k(\boldsymbol{x})$$

$$S(\boldsymbol{x}) = \sum_{k \in e} T_k w_k(\boldsymbol{x}) = \sum_{k \in e} T_k w_k(\boldsymbol{x})$$

then:

$$d_{ij}^{e}\mathbf{D} = \sum_{k\in e} S_k d_{ijk}^{e}, \qquad d_{ijk}^{e} = \int_{A^e} w_i w_j w_k dA$$

$$a_{ij}^{e} = \sum_{k\in e} T_k a_{ijk}^{e}, \qquad a_{ijk}^{e} = \int_{A^e} w_i [\nabla\cdot(w_k \nabla w_j)] dA$$

By expanding the dot product and making use of the identity $\nabla\cdot(w_i w_k \nabla w_j) = \nabla(w_i w_k)\cdot\nabla w_j + w_i w_k \nabla^2 w_j$, the coefficients a_{ijk} can be expressed as:

$$a_{ijk}^{e} = \int_{A^e} w_i(\nabla w_k\cdot\nabla w_j) dA + \int_{A^e} w_i w_k \nabla^2 w_j dA$$

$$= \int_{A^e} w_i(\nabla w_k\cdot\nabla w_j) dA + \int_{A^e} \nabla\cdot(w_i w_k \nabla w_j) dA - \int_{A^e} \nabla(w_i w_k)\cdot\nabla w_j dA$$

$$= \int_{\partial A^e} w_i w_k \nabla w_j \cdot \mathbf{n}\, ds - \int_{A^e} (\nabla w_i\cdot\nabla w_j) w_k dA$$

Laplace-Galerkin formulation of transient flow problem

At a given point $\boldsymbol{x}$ in a medium with transmissivity $T(\boldsymbol{x})$ and storativity $S(\boldsymbol{x})$, conservation of mass combined with Darcy's law yields the transient flow equation:

$$S\frac{\partial h}{\partial t} = \nabla\cdot(T\nabla h) + q_i\delta(\boldsymbol{x}-\boldsymbol{x}_i)$$

where h is hydraulic head, t is time, and q_i is the influx from a point source at $\boldsymbol{x}_i$.

Taking the Laplace transform with respect to t gives:

$$S(s\bar{h}-h_0) = \nabla\cdot(T\nabla\bar{h}) + \bar{q}_i\delta(\boldsymbol{x}-\boldsymbol{x}_i)$$

which may be written as:

$$sS\bar{h} \pm \nabla\cdot(T\nabla\bar{h}) - \bar{f} = 0$$

where:

$$\bar{f} = \bar{q}_i\delta(\boldsymbol{x}-\boldsymbol{x}_i) + Sh_0$$

and where the Laplace transform of any given function $F(\boldsymbol{x},t)$ is indicated by an overbar, *i.e.*:

$$\mathcal{L}[F(\boldsymbol{x},t)] = \int_0^\infty F(\boldsymbol{x},t)e^{-st}dt = \bar{F}(\boldsymbol{x},s)]$$

Let:

$$\hat{h}(\boldsymbol{x},t) = \sum_{j=1}^{N} h_j(t)w_j(\boldsymbol{x})$$

be a discrete approximation of $h(\boldsymbol{x},t)$, where $h_j(t)$ is the hydraulic head at the jth node, $j = 1, 2,$

... , N, and where $w_j(\boldsymbol{x})$ is some spatial weighting function. Taking the Laplace transform of the matrix flow equation and substituting for $\mathfrak{L}[\boldsymbol{h}]$ we obtain:

$$sS\sum_{j=1}^{N}\bar{h}_j w_j \pm \nabla\cdot\left(T\sum_{j=1}^{N}\bar{h}_j\nabla w_j\right) - \bar{f} = 0$$

or:

$$\sum_{j=1}^{N}\bar{h}_j[sSw_j \mp \nabla\cdot(T\nabla w_j)] - \bar{f} = 0$$

Requiring orthogonality with respect to the weighting functions, and choosing weighting functions that are defined piecewise on individual element areas A^e, so that $w_i = 0$ for $\boldsymbol{x}_i \notin A^e$, gives:

$$0 = \int_A\left\{\sum_{j=1}^{N}\bar{h}_j[sSw_j - \nabla\cdot(T\nabla w_j)] - \bar{f}\right\}w_i dA$$

$$= \sum_{j=1}^{N}\bar{h}_j\sum_e\int_{A^e}[sSw_i w_j - w_i\nabla\cdot(T\nabla w_j) - \bar{f}w_i]dA$$

$$= \sum_{j=1}^{N}\bar{h}_j\sum_e\left(\int_{A^e}sSw_i w_j dA - \int_{A^e}w_i\nabla T\cdot\nabla w_j dA - \int_{A^e}w_i T\nabla^2 w_j dA\right)$$
$$- \int_A\bar{q}_i w_i dA - \sum_{j=1}^{N}h_j(0)\sum_e\int_{A^e}Sw_i w_j dA$$

where the summation over e is understood to indicate summation over all elements e. If node locations are chosen such that any source/sink term q_i coincides with a node at $\boldsymbol{x}_i$, then

$\int_A\bar{q}_i w_i dA = \bar{q}_i$ since $w_i = 1$ at $\boldsymbol{x}_i$.

For constant $S(x) = S_e$ and $T(x) = T_e$ over each element, $\nabla T = 0$ giving:

$$\sum_{j=1}^{N} \bar{h}_j \sum_e \left(sS_e \int_{A^e} w_i w_j dA \pm T_e \int_{A^e} w_i \nabla^2 w_j dA \right) = \bar{q}_i + \sum_{j=1}^{N} h_j(0) \sum_e \left(S_e \int_{A^e} w_i w_j dA \right)$$

or:

$$\sum_{j=1}^{N} \bar{h}_j \sum_e (sS_e d_{ij}^e \pm T_e a_{ij}^e) = \bar{q}_i + \sum_{j=1}^{N} h_j(0) \sum_e S_e d_{ij}^e$$

where:

$$d_{ij}^e = \int_{A^e} w_i w_j dA$$

$$a_{ij}^e = \int_{A^e} w_i \nabla^2 w_j dA = \int_{A^e} \nabla \cdot (w_i \nabla w_j) dA - \int_{A^e} \nabla w_i \cdot \nabla w_j dA$$

$$= \int_{\partial A^e} w_i \nabla w_j \cdot \nabla \boldsymbol{n}\, ds - \int_{A^e} \nabla w_i \cdot \nabla w_j dA$$

by Gauss' divergence theorem. Defining the NxN matrices $\mathbf{A} = [\sum T_e a^e{}_{ij}]$ and $\mathbf{D} = [\sum S_e d^e{}_{ij}]$ and the 1xN column vectors $\boldsymbol{h}(t) = [h_j(t)]^T$ and $\boldsymbol{q}(t) = [q_i(t)]^T$, this may be written as:

$$[s\mathbf{D} \mp \mathbf{A}]\bar{\boldsymbol{h}}(s) = \bar{\boldsymbol{q}}(s) + \mathbf{D}\boldsymbol{h}(0)$$

where overbars denote Laplace transforms with respect to t.

The corresponding matrix equation for the case of steady-state flow is obtained in a similar fashion but without using the Laplace transform. Letting $\partial h/\partial t = 0$ in gives the steady-state flow equation:

$$S\frac{\partial h}{\partial t} + \nabla \cdot (T \nabla h) = q_i \delta(x - x_i)$$

By substituting the piecewise linear approximation for $h(x)$, and requiring orthogonality with respect to the weighting functions w_i, the matrix equation obtained is:

$$\mathbf{A}\boldsymbol{h}(t) = \boldsymbol{q}(t) + \mathbf{D}\boldsymbol{h}(0)$$

If instead of assuming constant $S(x)$and $T(x)$ over each element, these are taken to be piecewise linear:

$$T(x) = \sum_{k=1}^{N} T_k w_k(x) = \sum_e \sum_{k \in e} T_k w_k(x)$$

$$S(x) = \sum_{k=1}^{N} T_k w_k(x) = \sum_e \sum_{k \in e} T_k w_k(x)$$

then the matrices **A** and **D** are replaced by:

$$\mathbf{D} = \left[\sum_e \sum_{k \in e} S_k d^e_{ijk} \right], \qquad d^e_{ijk} = \int_{A^e} w_i w_j w_k \, dA$$

$$\mathbf{A} = \left[\sum_e \sum_{k \in e} T_k a^e_{ijk} \right], \qquad a^e_{ijk} = \int_{A^e} w_i [\nabla \cdot (w_k \nabla w_j)] \, dA$$

By expanding the dot product in the expresion for hte matrix coefficients a_{ijk} and making use of the identity $\nabla \cdot (w_i w_k \nabla w_j) = \nabla(w_i w_k) \cdot \nabla w_j + w_i w_k \nabla^2 w_j$, the coefficients a_{ijk} can be expressed as:

$$a_{ijk}(x) = \int_{A^e} w_i (\nabla w_k \cdot \nabla w_j) \, dA + \int_{A^e} w_i w_k \nabla^2 w_j \, dA$$

$$= \int_{A^e} w_i (\nabla w_k \cdot \nabla w_j) \, dA + \int_{A^e} \nabla \cdot (w_i w_k \nabla w_j) \, dA - \int_{A^e} \nabla (w_i w_k + w_i w_k) \cdot \nabla w_j \, dA$$

$$= \int_{\partial A^e} w_i w_k \nabla w_j \cdot \boldsymbol{n} \, ds - \int_{A^e} (\nabla w_i \cdot \nabla w_j) w_k \, dA$$

Laplace-Galerkin formulation of transport problem

At a given point $\boldsymbol{x}$ in a fracture zone with effective 2-D hydrodynamic dispersion tensor $\mathbf{D}(\boldsymbol{x})$, the mass balance equation for a single non-sorbing solute species is (neglecting matrix diffusion):

$$\frac{\partial c}{\partial t} + \boldsymbol{v}\cdot\nabla c - \nabla\cdot(\mathbf{D}\nabla c) + q_c = 0$$

where $\boldsymbol{v}(\boldsymbol{x})$ is the advective velocity ($\boldsymbol{q}/\theta$), c is the concentration (averaged over the aquifer thickness), and $q_c(\boldsymbol{x})$ is the total mass influx through the two sides of the fracture zone.

For the case of a linearly and reversibly sorbing tracer, the first term in Equation 1 is modified as:

$$R\frac{\partial c}{\partial t} + \boldsymbol{v}\cdot\nabla c - \nabla\cdot(\mathbf{D}\nabla c) + q_c = 0$$

where $R = R(\boldsymbol{x})$ is a retardation coefficient accounting for surface sorption. Taking the Laplace transform with respect to t gives:

$$R(s\bar{c} - c_0) + \boldsymbol{v}\cdot\nabla\bar{c} - \nabla\cdot(\mathbf{D}\nabla\bar{c}) + \bar{q}_c = 0$$

Let:

$$\hat{c}(\boldsymbol{x},t) = \sum_{j=1}^{N} c_j(t) w_j(\boldsymbol{x})$$

be a discrete approximation of $c(\boldsymbol{x},t)$, where $c_j(t)$ is the concentration at the jth node, $j = 1, 2, \ldots, N$, and where $w_j(\boldsymbol{x})$ is some spatial weighting function.

Taking the Laplace transform and substituting for $\mathcal{L}[c]$ in (4) we obtain:

$$R\left[s\sum_{j=1}^{N}\bar{c}_j w_j - \sum_{j=1}^{N} c_j(0) w_j\right] + \sum_{j=1}^{N}\bar{c}_j\left[\boldsymbol{v}\cdot\nabla w_j - \nabla\cdot(\mathbf{D}\nabla w_j)\right] + \bar{q}_c = 0$$

or:

$$\sum_{j=1}^{N}\bar{c}_j\left[Rs w_j + \boldsymbol{v}\cdot\nabla w_j - \nabla\cdot(\mathbf{D}\nabla w_j)\right] + \bar{q}_c - Rc_0\sum_{j=1}^{N} c_j(0) w_j = 0$$

Requiring orthogonality with respect to the weighting functions, and choosing weighting functions that are defined piecewise on individual element areas A^e, so that $w_i = 0$ for $\boldsymbol{x}_i \notin A^e$, gives:

$$0 = \int_A \left\{\sum_{j=1}^{N}\bar{c}_j\left[Rs w_j + \boldsymbol{v}\cdot\nabla w_j - \nabla\cdot(\mathbf{D}\nabla w_j)\right] + \bar{q}_c - R\sum_{j=1}^{N} c_j(0) w_j\right\} w_i dA$$

$$= \sum_{j=1}^{N}\bar{c}_j \sum_e \int_{A^e}\left[Rs w_i w_j + w_i \boldsymbol{v}\cdot\nabla w_j - w_i\nabla\cdot(\mathbf{D}\nabla w_j)\right] dA$$

$$+ \int_{A^e}\bar{q}_c w_i - \sum_{j=1}^{N} c_j(0)\sum_e \int_{A^e} R w_i w_j dA$$

or:

$$\sum_{j=1}^{N}\bar{c}_j \sum_e \left(s\int_{A^e} R w_i w_j dA + \int_{A^e} w_i \boldsymbol{v}\cdot\nabla w_j dA - \int_{A^e} w_i\nabla\cdot(\mathbf{D}\nabla w_j) dA\right)$$

$$= -\int_A \bar{q}_{c_i} w_i dA + \sum_{j=1}^{N} c_j(0)\sum_e \int_{A^e} R w_i w_j dA$$

where the summation over e is understood to indicate summation over all elements e, and

$$\int_A \bar{q}_{c_i} w_i dA = \bar{q}_{c_i}$$

where summation over the doubled indices m and n is implied.

If node locations are chosen such that any source/sink term q_{ci} coincides with a node at $\boldsymbol{x}_i$, then:

$$h(\boldsymbol{x}) \approx \sum_{k=1}^{N} h_k w_k(\boldsymbol{x}) \int_A \bar{q}_{c_i} w_i dA = \bar{q}_{c_i}$$

since $w_i = 1$ at $\boldsymbol{x}_i$.

Thus:

$$\sum_{j=1}^{N} \bar{c}_j \left(\sum_e s b_{ij} + \sum_e u_{ij} \right) = \sum_{j=1}^{N} c_j(0) \sum_e b_{ij} - \bar{q}_{c_i}$$

where:

$$b_{ij}^e = \int_{A^e} R w_i w_j dA$$

$$u_{ij}^e = \int_{A^e} w_i \boldsymbol{v} \cdot \nabla w_j dA - \int_{A^e} w_i \nabla \cdot (\mathbf{D} \nabla w_j) dA$$

The result can also be expressed in matrix notation as:

$$[s\mathbf{B} - \mathbf{U}]\bar{\boldsymbol{c}}(s) = \mathbf{B}\boldsymbol{c}(0) - \bar{\boldsymbol{q}}_c(s)$$

where **B** and **U** are NxN matrices $\mathbf{B} = [\sum b^e_{ij}]$ and $\mathbf{U} = [\sum u^e_{ij}]$ and $\boldsymbol{c}(t) = [c_j(t)]^T$ and $\boldsymbol{q}_c(t) = [q_{ci}(t)]^T$ are 1xN column vectors.

Under the assumption of a steady-state flow field, $\boldsymbol{v}$ is a constant vector satisfying $\boldsymbol{v} = -(T/b_T)\nabla h$, where b_T is an effective transport aperture (pore volume per unit area). Using the same piecewise-linear approximation for head as in the finite element flow model:

$$h(\boldsymbol{x}) \approx \sum_{k=1}^{N} h_k w_k(\boldsymbol{x})$$

where h_j are the nodal head coefficents determined from a steady-state flow calculation, this gives:

$$\boldsymbol{v}(\boldsymbol{x}) \approx \frac{-T(\boldsymbol{x})}{b_T(\boldsymbol{x})} \sum_{k \in e}^{N} h_k \nabla w_k(\boldsymbol{x})$$

Substituting this approximation into the previous expressions for the coefficents b_{ij} and u_{ij} gives:

$$b^e_{ij} = \int_{A^e} R w_i w_j dA$$

$$u^e_{ij} = \sum_{k \in e} h_k \int_{A^e} \frac{T}{b_T} w_i \nabla w_j \cdot \nabla w_k dA - \int_{A^e} w_i \nabla \cdot (\mathbf{D} \nabla w_j) dA$$

The above integrals depend only on the weighting functions, the calculated nodal heads, and the hydrologic properties **D**, T, and b_T, which are assumed to be constant with respect to time. Typically the principal directions of the dispersion tensor **D** will depend on the direction of the hydraulic gradient, and hence the last term in the result for u_{ij} will be related to the h_k.

Calculation of element coefficients

The principal directions of the local dispersion tensor $\mathbf{D} = [d_{ij}]$ $(i,j = 1,2)$ need to be determined from the local direction of the hydraulic gradient ∇h. Let $\boldsymbol{y}$ denote a 2-D system of Cartesian coordinates within the plane of an element, such that the coordinate y_1 is aligned with $-\nabla h$ and y_2 is in the perpendicular direction. The dispersion tensor in the $\boldsymbol{y}$ system is assumed to be:

$$\mathbf{D}_y = \begin{bmatrix} D_L + D_m & 0 \\ 0 & D_T + D_m \end{bmatrix}$$

where:

$D_L = v\alpha_L$ is the longitudinal dispersion coefficient,

$D_T = v\alpha_T$ is the longitudinal dispersion coefficient,

$v = |\boldsymbol{v}| = (T/b_T)|\nabla h|$ is the magnitude of the fluid velocity, and

D_m = coefficient of molecular diffusion.

For convenience we also define:

$$D_L' = D_L + D_m$$

$$D_T' = D_T + D_m$$

Let $\boldsymbol{x}$ denote a second 2-D system of Cartesian coordinates in the plane of the element (*e.g.*, the coordinates used to define the element geometry), with $\boldsymbol{x} = \mathbf{0}$ located at the same physical point as $\boldsymbol{y} = \mathbf{0}$. The coordinate transformation from the $\boldsymbol{y}$ system to the $\boldsymbol{x}$ system is defined in terms of a tensor with constant coefficients:

$$a_{ij} = \frac{\partial x_i}{\partial y_j}$$

so that $x_i = a_{ij}y_j$. The inverse transformation is:

$$a_{ij}' = \frac{\partial y_i}{\partial x_j} = a_{ji}$$

It is easily confirmed that the components a_{ij} are related to ∇h as:

$$\left[a_{ij}\right] = \frac{-1}{|\nabla h|}\begin{bmatrix} \dfrac{\partial h}{\partial x_1} & \dfrac{\partial h}{\partial x_2} \\ -\dfrac{\partial h}{\partial x_2} & \dfrac{\partial h}{\partial x_1} \end{bmatrix}$$

The scalar quantity $\nabla \cdot (\mathbf{D}\nabla c)$ must be invariant with respect to coordinate transformation, hence:

$$\nabla_x \cdot (\mathbf{D}_x \nabla_x c) = \nabla_y \cdot (\mathbf{D}_y \nabla_y c)$$

where the subscripts x and y denote which coordinate system is being referred to. In tensor notation (with the convention of summation on doubled indices) this can be written and expanded as:

$$\frac{\partial}{\partial x_i} d_{ij_x} \frac{\partial c}{\partial x_j} = \frac{\partial}{\partial y_k} d_{kl_y} \frac{\partial c}{\partial y_l}$$

$$a_{ik} \frac{\partial}{\partial y_k} d_{ij_x} a_{jl} \frac{\partial c}{\partial y_l} = \frac{\partial}{\partial y_k} d_{kl_y} \frac{\partial c}{\partial y_l}$$

$$\frac{\partial}{\partial y_k} a_{ik} d_{ij_x} a_{jl} \frac{\partial c}{\partial y_l} = \frac{\partial}{\partial y_k} d_{kl_y} \frac{\partial c}{\partial y_l}$$

yielding the relationship between the dispersion tensor components in the x and y systems:

$$d_{kl_y} = a_{ik} d_{ij_x} a_{jl}$$

Making use of the relationship between the forward and inverse transformations as given above, we obtain:

$$
\begin{aligned}
d_{kl_y} &= a'_{ki} d_{ij_x} a_{jl} \\
a_{mk} d_{kl_y} a'_{ln} &= a_{mk} a'_{ki} d_{ij_x} a_{jl} a'_{ln} \\
a_{mk} d_{kl_y} a_{nl} &= \delta_{mi} d_{ij_x} \delta_{jn} \\
a_{mk} d_{kl_y} a_{nl} &= d_{mn_x} \delta_{jn}
\end{aligned}
$$

which by replacing dummy indices yields the inverse relationship:

$$
d_{kl_x} = a_{ki} d_{ij_y} a_{lj}
$$

Expanding the second term in the previously obtained result for u_{ij} in tensor notation gives:

$$
\begin{aligned}
u^e_{ij\ II} = \int_{A^e} w_i \nabla\cdot(\mathbf{D}\nabla w_j) dA &= \int_{A^e} w_i \frac{\partial}{\partial x_m}\left(d_{mn_x} \frac{\partial w_j}{\partial x_n} \right) dA \\
&= \int_{A^e} w_i \frac{\partial d_{mn_x}}{\partial x_m} \frac{\partial w_j}{\partial x_n} dA + \int_{A^e} w_i d_{mn_x} \frac{\partial^2 w_j}{\partial x_m \partial x_n} dA
\end{aligned}
$$

For a uniform velocity field within a given element, ordinarily a uniform **D** will be assumed, so $\partial d_{mn}/\partial x_m = 0$ giving:

$$
u^e_{ij\ II} = \int_{A^e} w_i d_{mn} \frac{\partial^2 w_j}{\partial x_m \partial x_n} dA
$$

The integrand is invariant with respect to rotation of the coordinate system, since:

$$
\begin{aligned}
d_{mn_x}\frac{\partial^2 w_j}{\partial x_m \partial x_n}\,dA &= a_{mk} d_{kl_y} a_{nl}\frac{\partial y_p}{\partial x_m}\frac{\partial y_q}{\partial x_n}\frac{\partial^2 w_j}{\partial y_p \partial y_q} \\
&= a_{mk} d_{kl_y} a_{nl} a'_{pm} a'_{qn}\frac{\partial^2 w_j}{\partial y_p \partial y_q} \\
&= \delta_{pk} d_{kl_y} \delta_{ql}\frac{\partial^2 w_j}{\partial y_p \partial y_q} \\
&= d_{mn_y}\frac{\partial^2 w_j}{\partial y_m \partial y_n}
\end{aligned}
$$

In the y coordinate system, noting that $d_{11y} = D_L'$, $d_{22y} = D_T'$, and $d_{mny} = 0$ for $m \neq n$ we obtain:

$$
\begin{aligned}
u^e_{ij\ II} &= \int_{A^e} w_i \left(d_{11_y}\frac{\partial^2 w_j}{\partial y_1^2} + d_{22_y}\frac{\partial^2 w_j}{\partial y_2^2} \right) dA \\
&= D_T' \int_{A^e} w_i \left(r^2\frac{\partial^2 w_j}{\partial y_1^2} + \frac{\partial^2 w_j}{\partial y_2^2} \right) dA
\end{aligned}
$$

where $r = \sqrt{(D_L'/D_T')}$.

This integral can be evaluated more easily by mapping it to a modified coordinate system z : $\{z_1 = y_1/r, z_2 = y_2\}$, so $r^2\partial^2 w/\partial y_1^2 = \partial^2 w/\partial z_1^2$ and $dA_y = r dA_z$, giving:

$$u_{ij\ II}^{e} = D_T' \int_{A_z^e} w_i \left(\frac{\partial^2 w_j}{\partial z_1^2} + \frac{\partial^2 w_j}{\partial z_2^2} \right) r dA_z$$

$$= r D_T' \int_{A_z^e} w_i \nabla_z^2 w_j dA_z$$

$$= \sqrt{D_L' D_T'} \int_{A_z^e} w_i \nabla_z^2 w_j dA_z$$

$$= \sqrt{D_L' D_T'} \left[\int_{\partial A_z^e} w_i \nabla_z w_j \cdot \boldsymbol{n} ds_z - \int_{A_z^e} \nabla_z w_i \cdot \nabla_z w_j dA_z \right]$$

Note that the quantity in square braces is equal to a_{ij}^e / T_e as defined for the finite-element model for flow.

Thus in the case of uniform T_e and b_T within each element, the coefficients u_{ij}^e can be calculated as:

$$u_{ij}^{e} = u_{ij\ I}^{e} - u_{ij\ II}^{e}$$

where the first term:

$$u_{ij\ I}^{e} = \frac{T}{b_T} \sum_{k \in e} h_k \int_{A^e} w_i \nabla w_j \cdot \nabla w_k dA$$

contains an integral identical to the second term in the expression for a_{ijk}^e, and where the second term is readily calculated as:

$$u_{ij\ II}^{e} = \frac{\sqrt{D_L' D_T'}}{T_e} a_{ij\ z}^{e}$$

Appendix C Correspondence of particle radius distribution and penetration-distance relationship

For a matrix composed of a large assemblage of spherical particles with any radius distribution $f(r) \geq 0$ on $r = [0,\infty]$, satisfying:

$$\int_0^\infty f(r)dr = 1$$

Let $V(s)$ be the volume of matrix within a skin depth s of the surface of any particle. The complementary volume of matrix which is **not** within a skin depth s of the surface:

$$\overline{V}(s) = V_{total} - V(s)$$

is related to $f(r)$ by:

$$\overline{V}(s) = \int_s^\infty f(r)\tfrac{4\pi}{3}(r-s)^3 dr$$

Differentiating this with respect to the skin depth s (noting that s is in the lower limit of the integral as well as in the integrand) gives:

$$\frac{d\overline{V}}{ds} = -4\pi\int_s^\infty f(r)(r-s)^2 dr - f(r)\frac{4\pi}{3}(r-s)^3\Big|_{r=s} = -4\pi\int_s^\infty f(r)(r-s)^2 dr$$

Since V_{total} is constant, the first derivative of $V(s)$ is simply the negative of the preceding expression:

$$\frac{dV}{ds} = 4\pi\int_s^\infty f(r)(r-s)^2 dr$$

Exponential case

For the case of an exponential distribution of particle radius:

$$f(r) = \lambda e^{-\lambda r}$$

the corresponding first derivative of $V(s)$ is obtained by straightforward integration:

$$\frac{dV}{ds} = 4\pi \int_s^\infty \lambda e^{-\lambda r}(r-s)^2 dr = 4\pi\lambda e^{-\lambda s} \int_0^\infty e^{-\lambda t} t^2 dt = \frac{8\pi}{\lambda^2} e^{-\lambda s}$$

making use of the substitution $t = r–s$. Thus this function has the same form as the exponential distribution, but scaled by a constant $8\pi/\lambda^3$.

Appendix D Volume-depth relationship for a regular fractal assemblage of cubes

Consider the set of cube-shaped fragments formed by the following process: Beginning with an arbitrarily large cube of side length L_0, divide the cube into 8 equal cubes of side length $L_1 = L_0/2$, and choose a fraction $a/8$ of these cubes. For $n = 1,2, ..., \infty$, take the chosen fraction of cubes from the previous step, and subdivide each into 8 equal cubes of side length $L_n = L_{n-1}/2$, and choose the same fraction $a/8$ of those.

In the assemblage of cubes resulting from this process, each cube contains a copies of itself, scaled by a factor of ½. The similarity dimension of such a set (Falconer, 1990) is thus $D = -\log a/\log(½) = \log a/\log 2$.

The number of undivided cubes of a given side length $L_n = 2^{-n}L_0$ is $N(L_n) = (8-a)a^n$. For large n the limiting log slope of the particle size distribution $N(L_n)$ versus L_n is:

$$\lim_{n\to\infty}\frac{\log N(L_n)}{\log L_n} = \lim_{n\to\infty}\frac{\log L_0 + \log(8-a) + n\log a}{\log L_0 - n\log 2} = -\frac{\log a}{\log 2} = -D$$

Thus this assemblage has a (discrete) power-law size distribution with exponent $-D$.

We note that choosing $a = 1$yields a constant (discrete) distribution of particle sizes with $D = 0$. Choosing $a = 2$ yields $D = 1$, $a = 4$ yields $D = 2$, and $a = 8$ yields $D = 3$. These values pertain to space-filling processes of dimension D.

To illustrate this, suppose that at each step of the process, we always choose to subdivide $a = 2$ cubes along a major diagonal of the original cube. This process condenses to that diagonal line (a 1-D geometry). If at each step we always choose to subdivide $a = 4$ cubes along a vertical plane that slices diagonally across the original cube, this process condenses to that plane (a 2-D geometry). If at each step we choose to subdivide all $a = 8$ cubes, we fill the entire 3-D space of the original cube with vanishingly small cubes. In the case $a = 1$, the process condenses to a single point (a zero-dimensional geometry).

Thus we may regard the similarity dimension D as representing the dimension of the process. For values of a leading to non-integral values of D, we may regard D as the "fractal" dimension of this process, following Mandelbrot (1982). From this we may note the correspondence between the negative exponent of a power-law distribution of particle sizes, and the fractal dimension of the resulting set of particles.

For the present study we are interested in the incremental volume of matrix as a function of skin depth from the surface of a particle. For a given cube of side length L_n, the volume within a skin depth s of the surface is:

$$V_n(s) = \begin{cases} L_n^3 - (L_n - 2s)^3 & , s \le L_n / 2 \\ L_n^3 & , s \ge L_n / 2 \end{cases}$$

and the derivative of V_n with respect to s is:

$$V_n'(s) = \frac{dV_n}{ds} = \begin{cases} 3(L_n - 2s)^2 & , s \le L_n / 2 \\ 0 & , s \ge L_n / 2 \end{cases}$$

The total incremental volume function $V'(s)$ is obtained by summing over all cubes:

$$V'(s) = \sum_{n=0}^{\infty} N_n V_n'(s)$$

Since cubes of side length $L_n \le 2s$ do not contribute to $V'(s)$, we may limit the summation to:

$$V'(s) = \sum_{n=0}^{m} N_n V_n'(s), \qquad m = \text{int}\left(\frac{\log(L_0 / s)}{\log 2} \right) - 1$$

Substituting the previous expression for $N(L_n)$ and noting that $L_n = 2^{-n}L_0$, we obtain:

$$V'(s) = \sum_{n=0}^{m} (8-a)a^n \cdot 3\left(2^{-n}L_0 - 2s\right)$$

which simplifies to:

$$V'(s) = 6L_0(8-a)\sum_{n=0}^{m}\left(2^{-(n+1)} - \frac{s}{L_0}\right)a^n$$

with m as defined above. For comparison to data, we need only the log slope of $V'(s)$ vs. s.

Values of the log slope for different values of a, and the corresponding D, were calculated as listed in Table D-1. The arbitrary value of L_0 does not affect the results provided it is very large relative to the values of s considered; for these calculations, $L_0 = 10^{10}$ length units was used and slopes were fitted to logarithmically spaced values of s in the range 10^{-6} to 10^2 length units. For values of $1 < a < 4$ corresponding to $0 < D < 2$, the absolute value of p is close to zero; thus the incremental matrix volume with increasing skin depth is approximately constant for D in this range. For $4 < a < 8$ corresponding to $2 < D < 3$, we obtain $p \approx 2-D$ within the apparent numerical precision.

Table D-1. Numerically calculated values of p, the log slope of $V'(s)$ for the fractal cube model as a function of a and the corresponding fractal dimension D of the particle size distribution. Note the result for $a/8 = 1.000^{(*)}$ was obtained using $a = 8 - 10^{-6}$ since the above formula becomes indeterminate for this value.

$a/8$	D	p
0.1250	0.000	-2.4×10^{-8}
0.1875	0.585	-3.9×10^{-8}
0.2500	1.000	-1.8×10^{-7}
0.3125	1.322	-4.2×10^{-6}
0.3750	1.585	-1.2×10^{-4}
0.4375	1.807	-2.7×10^{-3}
0.5000	2.000	-0.040
0.5625	2.170	-0.174
0.6250	2.322	-0.322
0.6875	2.459	-0.460
0.7500	2.585	-0.585
0.8125	2.700	-0.701
0.8750	2.807	-0.808
0.9375	2.907	-0.908
0.9500	2.926	-0.927
0.9625	2.945	-0.946
0.9750	2.963	-0.964
0.9875	2.982	-0.983
0.9938	2.991	-0.992
0.9950	2.993	-0.994
0.9962	2.995	-0.995
0.9975	2.996	-0.997
0.9988	2.998	-0.999
$1.0000^{(*)}$	3.000	-1.000